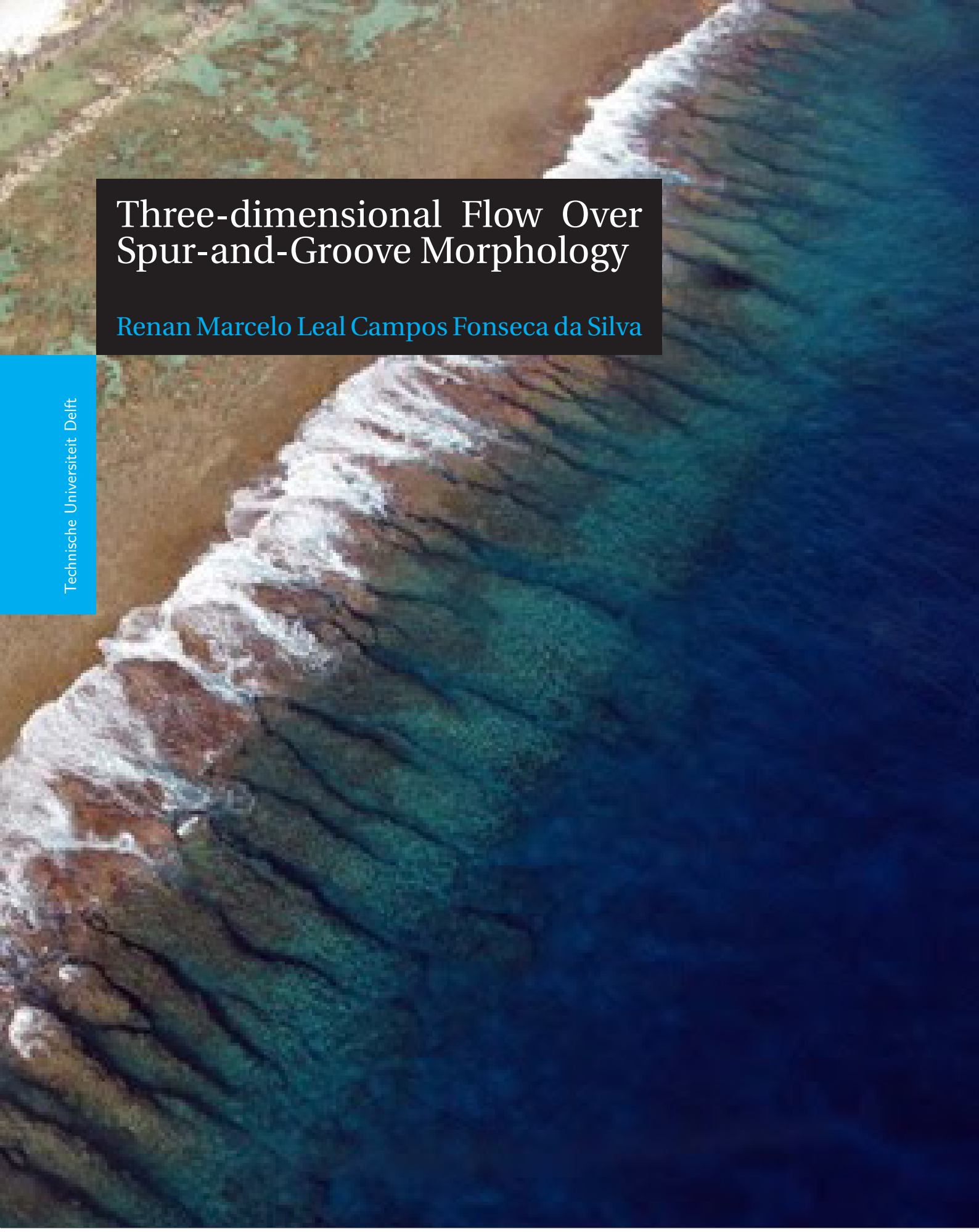

Three-dimensional Flow Over Spur-and-Groove Morphology

Renan Marcelo Leal Campos Fonseca da Silva

Technische Universiteit Delft

TU Delft Delft University of Technology

Challenge the future

ERASMUS +: ERASMUS MUNDUS MOBILITY PROGRAMME

Master of Science in

COASTAL AND MARINE ENGINEERING AND MANAGEMENT

CoMEM

Three-dimensional Flow Over Spur-and-Groove Morphology

Delft University of Technology
03/07/2017

Renan Marcelo Leal Campos Fonseca da Silva

The Erasmus+: Erasmus Mundus MSc in Coastal and Marine Engineering and Management is an integrated programme including mobility organized by five European partner institutions, coordinated by Norwegian University of Science and Technology (NTNU).

The joint study programme of 120 ECTS credits (two years full-time) has been obtained at two or three of the five CoMEM partner institutions:

- Norges Teknisk- Naturvitenskapelige Universitet (NTNU) Trondheim, Norway
- Technische Universiteit (TU) Delft, The Netherlands
- Universitat Politècnica de Catalunya (UPC). BarcelonaTech. Barcelona, Spain
- University of Southampton, Southampton, Great Britain
- City, University London, London, Great Britain

During the first three semesters of the programme, students study at two or three different universities depending on their track of study. In the fourth and final semester an MSc project and thesis has to be completed. The two-year CoMEM programme leads to a multiple set of officially recognized MSc diploma certificates. These will be issued by the universities that have been attended by the student. The transcripts issued with the MSc Diploma Certificate of each university include grades/marks and credits for each subject.

Information regarding the CoMEM programme can be obtained from the programme coordinator:

Øivind A. Arntsen, Dr.ing.
Associate professor in Marine Civil Engineering
Department of Civil and Transport Engineering
NTNU Norway
Telephone: +4773594625 Cell: +4792650455 Fax: + 4773597021
Email: oivind.arntsen@ntnu.no

CoMEM URL: https://www.ntnu.edu/studies/mscomem

CoMEM Master Thesis

This thesis was completed by:
Renan Marcelo Leal Campos Fonseca da Silva

Under supervision of:

Prof. dr. ir. A.J.H.M. Reniers, TU Delft
Dr. M.F.S. Tissier, TU Delft
Ir. Max Radermacher, TU Delft
Johan Reyns, Deltares IHE-Delft
Dr. Curt Storlazzi, USGS
Dr. ir. Robert McCall, Deltares
Dr. ir. Ap van Dongeren, Deltares

As a requirement to attend the degree of
Erasmus+: Erasmus Mundus Master in Coastal and Marine Engineering and Management (CoMEM)

Taught at the following educational institutions:

Norges Teknisk- Naturvitenskapelige Universitet (NTNU)
Trondheim, Norway

Technische Universiteit (TU) Delft
Delft, The Netherlands

University of Southampton,
Southampton, Great Britain

At which the student has studied from August 2015 to July 2017.

THREE-DIMENSIONAL FLOW OVER SPUR-AND-GROOVE MORPHOLOGY

by

Renan Marcelo Leal Campos Fonseca da Silva

in partial fulfillment of the requirements for the degree of

Master of Science
in Coastal & Marine Engineering and Management

at the Delft University of Technology,
to be defended publicly on Monday July 10th, 2017 at 02:00 PM.

An electronic version of this thesis is available at `http://repository.tudelft.nl/`.

Correspondance with the author may be directed to:
rfonsecadasilva@gmail.com

TU Delft Delft University of Technology

In collaboration with

Keywords: Spurs-and-grooves, Coral reef environments, Wave hydrodynamics, Delft3D, SWAN, 3D flow, Shoaling zone, Pre-littoral zone, Fore reef hydrodynamics.

Front Cover: This image shows spur and groove reef formation off Huahine Island, French Polynesia. Source: Living Ocean Foundations, 2012.

What I cannot create, I do not understand.

Richard Feynman

SUMMARY

Spurs-and-grooves (SAG) are a common and impressive characteristic of shallow fore reef areas worldwide. Although the existence and geometrical properties of SAG are well-documented ever since the 50's, the literature concerning specifically the hydrodynamics around them is sparse. This study provides a characterization of the 3D flow patterns found on SAG formations, and a sensitivity of that flow for a set of short wave and SAG geometry parameters, as well as for alongshore and long wave forcing. Its main interest is to provide scientists predictive capability of the flow conditions for a set of conditions commonly found on coral reef systems with SAG formations. Delft3D-FLOW coupled with SWAN/XBeach (3D phase-averaged) was applied to model schematic SAG formations.

Shore-normal shoaling waves on top of SAG formations are shown to drive two circulations cells, the first in deeper waters with offshore spur and onshore groove depth-averaged velocities (offshore cell), and the second in shallower depths with offshore groove and onshore spur depth-averaged currents (onshore cell). In the offshore cell, the cross-shore velocity profile shows vertically monotonic currents - onshore to grooves and offshore to spurs -, except for the bottom, at which velocities are always onshore. In the onshore cell, the velocity profile shows offshore surface velocities and onshore bottom currents for both spur and groove, with resulting depth-averaged offshore groove and onshore spur velocities.

The mechanism driving this flow results from the wave forcing being mostly balanced by pressure gradients both in the cross-shore and alongshore, and the mismatch between those is balanced by horizontal turbulent forces, that are higher in deeper waters, and friction, larger in shallower waters. Variations of this pattern are associated with changes in the velocity profile, that fundamentally depend on the wave, SAG geometry and alongshore forcing parameters.

The waves are the main driving of the SAG flow, and as such wave parameters play a fundamental role in the SAG hydrodynamics.

- Wave heights are the most important parameter associated with the flow strength - higher waves induce significantly stronger circulation cells. When wave heights start breaking due to depth limitation, the SAG circulation cell is lost, and the velocity profile shape starts having onshore surface and undertow with maximum values at mid depth; and
- Wave periods have moderate influence on the velocity values found on SAG circulation cells - higher wave periods induce slightly higher velocities. When the wave steepness reaches the breaking limit, the whitecapping results in changes of the velocity profile similarly to the case of depth-induced breaking waves.

The SAG geometry has a very important role associated with the resulting SAG hydrodynamics. Overall, the spur height, SAG wavelength and the SAG shape provide the biggest influence on the hydrodynamics.

- The spur heights have significantly influence in the strength of SAG circulation cells - higher spur heights are associated with stronger flows;
- The SAG wavelengths moderately influence the strength of the flow, with longer SAG wavelengths resulting in not much stronger SAG circulation cells. Shorter SAG wavelengths do not present the offshore SAG circulation cell, due to higher alongshore mixing of momentum that gives offshore spur and groove currents in that zone;
- The shape of the SAG formations is, together with the wave heights, the most important parameter influencing the strength of the flow. SAG formations with peak spur height located further onshore (Buttress type) have SAG circulation with higher velocities involved and the zonation of the SAG circulation cells changes accordingly, i.e., lower peak spur height depths have circulation cells shifted onshore, with widening of the offshore cell;
- The reef slope, without significant interference in the strength or velocity profile shape, also affects the zonation of SAG circulation cells, with steeper slopes providing wider SAG offshore circulation cells; and

- The groove width, the differential roughness between spur and groove, and the reef flat widths were shown to have a minor role in the SAG hydrodynamics.

The alongshore forcing leads to an alongshore transport system. The degree of the alongshore dominance is directionally proportional to the alongshore forcing. In the cross-shore direction, the onshore SAG circulation cell was persistent, while the offshore cell can be undermined with large alongshore forcing.

Long waves were shown to result in negligible influence in the mean SAG hydrodynamics, associated with the low long wave forcing observed in the SAG zone. They are primarily more important as approaching and within the reef flat, and the water exchange between this and the SAG zones was concluded to have limited influence in the SAG flow.

In terms of coral growth and health, bottom shear stresses were found to be systematically higher over spurs than grooves, resulting in a higher potential for coral development over them due to increasing water motion. Accordingly, sediment transport potential is higher over spurs, for which alongshore currents are higher than grooves, thus sediments would tend to drift towards the grooves, where they would more likely deposit due to lower shear stresses. The fact that SAG with distinct shapes - with significant different peak spur height depths - experience similar bottom shear stresses suggests the existence of a range of ideal hydrodynamics conditions for coral development.

CONTENTS

Summary v

List of Figures xi

List of Tables xix

List of Abbreviations xxi

List of Symbols xxiii

Acknowledgements xxv

1 Introduction 1
- 1.1 Motivation and Research Significance . . . 1
- 1.2 Research question . . . 2
- 1.3 Outline . . . 3

2 Background 5
- 2.1 Coral Reef Environments . . . 5
- 2.2 Spurs-and-grooves (SAG) formations . . . 8
  - 2.2.1 Formation of spurs-and-grooves . . . 9
  - 2.2.2 Spurs-and-grooves geometry . . . 9
  - 2.2.3 Hydrodynamic function of SAG formations . . . 14
- 2.3 Hydrodynamics in spurs-and-grooves . . . 15
- 2.4 Physical processes in SAG structures . . . 18
  - 2.4.1 Wave propagation . . . 18
  - 2.4.2 Wave forces . . . 19
  - 2.4.3 Wave effects on the mean flow . . . 22
  - 2.4.4 Wave induced currents . . . 22

3 Methodology 25
- 3.1 Selection of Model . . . 25
  - 3.1.1 Wave model concepts . . . 25
  - 3.1.2 Relevant processes . . . 27
  - 3.1.3 Selection . . . 28
  - 3.1.4 Model description . . . 28
- 3.2 Modelling Plan . . . 30
  - 3.2.1 Simulations to address research questions . . . 30
  - 3.2.2 Modelling approach . . . 31
  - 3.2.3 Range of parameters . . . 33
  - 3.2.4 Modelling steps . . . 35
  - 3.2.5 Model setup . . . 38

4 Calibration and Verification 45
- 4.1 Conventions . . . 45
- 4.2 Calibration . . . 46
  - 4.2.1 Wave propagation . . . 46
  - 4.2.2 Currents . . . 48
  - 4.2.3 Momentum balance . . . 52
  - 4.2.4 Overall evaluation and diffraction/refraction importance . . . 52
- 4.3 Verification . . . 55
  - 4.3.1 Schematic modelling of Palmyra Atoll . . . 55
  - 4.3.2 Linear wave theory prediction . . . 61

4.4 Optimization . . . 63
4.4.1 Number of SAG structures . . . 63
4.4.2 Time step . . . 64
4.4.3 Time length of simulation (spin-up period) . . . 64
4.4.4 Sponge layers . . . 64
4.4.5 Number of alongshore grids in groove . . . 64
4.4.6 Overall optimization parameters . . . 64

5 Results **65**
5.1 Base Case results . . . 65
5.1.1 Wave propagation . . . 66
5.1.2 3D velocity profile . . . 66
5.1.3 Depth-averaged flow . . . 71
5.1.4 Surface and bottom flow . . . 73
5.1.5 Momentum balance . . . 75
5.2 Influence of varying parameters . . . 77
5.2.1 Influence of short wave parameters . . . 79
5.2.2 Influence of SAG geometry . . . 80
5.2.3 Influence of alongshore current . . . 86
5.2.4 Importance of long waves . . . 86
5.3 Mechanisms and effects . . . 88
5.3.1 Short wave parameters . . . 89
5.3.2 SAG geometry . . . 91
5.3.3 Alongshore currents . . . 92
5.3.4 Overall mechanisms and effects . . . 92
5.4 Flow indicators . . . 94
5.4.1 Definition of indicators . . . 94
5.4.2 Results of indicators . . . 95
5.4.3 Overall results . . . 96
5.5 Flow pattern in SAG formations . . . 97
5.5.1 Types of flow . . . 97
5.5.2 Prediction of flow pattern . . . 97

6 Discussion **103**
6.1 Flow over SAG formations . . . 103
6.2 Implications of SAG hydrodynamics . . . 104
6.3 Limitations . . . 105
6.3.1 Model limitations . . . 105
6.3.2 Model approach limitations . . . 106

7 Conclusions and recommendations **107**
7.1 Conclusions . . . 107
7.1.1 First subobjective - horizontal and vertical flows . . . 107
7.1.2 Second subobjective - role of short wave variation . . . 107
7.1.3 Third subobjective - role of SAG geometry . . . 108
7.1.4 Fourth subobjective - role of SAG alongshore currents . . . 108
7.1.5 Fifth subobjective - role of long waves . . . 108
7.1.6 Sixth subobjective - implications of the hydrodynamics . . . 109
7.2 Recommendations . . . 109

Bibliography **111**

A List of simulations - Sensitivity and Permutation runs **115**

B Wave results - Sensitivity runs with and without refraction **129**
B.1 Influence of varying parameters . . . 129
B.1.1 Influence of short wave parameters . . . 129
B.1.2 Influence of SAG geometry . . . 132

C Alongshore velocities - Influence of varying parameters **137**
C.1 Influence of varying parameters . . . 137
C.1.1 Influence of short wave parameters . . . 137
C.1.2 Influence of SAG geometry . . . 137
C.1.3 Influence of alongshore current . . . 139
C.1.4 Importance of long waves . . . 139

D Results for D3D-FLOW + XBeach **147**
D.1 Significant long wave height and mean flow . . . 147
D.2 Intrawave flow . . . 150

E Results of indicators for varying wave parameters, SAG geometry and alongshore forcing **153**

F Role of varying wave angles and directional spreadings **159**
F.1 Influence of varying parameters . . . 159
F.1.1 Wave direction . . . 159
F.1.2 Directional spreading . . . 162
F.2 Mechanisms and effects . . . 162
F.2.1 Wave direction . . . 162
F.2.2 Directional spreading . . . 162
F.3 Results of indicators . . . 165

G Sensitivity for horizontal and vertical viscosities **173**
G.1 Influence in the velocity profile . . . 173
G.2 Mechanisms and effects . . . 173
G.3 Overall evaluation . . . 176

H Sensitivity for wave forces **177**
H.1 Momentum balance . . . 177
H.2 Overall evaluation . . . 177

LIST OF FIGURES

1.1 Spurs and grooves at Sombrero Key Reef – Florida Keys. Source: Lidz (2007). 1

2.1 Locations of atolls, fringing, and barrier reefs around the world. Source: Pearson (2016). 6
2.2 Global spatial and frequency distributions of annual mean Hs (a,b), MTR (c,d), and relative tidal range ($\frac{MTR}{Hs}$) (e,f) for warm-water coral reef systems. Source: Lowe and Falter (2015). 6
2.3 Offshore hydrodynamic parameters collected from field campaigns. Source: Kolijn (2014). . . . 7
2.4 Coral reef zonation at Shiraho, Ishigaki Island, Japan. Source: Kayanne et al. (2015). 7
2.5 Spurs and grooves in coral reefs from three world oceans. (a) Aerial photograph of reef and shallow fore reef on central Belize Barrier Reef (Atlantic Ocean). (b) Underwater photograph of spur and groove at same location, with up to 5-m-high spurs of Acropora palmata and Millepora sp. (c) Aerial photograph of reef and shallow fore reef on western side of Ari Atoll, central Maldives (Indian Ocean). (d) Underwater photograph at same location, north of Mandhoo Island, shows flat spurs, which are composed of coralline algae and some branched Acropora and V-shaped grooves about 1–2 m deep. (e) Aerial photograph of northeastern reef of Moorea, Society Islands, near airstrip (Pacific Ocean). (f) Underwater photograph of same area, with low relief spurs composed of coralline algae and branched Acropora. Grooves up to 2 m deep and V-shaped. Source: Gischler (2010). 8
2.6 Simplified, schematic cross section through Indo-Pacific (a) and Atlantic (b) spur and groove systems. Source: Gischler (2010). 11
2.7 (A) Bathymetry of Southern Moloka'i, Hawai'i. (B) Alongshore profile of 10 m isobath - bold white line in A. Source: Storlazzi et al. (2003). 12
2.8 Cross-section and longitudinal transect of the buttress zone in the reef near "Sombra", Ocho Rios. Source: Goreau (1959). 12
2.9 Distribution of SAG wavelength and spur height SAG formations at 5, 10, 15, and 20 m depth from southern Moloka'i, Hawai'i. Source: Rogers et al. (2013). 13
2.10 Comparison of SAGs around the world with respect to length and spacing. The four classes identified in Duce et al. (2016) are shown as triangles. The other sites in this figure were described in the following published works: Molokai: Storlazzi et al. (2003); Mururoa: Chevalier (1973); Grand Cayman: Roberts (1974); Palmyra: Rogers et al. (2015); Bikini: Munk and Sargent (1948); Chagos: Sheppard (1981); Alphonse: Hamylton and Spencer (2011); Jamaica: Goreau (1959); Florida Keys: Shinn (1963); Mariana: Cloud (1959). Source: Duce et al. (2016). 14
2.11 Field experiment images and spur and groove bathymetry, for NFR13 experiment (a–c), and SFR12 experiment (d–f). Source: Rogers et al. (2015). 16
2.12 Mean Lagrangian velocity, in the alongshore (y) and vertical (z) direction showing characteristic spur and groove circulation cells during NFR13 experiment. Blue and red colours indicate offshore and onshore flows, respectively. Source: Rogers et al. (2015). 17
2.13 Average profiles over depth for rms of mean Eulerian ($\overline{u_E}$), Stokes drift ($\overline{u_S}$), and Lagrangian velocities ($\overline{u_L}$) during NFR13 and SFR12 experiments. Source: Rogers et al. (2015). 17
2.14 Variation of wave height H and wave angle with SAG wavelength at x = 440 m. (a) Alongshore mean H (solid) and max/min H (dash), (b) alongshore mean (solid) and alongshore max/min (dash). Source: Rogers et al. (2013). 20

3.1 Comparison of cross-shore Stokes drift velocity (a) and radiation stress (b) for base configuration at top of spur. Blue solids indicate model results, while blue dashed shows the LWT expressions. Source: Rogers et al. (2013). 28

3.2 (a) Cross-shore and (b) alongshore and (c) top views of SAG schematic bathymetry, as represented in the modelling. Full black line represents the cross-shore axis of the spur, while dashed black line is the cross-shore axis of the groove. The grey line is the alongshore axis at a location close to where spur height is maximum along the cross-shore profile. The blue lines are mid positions between spur and groove, that are further used for plotting results. 32
3.3 Flowchart for modelling plan. 36
3.4 Schematic grid adopted for D3D-FLOW + SWAN. 39
3.5 Zoom of schematic grid adopted for D3D-FLOW + SWAN. 40
3.6 Vertical grid with 20 sigma-layers, which are represented by the horizontal dashed lines. 41
3.7 Friction values used for the Base Case scenario. 42

4.1 Rogers et al. (2013) wave propagation results for base configuration from Rogers et al. (2013).(a) Instantaneous surface η (t = 3600 s), (b) wave height H, (c) mean alongshore wave angle θ (red solid) and max/min alongshore θ (red dash), (d) mean setup $\overline{\eta}$, and (e) cross-shore depth h. Source: Rogers et al. (2013). 47
4.2 D3D + SWAN (without refraction) results for base configuration from Rogers et al. (2013) - significant wave height Hs, mean wave angle D_m, setup η, and cross-shore depth profile. 47
4.3 XBeach (non-hydrostatic) wave propagation results for base configuration from Rogers et al. (2013) - instantaneous surface η (t = 3600 s), wave height H, mean setup $\overline{\eta}$, and cross-shore depth h. 49
4.4 D3D + SWAN (with refraction) results for base configuration from Rogers et al. (2013) - significant wave height Hs, and cross-shore depth profile. 49
4.5 XBeach (wave-averaged) (with refraction) wave propagation results for base configuration from Rogers et al. (2013) - significant wave height Hs, and cross-shore depth profile. 49
4.6 Rogers et al. (2013) velocity and bed shear results for base configuration from Rogers et al. (2013).(a) Cross-shore Stokes drift U_S, (b) Eulerian velocity U_E, (c) Lagrangian velocity U_L, (d) average cross-shore bed shear stress τ_{bx}, and (e) cross-shore depth profile at spur (blue solid) and groove (green dash). Positive cross-shore indicate offshore velocities. Source: Rogers et al. (2013). 50
4.7 D3D + SWAN velocity and bed shear results for base configuration from Rogers et al. (2013) - cross-shore Stokes drift U_S, Eulerian velocity U_E, Lagrangian velocity U_L, average cross-shore bed shear stress τ_{bx}, and cross-shore depth profile at spur (solid) and groove (dash). Positive cross-shore indicate offshore velocities. 50
4.8 Rogers et al. (2013) Lagrangian velocities U_L and V_L results for base configuration from Rogers et al. (2013) - maximum velocity vector scale is 0.05m/s, and horizontal dashed blue line represents the offshore edge of the surf zone. Source: Rogers et al. (2013). 51
4.9 D3D + SWAN velocity Lagrangian velocities U_L and V_L results for base configuration from Rogers et al. (2013). 51
4.10 Rogers et al. (2013) phase-averaged cross-shore depth-averaged momentum terms at top of spur for base configuration from Rogers et al. (2013). (a) Cross-shore momentum terms and (b) cross-shore depth profile. NLM, NLW, PG and BT represent the streamwise advective acceleration, wave forces, pressure gradient and bottom shear stress, respectively. Source: Rogers et al. (2013). 53
4.11 D3D + SWAN cross-shore depth-averaged momentum terms at top of spur for base configuration from Rogers et al. (2013) - cross-shore momentum terms and cross-shore depth profile. MOM_UPRESSURE, MOM_UWAVES, MOM_UDUDX, MOM_UBEDSHEAR and MOM_UVISCO represent the pressure gradient, wave forces, streamwise advective acceleration, bottom shear stress and horizontal viscous forces, respectively. 53
4.12 Rogers et al. (2013) alongshore variation of phase-averaged cross-shore momentum terms and velocity for base configuration from Rogers et al. (2013). (a) Cross-shore momentum terms, (b) U_E, U_S and U_L velocities and (c) alongshore depth profile. NLM, NLW, PG and BT represent the streamwise advective acceleration, wave forces, pressure gradient and bottom shear stress, respectively. Source: Rogers et al. (2013). 54

4.13 D3D + SWAN alongshore variation of phase-averaged cross-shore momentum terms and velocity for base configuration from Rogers et al. (2013) - cross-shore momentum terms, U_E, U_S and U_L velocities and alongshore depth profile. MOM_UPRESSURE, MOM_UWAVES, MOM_UDUDX, MOM_UBEDSHEAR and MOM_UVISCO represent the pressure gradient, wave forces, streamwise advective acceleration, bottom shear stress and horizontal viscous forces, respectively. . . 54
4.14 Model results for depth-averaged velocities U_L, V_L, W_L and cross-shore depth profile for schematic simulation of NFR13 using shore-normal waves. 57
4.15 Alongshore view of model results for velocities u_L, v_L, w_L at depths of around 10 m with shore-normal waves. Blue and red colours indicate offshore and onshore flows, respectively. 57
4.16 Alongshore view of model results for velocities u_L, v_L, w_L at depths of around 10 m with oblique waves. Blue and red colours indicate offshore and onshore flows, respectively. 58
4.17 Model results for depth-averaged velocities U_L, V_L, W_L and cross-shore depth profile for schematic simulation of SFR12. 60
4.18 D3D-FLOW + SWAN and theoretical derivation results for wave forces MOM_UWAVES and MOM_VWAVES and alongshore depth profile at depths of around 15 m. 61
4.19 D3D-FLOW + SWAN and theoretical derivation results for wave forces MOM_UWAVES and MOM_VWAVES and alongshore depth profile at depths of around 10 m. 62
4.20 D3D-FLOW + SWAN and theoretical derivation results for wave forces MOM_UWAVES and MOM_VWAVES close to the top of spur and cross-shore depth profile. 63

5.1 Cross-shore view of Base Case results for significant wave height Hs, shoaling coefficient Ks, mean wave angle D_m, setup η, and cross-shore depth profile over spur and groove. 66
5.2 Cross-shore views of Base Case results for velocities u_L, v_L, w_L on top of groove, middle between groove and spur, spur, and middle between spur and groove. Blue and red colours indicate eastwards and westwards flows, respectively. 67
5.3 Cross-shore views of Base Case results for Eulerian u_E on top of groove and spur. 68
5.4 Cross-shore views of Base Case results for Stokes Drift velocities u_S on top of groove and spur. . 69
5.5 Alongshore view of Base Case results for velocities u_L, v_L, w_L at depths of around 20 m. Blue and red colours indicate offshore and onshore flows, respectively. 70
5.6 Alongshore view of Base Case results for velocities u_L, v_L, w_L at depths of around 15 m. Blue and red colours indicate offshore and onshore flows, respectively. 70
5.7 Alongshore view of Base Case results for velocities u_L, v_L, w_L at depths of around 10 m. Blue and red colours indicate offshore and onshore flows, respectively. 70
5.8 Alongshore view of Base Case results for velocities u_L, v_L, w_L at depths of around 5 m. Blue and red colours indicate offshore and onshore flows, respectively. 70
5.9 Cross-shore views of Base Case results for Lagrangian velocities v_L on cross-sections in the mid points between groove and spur (top), and spur and groove (bottom). 71
5.10 Map view of Base Case results for depth-averaged Lagrangian velocities U_L and V_L. 72
5.11 Map view of Base Case results for the cross-shroe and alongshore bottom shear stresses τ_{bx} and τ_{by}. 72
5.12 Cross-shore view of Base Case results for depth-averaged Lagrangian velocities U_L, V_L and W_L over spur and groove. 73
5.13 Map view of Base Case results for surface Lagrangian velocities $U_{L-0.5m-sur}$ and $V_{L-0.5m-sur}$. . . 74
5.14 Map view of Base Case results for bottom Eulerian velocities $U_{E-0.5m-bot}$ and $V_{EL-0.5m-bot}$. . . . 74
5.15 Cross-shore view of Base Case results for cross-shore surface velocities $U_{S-0.5m-sur}$, $U_{E-0.5m-sur}$ and $U_{L-0.5m-sur}$ over spur and groove. 74
5.16 Cross-shore view of Base Case results for cross-shore bottom velocities $U_{S-0.5m-bot}$, $U_{E-0.5m-bot}$ and $U_{L-0.5m-bot}$ over spur and groove. 75
5.17 Cross-shore views of Base Case results for cross-shore momentum terms on top of groove and spur. MOM_UWAVES, MOM_UPRESSURE, MOM_UBEDSHEAR, MOM_UVISCO, MOM_UDUDX and MOM_VDUDY represent the wave forces, pressure gradient, bottom shear stress, horizontal viscous forces, streamwise and lateral advective accelerations, respectively. 76
5.18 Cross-shore views of Base Case results for cross-shore momentum terms on top of groove and spur - imbalance between pressure gradient and wave forces. MOM_UWAVES, MOM_UPRESSURE, MOM_UVISCO, MOM_UDUDX and MOM_VDUDY represent the wave forces, pressure gradient, horizontal viscous forces, streamwise and lateral advective accelerations, respectively. . . . 76

5.19 Cross-shore views of Base Case results for alongshore momentum terms on cross-sections in the middle between groove and spur (top), and spur and groove (bottom). MOM_VWAVES, MOM_VPRESSURE, MOM_VBEDSHEAR, MOM_VVISCO, MOM_VDVDY and MOM_UDVDX represent the wave forces, pressure gradient, bottom shear stress, horizontal viscous forces, streamwise and lateral advective accelerations, respectively. 78
5.20 Cross-shore views of Base Case results for alongshore momentum terms on cross-sections in the middle between groove and spur, and spur and groove - imbalance between pressure gradient and wave force. MOM_VWAVES, MOM_VPRESSURE,MOM_VVISCO, MOM_VDVDY and MOM_UDVDX represent the wave forces, pressure gradient, horizontal viscous forces, streamwise and lateral advective accelerations, respectively. 78
5.21 Cross-shore views of results for cross-shore Lagrangian velocity u_L over spur and groove for varying significant wave height Hs 79
5.22 Cross-shore views of results for cross-shore Lagrangian velocity u_L over spur and groove for varying peak wave period Tp 80
5.23 Cross-shore views of results for cross-shore Lagrangian velocity u_L over spur and groove for spur height h_{spr} 81
5.24 Cross-shore views of results for cross-shore Lagrangian velocity u_L over spur and groove for varying spur wavelength λ_{SAG}. 82
5.25 Cross-shore views of results for cross-shore Lagrangian velocity u_L over spur and groove for varying groove width W_{grv}. 83
5.26 Cross-shore views of results for cross-shore Lagrangian velocity u_L over spur and groove for mild slope ($\tan\beta_f = 0.02$). 83
5.27 Cross-shore views of results for cross-shore Lagrangian velocity u_L over spur and groove for steep slope ($\tan\beta_f = 0.50$). 84
5.28 Cross-shore views of results for cross-shore Lagrangian velocity u_L over spur and groove for varying ratio of groove and spur friction coefficient $\frac{C_{D-grv}}{C_{D-spr}}$. 85
5.29 Cross-shore views of results for cross-shore Lagrangian velocity u_L over spur and groove for varying vertical position of maximum spur height z_μ. 85
5.30 Cross-shore views of results for cross-shore Lagrangian velocity u_L over spur and groove for varying alongshore wind speed U_{10}. 86
5.31 Cross-shore views of D3D-FLOW + XBeach surfbeat Base Case (Hawaiian type with z_μ = 17 m) results for significant long wave height Hs, cross-shore depth-averaged Lagrangian velocity $\hat{U}_L$ and cross-shore depth profile over spur and groove. 87
5.32 Cross-shore views of D3D-FLOW + SWAN and D3D-FLOW + XBeach surfbeat Base Case (Hawaiian type with z_μ = 17 m) results for cross-shore Lagrangian velocity $\hat{u_L}$ over spur and groove. . . 88
5.33 Results of the spatial mean along the SAG cross-shore section of the cross-shore momentum terms on top of the spur. MOM_UWAVES, MOM_UPRESSURE, MOM_UBEDSHEAR, MOM_UVISCO, MOM_UDUDX and MOM_VDUDY represent the wave forces, pressure gradient, bottom shear stress, horizontal viscous forces, streamwise and lateral advective accelerations, respectively. . . 89
5.34 Results of the spatial mean along the SAG cross-shore section of the alongshore momentum terms on mid point between spur and groove. MOM_VWAVES, MOM_VPRESSURE, MOM_VBEDSHEAR, MOM_VVISCO, MOM_VDVDY, MOM_UDVDX, and MOM_VWINDFORCE represent the wave forces, pressure gradient, bottom shear stress, horizontal viscous forces, streamwise and lateral advective accelerations, and wind forces, respectively. 90
5.35 Results of $\tau_{\text{bx-z}\mu}$ for the sensitivity simulations with varying short wave parameters, SAG geometry and alongshore forcing. 96
5.36 Type A of cross-shore flow pattern - Hs = 1 m, $\frac{\text{Hs}_0}{\text{Lp}_0}$ = 0.006 (Tp = 10 s), h_{spr} = 2 m, λ_{SAG} = 50 m and z_μ = 17 m. 98
5.37 Type B.1 of cross-shore flow pattern - Hs = 1 m, $\frac{\text{Hs}_0}{\text{Lp}_0}$ = 0.006 (Tp = 10 s), h_{spr} = 2 m, λ_{SAG} = 25 m and z_μ = 17 m. 99
5.38 Type B.2 of cross-shore flow pattern - Hs = 4 m, $\frac{\text{Hs}_0}{\text{Lp}_0}$ = 0.006 (Tp = 20 s), h_{spr} = 0.5 m, λ_{SAG} = 25 m and z_μ = 17 m. 99
5.39 Type C.1.1 of cross-shore flow pattern - Hs = 1 m, $\frac{\text{Hs}_0}{\text{Lp}_0}$ = 0.050 (Tp = 4 s), h_{spr} = 2 m, λ_{SAG} = 50 m and z_μ = 17 m. 100

5.40 Type C.1.2 of cross-shore flow pattern - Hs = 1 m, $\frac{Hs_0}{Lp_0}$ = 0.050 (Tp = 4 s), h_{spr} = 2 m, λ_{SAG} = 25 m and z_μ = 5 m. 100
5.41 Type C.2.1 of cross-shore flow pattern - Hs = 1 m, $\frac{Hs_0}{Lp_0}$ = 0.025 (Tp = 5 s), h_{spr} = 2 m, λ_{SAG} = 50 m and z_μ = 17 m. 101
5.42 Type C.2.2 of cross-shore flow pattern - Hs = 1 m, $\frac{Hs_0}{Lp_0}$ = 0.025 (Tp = 5 s), h_{spr} = 8 m, λ_{SAG} = 100 m and z_μ = 17 m. 101

B.1 Cross-shore views of results for significant wave height Hs over spur and groove for varying incoming Hs, including runs with and without refraction. 130
B.2 Cross-shore views of results for alongshore Lagrangian velocity u_L over spur and groove for varying peak wave period Tp, including runs with and without refraction. 130
B.3 Cross-shore views of results for significant wave height Hs over spur and groove for varying wave direction Dp, including runs with and without refraction. 131
B.4 Cross-shore views of results for significant wave height Hs over spur and groove for varying directional spreading m, including runs with and without refraction. 131
B.5 Cross-shore views of results for significant wave height Hs over spur and groove for varying spur height h_{spr}, including runs with and without refraction. 133
B.6 Cross-shore views of results for significant wave height Hs over spur and groove for varying spur wavelength λ_{SAG}, including runs with and without refraction. 133
B.7 Cross-shore views of results for significant wave height Hs over spur and groove for varying groove width W_{grv}, including runs with and without refraction. 134
B.8 Cross-shore views of results for alongshore Lagrangian velocity u_L over spur and groove for varying vertical position of maximum spur height z_μ, including runs with and without refraction. . . 134
B.9 Cross-shore views of results for significant wave height Hs over spur and groove for mild slope ($\tan\beta_f = 0.02$), including runs with and without refraction. 135
B.10 Cross-shore views of results for significant wave height Hs over spur and groove for steep slope ($\tan\beta_f = 0.50$), including runs with and without refraction. 135

C.1 Cross-shore views of results for alongshore Lagrangian velocity u_L on top of mid points between spurs and grooves for varying significant wave height Hs. 138
C.2 Cross-shore views of results for alongshore Lagrangian velocity u_L on top of mid points between spurs and grooves for varying peak wave period Tp. 138
C.3 Cross-shore views of results for alongshore Lagrangian velocity u_L on top of mid points between spurs and grooves for varying spur height h_{spr} 140
C.4 Cross-shore views of results for alongshore Lagrangian velocity u_L on top of mid points between spurs and grooves for varying spur wavelength λ_{SAG}. 140
C.5 Cross-shore views of results for alongshore Lagrangian velocity u_L on top of mid points between spurs and grooves for varying groove width W_{grv}. 141
C.6 Cross-shore views of results for alongshore Lagrangian velocity u_L on top of mid points between spurs and grooves for varying ratio of groove and spur friction coefficient $\frac{C_{D-grv}}{C_{D-spr}}$. 141
C.7 Cross-shore views of results for alongshore Lagrangian velocity u_L on top of mid points between spurs and grooves for mild slope ($\tan\beta_f = 0.02$). 142
C.8 Cross-shore views of results for alongshore Lagrangian velocity u_L on top of mid points between spurs and grooves for steep slope ($\tan\beta_f = 0.50$). 142
C.9 Cross-shore views of results for alongshore Lagrangian velocity u_L on top of mid points between spurs and grooves for varying vertical position of maximum spur height z_μ. 143
C.10 Cross-shore views of results for alongshore Lagrangian velocity u_L on top of mid points between spurs and grooves for varying alongshore wind speed U_{10}. 143
C.11 Cross-shore views of D3D-FLOW + SWAN and D3D-FLOW + XBeach surfbeat Base Case (Hawaiian type with z_μ = 17 m) results for alongshore shore Lagrangian velocity $\hat{v_L}$ on top of mid points between spurs and grooves. 144
C.12 Cross-shore views of D3D-FLOW + SWAN and D3D-FLOW + XBeach surfbeat Intermediate type (z_μ = 10 m) results for alongshore shore Lagrangian velocity $\hat{v_L}$ on top of mid points between spurs and grooves. 144

C.13 Cross-shore views of D3D-FLOW + SWAN and D3D-FLOW + XBeach surfbeat Buttress type ($z_\mu \approx$ 5 m) results for alongshore shore Lagrangian velocity $\hat{v_L}$ on top of mid points between spurs and grooves. . . . 145

D.1 Cross-shore views of D3D + XBeach surfbeat Intermediate type (z_μ = 10 m)) results for significant long wave height Hs, cross-shore depth-averaged Lagrangian velocity $\hat{U_L}$ and cross-shore depth profile over spur and groove. . . . 148
D.2 Cross-shore views of D3D-FLOW + SWAN and D3D-FLOW + XBeach surfbeat Intermediate type (z_μ = 10 m) results for cross-shore Lagrangian velocity $\hat{u_L}$ over spur and groove. . . . 148
D.3 Cross-shore views of D3D + XBeach surfbeat Buttress type ($z_\mu \approx$ 5 m) results for significant long wave height Hs, cross-shore depth-averaged Lagrangian velocity $\hat{U_L}$ and cross-shore depth profile over spur and groove. . . . 149
D.4 Cross-shore views of D3D-FLOW + SWAN and D3D-FLOW + XBeach surfbeat Buttress type ($z_\mu \approx$ 5 m) results for cross-shore Lagrangian velocity $\hat{u_L}$ over spur and groove. . . . 149
D.5 Time series for cross-shore and alongshore depth-averaged Lagrangian velocities (U_L and V_L) of D3D + XBeach surfbeat run with Hawaiann type (z_μ = 17 m). . . . 150
D.6 Time series for cross-shore and alongshore depth-averaged Lagrangian velocities (U_L and V_L) of D3D + XBeach surfbeat run with Intermediate type (z_μ = 10 m). . . . 151
D.7 Time series for cross-shore and alongshore depth-averaged Lagrangian velocities (U_L and V_L) of D3D + XBeach surfbeat run with Buttress type ($z_\mu \approx$ 5 m). . . . 151

E.1 Results of h_{cr} for the sensitivity simulations with varying short wave parameters, SAG geometry and alongshore forcing. . . . 154
E.2 Results of $\frac{V_{sp}}{U_{sp}}$ for the sensitivity simulations with varying short wave parameters, SAG geometry and alongshore forcing. . . . 155
E.3 Results of $\frac{U_{max}}{U_{max\text{-}BC}}$ for the sensitivity simulations with varying short wave parameters, SAG geometry and alongshore forcing. . . . 156
E.4 Results of $\frac{U_{sur}}{U_{sur\text{-}BC}}$ for the sensitivity simulations with varying short wave parameters, SAG geometry and alongshore forcing. . . . 157
E.5 Results of $\frac{U_{bot}}{U_{bot\text{-}BC}}$ for the sensitivity simulations with varying short wave parameters, SAG geometry and alongshore forcing. . . . 158

F.1 Cross-shore views of results for cross-shore Lagrangian velocity u_L over spur and groove for varying wave direction Dp . . . 160
F.2 Cross-shore views of results for cross-shore Lagrangian velocity u_L over spur and groove for varying directional spreading m . . . 160
F.3 Cross-shore views of results for alongshore Lagrangian velocity u_L on top of mid points between spurs and grooves for varying wave direction Dp . . . 161
F.4 Cross-shore views of results for alongshore Lagrangian velocity u_L on top of mid points between spurs and grooves for varying directional spreading m . . . 161
F.5 Results of the spatial mean along the SAG cross-shore section of the cross-shore momentum terms MOM_UDUDX, MOM_VDUDY, $MOM\_UPRESSURE$, MOM_UWAVES, MOM_UVISCO, $MOM\_UBEDSHEAR$, $MOM\_UPRESSURE + MOM\_UWAVES$ on top of the spur. . . . 163
F.6 Results of the spatial mean along the SAG cross-shore section of the alongshore momentum terms MOM_VDVDY, MOM_UDVDX, $MOM\_VPRESSURE$, MOM_VWAVES, MOM_VVISCO, $MOM\_VBEDSHEAR$, $MOM\_VWINDFORCE$ and $MOM\_VPRESSURE + MOM\_VWAVES$ on mid point between spur and groove. . . . 164
F.7 Results of h_{cr} for the sensitivity simulations with varying wave angle and directional spreading. 166
F.8 Results of $\frac{V_{sp}}{U_{sp}}$ for the sensitivity simulations with varying wave angle and directional spreading. 167
F.9 Results of $\frac{U_{max}}{U_{max\text{-}BC}}$ for the sensitivity simulations with varying wave angle and directional spreading. . . . 168
F.10 Results of $\frac{U_{sur}}{U_{sur\text{-}BC}}$ for the sensitivity simulations with varying wave angle and directional spreading. 169
F.11 Results of $\frac{U_{bot}}{U_{bot\text{-}BC}}$ for the sensitivity simulations with varying wave angle and directional spreading. 170
F.12 Results of $\tau_{bx\text{-}z\mu}$ for the sensitivity simulations with varying wave angle and directional spreading. 171

G.1 Cross-shore views of results for alongshore Lagrangian velocity u_L on top of spur and groove for varying horizontal viscosity ν_H. 174
G.2 Cross-shore views of results for alongshore Lagrangian velocity u_L on top of mid points between spurs and grooves for varying horizontal viscosity ν_H. 174
G.3 Cross-shore views of results for alongshore Lagrangian velocity u_L on top of spur and groove for varying vertical viscosity ν_V. 175
G.4 Cross-shore views of results for alongshore Lagrangian velocity u_L on top of mid points between spurs and grooves for varying vertical viscosity ν_V. 175
G.5 Results of the spatial mean along the SAG cross-shore section of the cross-shore momentum terms on top of the spur for varying viscosities. MOM_UWAVES, MOM_UPRESSURE, MOM_UBEDSHEAR, MOM_UVISCO, MOM_UDUDX and MOM_VDUDY represent the wave forces, pressure gradient, bottom shear stress, horizontal viscous forces, streamwise and lateral advective accelerations, respectively. 176
G.6 Results of the spatial mean along the SAG cross-shore section of the alongshore momentum terms on mid point between spur and groove for varying viscosities. MOM_VWAVES, MOM_VPRESSURE, MOM_VBEDSHEAR, MOM_VVISCO, MOM_VDVDY, MOM_UDVDX, and MOM_VWINDFORCE represent the wave forces, pressure gradient, bottom shear stress, horizontal viscous forces, streamwise and lateral advective accelerations, and wind forces, respectively. 176

H.1 Cross-shore views of Base Case results for cross-shore momentum terms on top of groove and spur - imbalance between pressure gradient and wave forces. MOM_UWAVES, MOM_UPRESSURE, MOM_UVISCO, MOM_UDUDX and MOM_VDUDY represent the wave forces, pressure gradient, horizontal viscous forces, streamwise and lateral advective accelerations, respectively. Full and dashed lines represent the result of simulation with and without the Stokes Drift divergence as part for the wave force output, respectively. 178

LIST OF TABLES

1.1 Research objectives. 2

2.1 Types of spurs and grooves and their suggested formation mechanisms from the published literature. Source: Duce et al. (2016). 10
2.2 SAG dimensions. 10
2.3 Geometric features observed in SAG classes according to Duce et al. (2016). 13
2.4 Geometry of SAG formations described on Rogers et al. (2015). 15

3.1 Wave models capabilities and required computational effort. 27
3.2 Simulations to answer research questions. 30
3.3 Range of Parameters – Wave, SAG Geometry and Alongshore Currents. 33
3.4 Base Case configuration. 38

4.1 Momentum terms nomenclature following D3D-FLOW convention. 46
4.2 Base Configuration run from Rogers et al. (2013). 46
4.3 Model setup for the verification runs - NFR13 and SFR12 based on information from Rogers et al. (2015). 56
4.4 Measured order of terms in depth-averaged momentum equations from NFR13 experiment in cross-shore and alongshore from Rogers et al. (2015). 56
4.5 Depth-averaged momentum terms over the spur at depth of around 10 m for schematic modelling with D3D + SWAN with shore-normal waves of NFR13 experiment. 59
4.6 Depth-averaged momentum terms over the spur at depth of around 10 m for schematic modelling with D3D + SWAN with oblique waves of NFR13 experiment. 59
4.7 Optimized model setup parameters 64

5.1 Important effects in the cross-shore velocity profile and associated mechanism – Wave, SAG Geometry and Alongshore Currents. The ratio of groove width and SAG wavelength $\frac{W_{grv}}{\lambda_{SAG}}$, the reef flat width W_{reef} and the presence of long waves were shown to play a minor role. 93
5.2 Indicators to quantify importance of Wave, SAG Geometry and Alongshore Currents. 94
5.3 Cross-shore flow patterns. 98

A.1 List of simulations - Sensitivity runs - Part 1/2. 116
A.2 List of simulations - Sensitivity runs - Part 2/2. 117
A.3 List of simulations - Permutation runs. 118

LIST OF ABBREVIATIONS

Abbreviation	Meaning
2DH	Two-dimensional, Depth integrated
3D	Three-dimensional
CBR	Capricorn-Bunker Group
D3D	Delft3D
DaD	Deep and disconnected
EWE	Exposed to wave energy
GBR	Great Barrier Reef
IG	Infragravity
JONSWAP	Joint North Sea Wave Project
LaP	Long and protected
LHS	Left-hand side
LWT	Linear wave theory
MTR	Mean Tidal Range
RHS	Right-hand side
RMS	Root mean square
SAG	Spur-and-groove
SaP	Short and protected
SWAN	Simulating Waves Nearshore
USGS	United States Geological Survey

LIST OF SYMBOLS

Symbol	Variable
α	Coefficient for schematic representation of spur-and-groove
β_f	Spur-and-groove cross-shore slope
γ	Overshoot parameter in the JONSWAP spectrum
ϵ	Spreading parameter for schematic representation of spur-and-groove
η	Instantaneous water surface elevation
θ	Spectral wave direction
λ_{grv}	Groove length
λ_{SAG}	Spur-and-groove wavelength
μ	Cross-shore position of maximum spur height
ν_H	Horizontal viscosity
ν_V	Vertical viscosity
ρ	Water density
σ	Spectral wave frequency
τ_{bi}	Bottom shear stress in i-direction
τ_{ij}	Shear stress in j-direction perpendicular to plane defined by i
ω	Angular wave frequency
a	Wave amplitude
b	Distance between two adjacent wave rays
C	Wave celerity
C_D	Friction coefficient
C_g	Wave group celerity
d	Water depth
Dm	Mean wave direction
Dp	Peak wave direction
E	Wave energy
F_i	Wave force in i-direction
h	Water depth
h_{base}	Reef profile
h_{spr}	Spur height
h_x	Cross-shore spur-and-groove shape function
h_y	Alongshore spur-and-groove shape function
H	Wave height
Hs	Significant wave height
Hs_{long}	Significant long wave height
k	Wave number

Symbol	Variable
K_S	Shoaling coefficient
K_R	Refraction coefficient
L	Wavelength
m	Directional spreading power coefficient
n	Coefficient from LWT that varies between 0.5 and 1.0
N	Wave action density
p_{wave}	Pressure due to wave
S	Source/sink in wave action balance equation
S_{ij}	Radiation stress with i-momentum in j-direction
Tm01	Mean wave period
Tp	Peak wave period
u_E	Cross-shore Eulerian velocity
u_L	Cross-shore Lagrangian velocity
u_S	Cross-shore Stokes Drift velocity
U_{10}	Wind speed at 10 m elevation
U_E	Depth-averaged cross-shore Eulerian velocity
U_L	Depth-averaged cross-shore Lagrangian velocity
U_S	Depth-averaged cross-shore Stokes Drift velocity
v_E	Alongshore Eulerian velocity
v_L	Alongshore Lagrangian velocity
v_S	Alongshore Stokes Drift velocity
V_E	Depth-averaged alongshore Eulerian velocity
V_L	Depth-averaged alongshore Lagrangian velocity
V_S	Depth-averaged alongshore Stokes Drift velocity
w_L	Vertical Lagrangian velocity
W_L	Depth-averaged vertical Lagrangian velocity
W_{grv}	Groove width
W_{reef}	Reef flat width
x	Cross-shore axis
y	Alongshore axis
t	Time
z	Vertical axis
z_μ	Vertical position of maximum spur height

ACKNOWLEDGEMENTS

This work concludes the Master of Science in Coastal and Marine Engineering and Management (CoMEM) Programme, that included studies at the Norwegian University of Science and technology (NTNU), Delft University of Technology (TU Delft) and University of Southampton (SOTON). The MSc thesis was carried out at Deltares, in collaboration with the TU Delft and the United States Geological Survey (USGS).

I would like to thank all the committee members for their contributions on this exciting project. At Deltares, I would like to thank Johan Reyns, my daily supervisor, for the continuous support, attention and guidance throughout the development of this work. I also thank Robert McCall for his great collaboration, always following the work steps and for the XBeach advices. Thank you to Ap van Dongeren, for the opportunity to experience Deltares and for the valuable ideas to the research.

This study was funded by the USGS through a cooperative agreement with Deltares. I would like to acknowledge USGS, and to say a special thank you to Curt Storlazzi for his encouraging support and involvement during the fortnightly meetings in the past 5 months.

At TU Delft, I would like to thank Marion Tissier for her construtive feedback, involvement, ideas and research advices even preceding this work. I also would like to thank professor Ad Reniers, head of my graduation committee, for the fruitful meetings and for the excellent, precise and insightful comments. Thank you to Max Radermacher for the helpful feedback and for the engagement in the research meeting discussions.

I would like to express my gratitude to the Deltares staff who contributed to my thesis, such as Bert Jagers and Adri Mourits, for the support on Delft3D model, and especially to Jan van Kester, for the excellent advice and help with the understanding of the Delft3D parameterization of the wave forces. I also would like to thank Amaury Camarena and Jacco Groeneweg for the valuable help with SWAN related issues. Thank you also to Martijn de Jong for taking the time to meet me and for the interest in my research.

I would like to thank Justin Rogers for the insightful discussions and for the great previous works that contributed significantly to the current research.

I would like to acknowledge the funding support of the EACEA/EU and CoMEM Board during the 2 years of the Master Programme. Thank you to Sonja Hammer for the always friendly attitude and support. At NTNU, I would also like to thank Øivind Arntsen for making CoMEM students feel at home in Trondheim. I also would like to thank Raed Lubbad for taking me as research assistant at NTNU.

I would like to thank all my previous lecturers/professors at Federal University of Rio de Janeiro - Paulo Rosman, Susana Vinzon, Nelson Violante-Carvalho and Geraldo Wilson, whose classes made me not only learn but also to be one more enthusiastic for coastal dynamics. One special thank to my former supervisor at work, Otavio Sayao, for the opportunity to work together since 2010 and for participating so close of my professional growth in coastal engineering. I also thank Gustavo Oliveira for the daily supervision in my first years working, that were fundamental in my learning process.

To my friends, I would like to thank for keeping in touch even with an ocean between us. A special thank you for the friends who could visit me here in Delft, entertaining my thesis experience in spit of the brief timeline. I also thank my fellow CoMEM students for the experiences we shared during those 2 wonderful years. To the fellow Deltares MSc students, thanks for the great moments we had during lunches, coffee and cake breaks.

Most of all, I would like to thank my family. To my sweet Bruna, for making my life meaningful, for the inspiration you provide me with every day and for joining me during those 2 excellent years of our lifes. To my Mom, I will be extremely grateful for the endlessly love which I grew up with. To my Dad, for inspiring me ever since the day I was born.

1

INTRODUCTION

1.1. MOTIVATION AND RESEARCH SIGNIFICANCE

Spurs-and-grooves (SAG) are a common and impressive characteristic of shallow fore reef areas worldwide. They are composed by series of shore-normal ridges (spurs) separated by channels (grooves) with a finger-like fashion, starting at the seawards edge of the reef flat extending down the reef slope into deeper water (Guilcher, 1988). An example of a SAG system from Florida Keys is shown in Figure 1.1.

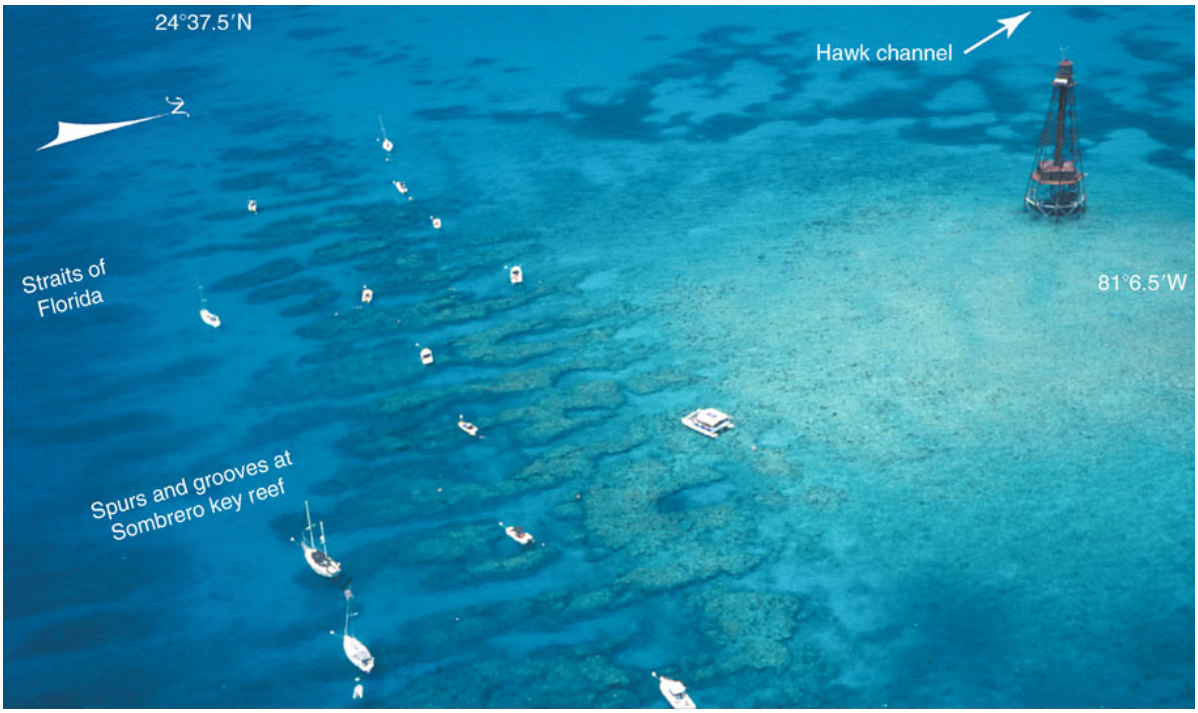

Figure 1.1: Spurs and grooves at Sombrero Key Reef – Florida Keys. Source: Lidz (2007).

SAG morphology is generally reported to be associated with the incoming wave conditions (Munk and Sargent, 1948; Roberts, 1974; Storlazzi et al., 2003; Duce et al., 2014). The importance of SAG structures is related to its potential role as regulator of hydraulic energy, sediments and nutrients, given its location between the reef flat and deep ocean and to the fact that they may host living corals with growing rates potentially faster than the rest of the reef (Munk and Sargent, 1948; Odum and Odum, 1955; Kan et al., 1997; Duce et al., 2014).

Even though the biotic processes dominate the dynamics of coral reefs habitats, physical aspects related to hydrodynamic might be relevant in the coral growth. Energetic environments might have limited reef

development, as extreme waves could break them or induce high abrasion by bedloads and suspended sediment concentrations, usually understood as a factor with potential to harm the coral health (Dollar, 1982; Storlazzi et al., 2003). On the other hand, increasing water motion may induce more mass transfer and nutrient uptake, enhancing photosynthetic production (Falter et al., 2004; Rogers et al., 2013).

The potential effects imposed by climate changes, comprising changes in sea level and in the wave climate, might be relevant to the coral health in the whole reef, including the SAG zone, whose importance as regular of energy and matter is not fully understood.

Although the existence and geometrical properties of SAG are well-documented, the literature concerning specifically the hydrodynamics around them is limited (Rogers et al., 2013, 2015). This study aims to contribute to the better understanding of hydrodynamics in the SAG zone of coral reefs environments.

1.2. RESEARCH QUESTION

This MSc thesis intends to describe in general how flow interacts with SAG formations. Its main interest is to provide scientists predictive capability of the flow conditions for a set of conditions commonly found on coral reef systems with SAG formations.

As it is covered in Chapter 2, SAG formations are more commonly found on wave-dominated environments, and wave energy is thought to be correlated to SAG distribution and morphology. This research is focused on describing the flow induced by waves.

This MSc thesis aims to fully describe the three-dimensional - both horizontal and vertical - flow patterns found within SAG formations and identify which are the dominant processes responsible for them. The research objectives of the current research are summarized in Table 1.1, divided in overall objective and subobjectives, as described below.

Table 1.1: Research objectives.

Type	**Content**
Overall Objective	To describe the flow patterns found within SAG formations and to identify what are the dominant processes involved in the flow around SAG
Subobjective 1	To characterize the horizontal – cross-shore and alongshore - and vertical flows involved in SAGs
Subobjective 2	To determine the role of short wave variation in the SAG flow
Subobjective 3	To determine the role of SAG geometry in the SAG flow
Subobjective 4	To determine the role of driving alongshore currents in the SAG flow
Subobjective 5	To determine the role of long waves in the SAG flow
Subobjective 6	To discuss what the implications of the hydrodynamic aspects could be for corals, sediments and nutrients in the context of coral health and growth

The main interest of this MSc thesis is to describe the three-dimensional circulation found on SAG formations. This research intends to characterize the horizontal – cross-shore and alongshore - and vertical flows involved in SAGs (Subobjective 1). Previous research suggests the existence of circulation cells over SAG, which is detailed in Chapter 2.3, and this is part of the current investigation.

The key point of this study is to identify what are the dominant processes involved in the flow around SAG. In order to do that, the role of the processes listed in Table 1.1 is investigated, as also described below.

This research intends to analyze how the flow around SAG changes for different short-wave conditions (Subobjective 2). The quantification of relative flow changes due to combinations of wave parameters – wave height, period and direction – is a fundamental question in the context of flow characterization, given the fact that SAG geometries are thought to be wave dominated, as explored in Chapter 2.2.3. Furthermore, the verification if circulation cells, explained in Chapter 2.3, might be enhanced or undermined for specific wave conditions is also a relevant question to be addressed.

Moreover, this MSc thesis intends to understand the influence of the SAG geometry on the flow pattern

(Subobjective 3). The variation of the flow circulation induced by SAG geometries are of special interest to the current research, given the variety of existing SAG bathymetries worldwide.

As it is covered in Chapter 2.2.3, SAG formations are usually found on wave-dominated shore-normal and perpendicular to the refracted incoming wave direction. Thus, the wave-induced flow is thought to be mostly in the cross-shore direction.

The contribution of the alongshore flow to the hydrodynamic of SAG bathymetries is another point of interest of this MSc thesis (Subobjective 4). Regardless of the generating mechanism– e.g. tides or winds -, the flow pattern in the presence of an alongshore flow might change, and those changes are evaluated by the current research. It is important to remark that this MSc thesis does not address specifically the flow forced by alongshore currents, but it aims to understand how wave-induced flow is sensitive to situations with alongshore forcing.

It is hypothesized that long waves could control large-scale circulation on the reef flat in a way that the circulation in SAG formations could be affected. This MSc thesis addresses the role of long waves in the SAG flow (Subobjective 5). The aim is to answer how lower frequency ranges could influence the circulation.

Even though the research questions are separated into distinct subobjectives, the current research aims to provide a holistic interpretation of the main contributors to the flow.

Finally, this research also aims to briefly address the transport of material within SAG bathymetries (Subobjective 6), providing a discussion about the implications of the hydrodynamics aspects for corals, nutrients and sediments transport in the context of the coral health and growth.

It is important to notice that this MSc thesis is not focused on describing the hydrodynamics conditions of a particular SAG formation, but instead it aims to predict in general how flow changes for different metocean conditions and SAG geometries.

1.3. OUTLINE

This MSc thesis is divided in the following chapters:

- Chapter 1: Introduction - The research significance and objective are provided.
- Chapter 2: Background - The literature review comprising SAG formations description, hydrodynamics over them and physical processes expected to be relevant in SAG formations.
- Chapter 3: Methodology - The selection of the model and the modelling plan to answer the research objectives are covered.
- Chapter 4: Calibration and Verification - Comparisons between the results of the model used in this MSc thesis and other models, theoretical results and measurements are provided.
- Chapter 5: Results - The results of the simulations to address the research objectives are presented in this chapter.
- Chapter 6: Discussion - The discussion about the results significance with regard to the research questions is provided.
- Chapter 7: Conclusion and Recommendations - The research questions are briefly answered and recommendations are provided.

2

BACKGROUND

This chapter presents the literature review for the development of the current research. Firstly, a brief characterization of coral environments is done in Chapter 2.1. Next, a detailed review of spurs-and-grooves bathymetries is presented in Chapter 2.2, including their formation, geometries and hydrodynamic function. The hydrodynamics itself in spurs-and-grooves is covered in Chapter 2.3. Finally, the physical processes relevant to SAG hydrodynamics are discussed in Chapter 2.4, mainly focused in wave propagation aspects, wave forces and wave-induced currents.

2.1. CORAL REEF ENVIRONMENTS

Coral reefs are calcium carbonate structures built by the polyps, small coralline organisms that extract calcium carbonate from seawater and grow by accretion into a variety of branching skeletal structures corals (Bird, 2008).

They form a diverse underwater ecosystem that is of special interest for scientists due to their unique properties. Their importance is mostly associated with the ecosystem services delivered by them, related to tourism, fisheries and flood protection. Climate changes effects may impose a potential threat to this ecosystem.

Coral reefs are typically found at low latitudes, where mainly the water temperature meets the appropriate conditions for their presence (Guilcher, 1988). In general terms, coral growth depends on the availability of sunlight and nutrients, among many other physical and biotic factors. Their high productivity rates are associated to their efficiency of trapping nutrients and plankton from surrounding waters (Odum and Odum, 1955; Yahel et al., 1998).

They are generally divided in three main geomorphological categories: fringing reefs (connected to the shoreline), barrier reefs (separated from the shore), and atolls (circular or ovoid reef surrounding a lagoon). The distribution of these three categories is shown in Figure 2.1, where it can be seen that most of the coral reefs are located in intertropical regions.

Most of the coral reef systems in the world are in wave-dominated environments, i.e., where the offshore wave height is comparable to or greater than the local tidal range (Lowe and Falter, 2015). Figure 2.2 shows the joint distribution of the significant wave height Hs and the mean tidal range MTR for coral reef systems across the world, where it is evident the the blueish colors (wave-dominated environments) are predominant, although tide-dominated coral reefs can be observed along northern Australia, east Africa, the Pacific coast of Central America, and parts of southeast Asia (Lowe et al., 2015).

In the Pacific and Indian Oceans, the coral reefs experience relatively energetic wave conditions, with annual mean Hs typically higher than 1.5 m. Milder wave climates are observed in the Caribbean, Southeast Asia, and northern parts of Australia (Lowe and Falter, 2015).

Kolijn (2014) assembled offshore wave data of various fringing reefs around the world, comprising measured wave period (Tp) and Hs (Figure 2.3). This dataset shows that:

- Both swell and sea conditions appear to be relevant in the offshore wave climate of those reefs;
- Typical peak wave periods range from 4 to 16 s;
- Most of the offshore Hs are situated between 0.5 and 3 m, with extreme values approaching 5 m; and

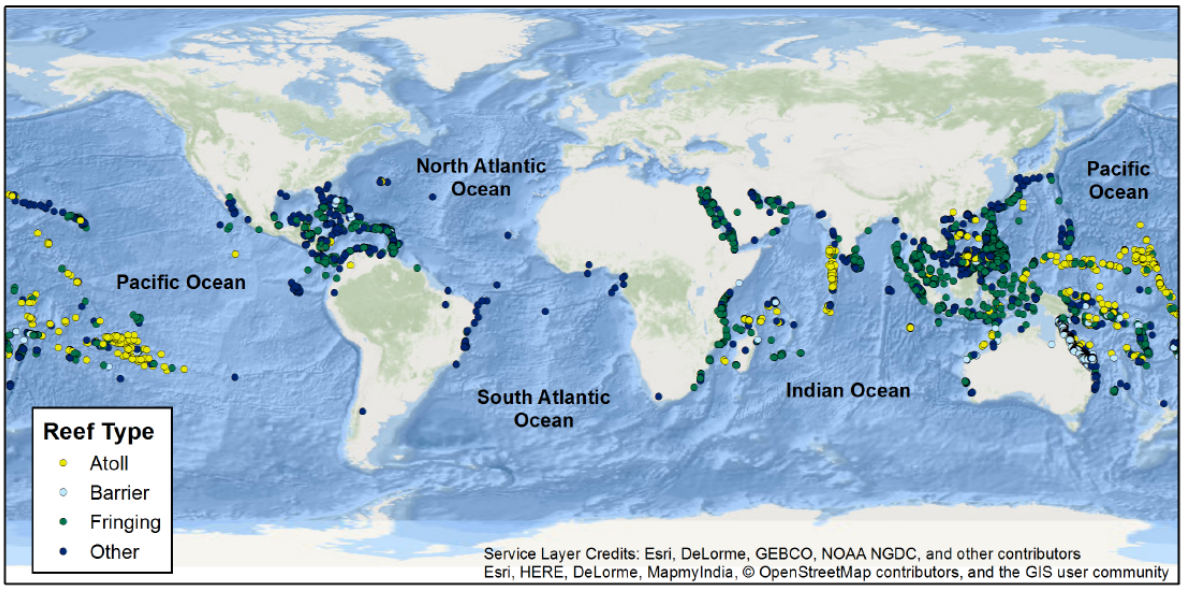

Figure 2.1: Locations of atolls, fringing, and barrier reefs around the world. Source: Pearson (2016).

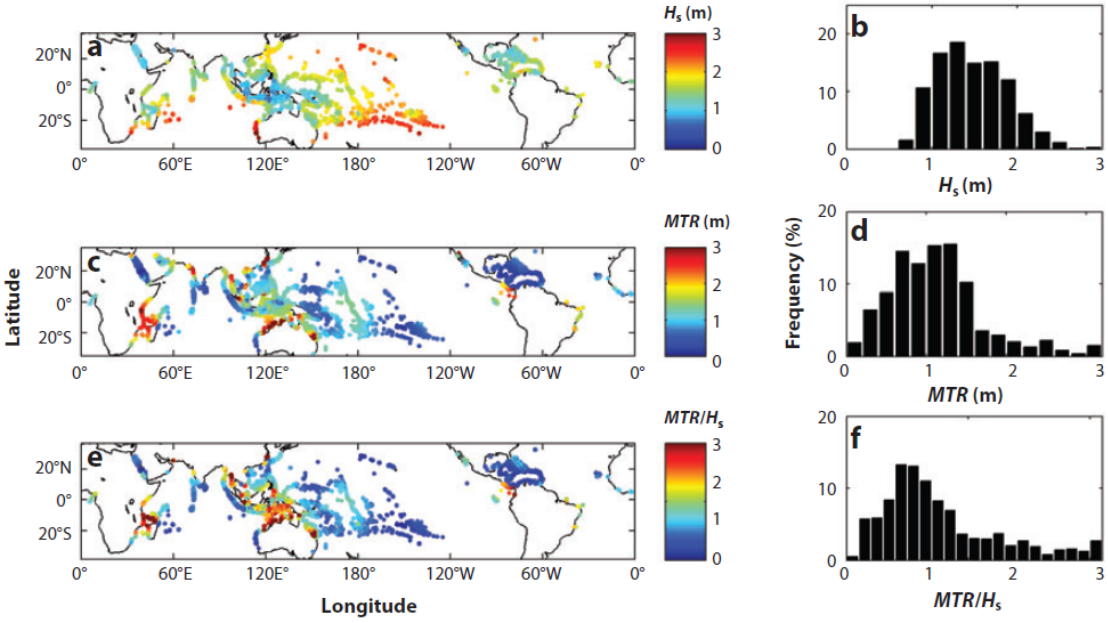

Figure 2.2: Global spatial and frequency distributions of annual mean Hs (a,b), MTR (c,d), and relative tidal range ($\frac{MTR}{Hs}$) (e,f) for warm-water coral reef systems. Source: Lowe and Falter (2015).

- The extreme Hs are in general associated with swell conditions, with higher Tp.

Most of coral reefs in the world are in microtidal or mesotidal regions (Figure 2.2). Macrotidal reef systems ($MTR > 3$ m) can also be found in regions off northern Australia, off east Africa, and off Central and South America (Lowe and Falter, 2015).

Regarding their geometry, a common coral reef zonation consists of three major zones from the shoreline to the ocean: a reef lagoon (back reef), a crest, and a reef front (fore reef). An example of a Japanese coral reef zonation with the presence of SAG in the fore reef is presented in Figure 2.4.

The fore reef can be divided into two regions:

- outer slope, which usually is very steep, possibly rising several thousands of metres from the deep sea-floor Guilcher (1988), and inner slope, which hosts the spurs and groove; and

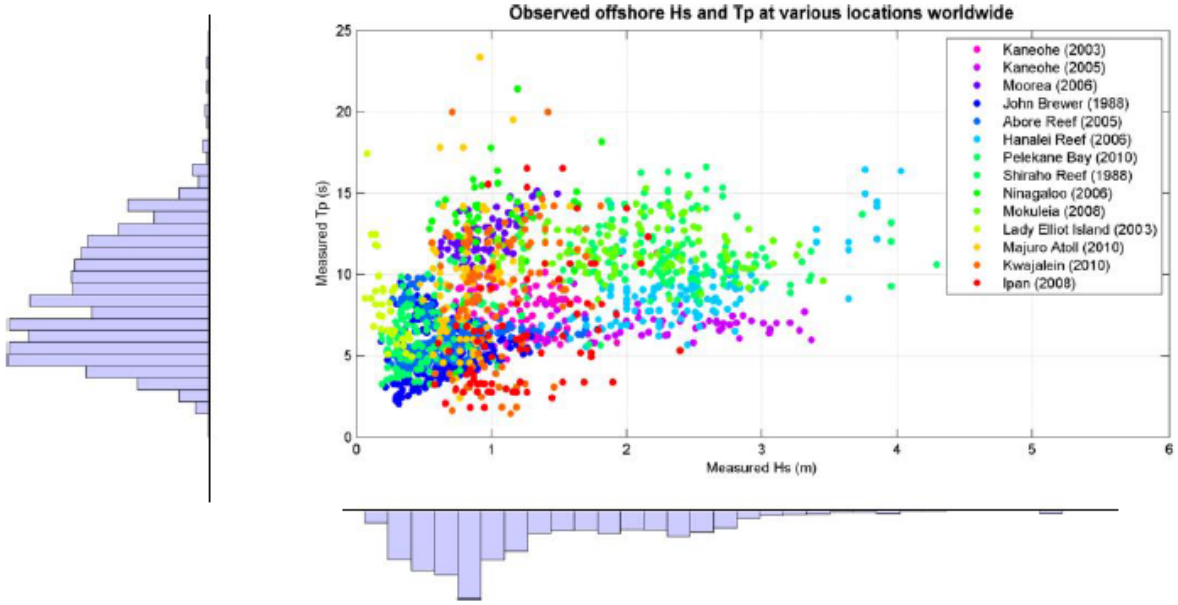

Figure 2.3: Offshore hydrodynamic parameters collected from field campaigns. Source: Kolijn (2014).

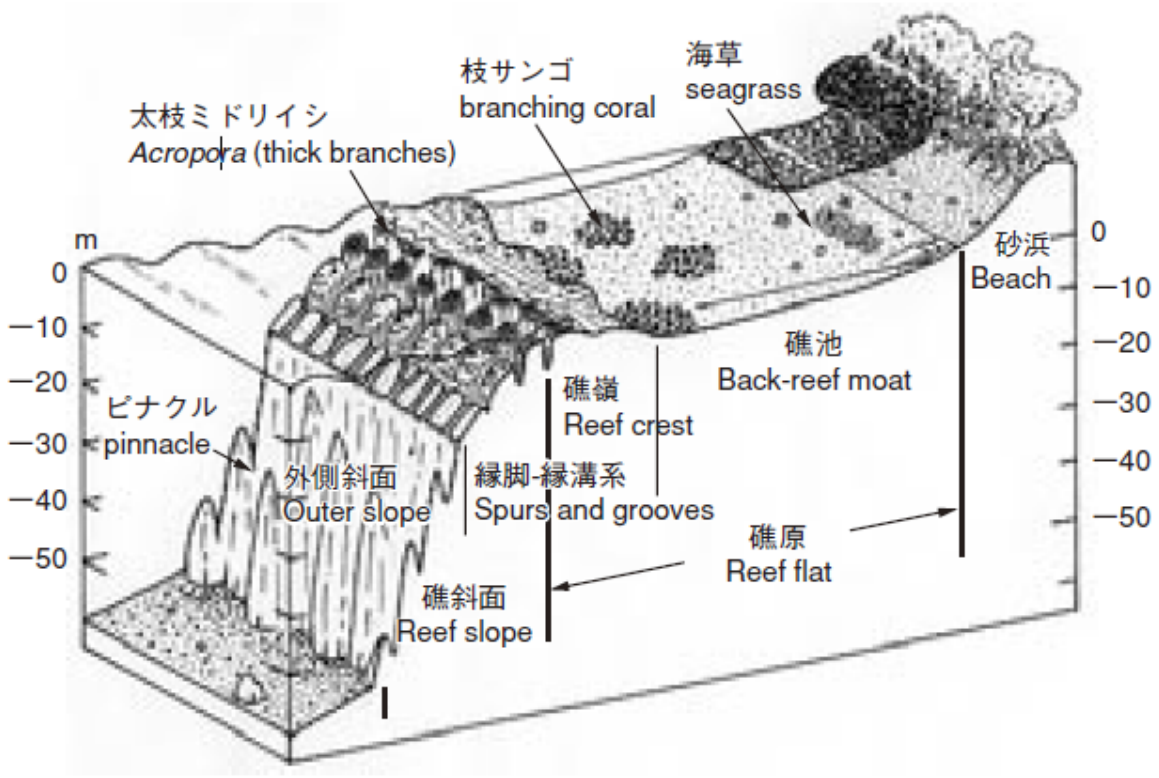

Figure 2.4: Coral reef zonation at Shiraho, Ishigaki Island, Japan. Source: Kayanne et al. (2015).

- inner slope, also named upper reef slope or outer edge of the reefs on the windward side, which hosts the SAG zone, detailed below.

The reef flat forms the widest part of a coral reef, extending from the reef crest to the shore, covered in coral, rubble, sand and algae (Hopley, 2011). Reef flats tend to be wider in shallower parts of the lagoon, and narrower where it is deep (Guilcher, 1988), with typical total width of 50-1000 m (Kolijn, 2014; Quataert et al., 2015).

2.2. SPURS-AND-GROOVES (SAG) FORMATIONS

Spur-and-groove (SAG) are submerged formations with elevated periodic shore-normal ridges of coral (spur) separated by shore-normal patches of sediments/reef debris (groove), typically found across the fore reef (Rogers et al., 2013).

Ever since the 50's (Ladd et al., 1950; Emery et al., 1959), SAG have been observed along reefs in the Pacific Ocean (Munk and Sargent, 1948; Cloud, 1959; Kan et al., 1997; Storlazzi et al., 2008), the Atlantic Ocean (Shinn et al., 1981; do Nascimento Araujo and do Amaral, 2016), the Indian Ocean (Weydert, 1979; Bouchon, 1981), Caribbean Sea (Newell et al., 1951; Goreau, 1959; Roberts, 1974; Roberts et al., 1977; Blanchon and Jones, 1995) and the Red Sea (Sneh and Friedman, 1980). SAG formations can be found in fringing reefs, barrier reefs, and atolls. Examples of SAG systems of the three world oceans are shown in Figure 2.5.

Figure 2.5: Spurs and grooves in coral reefs from three world oceans. (a) Aerial photograph of reef and shallow fore reef on central Belize Barrier Reef (Atlantic Ocean). (b) Underwater photograph of spur and groove at same location, with up to 5-m-high spurs of Acropora palmata and Millepora sp. (c) Aerial photograph of reef and shallow fore reef on western side of Ari Atoll, central Maldives (Indian Ocean). (d) Underwater photograph at same location, north of Mandhoo Island, shows flat spurs, which are composed of coralline algae and some branched Acropora and V-shaped grooves about 1–2 m deep. (e) Aerial photograph of northeastern reef of Moorea, Society Islands, near airstrip (Pacific Ocean). (f) Underwater photograph of same area, with low relief spurs composed of coralline algae and branched Acropora. Grooves up to 2 m deep and V-shaped. Source: Gischler (2010).

2.2.1. FORMATION OF SPURS-AND-GROOVES

The origin of SAG has been variously explained by erosion, oriented coral accretion, antecedent topography, and combinations of the above, with erosion predominant in grooves, and accretion by corals on spurs (Gischler, 2010). Duce et al. (2016) compiled the possible SAG formation processes based on other researchers in the following manner:

- Erosional processes
  - Wave and current driven abrasion of grooves by rubble and/or sediment (Cloud, 1954);
  - "pruning" of corals on spurs and spur walls by occasional hurricanes (Blanchon and Jones, 1997); and
  - limestone solution of antecedent topography fresh water flows during sea level low-stand to form grooves (Newell, 1954; Purdy, 1954).
- Constructional processes
  - water motion promoting aligned coral growth and eventual colony coalescence to form spurs (Shinn, 1963; Shinn et al., 1981; Kan et al., 1997); and
  - coral debris being washed together and rapidly cemented by robust, wave-resistant coralline algae forming spurs (Storlazzi et al., 2003; Hopley, 2011).

Shinn et al. (1981) analyzed the origin of SAG in Looe Kay reef (Florida) with drilling, and concluded that the shallow SAG are constructional, built by polyps and not related to bedrock topography, while deep SAG (depths higher than 15 m) are erosional, formed during lower stand of sea level.

Kan et al. (1997) studied the accretion process of the fringing reefs of the Ryukuy Islands (Japan) through excavation and radiocarbon dating. His data suggest that the growing of the spur was both reefwards and seawards, and not lateral, and the current spur formed a long axis perpendicular to reef-edge line. Sediment movement might undermine the lateral expansion of spurs - accretion of spurs into grooves (Blanchon and Jones, 1995) -, inducing the oriented coral accretion in the longitudinal, parallel to the reef-edge.

Gischler (2010) argued that Indo-Pacific SAG systems are dominantly formed by erosion (Newell et al., 1951; Cloud, 1951; Sheppard, 1981), while Atlantic/Caribbean region SAG are products of coral growth (Shinn, 1963; Shinn et al., 1981). He also suggests that their difference might be explained by the rate of reef accretion, that can also be a function of environmental factors, such as wave energy (Storlazzi et al., 2003) and the course of Holocene sea level.

Duce et al. (2016) combined the formation processes of previously reported SAG formations in a single table (Table 2.1), showing the diversity of reported SAG origins and suggested SAG types found in literature, explored in the next section.

2.2.2. SPURS-AND-GROOVES GEOMETRY

The geometric properties of SAG formations were described by numerous authors (Munk and Sargent, 1948; Cloud, 1959; Blanchon and Jones, 1997; Storlazzi et al., 2003).

Although SAG geometries are vastly reported in the scientific literature, most of the studies have been based in relatively qualitative data or quantitative data limited in resolution and spatial extent (Storlazzi et al., 2003). Duce et al. (2016) observed that there is no standard definition of morphometric parameters, and authors report different metrics, such as SAG wavelength, width and spacing of grooves, spur frequency and spur amplitude/height.

This MSc thesis adopts the measurable morphometric parameters for the SAG geometric description as defined in Table 2.2, predominantly using the same terminologies as Storlazzi et al. (2003) and Rogers et al. (2013).

The morphology of SAG formations varies not only between reefs but also within reefs (Duce et al., 2014). Even though spurs-and-grooves can be described as a superposition of coral ridges over sand-floored groove, the alongshore fashion of this variation is wide-ranging.

Table 2.1: Types of spurs and grooves and their suggested formation mechanisms from the published literature. Source: Duce et al. (2016).

Location (source)	Types and description	Data used	Suggested formation mechanisms
Caribbean, western Indian Ocean, French Polynesia (Gischler, 2010)	**Indo-Pacific** *Dimensions*: wide flat spurs. Narrow V-shaped grooves *Groove floor*: sparse sand and rubble *Spur cover*: coralline algae and few corals **Atlantic** *Dimensions*: U-shaped *Groove floor*: abundant sand *Spur cover*: high coral cover	Qualitative observations and literature review	**Indo-Pacific** - Erosion dominated **Atlantic** - largely constructive. Driven by differences in Holocene sea-level change (transgressive-regressive in the Indo-Pacific and transgressive in the western Atlantic)
Molokai, Hawaii (Storlazzi et al., 2003)	**Higher energy spur and groove** *Depth*: 5–10 m *Dimensions*: mean spur height 0.5 m, ~87 m between spur crests *Spur cover*: Lower total coral cover **Lower energy spur and groove** *Depth*: 15–20 m *Dimensions*: mean spur height 1.1 m, ~93 m between spur crests *Spur cover*: higher total coral cover	Quantitative bathymetric data and wave modelling	Waves are the primary control, light and antecedent topography plays a lesser role. **Higher energy spurs** constructed primarily by cementation of coral rubble. **Lower energy spurs** dominated by in situ coral growth.
Caribbean, Indo-Pacific (Blanchon and Jones, 1997; Blanchon, 2011)	**Shallow spur and groove (2 types)** *Depth*: to 15 m *Dimensions*: One spur every 6–10 m. Spurs 4–8 m wide, 2–8 m high with steep to overhanging sides. Grooves 1–3 m wide *Groove floor*: coral gravel *Spur cover*: ***1. Coralline algae dominated*** ***2. Coral dominated*** **Chute and buttress** *Depth*: ~25–60 m *Dimensions*: Buttresses ~100 m long, 10 m wide, tapering shoreward. One buttress every 30 m or more	Literature review, bathymetric data, short-cores and observations	Distribution and form controlled by wave energy. **Buttresses** and **coral dominated spurs** constructional and grow towards the reef shelf with "pruning" by storms. **Coralline algae dominated** spurs are similar but may (the age structure of these spurs remains unknown) grow seaward.
Grand Cayman Island (Caribbean) (Roberts et al., 1975; Roberts et al., 1977)	**Wave dominated spur and groove** *Depth*: to 8 m *Dimensions*: ~43 m between grooves *Groove floor*: little sediment *Spur cover*: moderate coral cover **Current dominated spur and groove** *Depth*: 8–22 m *Dimensions*: ~50 m between grooves *Groove floor*: extensive sediment *Spur cover*: abundant coral cover	Bathymetry, wave and current measurements	Associated with eustatic sea-level history. **Current dominated** SaGs initiated early in Holocene sea-level rise and have had longer to mature and continued to grow under less wave stress as water deepened.
French Polynesia (Battistini et al., 1975)	**Furrowed platform** *Dimensions*: ~30–40 m long **Buttresses and valleys** *Depth*: – to ~12 m *Dimensions*: ~60 m long *Groove floor*: bare or covered in reef detritus **Outer slope spur and grooves** *Depth*: ~12–27 m *Dimensions*: ~100 m long *Groove floor*: bare or covered in reef detritus	Qualitative observations	**Furrows** "cut in the direction of the slope".

Table 2.2: SAG dimensions.

Variable	Symbol	Definition
Spur height	h_{spr}	Elevation difference between spur and groove
Spur-and-groove wavelength	λ_{SAG}	Distance between two consecutive spur crests
Groove width	W_{grv}	Width of groove
Groove length	λ_{grv}	Length of the groove
SAG cross-shore slope	β_f	Slope of inner fore reef where SAG structure is located
Vertical position of peak spur height	z_μ	Depth where spur height is maximum in a cross-shore profile

Gischler (2010) proposed the two schematic representations of SAG formations presented in Figure 2.6:

- In the Indo-Pacific region, spurs are wide and flat, covered by crustose coralline red algae and few mostly acroporid corals, while grooves are V-shaped grooves, sparsely covered with sand and rubble; and
- In the Western Atlantic/Cabribbean region, spurs have larger coral cover, while grooves are U-shaped, covered with abundant sand.

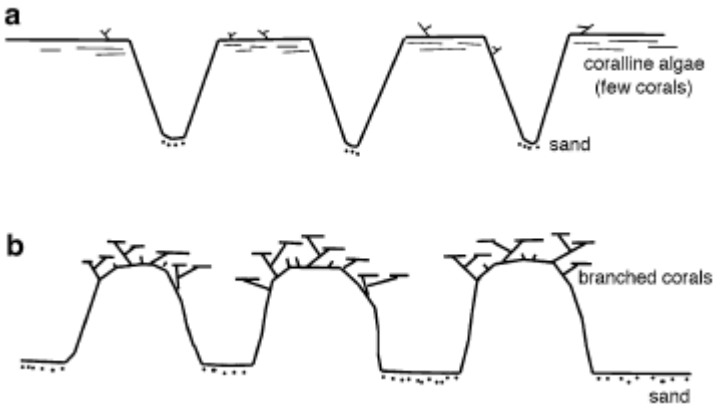

Figure 2.6: Simplified, schematic cross section through Indo-Pacific (a) and Atlantic (b) spur and groove systems. Source: Gischler (2010).

In the fringing reef of southern Moloka'i, Storlazzi et al. (2003) observed smoothly rounded spurs, as it can be seen in Figure 2.7. This figure also shows that:

- Although SAG are rhythmic formations, h_{spr}, λ_{SAG} and W_{grv} can vary significantly in a same region; and
- SAG features are typically shore-normal.

Another alongshore shape reported in the literature is the deeply cut rectangular or even overhanging channels. Goreau (1959) studied the Jamaican coral reefs zonation and referred to them as buttresses, instead of spurs, similarly to the terminology used by Munk and Sargent (1948) and Blanchon and Jones (1997), and canyons, instead of grooves. An example of this shape is shown in Figure 2.8.

In the southern Great Barrier Reef (GBR, Australia), Duce et al. (2016) identified all of these shapes - V-shaped, U-shaped, vertical/overhanging walls - in the SAG formations for a same region.

Although most of the studies on SAG are based on qualitative or limited quantitative observations, Storlazzi et al. (2003) and Duce et al. (2016) conducted extensive quantitative morphologic studies, briefly detailed below.

Storlazzi et al. (2003) characterized the SAG formations of the fringing reef in the Southern Moloka'i, Hawaii through extensive bathymetric data of nearly 5000 SAG structures, varying from 5 to 20 m depth (Figure 2.7). By dividing the studied region into high and low-energy environments relatively to Hawaii conditions, they showed that:

- Both the mean spur height and the mean SAG wavelength of low-energy environments are proportional to the depth up to a depth of 15 m. SAG structures are relatively small and narrow in shallow depths, and grows into larger and broader features in deeper water;
- For high-energy environments, both the mean spur height and the mean SAG wavelength remain relatively constant for all depths;
- Mean spur height and mean SAG wavelength of low-energy environments are larger than the ones from high-energy sites;

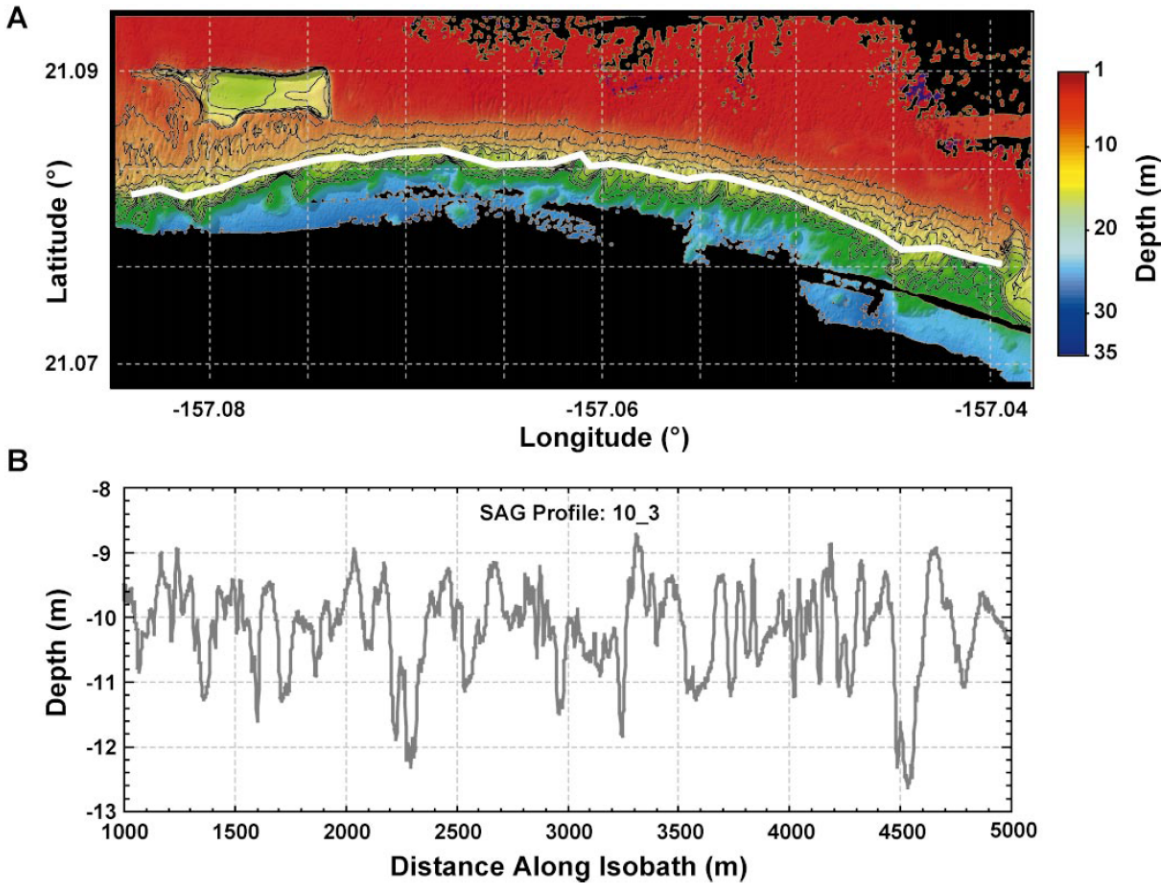

Figure 2.7: (A) Bathymetry of Southern Moloka'i, Hawai'i. (B) Alongshore profile of 10 m isobath - bold white line in A. Source: Storlazzi et al. (2003).

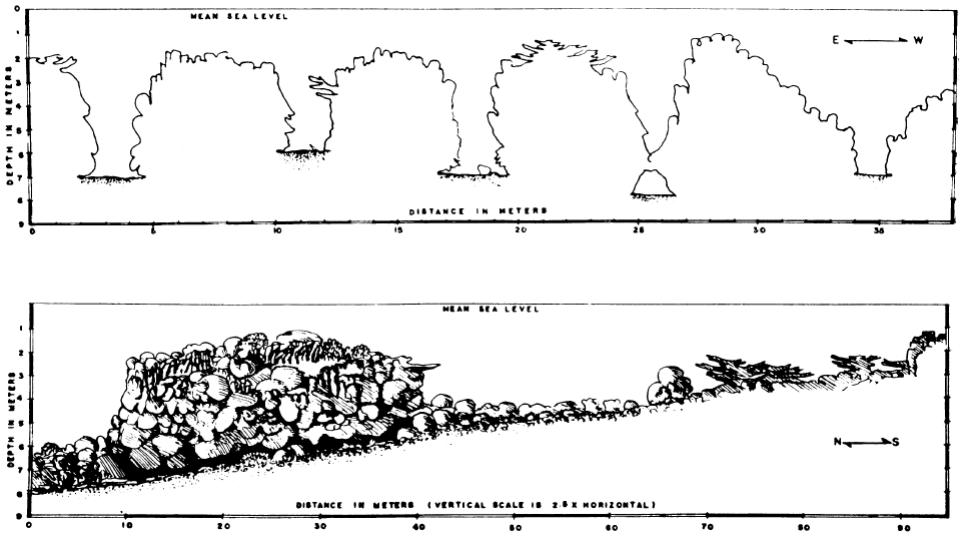

Figure 2.8: Cross-section and longitudinal transect of the buttress zone in the reef near "Sombra", Ocho Rios. Source: Goreau (1959).

- The ratio between groove width and spur width tends to grow in shallow water depths, especially in less sheltered areas;

- The reef flat width was found to exponentially decrease with increasing wave energy; and

- Waves are thought to be dominant in relation to SAG morphology of the analyzed area.

Rogers et al. (2013) presented the histogram of SAG wavelength and spur heights from the same area in Moloka'i, shown in Figure 2.9, where it can be seen that both morphometric parameters vary significantly, with typical values of about 70 and 2 m, respectively.

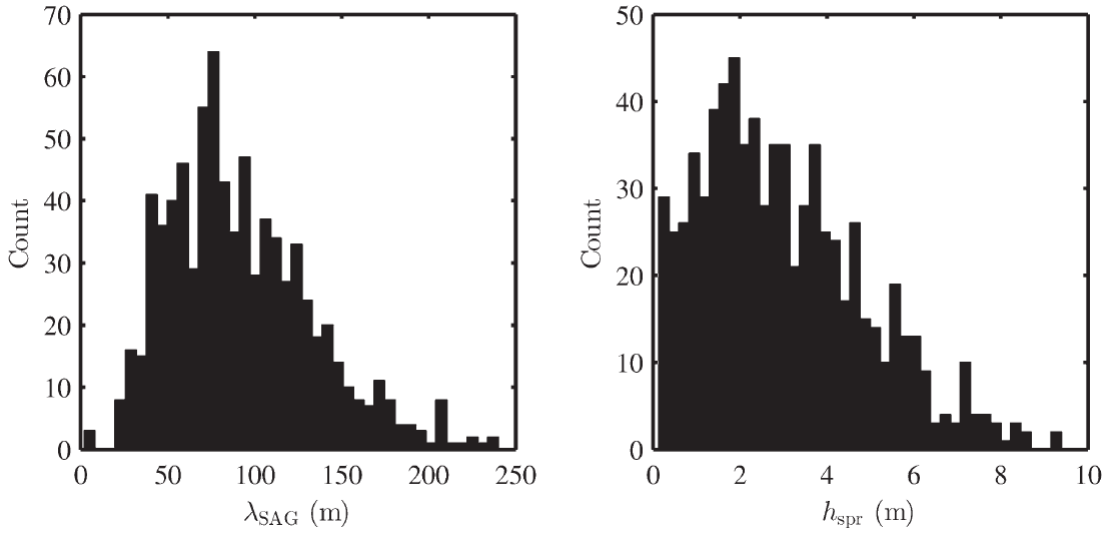

Figure 2.9: Distribution of SAG wavelength and spur height SAG formations at 5, 10, 15, and 20 m depth from southern Moloka'i, Hawai'i. Source: Rogers et al. (2013).

Duce et al. (2016) characterized the SAG structures of 17 reefs in the Capricorn-Bunker Group (CBG), southern GBR, through remotely sensed imagery and bathymetric data of about 12000 grooves. They identified four classes of SAG systems, namely: Deep and disconnected (DaD), Exposed to wave energy (EWE), Long and protected (LaP) and Short and Protected (SaP). Some of the geometric aspects of these classes are compiled in Table 2.3.

Table 2.3: Geometric features observed in SAG classes according to Duce et al. (2016).

Class name	**Morphology**	**Number of SAG**	**Mean depth (m)**	**Spur height (m)**	**Spur width (m)**	**Groove width (m)**	**Mean groove length (m)**	**SAG wave length at start**	**SAG wave length at h = 3 m**	**SAG wave length at h = 10 m**	**Mean slope**
Deep and disconnected (DaD)	V-shaped	1614 (14%)	11	0.5-1.5	6-10	0.5-2	75	42	69	45	1:19
Exposed to wave energy (EWE)	U-shaped	4971 (44%)	3	1.0-2.5	5-23	1-2	61	21	26	54	1:25
Long and protected (LaP)	Vertical or overhanging walls	604 (5%)	4	1.5-3.5	3-12	2-10	71	32	38	58	1:21
Short and protected (SaP)	Vertical or overhanging walls	4241 (37%)	4	1.5-4.0	4-12	1-6	23	27	34	44	1:21

Duce et al. (2016) concluded that in southern GBR wave energy is the most important factor controlling SAG distribution and morphology. Overall, the SAG wavelength was shown to decrease for lower depths (Table 2.3), which was interpreted as SAG formations dissipating the wave energy by increasing the surface area of the reef slope.

Another important conclusion of this study is that SAG are less likely to develop in steeply sloping (> 5° or 1:11), as more than 90% of the measured grooves have a mean slope in that range. Munk and Sargent (1948) also suggested that trend in Bikini Atoll, where steeper slopes were associated with smaller groove lengths. The width of the upper slope reef was also correlated to significantly lower groove lengths, as Short and Protected reefs (Table 2.3) presented the lowest values of both mean groove length and mean width upper slope (Duce et al., 2016).

Although Duce et al. (2016) proposed that classification, they also argued that SAG formations found worldwide vary significantly (Figure 2.10), and localized environmental factors besides wave energy might contribute to morphology and evolution. Figure 2.10 shows that Moloka'i has by far the largest grooves and the longest SAG wavelength (or mean spacing), possibly due to a more exposed environment and to the fact that it is a fringing reef, instead of a platform, and as such they suggested that another class might be needed (Duce et al., 2016).

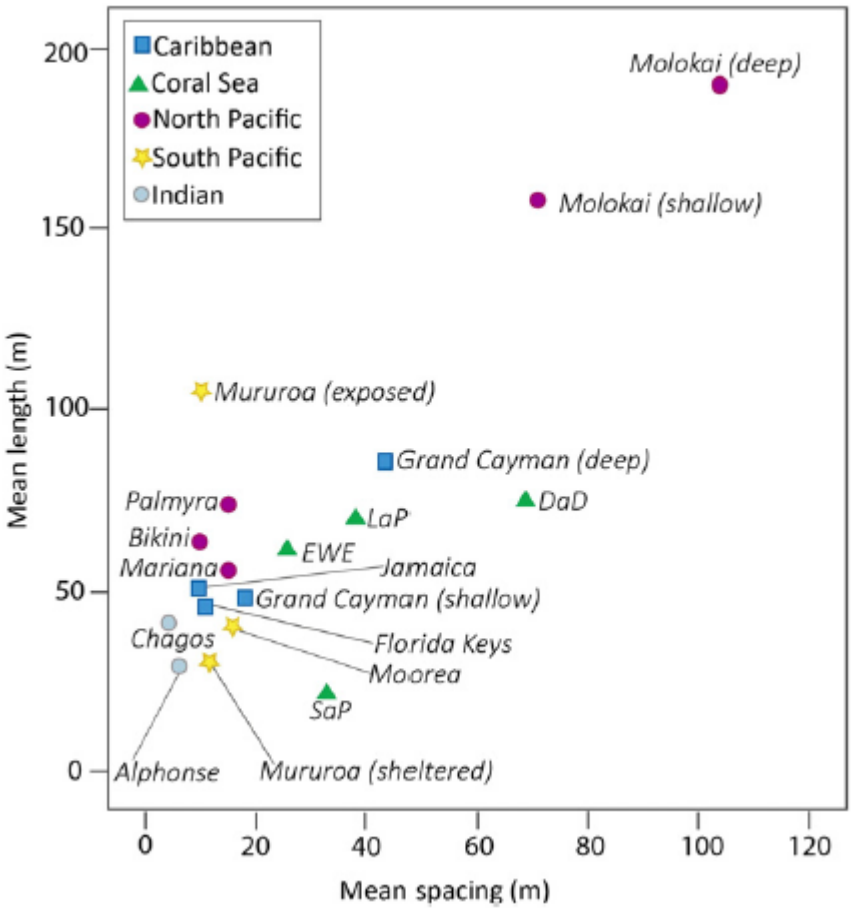

Figure 2.10: Comparison of SAGs around the world with respect to length and spacing. The four classes identified in Duce et al. (2016) are shown as triangles. The other sites in this figure were described in the following published works: Molokai: Storlazzi et al. (2003); Mururoa: Chevalier (1973); Grand Cayman: Roberts (1974); Palmyra: Rogers et al. (2015); Bikini: Munk and Sargent (1948); Chagos: Sheppard (1981); Alphonse: Hamylton and Spencer (2011); Jamaica: Goreau (1959); Florida Keys: Shinn (1963); Mariana: Cloud (1959). Source: Duce et al. (2016).

Rogers et al. (2013) pointed out that, although the scales of SAG vary worldwide, spur heights are of order 0.5 - 10 m, SAG alongshore wavelength varies between 5 and 150 m, while groove width grows from 1 to 100 m. SAG bathymetries can be found in depths from 0 to 45 m below mean sea level (Wood and Oppenheimer, 2000).

2.2.3. HYDRODYNAMIC FUNCTION OF SAG FORMATIONS

Numerous studies related the SAG geometry with the incident wave conditions (Munk and Sargent, 1948; Emery et al., 1959; Cloud, 1959; Storlazzi et al., 2003; Rogers et al., 2013).

Munk and Sargent (1948) showed that in Bikini Atoll well-developed SAG formations are located in more exposed areas by correlating the distribution of grooves with the distribution of wave power around the Atoll. Roberts (1974) and Duce et al. (2014) found the same trend on Grand Cayman and southern GBR, respectively. The SAG formations were interpreted by Munk and Sargent (1948) as a natural breakwater that withstand the wave forces before reaching the reef flat.

Spurs alignment is generally considered to be orthogonal to the direction of the main refracted incoming wave, which was noted by Shinn (1963), in southern Florida, by Roberts (1974), in Grand Cayman Island and by Duce et al. (2016), in southern GBR, Australia.

Weydert (1979) found that, for oblique waves, the orientation of the spurs is a resultant direction between the direction of the swell wave rays and the directon of the spurs and of the slope of the outer flat in southwest coast of Madagascar. Sneh and Friedman (1980) reported tangential spurs in the Red Sea.

It is remarkable the fact that Storlazzi et al. (2003) and Duce et al. (2016) encountered the same trends for SAG wavelengths variations over depth and wave power. Figure 2.10 shows that SAG wavelengths tend to be shorter both for more exposed/shallower areas - Grand Cayman deep, Moloka'i deep, Mururoa exposed and EWE (exposed) having longer SAG wavelengths than Grand Cayman shallow, Moloka'i shallow, Mururoa sheltered and SaP (sheltered), respectively.

These trends indicate that higher energy areas - regardless if due to a more exposed location in relation to the swell propagation or due to shoaling waves in shallower waters - are associated with closer groove spacing (or shorter SAG wavelengths), that suggest a significant correlation between wave energy and SAG morphology.

2.3. HYDRODYNAMICS IN SPURS-AND-GROOVES

Although the existence and geometrical properties of SAG are well-documented ever since the 50's, the literature concerning specifically the hydrodynamics around them is sparse. The author research indicates that a characterization of flow with measurement or quantitative model prediction was covered only by Roberts et al. (1977), Rogers et al. (2013) and Rogers et al. (2015), which are briefly detailed below.

Roberts et al. (1977) conducted field measurements on SAG bathymetry with a single dye release in a strong alongshore flow conditions (up to 0.5 m/s measured closeby) at Grand Cayman, and they measured 31 cm/s of horizontal near-bed velocity over the groove, carrying the dye plume onshore and up and over the spur before being advected alongshore, apparently tidally dominated.

Rogers et al. (2013) investigated the hydrodynamics of SAG with a two-dimensional Boussinesq-type model (funwaveC), and found that there is a nearshore Lagrangian circulation pattern or counter-rotating circulation cells, with transport offshore over the spur and onshore over the groove in the offshore region of the SAG, and with the reversed pattern closer to the surf zone. This type of circulation is hereafter referred to as SAG circulation cells.

They concluded that the alongshore imbalance between the pressure gradient and the nonlinear wave terms is the main mechanism driving this cell. Sensitivity analyses indicated that the circulation is enhanced for spur-normal waves, weak alongshore currents, larger wave heights, increased spur heights and decreased bottom drag.

Results of this modelling study are also further presented and discussed in Chapter 4.2, as the current research used it for calibration purposes.

Rogers et al. (2015) conducted two field campaigns in SAG formations on Palmyra Atoll, where measurements of velocities and pressures on top of spur and grooves were carried out. Two field campaigns were conducted on the atoll, namely, SFR12 and NFR13, whose SAG geometries are shown in Table 2.4 and Figure 2.11.

SFR12					**NFR13**				
Depth	h_{spr} (m)	λ_{SAG} (m)	W_{grv} (m)	$\tan\beta_f$	Depth	h_{spr} (m)	λ_{SAG} (m)	W_{grv} (m)	$\tan\beta_f$
8-10	1.8	15	2	0.15	8-11	1.9	14	1.4	0.07

Table 2.4: Geometry of SAG formations described on Rogers et al. (2015).

Their measurements show that there are situations with SAG circulation cells, especially in cases with low alongshore flow. A snapshot of one of those situations shows a strong offshore and downward Lagrangian

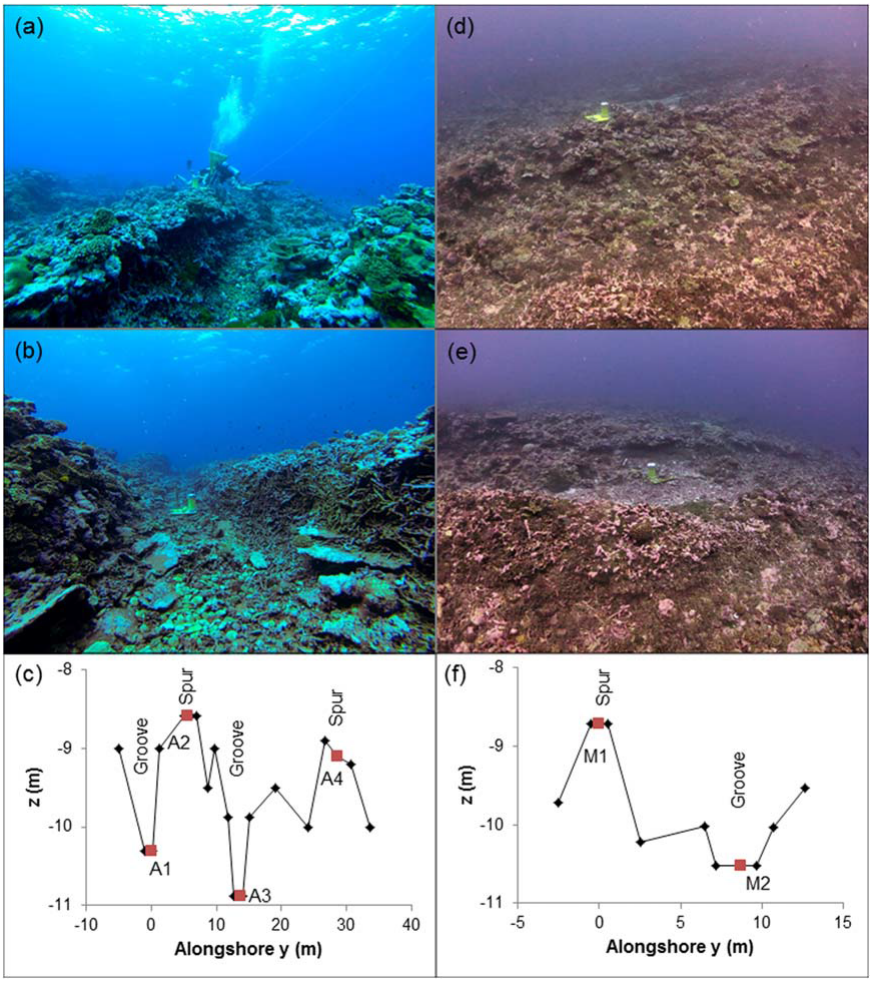

Figure 2.11: Field experiment images and spur and groove bathymetry, for NFR13 experiment (a–c), and SFR12 experiment (d–f). Source: Rogers et al. (2015).

flow over the spurs near the surface, and a moderated onshore and upward flow over the grooves (Figure 2.12).

Average profiles of the rms velocities over depth for both experiments (Figure 2.13) shows a complex shape of Eulerian velocities, with higher velocities close to the water surface and lower velocities approaching the bottom. SFR12 mean cross-shore Eulerian currents look approximately constant along the depth, with reduction in the lowest meters.

The mean cross-shore Stokes Drift velocities look one order of magnitude lower than mean Eulerian velocities for the NF13 experiment, while for SFR12 it scales with the mean Eulerian velocities. The mean alongshore Stokes Drift velocities for both experiments represent a small fraction of the cross-shore, showing that shore-normal waves are dominant during the experiments.

Even though waves are mostly shore-normal, the mean alongshore Eulerian and Lagrangian velocities are higher than the cross-shore currents. The shape of those alongshore velocities is predominantly logarithmic over the spurs, while over the grooves it looks the same, but with an offset of about the spur height (Rogers et al., 2015).

The main mechanism responsible for this circulation pattern was found to be the imbalance between the pressure gradient and the radiation stress gradients, that accelerates the flow until the nonlinear convective terms are large enough to balance it. The hydrodynamic conditions with stronger circulation had directly incident waves with low alongshore flow conditions, confirming the previous modelling study Rogers et al. (2013).

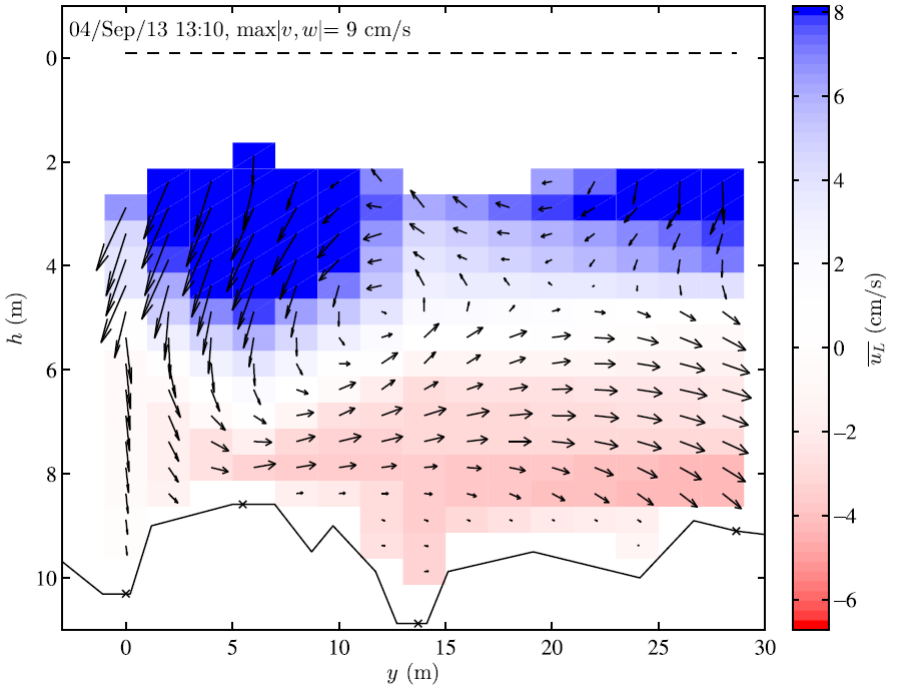

Figure 2.12: Mean Lagrangian velocity, in the alongshore (y) and vertical (z) direction showing characteristic spur and groove circulation cells during NFR13 experiment. Blue and red colours indicate offshore and onshore flows, respectively. Source: Rogers et al. (2015).

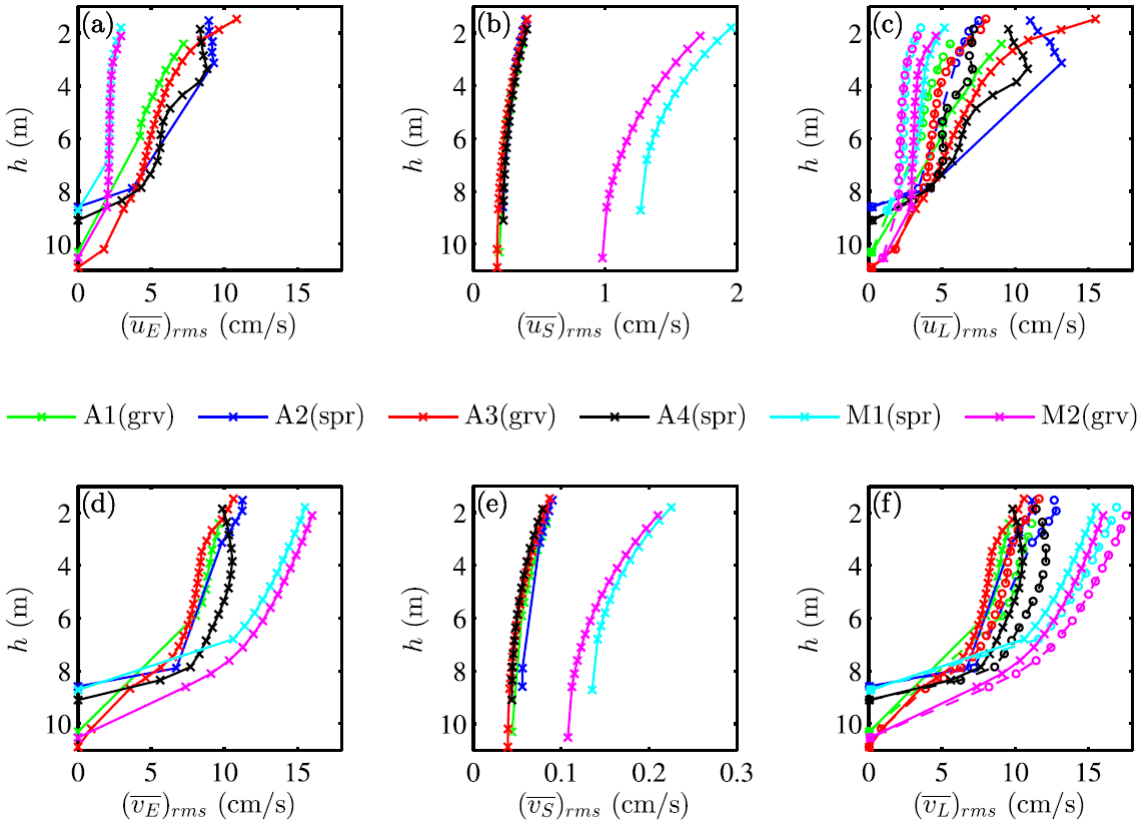

Figure 2.13: Average profiles over depth for rms of mean Eulerian ($\overline{u_E}$), Stokes drift ($\overline{u_S}$), and Lagrangian velocities ($\overline{u_L}$) during NFR13 and SFR12 experiments. Source: Rogers et al. (2015).

Rogers et al. (2015) also evaluated the implications of the measured hydrodynamic conditions concerning coral health aspects. They found out that more favorable conditions for coral recruitment and growth tend to appear over spurs rather than over grooves, as they experience higher mean alongshore velocity, downward vertical velocity, and higher turbulence, and as lower sedimentation takes places on top of them due to higher and more varied bottom shear stresses.

Results of experiments SFR and NFR13 are also further discussed in the Chapter 4.3, as this MSc thesis used them for model verification purposes.

2.4. PHYSICAL PROCESSES IN SAG STRUCTURES

As it was described in the past sections, waves seem to play a primary role in SAG morphologies and most of the coral reef systems in the world are in wave-dominated environments. This section describes the technical background for the understanding of how waves transform on SAG structures, and which effects could be expected on the flow pattern.

2.4.1. WAVE PROPAGATION

Waves approaching reef systems firstly encounter the outer steep slopes and then reach the fore reef, where SAG structures are located, with relatively milder slopes

Through a wave propagation point of view, the zone where SAG geometries are predominantly located is named shoaling/refraction zone, where both shoaling and refraction processes would be expected to be dominant, besides increasing friction with lower depths and diffraction, as explained below.

Normally incident waves traveling from deep to shallow water can be described by the following ordinary differential equation (2.1):

$$\frac{\mathrm{d}EC_g}{\mathrm{d}s} = 0 \tag{2.1}$$

where E is the wave energy, C_g is the wave group celerity and s is the wave propagation direction.

The wave energy is related to the wave height in the following way (2.2):

$$E = \rho g \frac{H^2}{8} \tag{2.2}$$

where ρ is the water density, g is gravity and H is the wave height.

With linear wave theory (LWT) approximation, the group wave celerity depends both on the depth and on the wavelength (2.3):

$$C_g = nC = n\frac{L}{T} \tag{2.3}$$

where C is the wave celerity, L is the wavelength, T is the wave period, and n is given by (2.4):

$$n = \frac{1}{2}(1 + \frac{2kd}{\sinh 2kd}) \tag{2.4}$$

where k is the wave number, given by $\frac{2\pi}{L}$, and d is the water depth. The wavelength L has the following implicit expression (2.5):

$$L = L_0 \tanh kd = \frac{gT^2}{2\pi} \tanh kd \tag{2.5}$$

where Lo is the deep water wavelength. The alterations in wave height experienced by waves that approach an alongshore uniform shore perpendicularly are called shoaling. As wave celerity changes as a result of wave propagation from offshore to shallow waters, the wave energy changes accordingly in the following manner (2.6):

$$EC_g = E_0 C_{g0} \tag{2.6}$$

By rearranging the terms in the previous equation, the wave height is given by (2.7):

$$H = H_0 \sqrt{\frac{1}{2}\frac{1}{n}\frac{1}{\tanh kd}} = H_0 K_s \tag{2.7}$$

where K_s is denominated the shoaling coefficient, which is 1 in deep water, decreases with water depth to 0.91 and then rises to infinity as the water depth approaches zero.

When waves approach shallower waters at an angle, wave crest might bend to align themselves with the bottom contours, making wave direction more perpendicular to the shore. This process is called refraction, and it occurs due to differential wave celerities for diffent depths.

By assuming constant energy flux between the wave rays from offshore to shallow waters, the following expression (2.8) can be written:

$$EC_g b = E_0 C_{g0} b_0 \tag{2.8}$$

where b is the distance between two adjacent wave rays or a segment of wave crest. By combining the previous equations, the wave height is provided by (2.9):

$$H = H_0 \sqrt{\frac{1}{2}\frac{1}{n}\frac{1}{\tanh kd}} \sqrt{\frac{b_0}{b}} = H_0 K_s K_r \tag{2.9}$$

where K_r is the refraction coefficient. Wave refraction calculations assume no crossing of the wave rays.

Wave diffraction is the transfer of the wave energy across wave rays, or the lateral spreading of wave energy perpendicular to the dominant wave direction. Although diffraction is usually exemplified in textbooks in cases of sudden changes in wave conditions such as obstructions, it might be also important in situations in which classical wave refraction effects alone would indicate zones of wave convergence and extremely high concentrations of wave energy (Dean and Dalrymple, 2001).

Refraction and diffraction take place simultaneously and the distinction between lateral and orthogonal transfer of energy relatively to the wave ray is purely an academic separation (Kamphuis, 2010).

Wave shoaling, refraction and diffraction transform the waves from deep water to the point where they break, characterized by a physical limit associated with a limit in the depth (H/d) or in the steepness (H/L). When one of these limits is exceeded, the wave heights start to decrease substantially due to energy dissipation.

As shown in the last sections, SAG structures are usually aligned to the main refracted incoming wave, and extend from offshore (depths of 30 m) up to the reef crest, where most of the wave breaking is expected due to lower depths.

By assuming idealized uninterrupted grooves extending from offshore up to the reef crest, and spurs as superposition of rhythmic coral ridges over grooves, both shore-normal and aligned with the main wave direction, it could be expected that refraction would tend to concentrate energy over spurs and deconcentrate over grooves due to the difference of depths between them.

Simultaneously, diffraction would tend to smear out those differences. In case diffraction is able to overcome refraction effects, low alongshore gradient of wave heights would occur due to the differential shoaling over spurs and grooves, purely given by depth differences between those.

For SAG systems, the dominance of diffraction over refraction depends on geometrical aspects - the spur height and the SAG wavelength - and on wave parameters - wave height and wavelength.

Rogers et al. (2013) found that for an idealized SAG geometry similar to the one described in the last paragraphs, with spur heights of 2.9 m, the difference in wave height over spur and groove would be negligible for SAG wavelengths with up to 100 m . A maximum difference of up to ±20% of the incoming wave over spur and groove, respectively, was obtained for SAG wavelengths of 175 m, as it is shown in Figure 2.14.

2.4.2. WAVE FORCES

Wave forces are generated when there is a change in the wave-induced momentum flux from one location to another. The wave-induced momentum flux can be either a net inflow or outflow of momentum due to the wave, and it consists of two parts:

- transfer of momentum due to advection by horizontal wave particle velocity; and
- wave-induced pressure force due to the wave pressure.

Radiation stress is defined as the depth-integrated and wave-averaged flux of momentum due to waves. Assuming a coordinate system with x and y as horizontal axes and z as vertical axis, with waves propagating at an angle with x, the wave-averaged transport of x-momentum in the x-direction or radiation stress S_{xx} is expressed as (2.10):

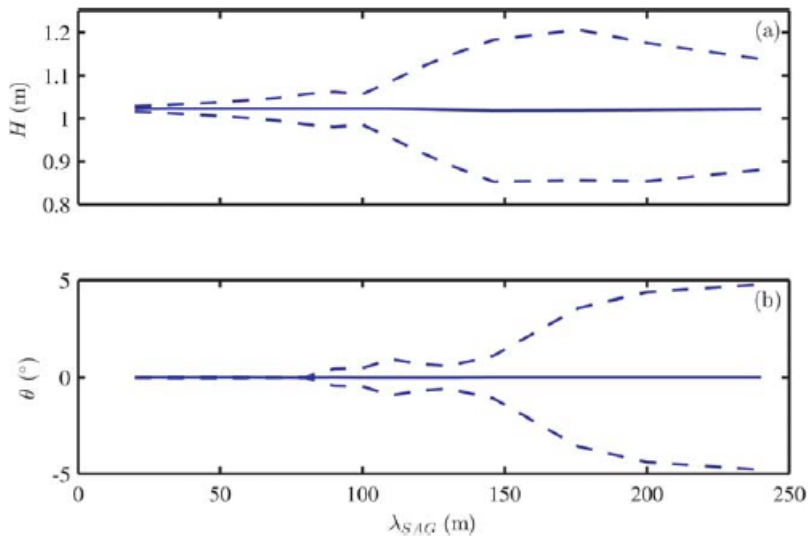

Figure 2.14: Variation of wave height H and wave angle with SAG wavelength at x = 440 m. (a) Alongshore mean H (solid) and max/min H (dash), (b) alongshore mean (solid) and alongshore max/min (dash). Source: Rogers et al. (2013).

$$S_{xx} = \overline{\int_{-h_0}^{\eta} (\rho u_x) u_x dz} + \overline{\int_{-h_0}^{\eta} p_{wave} dz} \tag{2.10}$$

where h_0 is the water depth, η is the instantaneous water surface, ρ is the water density, u_x is the wave particle velocity in x-direction, p_{wave} is the wave-induced pressure. S_{xx} is directed in the x-direction and it acts normally to the x-direction. Both the advection by horizontal wave particle velocity (first term of RHS on 2.10) and the wave pressure (second term of RHS on 2.10) contribute to S_{xx}.

The radiation stress S_{xy}, or the shear component of radiation stress, is wave-averaged transport of x-momentum in the y-direction, and it is given by (2.11):

$$S_{xy} = \overline{\int_{-h_0}^{\eta} (\rho u_x) u_y + \tau_{xy} dz} \tag{2.11}$$

where τ is the shear stress due to waves, which is zero for an irrotational ideal fluid, one of the assumptions in the linear wave theory. S_{xy} is directed in the x-direction and it acts normally to the y-direction. Thus, for an irrotational ideal fluid, only the advection by horizontal wave particle velocity (first term on RHS of 2.11) contributes to S_{xy}.

The radiation stress S_{yy}, is the wave-averaged transport of y-momentum in the y-direction, and it is given by (2.12):

$$S_{yy} = \overline{\int_{-h_0}^{\eta} (\rho u_y) u_y dz} + \overline{\int_{-h_0}^{\eta} p_{wave} dz} \tag{2.12}$$

where u_y is the particle velocity in x-direction. S_{yy} is directed in the y-direction and it acts normally to the y-direction. Both the advection by horizontal particle velocity (first term on RHS 2.12) and the wave pressure (second term of RHS on 2.12) contribute to S_{yy}.

In case waves propagate at x-direction, no orbital velocities exist in y-direction, thus S_{xy} is 0 and S_{yy} becomes (2.13):

$$S_{yy} = \overline{\int_{-h_0}^{\eta} p_{wave} dz} \tag{2.13}$$

with contribution due the pressure part only.

With LWT derivations, and assuming waves traveling at angle θ with x-direction, S_{xx}, S_{xy} and S_{yy} are provided by (2.14), (2.15) and (2.16), respectively:

$$S_{xx} = (n - 0.5 + n\cos^2\theta)E \tag{2.14}$$

$$S_{xy} = n\cos\theta\sin\theta E \tag{2.15}$$

$$S_{yy} = (n - 0.5 + n\cos^2\theta)E \tag{2.16}$$

For the situation with waves propagating at x-direction, S_{xy} and S_{xy} are 0, and S_{xx} and S_{yy} become (2.17) and (2.18), respectively:

$$S_{xx} = (2n - 0.5)E \tag{2.17}$$

$$S_{yy} = (n - 0.5)E \tag{2.18}$$

The equations above show that radiation stress expressions with LWT derivation are function of n (2.4), E (2.2) and θ. Those parameters change in the following manner:

- n gradually increases from 0.5 (deep water) to 1 (shallow water);
- E is a function of shoaling, refraction and diffraction. For a shoaling only situation, E varies as quadratic function of H, namely, it decreases from deep water up to a location where K_s equals 0.91 and then increases up to the edge of the surf zone, where it starts decreasing again; and
- θ is a function of refraction and diffraction. For a refraction only case, it gradually decreases from deep water to shallow water, as wave crest tend to align with bottom contours.

As waves propagate (2.1), momentum flux due to waves can be changed through changes of all those parameters.

Horizontal wave forces are generated when horizontal gradients in radiation stresses exist, as shown in (2.19) and (2.20):

$$F_x = -(\frac{\partial S_{xx}}{\partial x} + \frac{\partial S_{xy}}{\partial x}) \tag{2.19}$$

$$F_y = -(\frac{\partial S_{yy}}{\partial y} + \frac{\partial S_{yx}}{\partial x}) \tag{2.20}$$

In case waves propagate at x-direction, wave forces F_x and F_y become (2.21) and (2.22), respectively:

$$F_x = -(\frac{\partial S_{xx}}{\partial x}) \tag{2.21}$$

$$F_y = -(\frac{\partial S_{yy}}{\partial y}) \tag{2.22}$$

SAG systems are shore-normal and commonly orthogonal to the main wave direction. Assuming x-axis in the shore-normal direction, waves in x-direction and that diffraction overcomes refraction effects, it could be expected that S_{xy} would be 0, making S_{xx} and S_{yy} represented by (2.17) and (2.18), respectively. Thus, wave forces at x-direction would be provided by (2.21), while at y-direction they would be given by (2.22).

The depth-averaged wave forces in x-direction are function of the cross-shore gradient of radiation stress, function of n and E. They are expected to grow in absolute value from the point where $K_s = 0.91$ up to the breaking point in case of monotonic increase in depth from offshore to the shoreline, since both n and E increase shorewards. Assuming a constant slope in the SAG zone, this behavior would be expected to occur over the grooves, while over the spurs it would depend on the cross-shore slope of the spur heights.

The depth-averaged wave forces in y-direction are also function of alongshore gradient of radiation stress, function of n and E. With dominant diffraction, the alongshore gradient of E tends to be low, and the alongshore gradient of n is small, since n varies between a minimum value of 0.5 up to 1. This means that the force term in the momentum balance equation (2.23), $\frac{F_y}{\rho(h_0+\overline{\eta})}$, is expected to be dominated by changes in depth, thus related to the spur height. The depth-averaged momentum balance equation is discussed in Chapter 2.4.3).

2.4.3. WAVE EFFECTS ON THE MEAN FLOW

The last section covered the depth-integrated wave-averaged forces. Those forces are driving mechanisms for the hydrodynamics, either changing the water level (set-up and set-down) or inducing currents.

The depth-integrated wave-averaged momentum conservation equation without Coriolis and surface forcing can be written as (2.23):

$$\underbrace{\frac{\partial U_i}{\partial t}}_{1} + \underbrace{U_j \frac{\partial U_i}{\partial x_j}}_{2} = \underbrace{-g\frac{\partial \overline{\eta}}{\partial x_i}}_{3} \underbrace{-\frac{\tau_{bi}}{\rho h}}_{4} \underbrace{-\frac{F_i}{\rho h}}_{5} + \underbrace{\frac{1}{\rho}\frac{\partial \tau^T_{ij}}{\partial x_j}}_{6} \qquad i,j = \{1,2\} \tag{2.23}$$

where τ_b is the bottom shear stress and τ^T_{ij} is the horizontal turbulent stress (or viscous forces). The equation (2.23) is basically Newton's second law, with the acceleration (momentum change rate) on the LHS and forces on the RHS, and the interpretation of each of the terms in (2.23) is shown below:

- (1) is the local acceleration term;
- (2) is the horizontal advective acceleration;
- (3) is the pressure gradient term;
- (4) is the bed shear stress;
- (5) is the wave force (2.19 and 2.20); and
- (6) is the horizontal turbulent stress.

The description of the 3D flow equation is further covered in Chapter 3.1.4.

Assuming the wave force being balanced solely by the pressure gradient term, a water level difference results from changing radiation stresses as wave propagates. In the shoaling zone, where SAG formations are predominantly located, progressively increasing wave heights lead to slightly decreasing water levels, called set-down. In the breaking zone, decreasing wave heights result in the increasing water levels, referred to as set-up.

With pressure gradient balancing wave forces offshore of the surf zone, Longuet-Higgins and Stewart (1964) deduced an expression for the mean set-down for alongshore-uniform bathymetries, shown below (2.24):

$$\overline{\eta} = -\frac{kH^2}{8\sinh 2kh} \tag{2.24}$$

With wave forcing (term 5 in 2.23), the wave-averaged momentum balance is closed with the remainder terms - pressure gradient, bottom friction, viscous forces and acceleration. If this balance is not exclusively closed with pressure gradient, currents are induced, covered in the next section.

2.4.4. WAVE INDUCED CURRENTS

In general, three types of wave-induced currents are referred to when dealing with waves: Eulerian velocities, Stokes Drift velocities and Lagrangian velocities.

Eulerian velocities can be understood as flow velocities from a fixed viewpoint, such as in the measurement instruments or fixed grid point in numerical models. On the other hand, Lagrangian velocities assume flow velocities from a moving viewpoint, such as a moving particle.

In wave-averaged timescales, net-averaged wave forces induce Lagrangian or Eulerian currents, depending on which reference frame is used to solve the momentum balance.

The net forward motion of particle trajectories after a wave cycle is called Stokes Drift. The Stokes Drift velocity is defined as the speed of this net forward motion in the wave propagation direction.

The relation between Eulerian (u_E), Stokes Drift (u_S) and Lagrangian (u_L) velocities is described by Longuet-Higgins (1969), as follows (2.25 and 2.26):

$$u_L = u_E + u_S \qquad (3D) \tag{2.25}$$

$$U_L = U_E + U_S \qquad (2DH) \tag{2.26}$$

With LWT expressions for velocity including second order effects of a vertical gradient in horizontal velocity magnitude, the Stokes Drift velocity u_S in the wave propagation direction along the depth can be calculated as (2.27):

$$u_S = \omega k a^2 \frac{\cosh 2k(h_0 + z)}{2\sinh^2 kh} \tag{2.27}$$

where ω is equal to $\frac{2\pi}{T}$, a is the wave amplitude ($\frac{H}{2}$) and z is the vertical position (Dean and Dalrymple, 2001). This results in a vertical shape with higher Stokes Drift velocities close to the surface and lower values approaching the bottom. The depth-averaged Stokes drift velocities in the wave propagation direction reads (2.28):

$$U_S = \frac{g k a^2}{2(h_0 + \overline{\eta})\omega} \tag{2.28}$$

In a wave-averaged depth-integrated perspective (2.23), the Lagrangian velocities can be described as (2.29)

$$U_L = \frac{\overline{(h_0 + \eta) U_E}}{\overline{(h_0 + \eta)}} \tag{2.29}$$

where it is shown that Lagrangian velocities equal mass flux ($\overline{(h_0 + \eta) u}$) over the mean water depth ($\overline{(h_0 + \eta)}$). For Eulerian velocities in phase with water levels, as given by LWT for progressive waves, Lagrangian velocities are not zero, as opposed to standing waves, for which water levels and Eulerian velocities are 90° out of phase.

3

METHODOLOGY

This MSc thesis intends to provide a full characterization of the flow pattern around SAG.

The only known extensive set of measured data in SAG formations was made in Palmyra Atoll, as presented by Rogers et al. (2015), where currents and pressures were obtained for depths of around 10 m in two field campaigns (Chapter 2.3). Considering the broad scope of the MSc thesis, this set of data could not be solely used to answer the research questions.

This MSc thesis uses numerical modelling as a tool to address the research questions. The main advantages of this approach compared to physical modelling are the easiness and fastness to provide sensitivity analysis, varying the input parameters and easily including and excluding processes.

The first modelling approach decision is to determine which model to be used. The model decision is described in Section 3.1, based both on the relevant physical processes over SAG formations to be solved, already discussed in Chapter 2, and the model capabilities.

Next, the modelling plan, covering the simulations addressing the research questions and the modelling approach, is provided in Chapter 3.2.

3.1. SELECTION OF MODEL

This section covers the selection of the model to solve flow over SAG formations.

As it was discussed in Chapter 2, waves are thought to be the main driving mechanism of the flow over SAG bathymetries. Firstly, a briefly review of the existent wave model types is briefly presented in Chapter 3.1.1, comprising the respective processes solved by each of them.

The context for the model decision is provided in Chapter 3.1.2, including a discussion about which processes are considered as important for the flow based on the literature review.

3.1.1. WAVE MODEL CONCEPTS

In coastal engineering, wave models are widely applied, supporting the understanding of coastal dynamics and in the solution of coastal problems. Wave models comprise since LWT expressions, commonly employed in the daily coastal engineer calculations for fast estimations, to more robust numerical wave propagation models, once dealing with detailed calculations.

Regarding the timescale upon which wave processes are solved, there are three main types of wave models usually applied in engineering problems:

- wave resolving models;
- long wave resolving, wave-averaged models; and
- wave-averaged models.

, briefly described below.

Wave resolving models solve the wave field on the timescale of individual waves, i.e., solves the intra-wave motion. This type of model is capable of calculating the non-linear evolution of the wave field (Roelvink et al., 2010). These models solve shoaling, refraction and diffraction acting simultaneously within a short wave cycle, instead of representing their effects in average.

There are several concepts upon which wave resolving models are based on, such as Boussinesq-type equations, mild-slope equation and non-hydrostatic model (van Mierlo, 2014). Each one of them has a different approach to solve the wave field, e.g. Boussinesq-type models assume irrotational flows, while in non-hydrostatic models the horizontal turbulent stresses are present.

These models can either be three-dimensional (3D) or depth-averaged (2DH) models, and can compute monochromatic (thus, without generating long waves) or irregular, depending on the model applied. Examples of wave-resolving models include SWASH (3D/2DH; Zijlema et al. (1969)), XBeach (2DH; Smit et al. (2014)) and Bouss-2D (2DH; Nwogu and Demirbilek (2001)).

Models solving the intra-wave motion usually require low grid sizes and time steps, making them computationally expensive.

Models that do not solve the phase of the wave represent its effect averagely, and as such are called wave-averaged models. In the short wave timescale, these models solve the wave action balance equation. The wave action density N is determined as (3.1):

$$N(x,y,\theta) = \frac{E(x,y,\theta)}{\sigma(x,y)} \tag{3.1}$$

where σ is the wave frequency.

The wave action balance (Mei, 1983) reads as follows (3.2):

$$\underbrace{\frac{\partial N}{\partial t}}_{1} + \underbrace{\frac{\partial C_{gx}N}{\partial x}}_{2} + \underbrace{\frac{\partial C_{gy}N}{\partial y}}_{3} + \underbrace{\frac{\partial C_{\sigma}N}{\partial \sigma}}_{4} + \underbrace{\frac{\partial C_{\theta}N}{\partial \theta}}_{5} = \underbrace{-\frac{S}{\sigma}}_{6} \tag{3.2}$$

where C_σ and C_θ are the propagation velocities in the spectral space (σ,θ) and S is the source/sink term. The equation (3.1) can be understood as the spatial propagation of wave energy for a given frequency, similar to 2.1 with a sink term, and the interpretation of each of the terms is provided below:

- (1) represents the local non-stationary term;
- (2) and (3) are the horizontal advective terms in x and y directions, respectively;
- (4) represents the effect of shifting of the wave frequency due to variations in depth;
- (5) provides the effects of refraction due to depth changes; and
- (6) is the source/sink term and represents processes that might generate, dissipate or redistribute wave energy, such as wind action and wave breaking.

As it was discussed in Chapter 2.4, diffraction is not taken into account in the propagation of wave energy or wave action balance equation, as wave energy propagates only in the wave direction, without crossing of wave rays.

Long wave resolving models, such as XBeach in surfbeat mode (Roelvink et al., 2009), computes the short wave transformation processes, solving the wave action balance (3.2). The difference is that they also solve the wave-induced flow forcing on the wave group timescale (Roelvink et al., 2010). This means that the momentum balance equation (2.23) solved by them includes the terms for infragravity (IG) waves to generate (2.19 and 2.20 on wave group timescale), propagate and dissipate ((2) and (4) in (2.23), respectively).

XBeach in surfbeat mode solves the momentum balance equation in 2DH, with wave forcing calculated from the wave action balance. This wave forcing occurs on the wave group time scale, allowing the generation of infragravity waves. Both regular and spectral wave conditions can be imposed as forcing waves at the boundary.

These models are especially important closer to the shoreline, where long waves might become larger, potentially allowing more inundations. In reefs environments, infragravity waves would tend to be more important closer to the reef crest.

The last type of wave models are the wave-averaged models solving only the wave action balance, i.e., computing short wave transformation processes, but not solving momentum conservation balance at any point. In case (3.1) is solved for the full spectrum, the model is called spectral. Example of spectral models from that group include SWAN (Booij et al., 1999) and STWAVE (Massey et al., 2011).

The theoretical computational demand of wave-averaged models with the surfbeat is higher than without surfbeat, since both of them solve the wave action balance, but the former also solves the momentum balance equation.

Although the standalone wave-averaged models do not solve the momentum conservation equation, they might be coupled with other models that do so, providing them the wave forcing while receiving the mean flow conditions (e.g. water levels and velocities). An example of this type of coupling is Delft3D-FLOW (Deltares, 2016) coupled with Delft3D-Waves (SWAN), that allows the calculation of 3D/2DH flow with wave forcing.

Another type of coupling between models that enhance capabilities is between XBeach and D3D-FLOW, where the wave forcing in the wave group timescale from XBeach is communicated to D3D-FLOW, that solves the 3D momentum balance. The advantage of that coupling is that XBeach surfbeat standalone can calculate only in 2DH mode, while D3D-FLOW solves the flow also in the vertical.

An overview of wave models considered to be used in this research, their capabilities, and computational demand is shown in Table 3.1. The computational effort of models was estimated comparatively based on experts opinions.

Table 3.1: Wave models capabilities and required computational effort.

Model	**Intra-wave hydrodynamics**	**IG waves**	**Flow**	**Computational demand**
Delft3D-Flow + SWAN	no	yes	3D/2DH	+++
Delft3D-Flow + XBeach	no	yes	3D/2DH	+++
SWAN	no	no	none	+
SWASH	yes	yes	3D/2DH	+++++
XBeach	no	yes	2DH	+++

3.1.2. RELEVANT PROCESSES

According to the research objectives (Chapter 1.2), the model to be used needs to be able to solve the 3D flow forced by wave processes and alongshore currents. Table 3.1 shows that the only models solving 3D flow are Delft3D + SWAN/XBeach and SWASH.

SWASH solves the intra-wave motion, and as such it is able to calculate the non-linear evolution of the wave field. Wave forces are directly obtained from the momentum conservation solved in the timescale of short waves. Shoaling, refraction and diffraction are calculated simultaneously from the momentum balance.

Delft3D-FLOW imposes the wave forcing calculated from SWAN or XBeach, i.e., the wave force terms are not solved from the intra-wave motion, but are calculated with LWT expressions (2.19 and 2.20), representing the averagely excess of momentum due to linear waves (Chapter 2.4). SWAN and XBeach essentially do not solve diffraction, thus its effects are not taken into account in the momentum balance solved by Delft3D-FLOW.

As discussed in Chapter 2.3, Rogers et al. (2013) conducted an investigation of the hydrodynamics of SAG formations by using funwaveC, a 2DH phase resolver (Boussinesq-type) model that considers monochromatic waves. As this model solves the intra-wave motion, the radiation stress was effectively solved with (2.10) and Stokes drift velocities were calculated with (2.26) and (2.29).

They compared the calculated cross-shore radiation stress and Stokes drift velocity with LWT expressions for those (2.10 and 2.28), which is shown in Figure 3.1.

These results show that:

- The cross-shore radiation stress results calculated by funwave fits well with LWT expression all along the SAG profile; and
- Stokes drift velocity formula agreed well offshore of wave breaking zone, and it has not as good results from the surf zone further onshore.

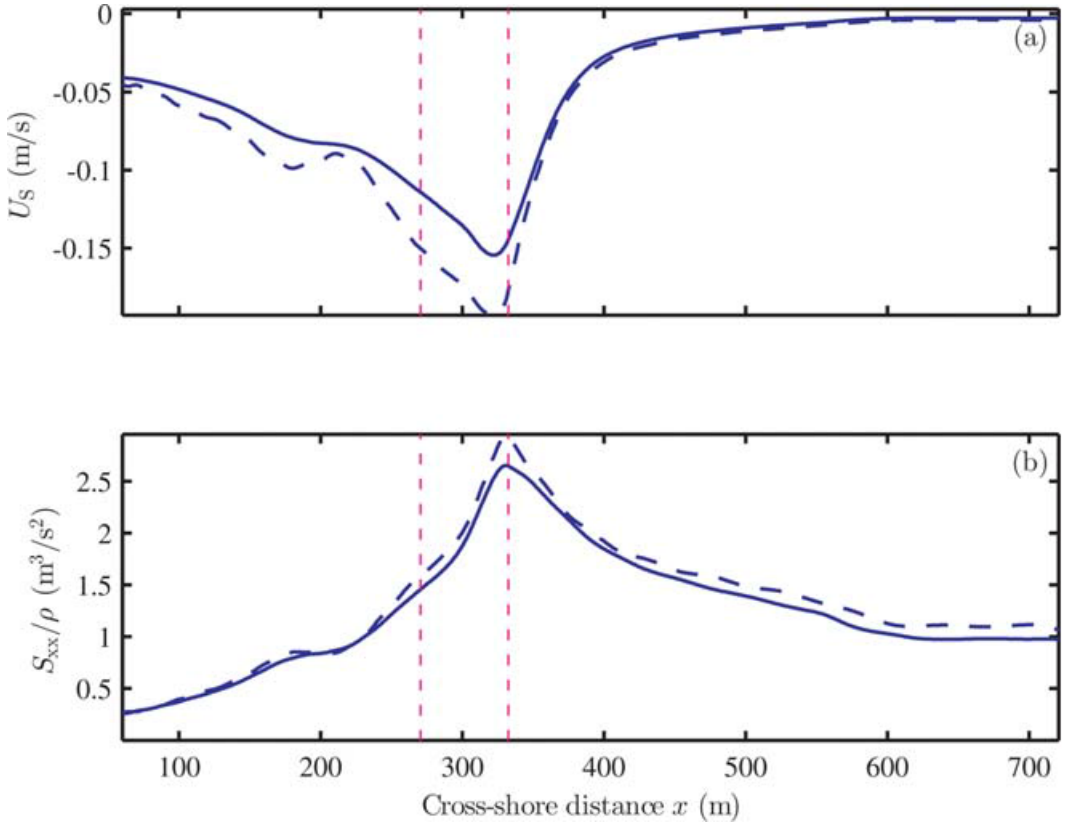

Figure 3.1: Comparison of cross-shore Stokes drift velocity (a) and radiation stress (b) for base configuration at top of spur. Blue solids indicate model results, while blue dashed shows the LWT expressions. Source: Rogers et al. (2013).

As SAG formations are predominantly located in the seaward of the surf zone, the linear character of waves in that region seems to be still dominant, given that LWT provides reasonable results.

3.1.3. SELECTION

The choice of which wave model to use depends essentially on:

- the objective of the research (discussed in Chapter 1.2);
- the relevant processes found on SAG formations (discussed in Chapters 2.3, 2.4 and 3.1.2);
- the processes solved by each model (discussed in Chapter 3.1.1); and
- the computational time demanded by each model (also provided in Chapter 3.1.1).

The fundamental decision is if the intra-wave hydrodynamics is fundamental for the understanding of hydrodynamics over SAG formations. While SWASH represents wave flow and forcing within the short wave period, it requires considerably more computational effort than Delft3D + SWAN/XBeach.

Considering the reasonable theoretical results using the LWT obtained in Rogers et al. (2013), the fact that SAG formations are generally located offshore of the surf-zone (Storlazzi et al., 2003) and their significantly lower computational time, wave-averaged models are considered to be more resourceful regarding the challenges imposed by research questions.

This MSc thesis opted to use Delft3D-FLOW + SWAN/Xbeach numerical models to the analyses. A brief description of those models is found below.

3.1.4. MODEL DESCRIPTION

Delft3D (D3D) is a fully integrated computer software suite for a multi-disciplinary approach and 3D computations for coastal, river and estuarine areas. The D3D suite is composed of several modules, which are able

to interact with each other using a common interface (Deltares, 2016). In this MSc thesis, the coupling between D3D-FLOW and D3D-WAVES (SWAN) and coupling between D3D-FLOW and XBeach surfbeat mode are applied.

The D3D-FLOW module solves the Navier-Stokes equations (the mass-balance or continuity equation, and momentum balance equations) for incompressible free surface flow under the shallow water and the Boussinesq assumptions (Deltares, 2016). The numerical method is based on finite differences, with curvilinear grids. A staggered grid is used, with water level solved at cells centres and momentum balance in cell interfaces.

In D3D-FLOW, the Generalized Lagrangian Mean (GLM) formulation is used to solve the shallow water momentum equations (Andrews and McIntyre, 1978). The 3D mass-balance without sources and sinks equation reads (3.3):

$$\frac{\partial u_{Li}}{\partial x_i} + \frac{\partial w_L}{\partial z} = 0 \tag{3.3}$$

where u_{Li} and w_L represents the Lagrangian horizontal and vertical velocities, respectively.

The wave-averaged 3D momentum balance equations without Coriolis forcing is written below (3.4):

$$\underbrace{\frac{\partial u_{Li}}{\partial t}}_{1} + \underbrace{u_{Lj}\frac{\partial u_{Li}}{\partial x_j}}_{2} + \underbrace{w_L\frac{\partial u_{Li}}{\partial z}}_{3} = \underbrace{-g\frac{\partial \eta}{\partial x_i}}_{4}\underbrace{-F_i}_{5} + \underbrace{\frac{\partial}{\partial x_j}\left[\frac{\tau^T_{ij}}{\rho}\right]}_{6} + \underbrace{\frac{\partial}{\partial z}\left[\frac{\tau^T_{i3}}{\rho}\right]}_{7} \qquad i,j = \{1,2\} \tag{3.4}$$

where F_i is the wave force, τ^T_{i3} is the vertical turbulent stress. The equation (3.4) is conceptually similar to the momentum balance written in (2.23), but now solved in 3D. The meaning of each of the terms in (3.4) is shown below:

- (1) is the local acceleration term;
- (2) is the horizontal advective acceleration;
- (3) is the vertical advective acceleration;
- (4) is the pressure gradient term;
- (5) is the wave force distributed along the depth;
- (6) is the horizontal turbulent stresses; and
- (7) is the vertical turbulent stress, or vertical diffusion of momentum.

The D3D-WAVE (SWAN) uses the wave action balance equation (3.2) to calculate the propagation of wave fields over the space and receives from D3D-FLOW mean flow conditions (e.g. water levels), as previously described. With the wave energy obtained along the entire domain, the radiation stresses (2.10 and 2.11) and wave forces (2.19 and 2.20) are calculated and communicated to D3D-FLOW, that impose them as term (5) in (3.4).

The wave forces are calculated as horizontal gradients of momentum flux, which are function of the wave energy (or wave height). Those changes are described as wave energy dissipation, and SWAN calculates and communicates to D3D-FLOW three types of dissipation: dissipation due to depth-induced breaking and whitecapping at the top-layer and dissipation due to bottom friction at the bed layer. The remainder part of the wave forces - after wave dissipation has been subtracted - is added to the momentum equations, with the effect spread over the water column (Deltares, 2016). D3D-FLOW also considers as wave force an extra term to account for the Stokes Drift divergence ($\frac{\partial}{\partial z}[\nu_V \frac{\partial u_{Si}}{\partial z}]$, where ν_V is the vertical viscosity). This term is analogous to the vertical turbulent stresses (7), but considering Stokes Drift velocities, thus essentially a function of the vertical distribution of u_S (2.27).

As described in Chapter 3.1.1, XBeach in surfbeat mode also solves the wave action balance equation for the wave propagation, but not taking into account the frequency shifting term (4) in (3.1). The wave forcing is calculated in the same manner as SWAN, except that it is done in the wave group time scale, allowing the generation of infragravity waves.

Although (3.4) is solved in Lagrangian perspective, term (7) in the bed layer - or the bed shear stress - uses Eulerian velocities. Thus, the bottom stress is corrected for the Stokes drift.

3.2. MODELLING PLAN

This section covers the modelling plan applied to answer the research questions. Firstly, a summarized list of the simulations addressing directly each of the subobjective of this MSc thesis is proposed (Chapter 3.2.1). Then, the modelling approach is discussed in Chapter 3.2.2, followed by a discussion about the range of parameters (Chapter 3.2.3) imposed as boundary conditions or bathymetry (i.e. wave parameters, SAG geometry and alongshore forcing). The modelling steps are listed and detailed in Chapter 3.2.4. The last section of this chapter (Chapter 3.2.5) presents the model setup.

3.2.1. SIMULATIONS TO ADDRESS RESEARCH QUESTIONS

The research goal of this MSc thesis is to describe the circulation patterns found within SAG formations and to identify the governing mechanisms of the hydrodynamics around SAG. This objective was divided in subobjectives, as shown in Table 1.1 in Chapter 1.2.

This MSc thesis uses numerical modelling to answer the research questions. The simulations addressing each of the subobjectives are proposed in Table 3.2.

Table 3.2: Simulations to answer research questions.

Type	Content
Subobjective 1	The whole set of simulations is considered
Subobjective 2	Simulations that consider different combination of short wave parameters (e.g. wave height and period) for operational and extreme wave climates (see Chapter 3.2.3)
Subobjective 3	Simulations with different sets of SAG geometry (e.g. spur heights h_{spr} and SAG alongshore wavelength λ_{SAG}) covering the variety of SAG formations found worldwide (see Chapter 3.2.3)
Subobjective 4	Simulations varying the forcing alongshore currents (see Table 3.3)
Subobjective 5	Simulations with/without long waves
Subobjective 6	The whole set of simulations is considered

The general characterization of the flow pattern (Subobjective 1), as well as the implications of the flow for sediments and nutrients (Subobjective 6) takes into account the whole set of simulations performed in order to consider the wide variety of SAG geometries and hydrodynamics forcing conditions.

A series of runs was carried out to understand the importance of the incoming short-wave properties in the flow around SAG (Subobjective 2). Variations of wave height, wave period, wave direction and directional spreading are considered to simulate a variety of sea states that consider operational and extreme wave climates (Chapter 3.2.3).

Further series of simulations was used to investigate the flow characteristics for different SAG geometries (Subobjective 3). Different sets of spur heights, SAG alongshore wavelength, groove width, bed slope, reef flat width, friction, and peak spur height depth (Chapter 3.2.3) are used so as to understand the effect of geometry in the flow within SAG.

The response of the flow to different strengths of alongshore flows (Subobjective 4) was evaluated with simulations varying the forcing alongshore currents. Wind was used as alongshore forcing, as discussed in Chapter 3.2.3.

The importance of lower wave frequencies to the flow pattern (Subobjective 5) is determined with the results of simulations with and without long waves.

This MSc thesis used Delft3D-FLOW + SWAN/XBeach numerical models to the analyses. As it is shown in Chapter C.1.4, sensitivity results with the surfbeat mode showed that long waves do not interfere significantly the flow pattern. Therefore, the coupling between Delft3D-FLOW + XBeach was used only for those simulations, and the remainder runs applied Delft3D-FLOW + SWAN.

3.2.2. MODELLING APPROACH

As discussed in Chapter 1.2, the objective of the research is not to describe the hydrodynamics conditions of a particular SAG formation, but instead to predict in general how sensitive is the flow to changing situations.

In Chapter 1.2, the SAG morphology was discussed, and it was shown that the SAG formations found worldwide can vary significantly not only between reefs but also within reefs (Duce et al., 2014). In order to represent such a variety of SAG formations, schematic bathymetries are used in the modelling, with conceptual bathymetry equivalent to Rogers et al. (2013).

Rogers et al. (2013) conducted a numerical modelling study with idealized SAG bathymetry, whose profile shape is based on 10 prominent SAG formations from areas with documented active coral growth on the southwestern coast of Moloka'I Hawaii, according to (Storlazzi et al., 2008). This study concluded that the geometric shape of the SAG bathymetries can be simplified by a superposition of spurs on top of the reef profile, represented as a cosine function in the alongshore direction and a skewed Gaussian function in the cross-shore direction, as shown in (3.5):

$$h(x,y) = h_{base} - h_{spr} h_x h_y \tag{3.5}$$

where h is the depth, x is the cross-shore axis positive offshore, y is the alongshore axis, $h_{base}(x)$ is the reef profile, h_{spr} is the spur height, and h_x and h_y are the cross-shore and alongshore SAG shape functions, provided by (3.6 and 3.7):

$$h_x = exp\big[-\frac{(x-\mu)^2}{2\epsilon^2}\big] \tag{3.6}$$

$$h_y = max\big[(1+\alpha)\Big|\cos\frac{\pi y}{\lambda_{SAG}}\Big| - \alpha, 0\big] \tag{3.7}$$

where μ is the x for the maximum spur height, $\epsilon(x)$ is a spreading parameter, with $\epsilon = \epsilon_1$ for $x >= \mu$ and $\epsilon = \epsilon_2$ for $x < \mu$), while α is the coefficient defined below (3.8):

$$\alpha = \frac{\Big|\cos\big[\frac{\pi}{2}(1+\frac{W_{grv}}{\lambda_{SAG}})\big]\Big|}{1-\Big|\cos\big[\frac{\pi}{2}(1+\frac{W_{grv}}{\lambda_{SAG}})\big]\Big|} \tag{3.8}$$

The cross-shore and alongshore views of how (3.5) represents the SAG bathymetric features are provided in Figure 3.2, showing that:

- As previously explained, spurs emerge on top of grooves (or undisturbed reef profile), and the spur heights vary both in the cross-shore with a skewed Gaussian profile - and in the alongshore - with a cosine function for spurs followed by channelized grooves;
- The orientation of both SAG formations is assumed to be always orthogonal to the shoreline, consistent with most of the reported SAG formations;
- With constant orthogonal orientations, spurs axis never crosses grooves, resulting in uninterrupted grooves, whose length is a function of μ and z_μ;
- The reef slope is assumed to have a single value between depths of 0.5 (reef crest) and 22 m (offshore limit of model grid);
- There is a flat horizontal platform at a depth of 0.5 m, i.e., a horizontal reef flat was assumed;
- Further onshore, a beach at a depth of -0.5 m was considered, with a constant slope of 1/20.

The use of a schematic bathymetry allows the representation of a complex morphology in relatively easy terms, with final shape remaining similar to measurements. As the bottom profile variations in the model grid are representative of SAG structures, it is expected that the model application provides consistent results.

Another advantage of using a schematic bathymetry is its potential to vary the SAG bathymetry as function of SAG geometry parameters, such as spur height and SAG wavelength. This might allow the understanding of how sensitive is the hydrodynamics to those parameters.

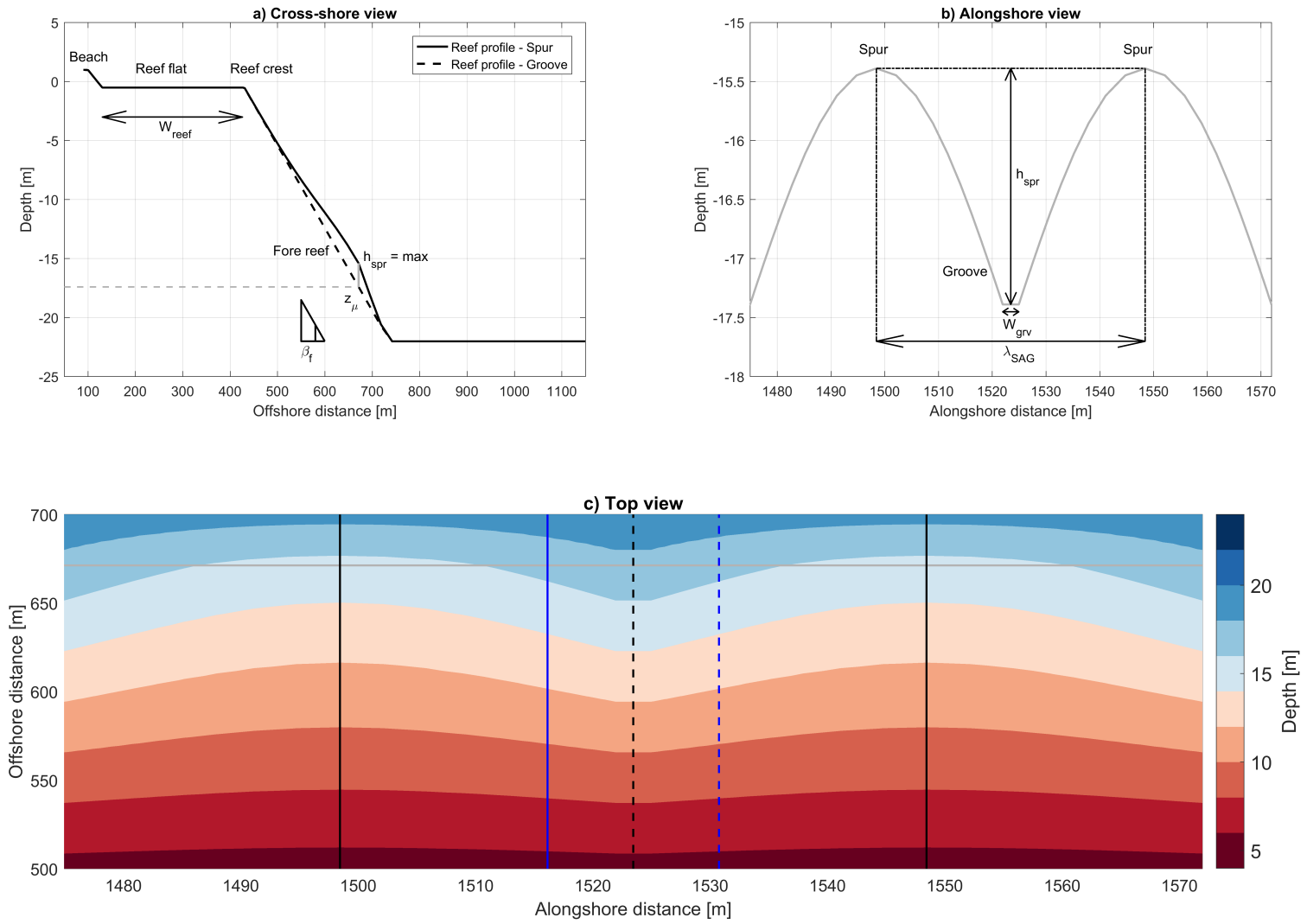

Figure 3.2: (a) Cross-shore and (b) alongshore and (c) top views of SAG schematic bathymetry, as represented in the modelling. Full black line represents the cross-shore axis of the spur, while dashed black line is the cross-shore axis of the groove. The grey line is the alongshore axis at a location close to where spur height is maximum along the cross-shore profile. The blue lines are mid positions between spur and groove, that are further used for plotting results.

One of the limitations of using (3.5) is related to the fact that it is implicitly assumed that SAG wavelengths are not varied with depth, contrary to the findings by (Storlazzi et al., 2003; Duce et al., 2016), that observed that increasing depths lead to longer SAG wavelengths.

Moreover, the application of (3.5) results in uninterrupted grooves, which does not necessarily hold, as the groove lengths vary and tend to be higher in more exposed areas (Munk and Sargent, 1948; Duce et al., 2016).

3.2.3. RANGE OF PARAMETERS

The range of parameters - short wave parameters, SAG dimensions and alongshore forcing - simulated in the current research is presented in Table 3.3 and each of the parameter is discussed below.

Table 3.3: Range of Parameters – Wave, SAG Geometry and Alongshore Currents.

Type	Variable	Symbol	Range of values	Unit
Wave parameters	Significant wave height	Hs_0	0.5 - 6	m
	Wave steepness	$\frac{Hs_0}{Lp_0}$	0.006 - 0.050	-
	Peak wave direction	Dp_0	0 - 30	°
	Directional spreading	m in $\cos^m\theta$	2 - 30	-
SAG geometry	Spur height	h_{spr}	0.5 - 8.0	m
	Spur wavelength	λ_{SAG}	25 - 200	m
	Ratio of groove width and SAG wavelength	$\frac{W_{grv}}{\lambda_{SAG}}$	0.01 - 0.82	-
	SAG cross-shore slope	$\tan\beta_f$	0.02 - 0.50	-
	Reef flat width	W_{reef}	50 - 1000	m
	Ratio of friction coefficient between groove and spur	$\frac{C_{D\text{-}grv}}{C_{D\text{-}spr}}$	1/6 - 0.5	-
	Vertical position of maximum spur height	z_μ	5 - 17	m
Alongshore forcing	Alongshore wind speed	U_{10}	0 - 20	m/s

SHORT WAVE PARAMETERS

In order to study how circulation over SAG bathymetry varies as a function of short waves, four wave parameters were chosen to be varied:

- Significant Wave Height (Hs_0);
- Wave Steepness ($\frac{Hs_0}{Lp_0}$);

- Peak Wave Direction (Dp); and
- Directional Spreading (m in $\cos^m \theta$).

The selection of short wave parameters took into consideration previous research both specifically on SAG hydrodynamics (Rogers et al., 2013) and on coral reefs (Kolijn, 2014; Quataert et al., 2015; Lowe and Falter, 2015; Pearson, 2016). The reasoning for the choice of these parameters was to represent the variety of sea states found on previously studied coral reef systems (see Chapter 2.1), comprising low and high energy sites, sea and swell conditions, operational and extreme wave conditions (Figures 2.2 and 2.3), as well as a range of incoming wave directions, consistent with Rogers et al. (2013).

SAG GEOMETRY

The study of how the hydrodynamics is sensitive to SAG structures considers the following set of SAG geometry parameters:

- Spur height (h_{spr});
- Spur wavelength (λ_{SAG});
- Ratio of groove width and spur wavelength ($\frac{W_{grv}}{\lambda_{SAG}}$);
- Cross-shore slope (β_f);
- Reef flat width (W_{reef});
- Ratio of groove and spur friction coefficient ($\frac{C_{D-grv}}{C_{D-spr}}$); and
- Cross-shore position of maximum spur height (z_μ).

In Chapter 2.2.2, the description of the existent SAG geometries was presented, while Chapter 2.2.3 shows that the wave conditions can be correlated with SAG morphology. The reasoning for the selection of the SAG geometry parameters shown above is to represent the range of SAG formations found worldwide, as discussed below.

In general, the choice of the three first parameters - h_{spr}, λ_{SAG} and $\frac{W_{grv}}{\lambda_{SAG}}$ - considered sets of SAG geometries reported in numerous research publications (Munk and Sargent, 1948; Tracey et al., 1948; Stearn et al., 1977; Sheppard, 1981; Shinn et al., 1981; Bouchon, 1981; Choi, 1982; Chapman and Kramer, 2000; Wood and Oppenheimer, 2000; Camoin et al., 2001; Storlazzi et al., 2003; Nunez-Lara et al., 2005; Gischler, 2010; Rogers et al., 2013; Kayanne et al., 2015; Rogers et al., 2015; Duce et al., 2016). The reasoning for choosing the ratio of groove width and SAG wavelength, instead of simply the groove width, was to increase the number of simulated groove widths.

Although the SAG cross-shore slope is highly variable in nature, a single slope between the depths of 0.5 (reef crest) and 22 m (offshore limit of model grid) is assumed for simplicity. The slope range was defined taken into account both specific reported SAG geometries (Sheppard, 1981; Shinn et al., 1981; Camoin et al., 2001; Rogers et al., 2013, 2015; Duce et al., 2016) and coral reef formations literature (Quataert et al., 2015). Although Duce et al. (2016) showed that it is less likely the SAG development for reefs with $\beta_f > 5°$, a wider range of slopes, consistent with coral reefs environments, was selected to investigate potential effects of flow over SAG formations with steeper slopes.

Although the reef flat is located further onshore in the SAG profile (Figure 2.4), it is hypothesized that larger reef flats could retain more water, and interfere on the return flow and subsequently in the flow over the SAG zone. This research investigates if different reef flat widths could affect the flow pattern.

The reef flat geometry is also highly variable, and for simplicity a flat horizontal platform from the depth of 1 m up to -1 m (beach level) was assumed. The reef flat width was selected to vary between 50 and 1000 m, according to values reported in literature (Kolijn, 2014; Quataert et al., 2015).

The roughness for SAG bathymetries might be highly variable, as spurs can contain different coral and algae species, while grooves are often covered with sediments and coral debris. A constant friction coefficient $C_{D-spur} = 0.06$ was used for all simulations, consistent with literature (Rosman and Hench, 2011). The ratio of friction coefficient between groove and spur was chosen to be investigated, since it is hyphotesized that the relative difference of roughness between spur and groove could be associated with circulation. This value was assumed to vary from 1/6 and 1, similar to the range of values used by Rogers et al. (2013).

As discussed in Chapter 2.2.2, Storlazzi et al. (2003) showed that spur height increases for higher depths in low-energy sites of southern Moloka'i. They suggest that the peak spur height would occur as result of balance of higher growth due to photosynthesis and lower survivability due to higher wave action (and thus greater breakage). Both of these parameters decrease non-linearly with depth. This reasoning leads to the supposition that environments with lower degrees of exposure to waves would tend to have maximum spur height in shallower depths.

The buttress zone described by Goreau (1959), sketched in Figure 2.8, corresponds to a SAG with peak spur height in a depth of around 5 m, and it is located in the Jamaican coast, in the Caribbean sea, that in general experiences relatively mild wave climates (Figure 2.2), corroborating Storlazzi et al. (2003) conclusions.

This MSc thesis assumes the vertical position of maximum spur height as an indication of the degree of exposure to wave energy. The range of values for that parameter was defined taken into consideration SAG formations varying from buttress style (z_μ = 5 m) to more exposed locations (z_μ = 17 m), hereafter referred to as Hawaiiann style SAG.

ALONGSHORE FORCING

In order to identify how 3D circulation over SAG bathymetries changes with alongshore driving, the alongshore wind speed was selected to represent an alongshore flow. A range of wind speeds was defined, with maximum value of 20 m/s, that corresponds to a strong wind, but still relatively easily found in stormy situations.

As already mentioned, it is important to reinforce that this research does not aim to understand the flow pattern due to wind, but to study how the wave-induced flow is sensitive to an alongshore forcing.

3.2.4. MODELLING STEPS

The modelling plan comprises two main steps (Figure 3.3): Calibration/Verification and Research Simulations.

In general terms, Calibration/Verification parts aims to demonstrate that the model and its application are capable of providing results matching previous observations, and it takes into consideration both Rogers et al. (2015) measurements in Palmyra Atoll and Rogers et al. (2013) modelling study. An Optimization of the model setup to save computational time is the last step before proceeding to the Research Simulations.

Following the Calibration/Verification part, the Research Simulations part comprises a sequence of sensitivity analyses corresponding to the simulations shown in Table 3.2 in order to identify the relevant processes interfering in the flow pattern.

The modelling steps - Calibration/Verification and Research Simulations - are detailed below.

CALIBRATION/VERIFICATION

As shown in Chapter 2.3, the hydrodynamics over SAG formations is still a topic with limited research. The only extensive set of measured data was made in Palmyra Atoll, and it still represents punctual measurements for relatively short periods. This data set likely does not represent the variety of SAG formations and thus was not retained for calibration purposes, but for verification, as discussed below.

Calibration

Rogers et al. (2013) investigated the hydrodynamics of SAG by applying a 2DH Boussinesq-type model. They assumed a schematic bathymetry to represent the SAG formations, and used different sets of short wave parameters, SAG geometries, tides and wind. Results of the Base Configuration run of that research were extensively plotted and discussed in that publication, allowing comparisons with the current study results.

As discussed in Chapter 3.2.2, this MSc thesis uses a similar schematic bathymetry to reproduce SAG formations. However, instead of using a phase-resolver model, a wave-averaged model is applied. This MSc thesis calibrates D3D-FLOW coupled with SWAN by replicating Rogers et al. (2013) Base Configuration simulation (see Chapter 4.2).

The overall aim of this step is to reproduce the same conceptual results obtained in that study, such as the existence of circulation cells, with depth-averaged onshore flow over spurs and offshore flow over grooves in the outer SAG profile and the reverse pattern in the inner SAG profile. The cross-shore and alongshore distribution of cross-shore momentum is also compared to ensure that the same mechanisms are responsible for the characteristic hydrodynamics.

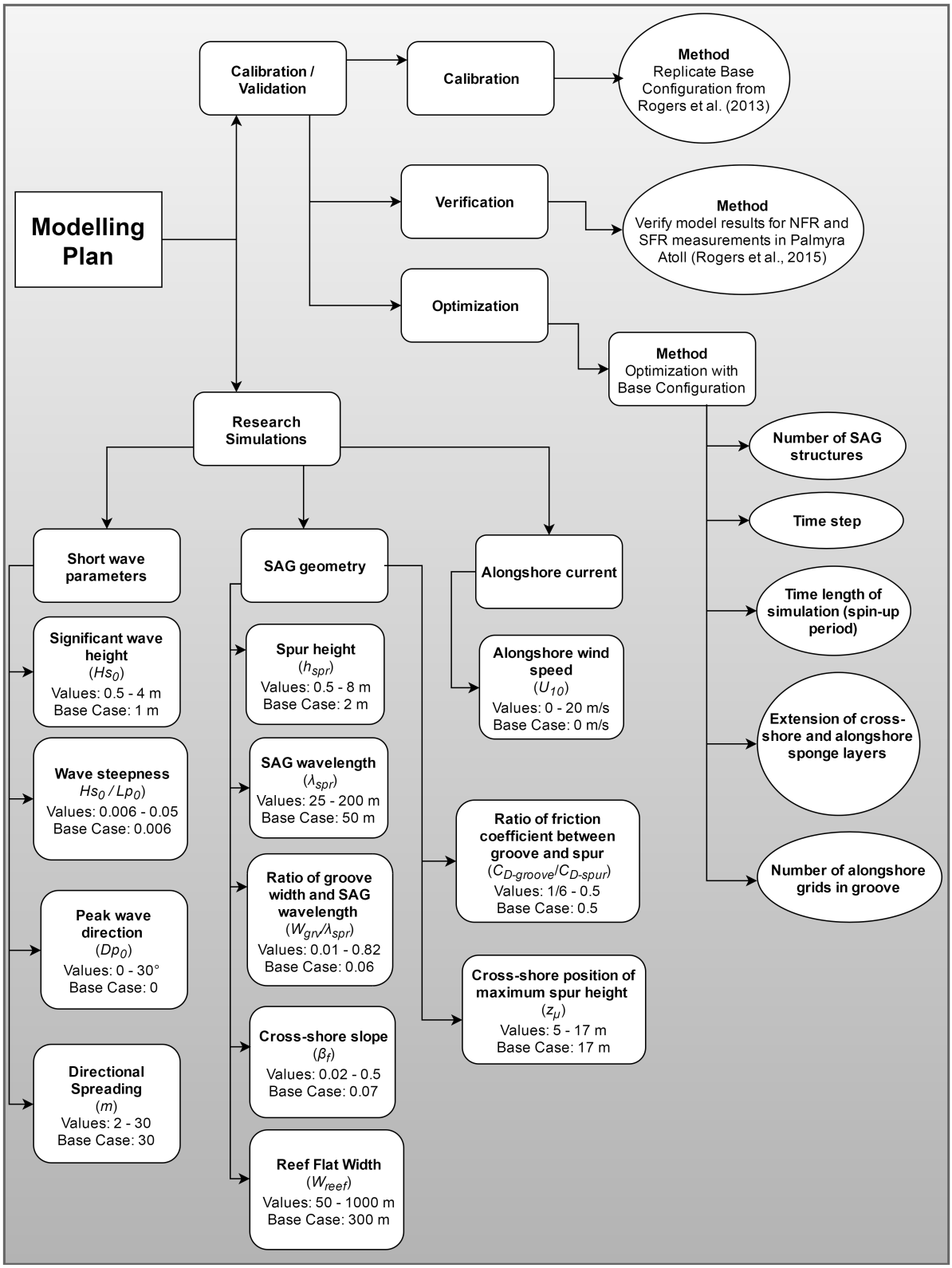

Figure 3.3: Flowchart for modelling plan.

The advantage of calibrating D3D-FLOW coupled with SWAN (wave-averaged) with funwave (phase-resolver) is that a more powerful model including the intra-wave motion is used, putting the limitations due to the timescale in perspective. However, it allows only comparison in a depth-integrated sense, since the velocity along the vertical is not solved by Boussinesq-type models. Also, D3D-FLOW considers the horizontal

turbulent stresses (term 6 in (3.4)), while Boussinesq-type models assume irrotational flows, thus neglecting those forces.

The results of the calibration part are shown in Chapter 4.2.

Verification

The verification of the model results is carried out both using measurements in Palmyra Atoll and with theoretical assumptions using LWT equations, as shown below.

Rogers et al. (2015) conducted two field campaigns in SAG formations on Palmyra Atoll - SFR 12 and NFR13. As a verification part, this MSc thesis applies Delft3D-FLOW coupled with Delft3D-WAVES to reproduce schematically NFR13 and SFR12 conditions. This means that for example the alongshore profile is reproduced by a single SAG wavelength, spur height and groove width, instead of having a more complex geometry, as showed in Figure 2.11.

The objective of the verification with measurements is to compare model results with the patterns of circulations cells found in those sites, with an offshore and downward Lagrangian flow over the spurs near the surface, and an onshore and upward flow over the grooves. The order of magnitude of Lagrangian currents (both NFR13 and SFR12) and the momentum terms (only provided for NFR13) are considered in that comparison.

In Chapter 2.4, the mechanisms expected to be dominant in SAG formations along the wave propagation and the resulting wave forcing were discussed. Assuming shore-normal waves and with diffraction overcoming refraction effects, the wave forces in the cross-shore and in the alongshore direction can be estimated with (2.21) and (2.22), respectively.

The verification with theoretical assumptions aims to compare the cross-shore and alongshore wave forces calculated from D3D-FLOW + SWAN and the ones with (2.21) and (2.22) for a same bathymetry.

The results of the verification part are shown in Chapter 4.3.

Optimization

Following the calibration using Rogers et al. (2013) modelling study, an optimization of the Base Configuration (Rogers et al., 2013) simulation conditions was performed through variations of the parameters shown below, aiming to reduce the computational time keeping sufficient accuracy:

- Number of SAG structures;
- Time step;
- Time length of the simulation;
- Sponge layers; and
- Number of alongshore grids in groove.

The results of the optimization part are shown in Chapter 4.4.

RESEARCH SIMULATIONS

The Research Simulations part addresses the core of this MSc thesis, i.e., it is directly related to the research objectives presented in Table 1.1, and it is divided in two steps:

- The first step is to define a Base Case scenario, and to study the sensitivity of the flow due to each of the varying parameters - short wave parameters, SAG geometry, forcing alongshore flow and presence of long waves-, hereafter referred to as sensitivity runs. In those runs, the runs are similar to Base Case run, except for the varying parameters, one at a time. The importance of long wave forcing was studied assuming the Base Case setup with varying peak spur heights z_μ. The sensitivity runs allowed the definition of the parameters with greatest influence on the flow strength (see Chapter 5.4):
  - Significant Wave Height (Hs_0);
  - Wave Steepness ($\frac{Hs_0}{Lp_0}$);
  - Spur height (h_{spr});
  - Spur wavelength (λ_{SAG}); and

– Vertical position of maximum spur height (z_μ).

- In the second step, these parameters - Hs_0, $\frac{Hs_0}{Lp_0}$, h_{spr}, λ_{SAG} and z_μ - were chosen to be varied simultaneously, hereafter identified as permutation runs, so as to obtain the largest variety of flows over SAG formations.

The configuration of the Base Case scenario is shown in Table 3.4. This Base corresponds to a typical SAG formation found in southern Moloka'i, as described by Storlazzi et al. (2003) and Rogers et al. (2013) (Figures 2.7 and 2.9).

Table 3.4: Base Case configuration.

Hs_0	$\frac{Hs_0}{Lp_0}$	Dp_0	m	h_{spr}	λ_{SAG}	$\frac{W_{grv}}{\lambda_{SAG}}$	$\tan\beta_f$	W_{reef}	$\frac{C_{D\text{-}grv}}{C_{D\text{-}spr}}$	z_μ	U_{10}
m	-	°	-	m	m	-	-	m	-	m	m/s
1	0.006	0	30	2	50	0.06	0.07	300	0.5	17	0

The list of all simulations performed in this MSc thesis, including both sensitivity and permutation runs, is provided in Appendix A.

The results of the Research Simulations are shown in Chapter 5 and discussed in Chapter 6.

3.2.5. MODEL SETUP

This section describes the implementation of the schematic bathymetry explained in Chapter 3.2.2 in a numerical grid and provides the model parameters assumed as constant for all simulations.

Delft3D-FLOW version 3.59.01.48550 coupled with SWAN version 40.72 were used for all the simulations without long waves, while a research version of Delft3D-FLOW coupled with XBeach was used for the simulations with long waves.

MODEL GRID AND RESOLUTION

The model grid for the Base Case scenario is shown in Figures 3.4 and 3.5, where both SWAN and D3D-FLOW grids are identified, with D3D-FLOW grid located at the centre of SWAN grid. XBeach grid was assumed the same as the one from D3D-FLOW.

The grid shows that the SAG zone is located at the centre of D3D-FLOW grid, and the remainder of both D3D-FLOW and SWAN grids have alongshore uniform depths equivalent to the groove profile. From the alongshore boundaries to the center, one alongshore sponge layer was introduced, with alongshore resolution of 50 m, to prevent border effects both from SWAN and D3D-FLOW. From the end of the alongshore sponge to the center, an alongshore transition layer was implemented so as to gradually decrease the resolution of 50 m to the finer SAG resolution, considering the smoothness recommendations for D3D-FLOW (up to 20% variation in spacing according to Deltares (2016)).

The alongshore resolution in the SAG zone was defined with the method described below:

- Firstly, the number of grids (or grid lines) to represent the groove was chosen. The final number concluded to represent accurately was 4 grid lines (or 3 grids), as discussed in Chapter 4.4, which is also shown in Figure 3.5. For the Base Case scenario, it results in an alongshore resolution of 1 m;
- Over the first half of the spur, the alongshore spacing was gradually increased with a maximum variation of 20% in spacing up to the top of spur; and
- The second half of the spur was defined to be a mirror of the first half, with alongshore spacing decreasing from the top of the spur up to the next groove.

The model alongshore resolution varies approximately from 50 m (outside the SAG zone) up to 3 m over the spur and 1 m in the groove for the Base Case scenario.

The cross-shore resolution was defined by taking into account the cross-shore profile of the groove, with progressive increase of the resolution as moving onshore, with lower depths, and respecting the grid size smoothness constraints. Once reaching the reef flat zone, the cross-shore grid spacing increases up to 10 m, as the focus of this research is not in that zone.

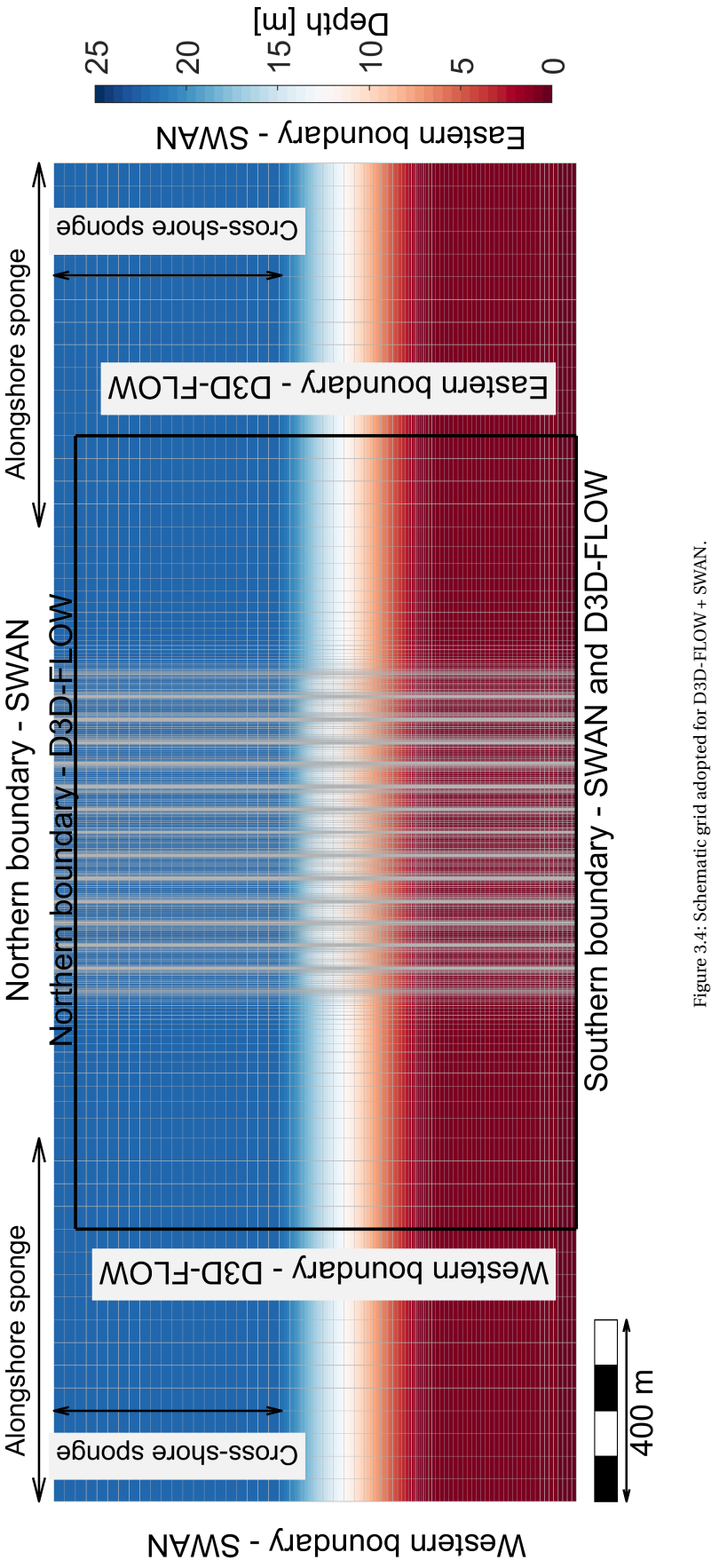

Figure 3.4: Schematic grid adopted for D3D-FLOW + SWAN.

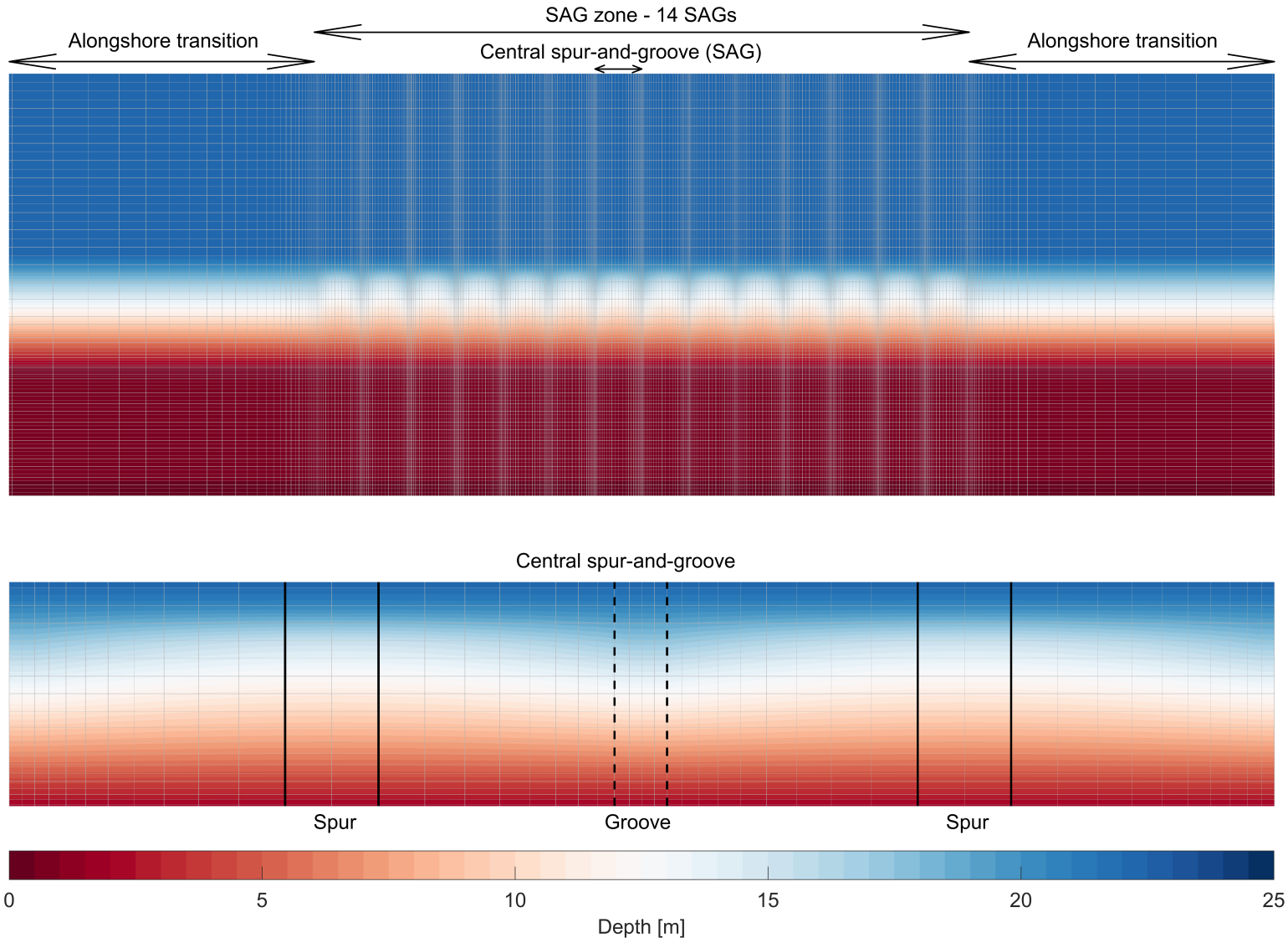

Figure 3.5: Zoom of schematic grid adopted for D3D-FLOW + SWAN.

The cross-shore resolution varies approximately from 25 to 3 m in the start of the reef flat, for the Base Case scenario.

Regarding the vertical resolution, sigma-layers are used, i.e., the vertical distribution is not fixed for all grid points, but depend on the depth. The sigma-layers were distributed so as to have finer grids close to the bottom and to the water surface, as shown in Figure 3.6. In a depth of 22 m - the highest simulated depth -, the lowest and largest grid spacings were of 6 cm and 4.2 m, found on the bottom/surface layers and in mid-depth, respectively. Sensitivity calculations of the wave boundary layer using Jensen et al. (1989) indicated that this resolution is not enough to reproduce accurately the wave streaming.

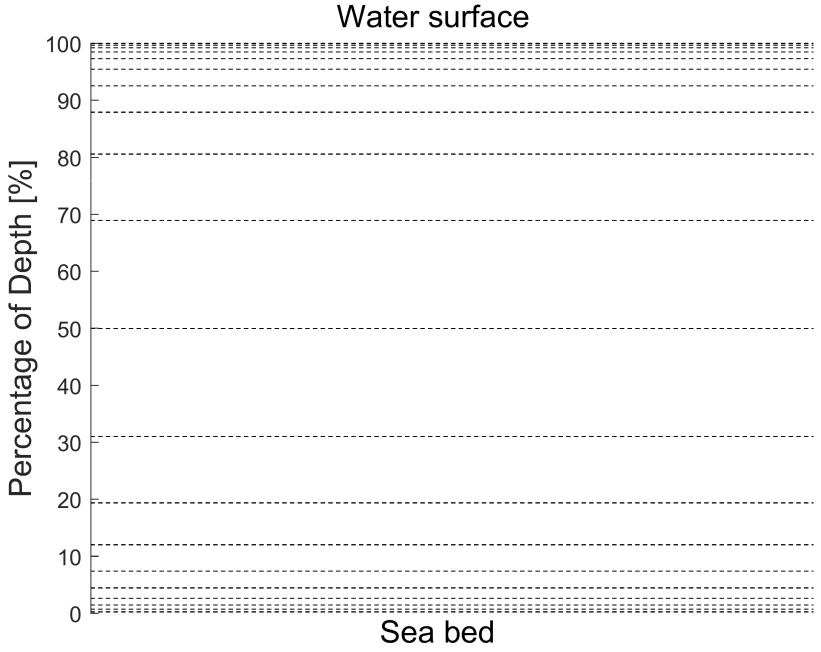

Figure 3.6: Vertical grid with 20 sigma-layers, which are represented by the horizontal dashed lines.

As discussed in Chapter 3.2.2, SAG formations are introduced as a superposition of spurs over grids. The first tests with the model grid indicated the need of representing several SAG formations, as spurious numerical fluctuations occur in the model in the first SAG formation in both sides. A total number of 14 SAGs are shown, which were concluded as the optimum number, as discussed in Chapter 4.4.

Although several SAG formations are modelled, results are analyzed only the for the central SAG formations, indicated in Figure 3.5.

BOUNDARY CONDITIONS

SWAN and XBeach boundary conditions are essentially the imposition of JONSWAP spectrum in the northern, western and eastern boundaries (Figure 3.4), with γ of 3.3, and all the remainder parameters varying depending on the simulation.

As no tides are considered, D3D-FLOW simulations assumed Neumann boundary conditions on the western and eastern boundaries (Figure 3.4), with zero amplitude and phase. In the northern boundary, an astronomic forcing of water level with zero amplitude and phase were considered.

ROUGHNESS

As discussed in Chapter 3.2.3, each model run has a ratio of groove and spur friction coefficient ($\frac{C_{D-grv}}{C_{D-spr}}$). A constant friction coefficient $C_{D-spur} = 0.06$ was used the spur, resulting in a given groove friction for each run.

The friction values were assigned as proportional to the spur height in the grid. Therefore, in the transition between spur and groove, intermediate values between spur and grove were considered. In the reef flat, half of the roughness value ($\frac{C_{D-grv}+C_{D-spr}}{2}$) between spur and groove assumed, also specific to every simulation. Outside the SAG zone (alongshore sponge and transition layers), friction values were assumed to have the same values as the grooves.

In D3D-FLOW, friction was prescribed with Chezy values C_D were converted to Chezy values. Figure 3.7 presents the C_D values used to the Base Case scenario. The friction in D3D-FLOW is related to the term (7) in (3.4) in the bottom layer.

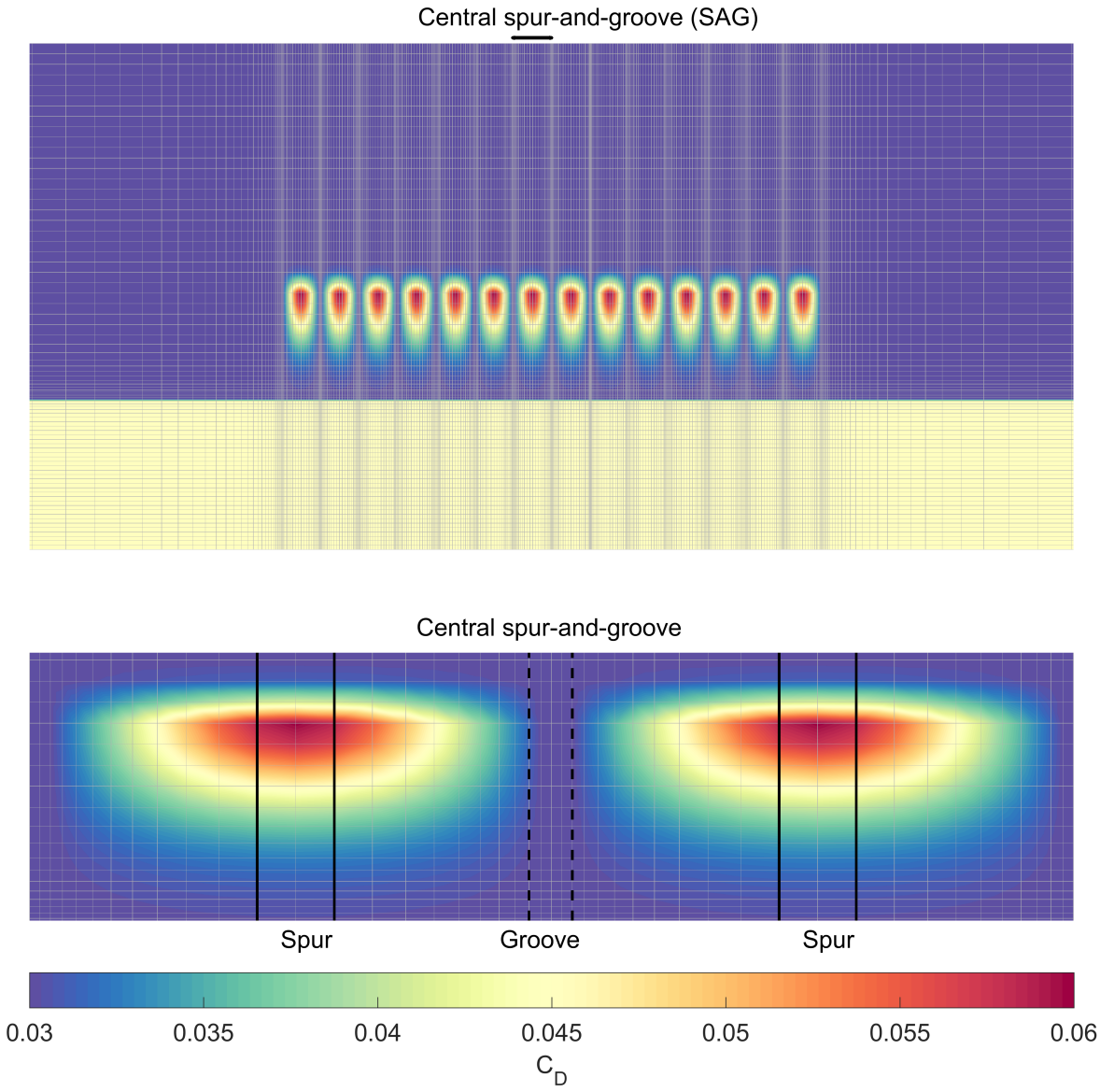

Figure 3.7: Friction values used for the Base Case scenario.

In SWAN, friction was assumed to have constant values of $0.067 \frac{m^2}{s^3}$. The friction in SWAN is related to the term (6) in (3.2), and it is usually negligible outside the surf zone.

MODEL PARAMETERS

This MSc thesis applies D3D-FLOW coupled with SWAN and XBeach. In Chapter 4.4, it is shown that a time length and time steps of 3 h and 0.01 min (0.6 s) were defined as optimum parameters for D3D-FLOW + SWAN. The results used for the analysis correspond to the end output of each simulation, i.e., after 3 h. As for D3D-FLOW coupled with XBeach, a time length of 3 h was also used, and results from the last 2 h were retained for the analysis.

SWAN communicates results with D3D-FLOW every 10 minutes, thus for each run 18 SWAN runs were carried out. SWAN uses water levels from D3D-FLOW, while it exports to D3D-FLOW the wave forces, and Stokes drift velocities.

SWAN was simulated in stationary mode, thus with (1) in (3.2) equal to 0. Winds were not considered for SWAN, even in the simulations with alongshore winds, thus term (6) in (3.2) does not consider wind as a source of energy.

A spectral resolution with 24 bins, varying from 0.05 to 1 Hz, for runs with Tp lower than 20 s, and from 0.04 to 1 Hz for the remainder cases. The directional resolution assumed 36 bins uniformly distributed, thus a directional resolution of 10° was used.

SWAN numerical parameters were assumed as 1 for the spectral space (CDD) and 0.5 for the frequency space (CSS), and the percentage of 99.9% of wet grid points was used as accuracy criteria, with 2% of relative changes for Hs, $Tm01$ (mean wave period), and $\frac{Hs}{Tm01}$, with a maximum number of iterations of 100.

While SWAN calculates the wave parameters for every grid corners, D3D-FLOW uses staggered grid, as explained in Chapter 3.1.4. As SWAN and D3D-FLOW coincides (Figure 3.4), wave parameters are calculated in different places than water levels and velocities, thus interpolation takes place between these models.

In D3D-FLOW, a uniform horizontal eddy viscosity of $0.1\,\frac{m^2}{s}$ was adopted for all simulations, estimated as 10% of the lowest grid spacing (≈1 m). The vertical eddy viscosity was assumed to be $10^{-6}\,\frac{m^2}{s}$. The k-epsilon model for 3D turbulence was used for all simulations. A discussion about the sensitivity of the flow for varying viscosities is addressed in Appendix G, where it is shown that the used values seem to reasonably represent the flow pattern.

4

CALIBRATION AND VERIFICATION

This chapter presents the calibration and verification results obtained in this MSc thesis. Firstly, the conventions adopted for all model results are presented in Chapter 4.1.

The first step (Chapter 4.2) of the calibration was to reproduce the Base Configuration from Rogers et al. (2013), that used a Boussinesq-type model to understand the circulation over SAG formations.

Next, the calibrated model was applied in the two measurement experiments - NFR13 and SFR12 -, presented in Rogers et al. (2015), and the comparison between measured and calculated flow is provided in Chapter 4.3.1.

Another verification step with comparison between theoretical and calculated wave forces was conducted, with results reported in Chapter 4.3.2.

Finally, the optimization of the calibrated model (Chapter 4.4) - with the Base Configuration from Rogers et al. (2013) - was conducted to reduce the computational time keeping accuracy.

4.1. CONVENTIONS

The following conventions were used for all results:

- The shoreline has a west-east orientation, with shore-normal waves coming North (0 degree North), as presented in Figure 3.4;
- The subscripts x, y and z represent the cross-shore, alongshore and vertical axes;
- The letters u, v and w represents the cross-shore, alongshore and vertical velocities;
- Positive velocities indicate offshore or northern (u), eastern (v) and upwards (w) velocities. Blue and red colours represent the offshore and onshore velocities, respectively;
- Capital letters - U, V and W - denote depth-averaged velocities;
- The variables $U_{0.5m-bottom}$ and $U_{0.5m-surface}$ represent the cross-shore velocities integrated over the lowest and top 0.5 m, respectively;
- The subscripts L, S and E represent the Lagrangian, Stokes Drift and Eulerian velocities, respectively, as covered in Chapter 2.4; and
- The reef profile with spur is shown with a black solid line, while the groove appears with a black dashed line.

Regarding the momentum terms presented in (3.4), the nomenclature defined by D3D-FLOW is used (Deltares, 2016), as shown in Table 4.1.

D3D-FLOW version 3.59.01.48550 (Deltares, 2016) provides as output all the momentum terms, except for the vertical advective acceleration (term 3) and the vertical turbulent stress along the water column (term 7). The wave forces (term 5) are provided with total values, without separating into streamwise and lateral radiation stress gradients (2.19 and 2.20).

Table 4.1: Momentum terms nomenclature following D3D-FLOW convention.

Term in (3.4)	**Short description**	**Term in x-direction**	**Term in y-direction**
(1)	local acceleration	*MOM_DUDT*	*MOM_DVDT*
(2)	streamwise advective acceleration	*MOM_UDUDX*	*MOM_VDVDY*
(2)	lateral advective acceleration	*MOM_VDUDY*	*MOM_UDVDX*
(3)	vertical advective acceleration	*MOM_WDUDZ*	*MOM_WDVDZ*
(4)	pressure gradient	*MOM_UPRESSURE*	*MOM_VPRESSURE*
(5)	wave force	*MOM_UWAVES*	*MOM_VWAVES*
(6)	horizontal turbulent stress	*MOM_UVISCO*	*MOM_VVISCO*
(7)	vertical turbulent stress at bottom	*MOM_UBEDSHEAR*	*MOM_VBEDSHEAR*
(7)	vertical turbulent stress at surface	*MOM_UWINDFORCE*	*MOM_VWINDFORCE*

Momentum terms are provided as output only as instantaneous values. D3D-FLOW coupled with XBeach was not used for the analysis of the momentum balance, due to the absence of the Fourier type of output for momentum terms (Deltares, 2016). Fourier outputs were used for the velocities in cases with long waves, as further explained in Chapter C.1.4.

This MSc theses adopted the Lagrangian velocities for the flow characterization. Eulerian velocities are considered mainly close to the bottom, where corals live.

4.2. CALIBRATION

As covered in Chapters 2.3 and 3.2.2, Rogers et al. (2013) investigated the hydrodynamics of SAG with a Boussinesq-type model (funwaveC), with schematic SAG bathymetry. Their approach was to initially use a Base Configuration run, and then to vary the input conditions to understand the flow circulation.

This MSc thesis used the Base Configuration simulation from Rogers et al. (2013) to calibrate D3D-FLOW + SWAN. The model setup used for this run is shown in Table 4.2, with setup similar to the Base Case of the current research, except for the spur height h_{spr} and ratio of friction $\frac{C_{D-grv}}{C_{D-spr}}$, equals to 2 and 0.5, respectively.

Table 4.2: Base Configuration run from Rogers et al. (2013).

Hs_0	$\frac{Hs_0}{Lp_0}$	Dp_0	m	h_{spr}	λ_{SAG}	$\frac{W_{grv}}{\lambda_{SAG}}$	$\tan\beta_f$	W_{reef}	$\frac{C_{D\text{-}grv}}{C_{D\text{-}spr}}$	z_μ	U_{10}
m	-	°	-	m	m	-	-	m	-	m	m/s
1	0.006	0	30	2.9	50	0.06	0.07	300	1	17	0

4.2.1. WAVE PROPAGATION

The wave propagation results from Rogers et al. (2013) are shown in Figure 4.1, where it is shown that the SAG location is in the shoaling zone, with gradual increase of the wave height up to breaking. The wave heights over the spur are slightly higher than over the groove, consistent with shoaling waves over slightly different bathymetries. A set-down of *O* (3 cm) is also observed in the SAG zone, that further turns into a set-up of *O* (5 cm) once the wave starts breaking. The mean wave direction stays zero, corresponding to a shore-normal wave, while fluctuations of the wave directions reach angles of up to 1 degree.

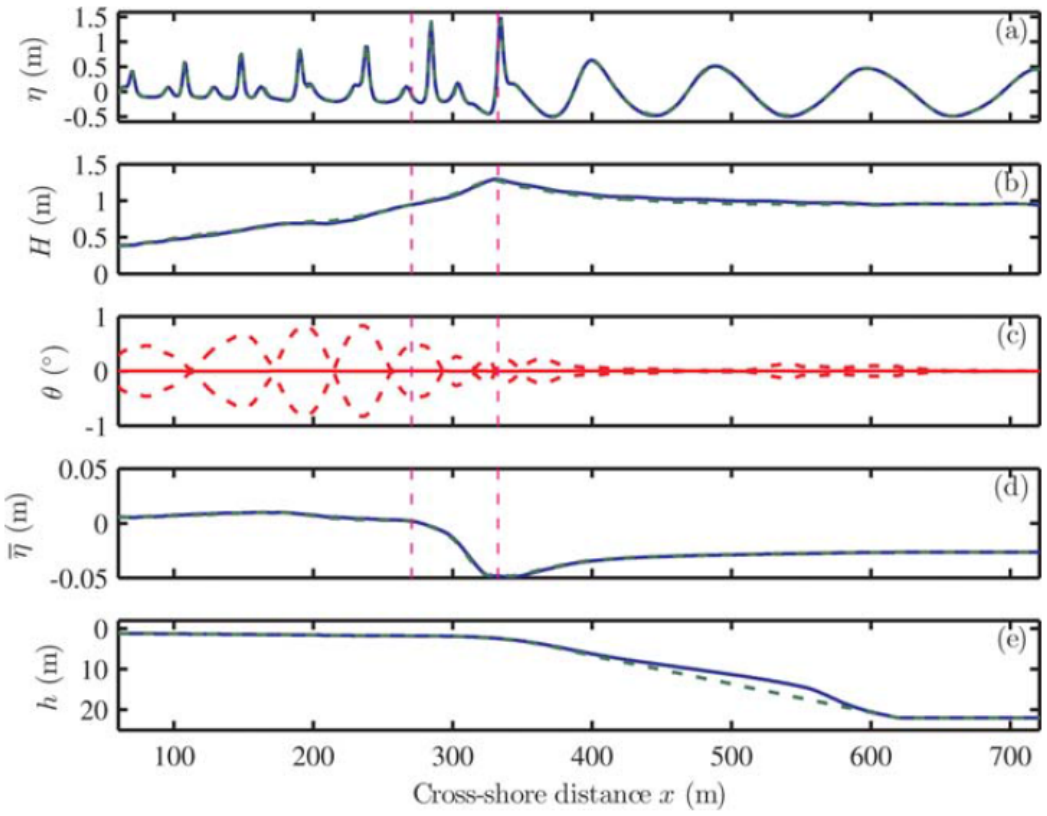

Figure 4.1: Rogers et al. (2013) wave propagation results for base configuration from Rogers et al. (2013).(a) Instantaneous surface η (t = 3600 s), (b) wave height H, (c) mean alongshore wave angle θ (red solid) and max/min alongshore θ (red dash), (d) mean setup $\overline{\eta}$, and (e) cross-shore depth h. Source: Rogers et al. (2013).

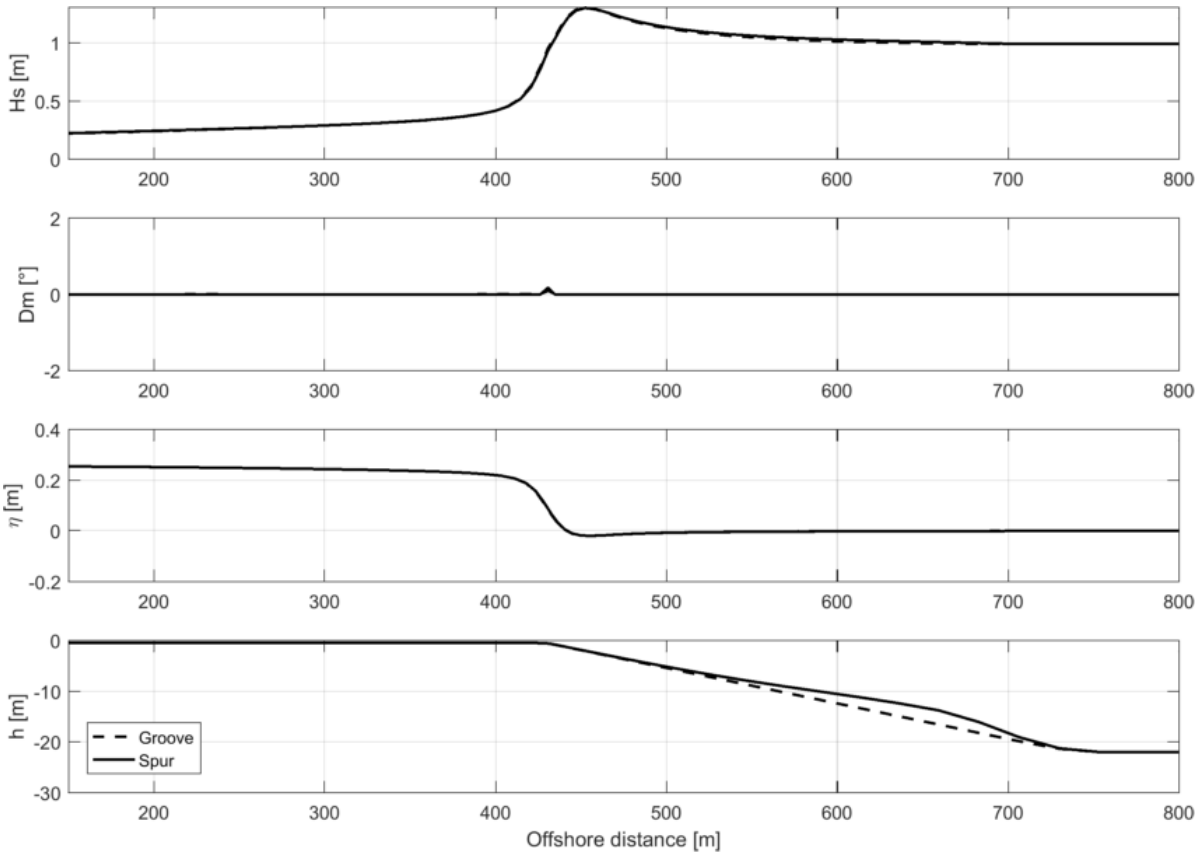

Figure 4.2: D3D + SWAN (without refraction) results for base configuration from Rogers et al. (2013) - significant wave height Hs, mean wave angle D_m, setup η, and cross-shore depth profile.

The first runs with SWAN showed wave heights over the spur much higher than over the groove (Figure 4.4), reaching a ratio of wave heights of around 100% at x ≈ 600 m. This is consistent with a dominant refraction, that converges energy towards the spur, while deconcentrating it over the groove, resulting in a high alongshore gradient of wave height along half a spur wavelength. As discussed in Chapter 3.1.1, SWAN does not include the diffraction, as it does not allow energy to propagate perpendicular to the wave rays. This means that there is no mechanism in its core equation to attenuate the alongshore gradient of wave height coming from refraction.

In order to investigate further the diffraction dominance in the Base Configuration SAG formation, XBeach non-hydrostatic was applied with same geometry as previously described and with a monochromatic shore-normal wave. As described in Chapter 3.1.1, XBeach non-hydrostatic is a 2DH phase-resolver model, with capabilities similar to the model applied by Rogers et al. (2013). The results shown in Figure 4.3 indicate wave heights slightly higher over spur than over the groove, similar to Rogers et al. (2013), corroborating the idea that diffraction effects undermine refraction, resulting in shoaling waves over distinct cross-shore depth profiles - spur and groove.

XBeach wave-averaged model, whose core equation is the same as SWAN, was also applied for the Base Configuration case to verify if results similar to SWAN were obtained. A monochromatic wave was applied, instead of a JONSWAP spectrum as in SWAN. Figure 4.5 shows that the resulting difference between spur and groove wave heights is even larger, consistent with dominant refraction.

These first investigations with different numerical models suggest that diffraction overcomes refraction effects. This case configures the situation related by Dean and Dalrymple (2001) in which classical wave refraction indicate zones of wave convergence and extremely high concentrations of wave energy, also discussed in Chapter 2.4.

As the wave heights over spur and groove are consistent with a cross-shore profile of a wave that only shoals, the next step was to apply SWAN without refraction, i.e., term 5 in (3.2) becomes zero. The wave propagation results are shown in Figure 4.2, where wave heights similar to the ones found by Rogers et al. (2013) were obtained, with slightly higher waves over the spur. Mean wave directions equal to zero degree (shore-normal waves) were found, as expected for shore-normal waves without refraction, matching Figure 4.2. A similar set-down with O (3 cm) was calculated in the SAG zone, followed by a set-up with O (20 cm) over the reef flat, that matches with XBeach non-hydrostatic results (4.3).

The wave propagation results indicate that SWAN without refraction produces results that are nearly similar to the waves calculated with a phase-resolver model, that considers both refraction and diffraction simultaneously. The next step of the calibration was to verify if the currents calculated by D3D-FLOW + SWAN also matches the results found by Rogers et al. (2013).

4.2.2. CURRENTS

The model used by Rogers et al. (2013) solves the 2DH momentum balance (2.23) and mass conservation for the Eulerian velocities, and with (2.29) the Lagrangian velocities are obtained. The Stokes Drift velocities are further calculated with (2.26). D3D-FLOW calculates the 3D momentum balance (3.4) and mass conservation (3.3) with GLM formulation, thus solving the Lagrangian velocities, and then assuming (2.27) to obtain the Stokes Drift velocities and (2.25) for the Eulerian velocities. The fundamental way that both models use to solve the flow is different, since for D3D-FLOW the Stokes Drift occurs at every cell as a result of LWT formualtion, while in funwave-c it comes essentially from mass balance.

The Lagrangian depth-averaged velocities found by Rogers et al. (2013) in Figure 4.6 indicate that the there are two circulation cells in the SAG zone, one starting from offshore up to x ≈ 500 m, and another from that point up to to start of the surfzone (x ≈ 300 m). In the first circulation cell, the spur velocities grow from nearly zero up to a peak of around 5 cm/s, and then decay back to zero, while the groove velocities decay from zero to a minimum of about -5 cm/s, then growing back to zero. The second circulation cell contains onshore and offshore velocities over the spur and the groove, respectively, with O (1 cm/s), relatively lower than in the offshore zone.

The offshore peak of Lagrangian depth-averaged velocity coincides with offshore peaks of Eulerian depth-averaged velocities, precisely at the only point where Eulerian velocities are negative (onshore) over the groove. In general, the Eulerian velocities grow from the start of the second circulation cell up to breaking, when they start decaying. Stokes Drift velocities show a gradual increase from offshore up to x ≈ 400 m, where they start to grow fast, up to breaking, when they decrease back again. The cross-shore bottom shear stresses follow the same trend as the Eulerian velocities with opposite sign, consistent with a shear stress being a function of the square of the Eulerian velocities.

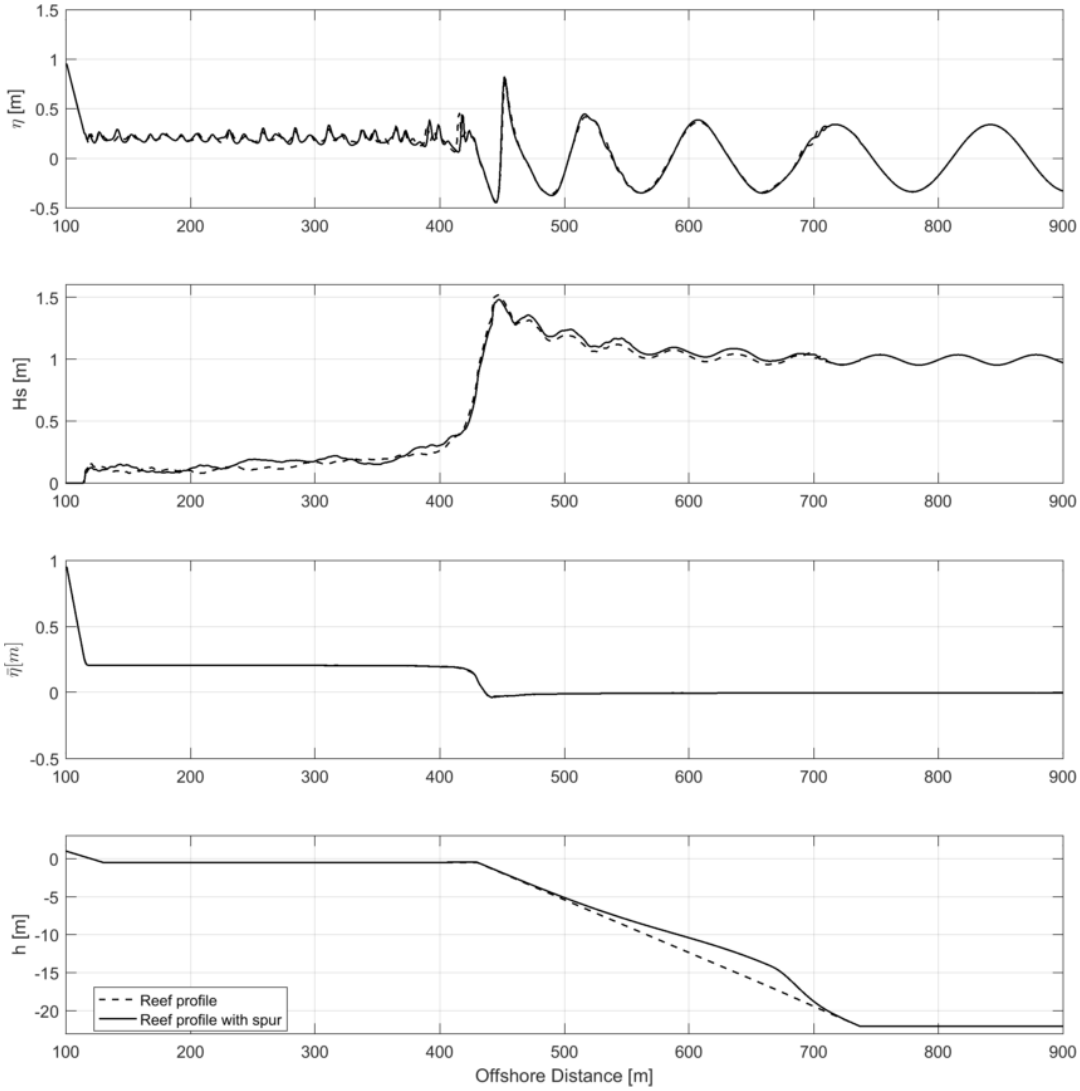

Figure 4.3: XBeach (non-hydrostatic) wave propagation results for base configuration from Rogers et al. (2013) - instantaneous surface η (t = 3600 s), wave height H, mean setup $\overline{\eta}$, and cross-shore depth h.

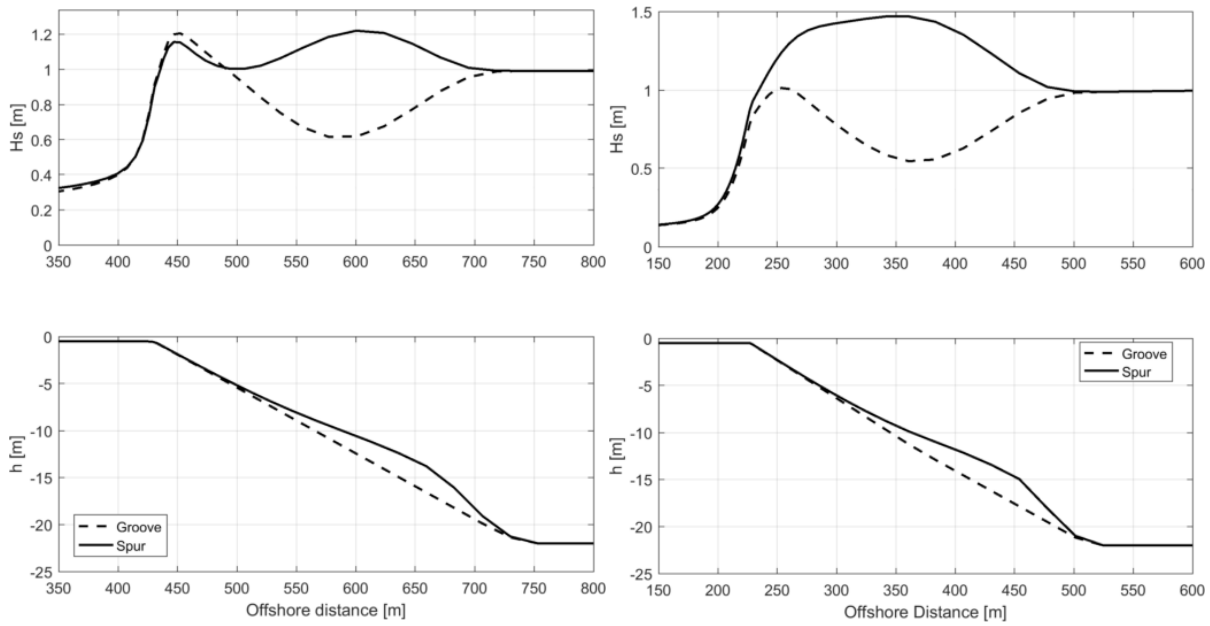

Figure 4.4: D3D + SWAN (with refraction) results for base configuration from Rogers et al. (2013) - significant wave height Hs, and cross-shore depth profile.

Figure 4.5: XBeach (wave-averaged) (with refraction) wave propagation results for base configuration from Rogers et al. (2013) - significant wave height Hs, and cross-shore depth profile.

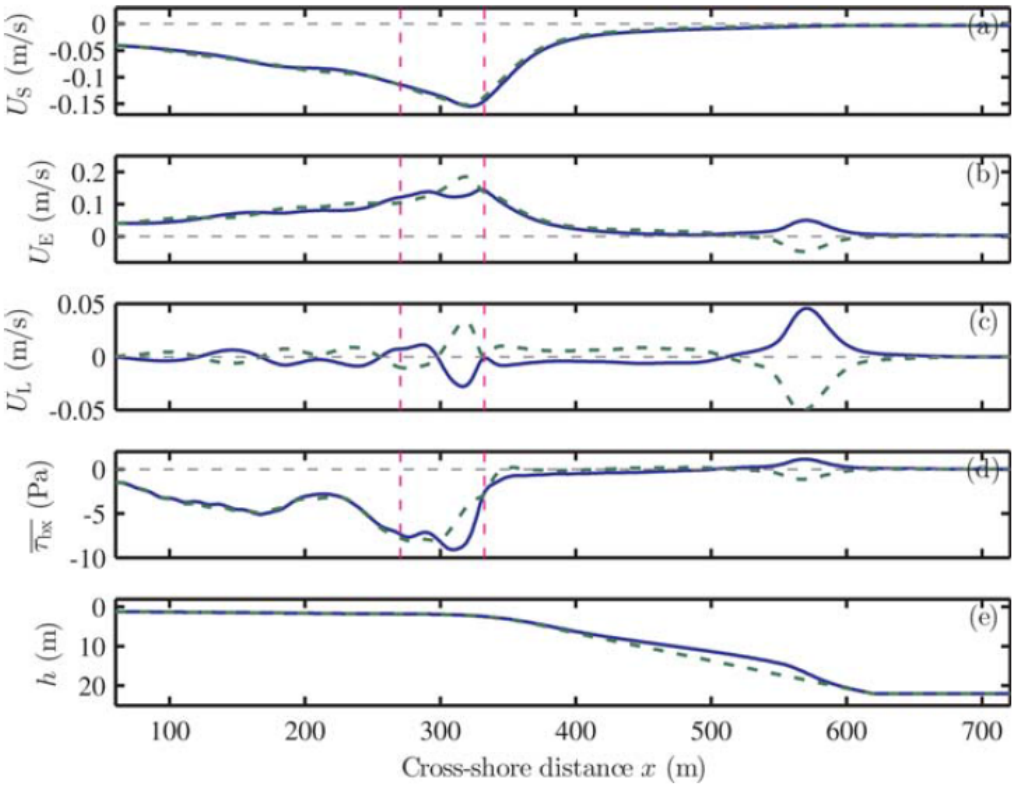

Figure 4.6: Rogers et al. (2013) velocity and bed shear results for base configuration from Rogers et al. (2013).(a) Cross-shore Stokes drift U_S, (b) Eulerian velocity U_E, (c) Lagrangian velocity U_L, (d) average cross-shore bed shear stress τ_{bx}, and (e) cross-shore depth profile at spur (blue solid) and groove (green dash). Positive cross-shore indicate offshore velocities. Source: Rogers et al. (2013).

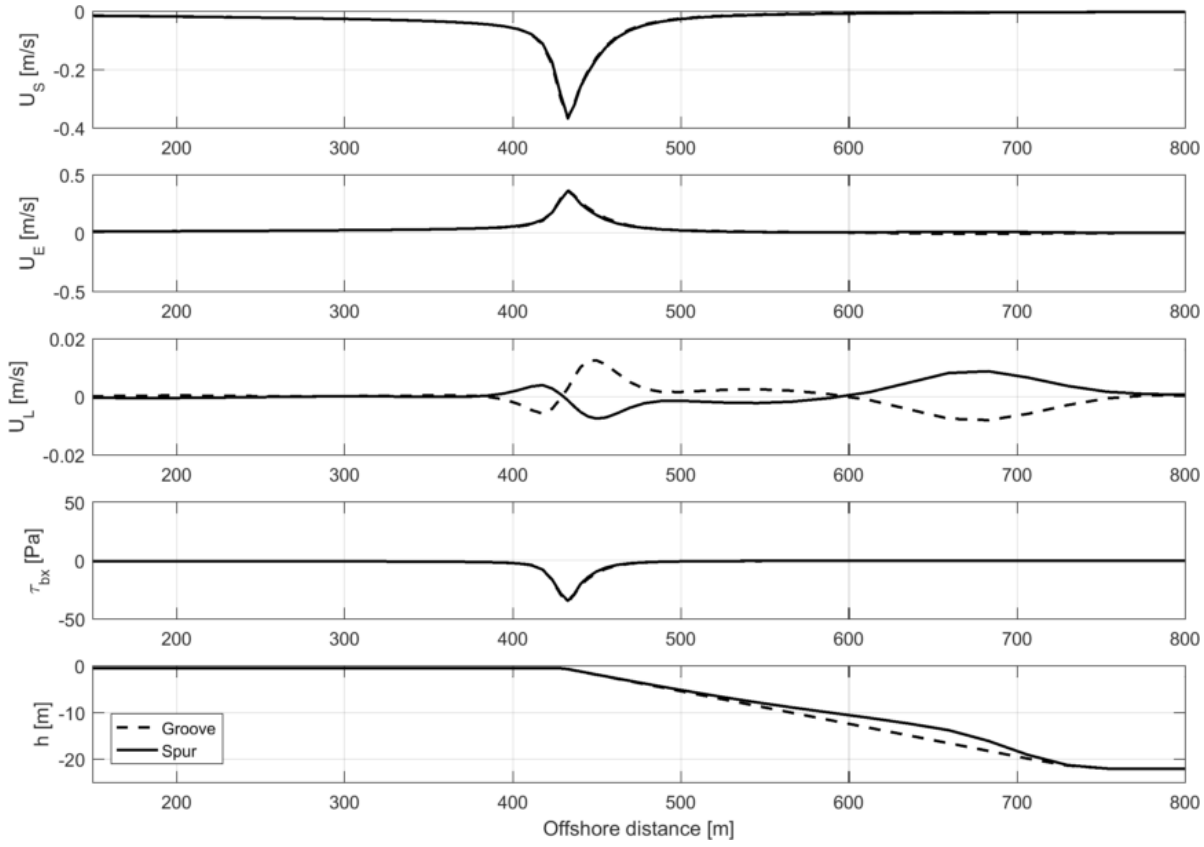

Figure 4.7: D3D + SWAN velocity and bed shear results for base configuration from Rogers et al. (2013) - cross-shore Stokes drift U_S, Eulerian velocity U_E, Lagrangian velocity U_L, average cross-shore bed shear stress τ_{bx}, and cross-shore depth profile at spur (solid) and groove (dash). Positive cross-shore indicate offshore velocities.

D3D-FLOW results (Figure 4.7) show that in the SAG zone the same trend for the Lagrangian depth-averaged velocities found by Rogers et al. (2013) was obtained, with offshore peaks and the two aforementioned circulation zones. The first offshore peak of Lagrangian velocities also coincides with the only point where Eulerian velocities are onshore. From the surfzone and further onshore, results do not match with Rogers et al. (2013), possibly due to nonlinear effects becoming predominant as waves start to break, as discussed in Chapter 3.1.2 and shown in Figure 3.1.

Map results for the Lagrangian depth-averaged velocities from both Rogers et al. (2013) and D3D-FLOW are shown in Figures 4.8 and 4.9. Both maps indicate the same flow pattern, with circulation cells and predominant cross-shore velocities. Alongshore depth-averaged velocities appear to have limited values relatively to the cross-shore, and in both plots look close to zero over the spur and the groove.

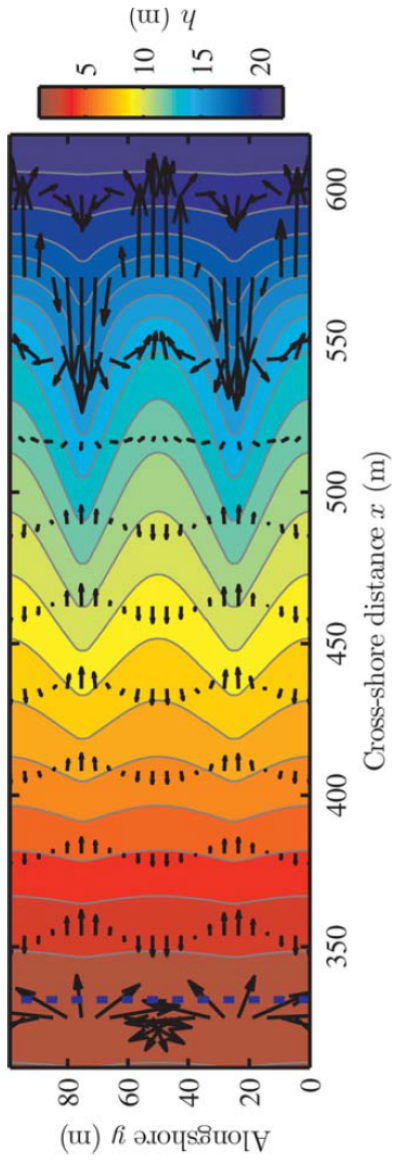

Figure 4.8: Rogers et al. (2013) Lagrangian velocities U_L and V_L results for base configuration from Rogers et al. (2013) - maximum velocity vector scale is 0.05m/s, and horizontal dashed blue line represents the offshore edge of the surf zone. Source: Rogers et al. (2013).

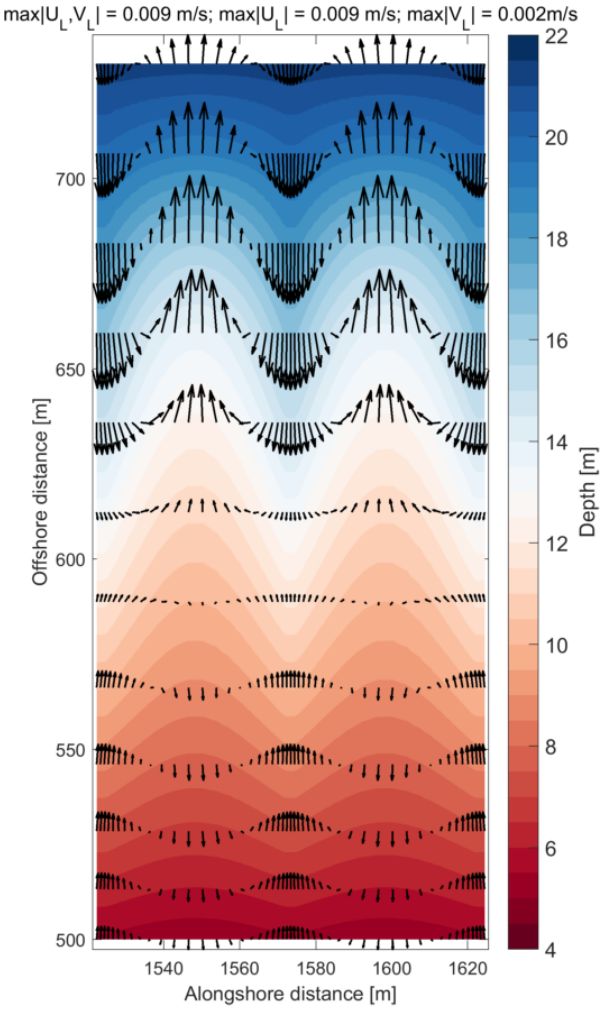

Figure 4.9: D3D + SWAN velocity Lagrangian velocities U_L and V_L results for base configuration from Rogers et al. (2013).

4.2.3. MOMENTUM BALANCE

Rogers et al. (2013) evaluated the mechanisms explaining the flow pattern with analysis of the phase and depth-averaged momentum balance terms. The terms considered in their analysis are the wave forces, the pressure gradient (term 3 in 2.23), bottom friction (term 4 in 2.23) and streamwise advective acceleration (terms 5, 3, 4 and 2 in 2.23, respectively), with the remaining terms concluded to be negligible. It is important to mention that, as covered in Chapter 3.1.1, Boussinesq-type models assume irrotational flows, thus the horizontal turbulent stresses (term 6 in 2.23) are not included in the calculation.

The cross-shore plot of the cross-shore momentum terms over the spur from Rogers et al. (2013) is shown in Figure 4.10, where it can be seen that wave forces are mainly balanced by the pressure gradient, and that bottom friction starts to be more important in shallower waters. The streamwise advective acceleration has a limited role in that analysis.

D3D-FLOW results for the depth-averaged cross-shore momentum terms over the spur in Figure 4.11 show very similar patterns, with pressure gradient balancing the wave forces, and growing friction as approaching the surfzone. Similar order of magnitudes were also found.

Rogers et al. (2013) also plotted the phase and depth-averaged cross-shore momentum terms in the alongshore view at a depth of around 9 m, shown in Figure 4.12. In essence, they concluded that the imbalance between pressure gradient and wave forces accelerates the flow until shear stress balance it, driving offshore Eulerian currents. This mismatch between them was found to be zero over the spur, meaning the pressure gradient and wave forces balance the flow, which is known as the set-down balance, as explained in Chapter 2.4.3. The imbalance is maximum in magnitude precisely over the groove, where wave forces are higher than pressure gradient and friction balances it, leading to maximum Eulerian currents. This alongshore variation leads to reverse depth-averaged Lagrangian currents over spur and groove, characteristic of the SAG circulation cell. Stokes Drift velocities look approximately the same over the spur and groove, consistent with diffraction overcoming refraction.

The equivalent plot of D3D-FLOW for that alongshore variation is presented in Figure 4.13, where it can be seen that the overall pattern for the momentum terms looks the same, with maximum absolute values of the mismatch between wave forces and pressure gradients located over the groove, coinciding with maximum friction and maximum Eulerian currents. The depth-averaged horizontal turbulent stresses are also shown, with relatively minor importance for that depth. The resulting pattern of depth-averaged Lagrangian velocities looks the same as Rogers et al. (2013), with offshore velocities over the groove and onshore over the spur for that location. Order of magnitude of all terms in Figures 4.12 and 4.13 looks equivalent.

4.2.4. OVERALL EVALUATION AND DIFFRACTION/REFRACTION IMPORTANCE

The overall comparison between Rogers et al. (2013) and D3D-FLOW + SWAN results suggests that the application of a phase-averaged model neglecting refraction processes is adequate for the Base Configuration case.

As discussed in Chapter 2.4, Rogers et al. (2013) found that the relative difference between wave heights over spur and groove starts to be more relevant only for higher values of SAG wavelengths, approximately more than 100 m for the Base Configuration. SWAN results including refraction (Figure 4.4) show that for a spur and groove wavelength of 50 m the alongshore difference of wave heights between spur and groove is already as high as the maximum difference found by Rogers et al. (2013) for higher spur and grove wavelengths.

Most of the spur and groove wavelengths reported in the literature have mean SAG wavelengths shorter than 100 m (Figure 2.10). Even for a more exposed environment like Hawaii, the SAG wavelength of more than 100 m is relatively less frequent (Figure 2.9). Thus, it can be inferred that diffraction processes tend to be dominant in SAG formations.

As covered in Chapter 2.4, the wave forces come from gradients of radiation stresses, that are among others function of wave heights. The momentum balance conservation equation (2.23) shows that the wave force is divided by the depth (term 5). This suggests that for alongshore sections where spur heights are higher the relative importance of the depth term in the wave force term tends to be larger. Sensitivity runs with refraction for the Base Configuration showed that the alongshore gradient of the wave force is even higher, due to the extremely high concentrations of wave energy, resulting in different flow pattern. With refraction off, the alongshore gradient becomes smooth (Figure 4.12), and flow pattern becomes equivalent to results from Rogers et al. (2013).

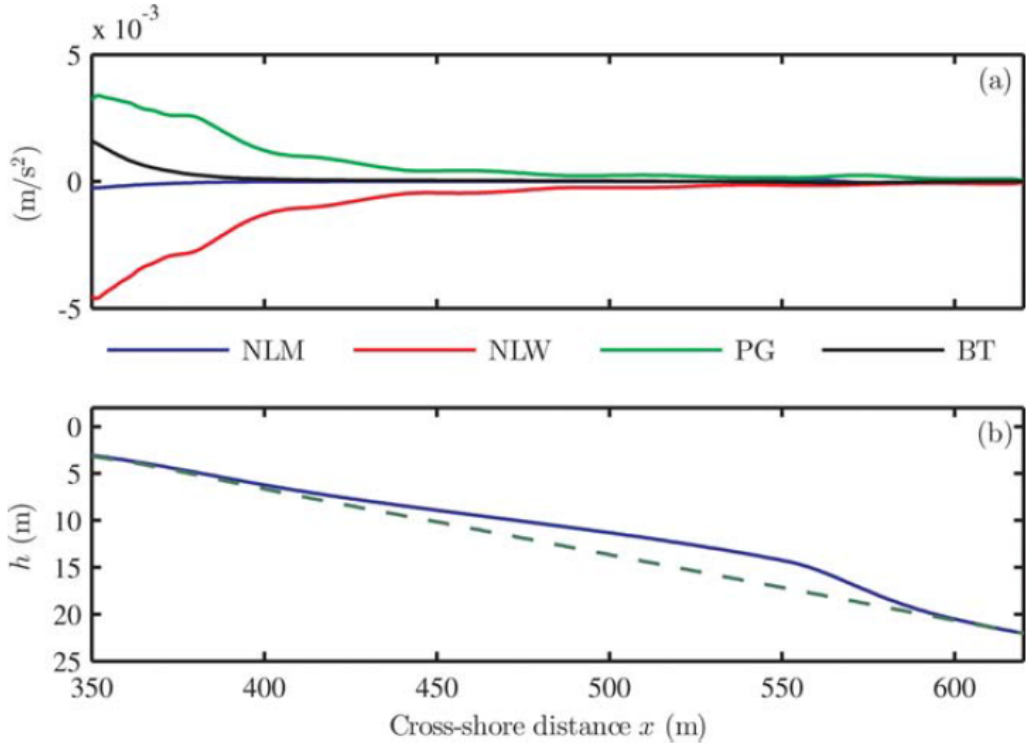

Figure 4.10: Rogers et al. (2013) phase-averaged cross-shore depth-averaged momentum terms at top of spur for base configuration from Rogers et al. (2013). (a) Cross-shore momentum terms and (b) cross-shore depth profile. NLM, NLW, PG and BT represent the streamwise advective acceleration, wave forces, pressure gradient and bottom shear stress, respectively. Source: Rogers et al. (2013).

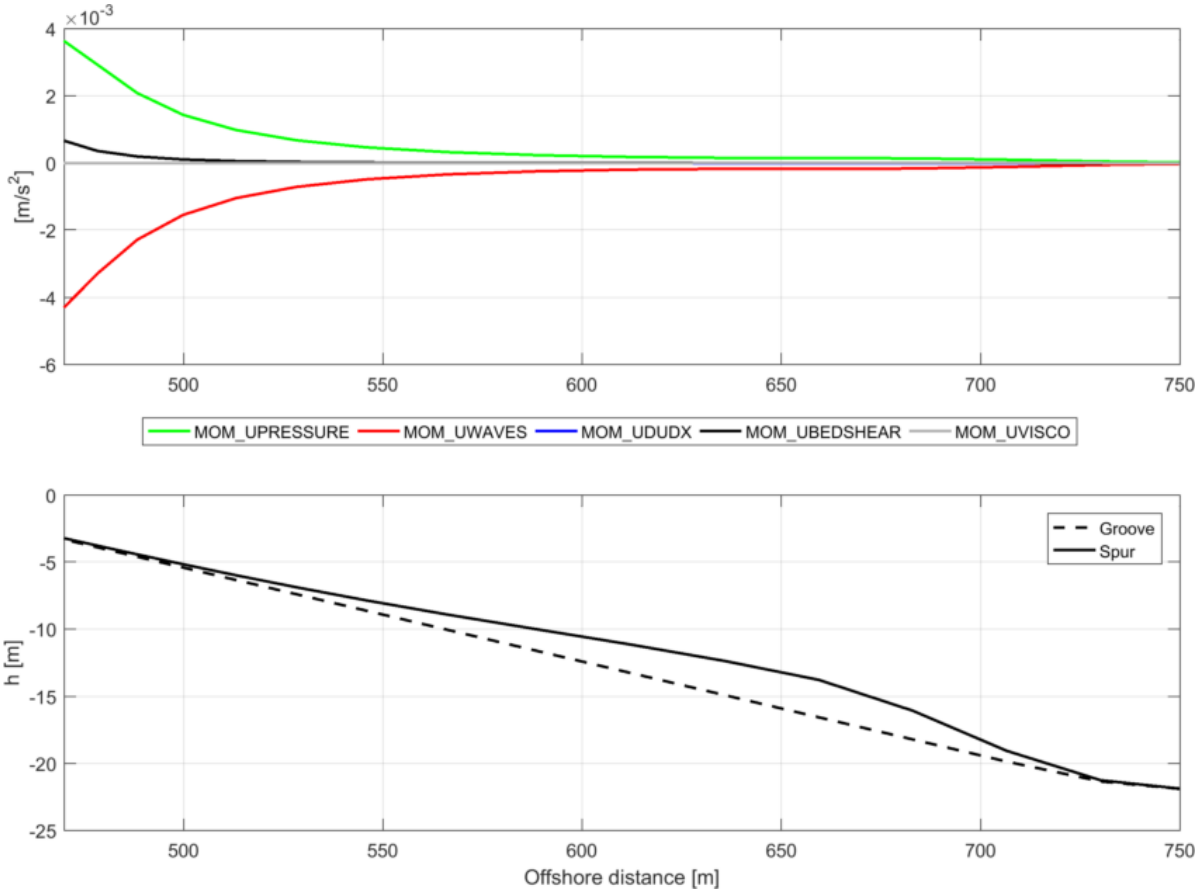

Figure 4.11: D3D + SWAN cross-shore depth-averaged momentum terms at top of spur for base configuration from Rogers et al. (2013) - cross-shore momentum terms and cross-shore depth profile. MOM_UPRESSURE, MOM_UWAVES, MOM_UDUDX, MOM_UBEDSHEAR and MOM_UVISCO represent the pressure gradient, wave forces, streamwise advective acceleration, bottom shear stress and horizontal viscous forces, respectively.

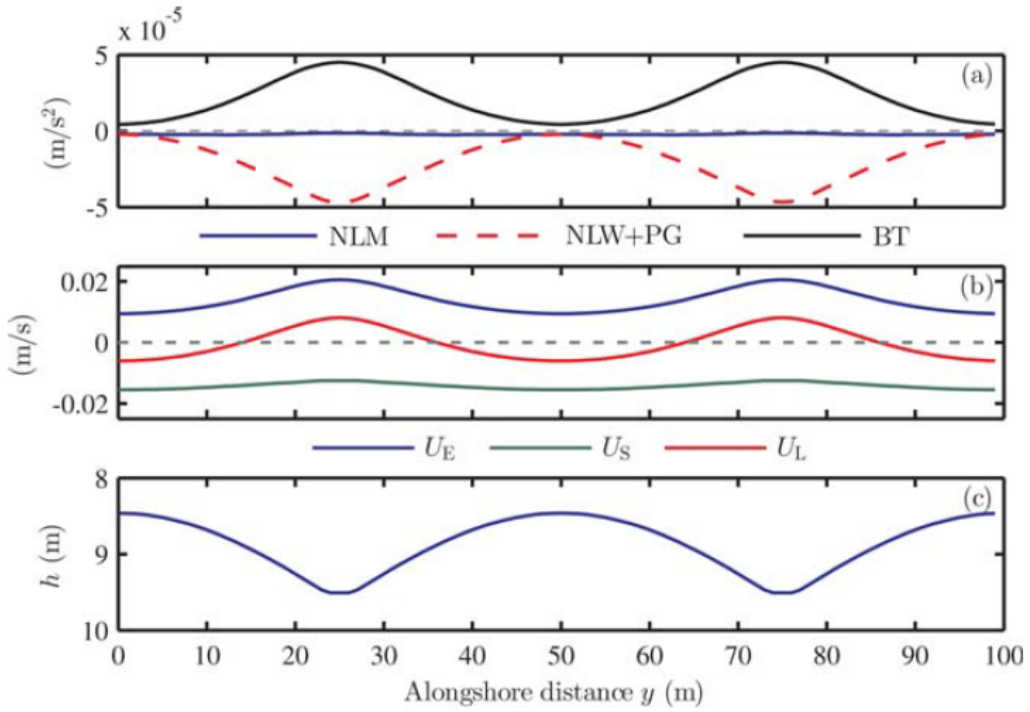

Figure 4.12: Rogers et al. (2013) alongshore variation of phase-averaged cross-shore momentum terms and velocity for base configuration from Rogers et al. (2013). (a) Cross-shore momentum terms, (b) U_E, U_S and U_L velocities and (c) alongshore depth profile. NLM, NLW, PG and BT represent the streamwise advective acceleration, wave forces, pressure gradient and bottom shear stress, respectively. Source: Rogers et al. (2013).

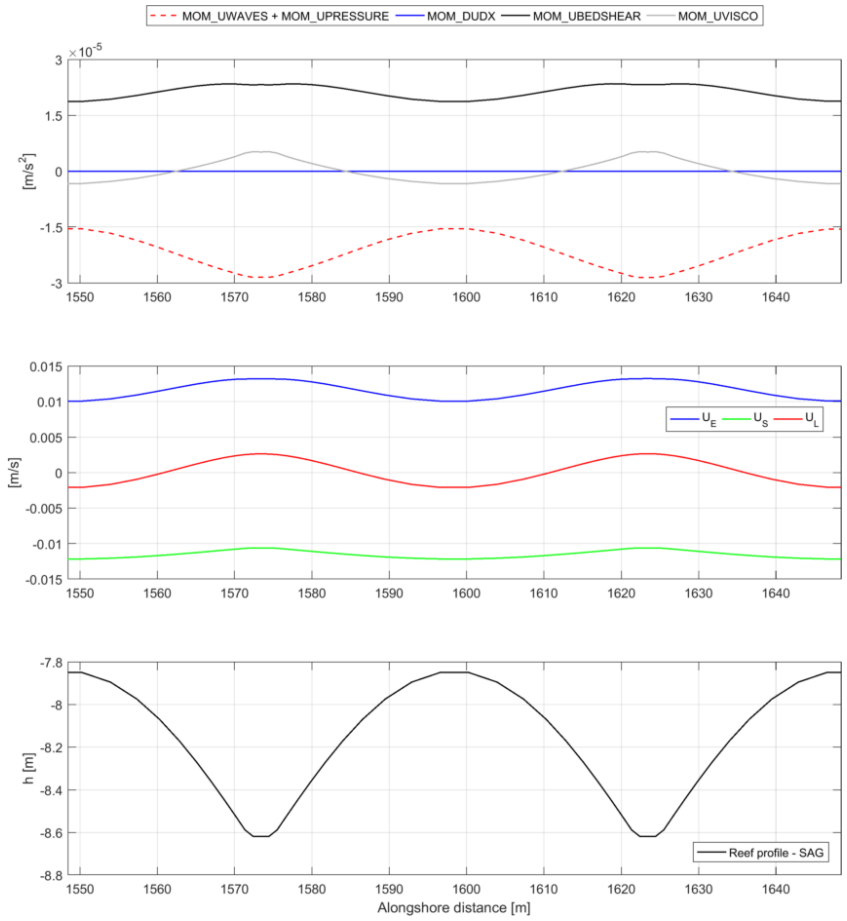

Figure 4.13: D3D + SWAN alongshore variation of phase-averaged cross-shore momentum terms and velocity for base configuration from Rogers et al. (2013) - cross-shore momentum terms, U_E, U_S and U_L velocities and alongshore depth profile. MOM_UPRESSURE, MOM_UWAVES, MOM_UDUDX, MOM_UBEDSHEAR and MOM_UVISCO represent the pressure gradient, wave forces, streamwise advective acceleration, bottom shear stress and horizontal viscous forces, respectively.

In order to further investigate the refraction effects, runs with and without refraction were performed for all the sensitivity runs reported in Chapter 3.2.4. The wave results for those sensitivity runs are shown in Appendix B. Overall, they indicate that including refraction leads to high overall alongshore gradient of wave heights, incompatible with the findings from Rogers et al. (2013) and with sensitivity runs with XBeach non-hydrostatic.

Considering the previous findings, this MSc thesis opted to apply D3D-FLOW + SWAN/XBeach without taking into account the refraction processes for all simulations performed. The limitations from that modelling decision are further discussed in Chapter 6.3.

As for the influence of oblique waves and of directional spreading, both simulations with and without refraction indicated results with some degree of uncertainty. Simulations with refraction for oblique waves shows focusing of energy over spur or groove, depending on the wave angle, that yields in both cases a significant alongshore gradient of wave heights. On the other hand, the results without refraction show smooth gradient of wave heights between spur and groove, but an unchangeable wave direction in the SAG zone. Considering those uncertainties, the current research opted not to investigate the role of varying wave angles and directional spreadings. An initial evaluation of their potential influence in the SAG flow for runs without refraction is further addressed in Appendix F.

4.3. VERIFICATION

The verification of the calibrated model - D3D-FLOW + SWAN without refraction - was firstly carried out with measured data in Palmyra Atoll (Chapter 4.3.1), as reported by Rogers et al. (2015). The objective of this first step was to verify if the application of a schematic modelling produces overall results similar to measurements, and to discuss the capability and limitations of this kind of approach.

The second step (Chapter 4.3.2) was to compare the wave forces calculated by D3D-FLOW + SWAN with estimations using a simplified model that uses LWT expressions for shoaling waves over spur and grooves, i.e., assuming diffraction overcoming refraction effects. The objective of this step was to verify if wave forces - both in the alongshore and in the cross-shore - obtained by D3D-FLOW + SWAN are consistent with simplified estimations.

4.3.1. SCHEMATIC MODELLING OF PALMYRA ATOLL

As discussed in Chapter 2.3, Rogers et al. (2015) conducted two field campaigns in SAG formations on Palmyra Atoll, SFR12 and NFR13. The variability of both geometries are shown in Figure 2.11, showing the complexity of the local alongshore profile as compared to the schematization undertaken in the current research (Figure 3.4).

Based on the mean SAG geometry parameters for SFR12 and NFR13 and typical wave conditions during those experiments provided in Rogers et al. (2015), the verification runs with model setup shown in Table 4.3 were carried out, with results discussed below. As for the NFR13, two wave directions were simulated, as more oblique waves were encountered for that experiment.

NFR13

The NFR13 measurements showed that the cross-shore depth-averaged velocities U_L were predominantly offshore, with values of O (10 cm /s). The alongshore depth-averaged velocities V_L presented values of similar order of magnitude, while the vertical depth-averaged velocities W_L were relatively lower, although with similar order of magnitude. All those values were found both over the spur and groove.

Rogers et al. (2015) used another variable to estimate the strength of circulation, referred to as the cross-shore circulation velocity U_C (4.1):

$$U_C = (U_L - \langle U_L \rangle) \cos\phi \tag{4.1}$$

where $\langle U_L \rangle$ is the spatial average in the alongshore direction to remove the average cross-shore reef flow and ϕ is the angle between the cross-shore and the alongshore Lagrangian velocities. This velocity tends to be zero in case of strong alongshore flow and it approaches U_L for strong cross-shore current. The cross-shore circulation velocity U_C was found to be nearly always positive over the spurs and negative over the grooves, with O (1 cm/s).

Rogers et al. (2015) estimated the mean of the absolute depth-averaged momentum terms from NFR13 experiment both in the cross-shore and in the alongshore, as shown in Table 4.4. In the cross-shore direction, the main terms were found to be the lateral advective term, the pressure gradient and the lateral radiation

stress, while in the alongshore the streamwise advective term, the pressure gradient and the streamwise radiation stress appear to be the significant terms, all with $O\,(10^{-4})$ m/s^2.

Table 4.3: Model setup for the verification runs - NFR13 and SFR12 based on information from Rogers et al. (2015).

Run	Hs_0	$\frac{Hs_0}{Lp_0}$	Dp_0	m	h_{spr}	λ_{SAG}	$\frac{W_{grv}}{\lambda_{SAG}}$	$\tan\beta_f$	W_{reef}	$\frac{C_{D\text{-}grv}}{C_{D\text{-}spr}}$	z_μ	U_{10}
-	m	-	°	-	m	m	-	-	m	-	m	m/s
NFR13 (shore-normal)	1	0.006	0	30	1.9	14	0.1	0.07	300	0.5	10	0
NFR13 (oblique)	1	0.006	15	30	1.9	14	0.1	0.07	300	0.5	10	0
SFR12 (shore-normal)	1.1	0.006	0	30	1.8	15	0.13	0.15	300	0.5	12	0

Table 4.4: Measured order of terms in depth-averaged momentum equations from NFR13 experiment in cross-shore and alongshore from Rogers et al. (2015).

	Cross-shore		**Alongshore**	
Description	**Term**	O (m/s^2)	**Term**	O (m/s^2)
Local acceleration	$\frac{\partial U_L}{\partial t}$	1×10^{-5}	$\frac{\partial V_L}{\partial t}$	2×10^{-5}
Streamwise advective term	$U_L\frac{\partial U_L}{\partial x}$	1×10^{-5}	$V_L\frac{\partial V_L}{\partial y}$	2×10^{-4}
Lateral advective term	$V_L\frac{\partial U_L}{\partial y}$	2×10^{-4}	$V_L\frac{\partial V_L}{\partial y}$	2×10^{-5}
Mean pressure gradient	$g\frac{\partial\overline{\eta}}{\partial x}$	2×10^{-4}	$g\frac{\partial\overline{\eta}}{\partial y}$	6×10^{-4}
Streamwise radiation stress	$\frac{1}{\rho(\overline{\eta}+h)}\frac{\partial S_{xx}}{\partial x}$	4×10^{-5}	$\frac{1}{\rho(\overline{\eta}+h)}\frac{\partial S_{yy}}{\partial y}$	6×10^{-4}
Lateral radiation stress	$\frac{1}{\rho(\overline{\eta}+h)}\frac{\partial S_{xy}}{\partial y}$	3×10^{-4}	$\frac{1}{\rho(\overline{\eta}+h)}\frac{\partial S_{yx}}{\partial y}$	6×10^{-6}
Bottom stress	$\frac{1}{\rho(\overline{\eta}+h)}\overline{\tau_{bx}}$	2×10^{-5}	$\frac{1}{\rho(\overline{\eta}+h)}\overline{\tau_{by}}$	1×10^{-5}
Surface stress	$\frac{1}{\rho(\overline{\eta}+h)}\overline{\tau_{sx}}$	2×10^{-6}	$\frac{1}{\rho(\overline{\eta}+h)}\overline{\tau_{sy}}$	2×10^{-6}

Regarding the model results calculated with shore-normal waves for NFR13 (Table 4.3), the cross-shore depth-averaged velocities along the cross-shore profile are shown in Figure 4.14. The modelled cross-shore velocity at a depth of 10 m was of 1 cm/s over both spur and grooves. This value is consistent with the measured range of values, showing offshore flow both over spur and groove. This figure also shows that the depth-averaged velocities are nearly always offshore from offshore up to point where the spur velocities reverse (x $\approx$ 500 m). As it is discussed further in Chapter 5.2.2, this pattern with offshore velocities both over spur and

groove are likely due to the short SAG wavelength, that enhances the horizontal turbulent stresses mixing momentum in the alongshore.

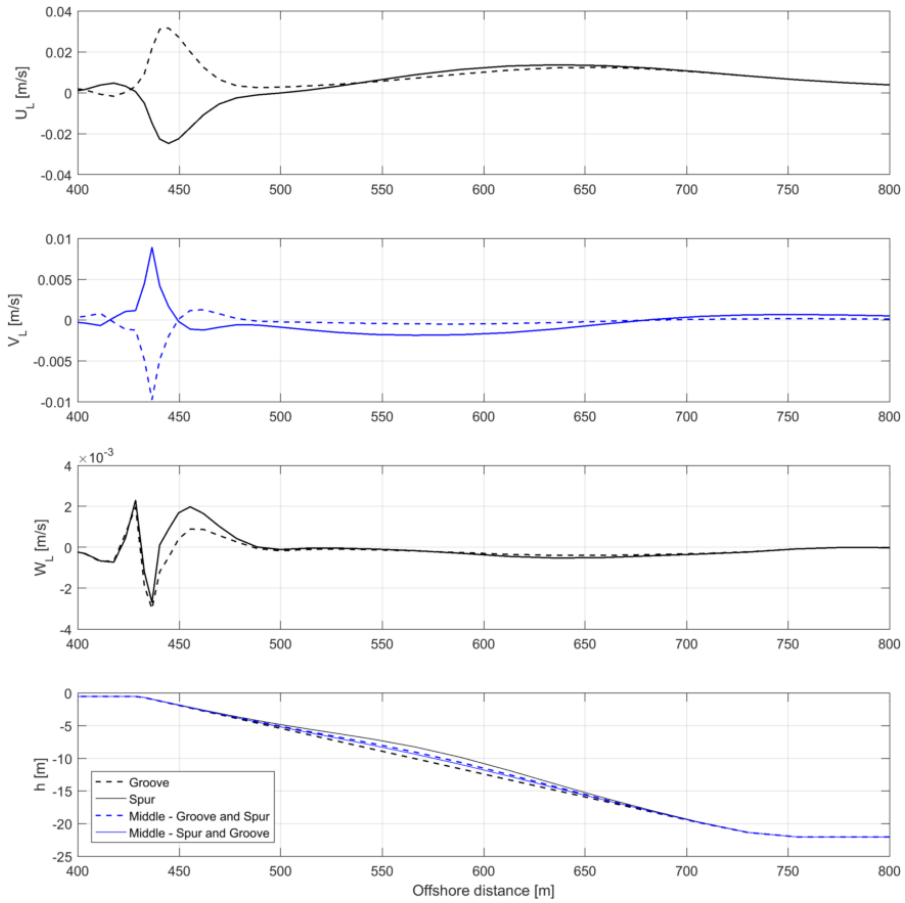

Figure 4.14: Model results for depth-averaged velocities U_L, V_L, W_L and cross-shore depth profile for schematic simulation of NFR13 using shore-normal waves.

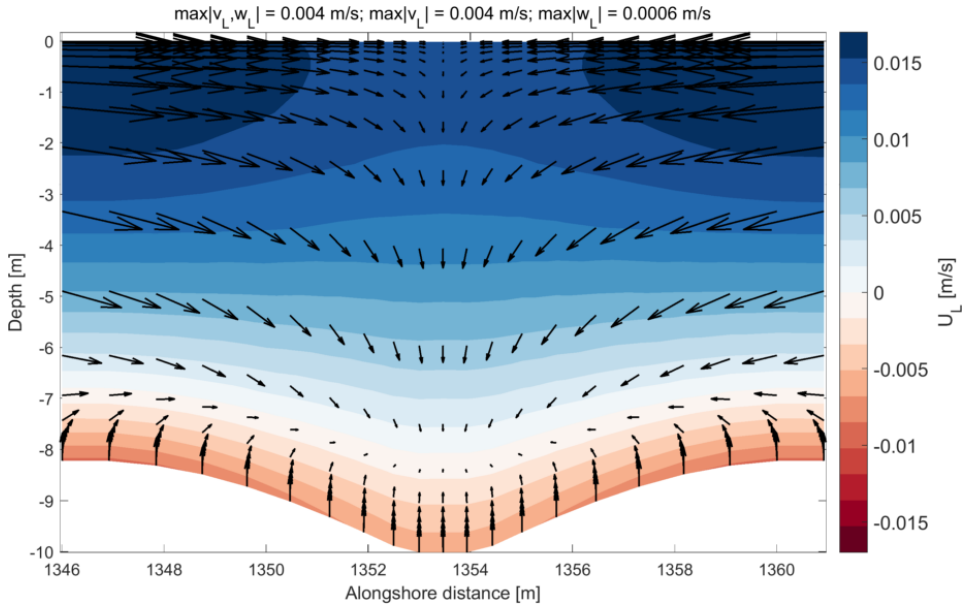

Figure 4.15: Alongshore view of model results for velocities u_L, v_L, w_L at depths of around 10 m with shore-normal waves. Blue and red colours indicate offshore and onshore flows, respectively.

The alongshore and vertical velocities calculated by the model with shore-normal waves were found to be much lower than the range of values found on NFR13.

The alongshore view of the model Lagrangian currents at a depth of 10 m is shown in Figure 4.15. This figure shows that there is offshore flow near the surface both over the spur and over the groove, although it is higher for the former. Alongshore currents converge to the groove, where they are nearly zero, and vertical velocities are extremely low, even compared to the already low alongshore values.

The comparison between Figures 4.15 and 2.12, that illustrates the characteristic circulation cell, shows some similarities, such as offshore flow over spurs near the surface and low offshore velocity near the surface over the groove, although the depth-averaged flow over the groove is onshore.

As for the model results for NFR13 with oblique waves (Table 4.3), a similar plot (Figure 4.16) shows alongshore velocities with similar values as measured (maximum values of 10 cm/s), as shown in Figure 2.12. The cross-shore current have no longer maximum and minimum values near the surface over the spurs and groove, but somewhere in the middle.

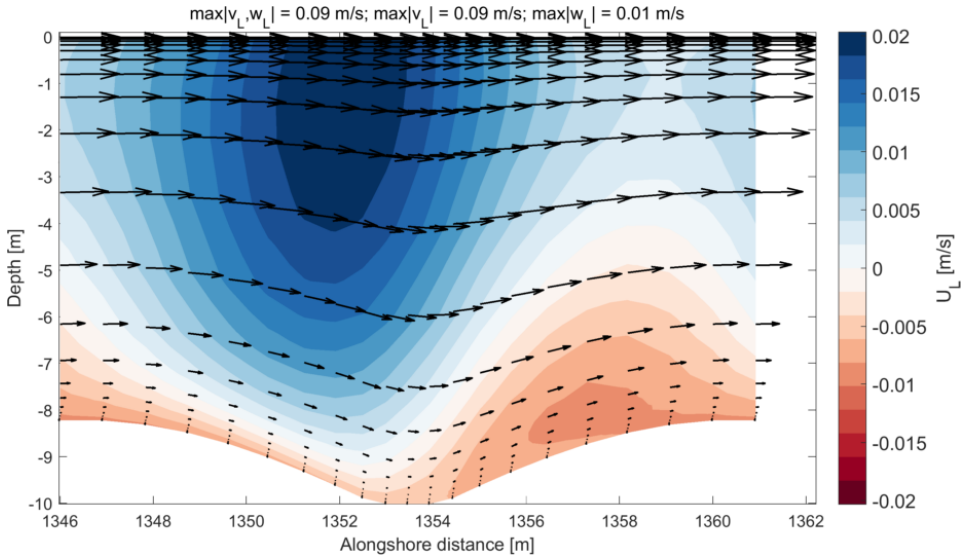

Figure 4.16: Alongshore view of model results for velocities u_L, v_L, w_L at depths of around 10 m with oblique waves. Blue and red colours indicate offshore and onshore flows, respectively.

The shape of the alongshore profile remains logarithmic for both runs with shore-normal and oblique waves, consistent with the reported mean profiles by Rogers et al. (2015), as discussed in Chapter 2.3.

The estimated momentum terms over the spur for both runs with shore-normal and oblique waves are presented in Tables 4.5 and 4.6. As for the shore-normal waves, similar wave forces and pressure gradients were found in both cross-shore and alongshore directions, consistent with measurements (Table 4.4).

The measurements also indicate that the wave forces occur mainly due to the lateral radiation stress in the cross-shore direction and due to the streamwise radiation stress in the alongshore direction. This reflects the importance of oblique waves in SAG geometries, i.e., waves at an angle combined with alongshore gradient of depth found on SAG make the alongshore variation relatively more important than the cross-shore variation for the wave force.

The measurements also show that the lateral advective term in the cross-shore direction and streamwise advective term in the alongshore direction are also important. As covered further in Chapter 4.3.2, the model results with shore-normal waves have nearly zero S_{xy} and S_{yx}, leading to wave forces calculated by (2.21) and (2.22). Therefore, even if wave forces with shore-normal waves provided the correct order of magnitude as measurement, the mechanism generating that force is likely not the same.

The model results with oblique waves show that wave forces, pressure gradient, lateral advective acceleration and viscous forces are the main terms in the cross-shore direction, while for the alongshore the same terms are the most important in general have lower values. Those runs comparatively to the ones with shore-normal waves obtained much larger alongshore variation of advective acceleration, matching the trends observed in measurement.

For both runs with shore-normal and oblique waves, the shear stresses calculated by D3D-FLOW were some orders of magnitude higher than measurements. As D3D-FLOW calculates the shear stress imposed

in the lowest layer in the water column, with thickness of O (1 cm), the acceleration term due to the shear stress is higher than usual calculations for 2DH cases considering the full depth. The bottom shear stresses expressed as an acceleration term needs to be multiplied by the depth and by the water density to have units of stress, as shown in (2.23). The converted measured and modelled shear stresses have similar order of magnitudes of O (0.1 Pa), except for the alongshore shear stress for the run with shore-normal waves. The modelled shear stress over the spur was found to be higher than over the groove, which another trend also observed by Rogers et al. (2015), explored further in Chapter 5.4

Table 4.5: Depth-averaged momentum terms over the spur at depth of around 10 m for schematic modelling with D3D + SWAN with shore-normal waves of NFR13 experiment.

Cross-shore			**Alongshore**		
	O (m/s^2)			O (m/s^2)	
Term	D3D	Measured	**Term**	D3D	Measured
MOM_DUDT	$2x10^{-9}$	1×10^{-5}	MOM_DVDT	1×10^{-9}	2×10^{-5}
MOM_UDUDX	9×10^{-7}	1×10^{-5}	MOM_VDVDY	3×10^{-7}	2×10^{-4}
MOM_VDUDY	4×10^{-9}	2×10^{-4}	MOM_UDVDX	8×10^{-8}	2×10^{-5}
MOM_UPRESSURE	5×10^{-4}	2×10^{-4}	MOM_VPRESSURE	2×10^{-4}	6×10^{-4}
MOM_UWAVES	6×10^{-4}	3×10^{-4}	MOM_VWAVES	2×10^{-4}	6×10^{-4}
MOM_UVISCO	2×10^{-6}	-	MOM_VVISCO	1×10^{-6}	-
MOM_UBEDSHEAR	2×10^{-2}	2×10^{-5}	MOM_VBEDSHEAR	1×10^{-3}	2×10^{-6}

Table 4.6: Depth-averaged momentum terms over the spur at depth of around 10 m for schematic modelling with D3D + SWAN with oblique waves of NFR13 experiment.

Cross-shore			**Alongshore**		
	O (m/s^2)			O (m/s^2)	
Term	D3D	Measured	**Term**	D3D	Measured
MOM_DUDT	$5x10^{-9}$	1×10^{-5}	MOM_DVDT	2×10^{-8}	2×10^{-5}
MOM_UDUDX	1×10^{-7}	1×10^{-5}	MOM_VDVDY	1×10^{-5}	2×10^{-4}
MOM_VDUDY	2×10^{-4}	2×10^{-4}	MOM_UDVDX	5×10^{-7}	2×10^{-5}
MOM_UPRESSURE	5×10^{-4}	2×10^{-4}	MOM_VPRESSURE	7×10^{-5}	6×10^{-4}
MOM_UWAVES	6×10^{-4}	3×10^{-4}	MOM_VWAVES	3×10^{-4}	6×10^{-4}
MOM_UVISCO	1×10^{-4}	-	MOM_VVISCO	5×10^{-5}	-
MOM_UBEDSHEAR	2×10^{-2}	2×10^{-5}	MOM_VBEDSHEAR	5×10^{-2}	2×10^{-6}

SFR12

The SFR12 measurements showed that the cross-shore depth-averaged velocities U_L were predominantly onshore, with values of O (1 cm/s). The alongshore depth-averaged velocities V_L presented higher values, with O (20 cm/s), while the cross-shore circulation velocity U_C had O (1 cm/s). Rogers et al. (2015) argued hat

this lower value of cross-shore circulation velocity relatively to NFR13 was due to higher waves, smaller and less well-defined SAG formations, and higher alongshore V_L.

The modelled depth-averaged velocities U_L, V_L and W_L over spur and groove are presented in Figure 4.17. The calculated cross-shore velocity over the spur is of 1 cm/s towards offshore, while it is almost zero over the groove, close to the first reversing point where groove currents become onshore. As it is further discussed in Chapter 5.5, this type of flow pattern with onshore currents over the spur was not observed in the current research.

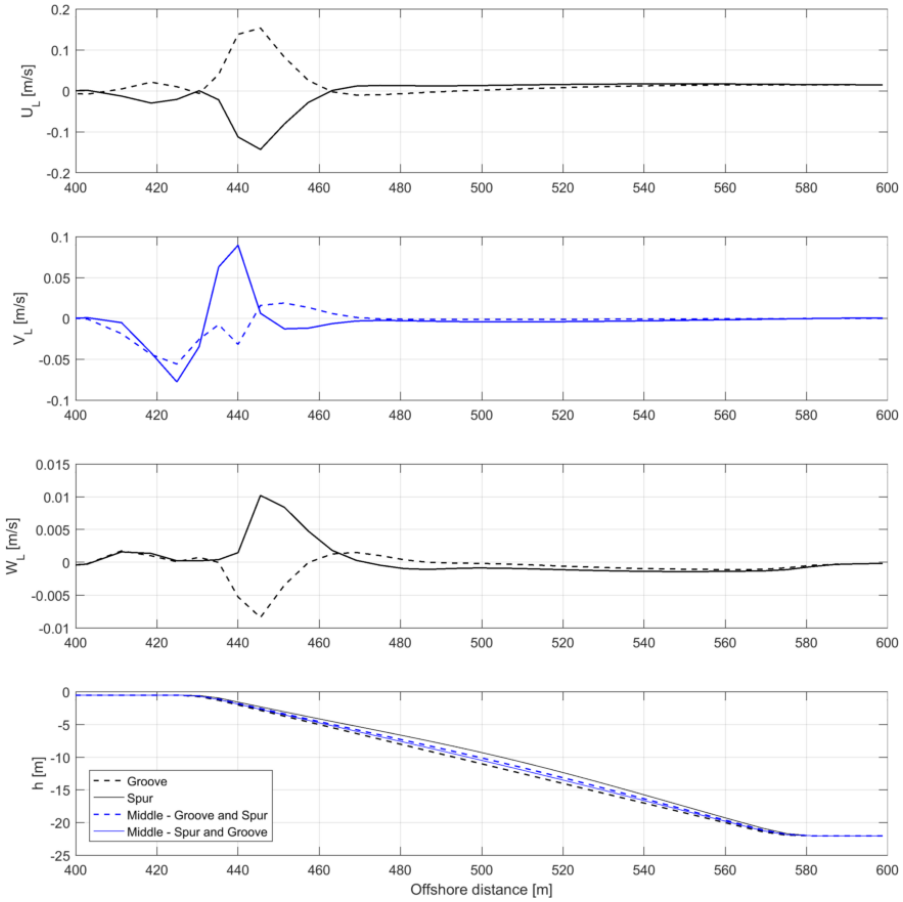

Figure 4.17: Model results for depth-averaged velocities U_L, V_L, W_L and cross-shore depth profile for schematic simulation of SFR12.

The calculated alongshore and vertical currents are lower than the observed values, possibly due to the absence of alongshore component of the wave component, as shown for the modelling of NFR13. In Chapter 5.2.2, the role of different slopes is discussed, and it is shown that alongshore currents tend to grow with steeper reef profiles. The reef slope for SFR12 experiment is relatively steep for SAG formations, as suggested by Duce et al. (2016).

OVERALL EVALUATION

As discussed in Chapters 1.2 and 3.2.2, this MSc thesis aims to describe the flow pattern found on SAG formations and how sensitive is the flow to varying conditions. Although the measurements in Palmyra Atoll are insightful on the wave hydrodynamics on SAG formations, they represent wave flow conditions found on specific geometries.

Similarities between model results and measurements were reported, such as similar order of magnitude for cross-shore Lagrangian currents and general agreement of the main depth-averaged momentum terms. Considering the fact that the model represented SAG geometries in a idealized way, with very limited data even for that schematic bathymetry, the overall result is considered to be adequate for the current research.

4.3.2. LINEAR WAVE THEORY PREDICTION

This MSc thesis applied D3D-FLOW + SWAN without taking refraction into account, meaning that diffraction overcomes refraction processes, as discussed in Chapter 4.2. This means that for shore-normal waves, which are commonly reported in the literature as dominant in SAG formations (2.2.3), wave forces can be predicted with (2.21) and (2.21), as explained in Chapter 3.1.2. Therefore, the wave forces calculated by D3D-FLOW + SWAN both in the cross-shore and alongshore directions could be verified, described below.

The verification of the wave forces was conducted for the Base Configuration from Rogers et al. (2013). The Base Configuration geometry from Rogers et al. (2013) was represented following the method described in Chapter 3.2.2, now with resolution of 1 m both in the cross-shore and in the alongshore, which represents a more refined resolution than the one used in this research (see Chapter 3.2.5). Two SAG formations were discretized, with total lengths of 100 m in the alongshore, and around 800 m in the cross-shore (Table 4.2).

The streamwise radiation stresses for shore-normal waves are provided by (2.17) and (2.18). The lateral radiation stresses become zero, due to the absence of alongshore wave component. As wave propagates along the cross-shore depth profile, the energy parameter n and shoaling wave heights can be predicted with (2.2), (2.7), (2.4), and (2.5). Wave heights were checked with regard to breaking limits, and results onshore of the breaking points were neglected for this analysis.

The gradients of radiation stresses (2.21) and (2.21) were calculated numerically in the mid grid points both in the cross-shore and alongshore, and then interpolated back to the grid points.

The alongshore views of the depth-averaged wave forces at a depth of 8 and 15 m as calculated by this method and by D3D-FLOW + SWAN for the Base Configuration from Rogers et al. (2013) are shown in Figures 4.18 and 4.19.

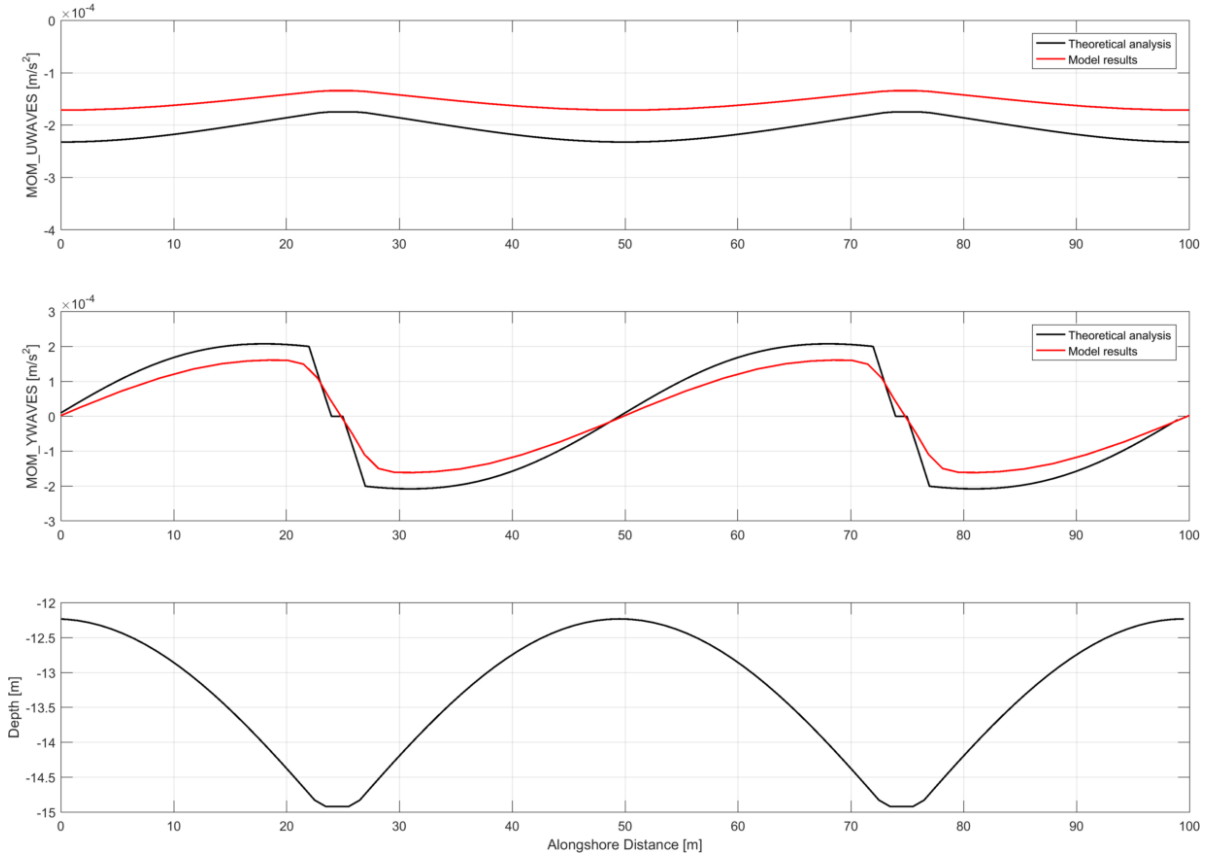

Figure 4.18: D3D-FLOW + SWAN and theoretical derivation results for wave forces MOM_UWAVES and MOM_VWAVES and alongshore depth profile at depths of around 15 m.

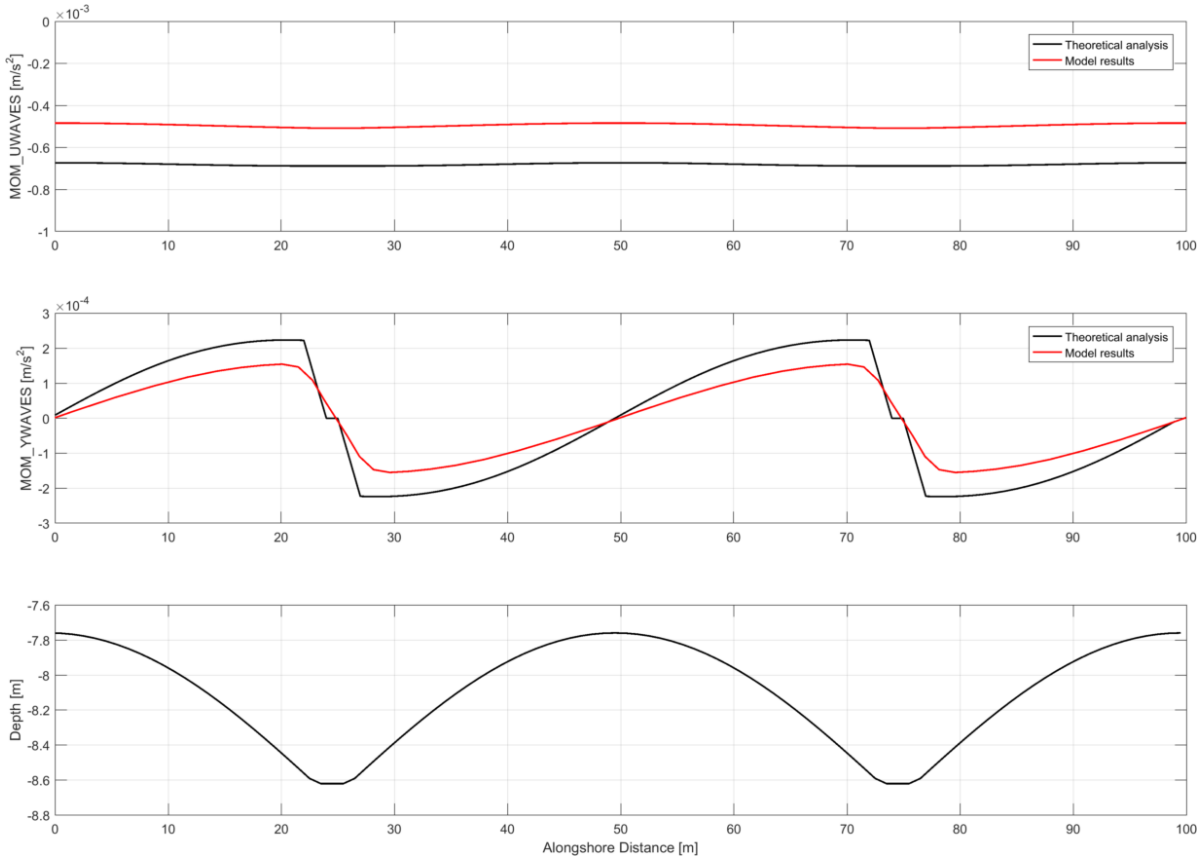

Figure 4.19: D3D-FLOW + SWAN and theoretical derivation results for wave forces MOM_UWAVES and MOM_VWAVES and alongshore depth profile at depths of around 10 m.

In the cross-shore, it can be seen that the general shape and order of magnitude of the wave force for both models is the same, with higher absolute values over the spur and lower over the groove for the depth of 15 m, and the reverse trend at the depth of 8 m. The cross-shore wave forces are essentially function of the changes in wave forces in x-direction, which are among others due to the cross-shore slope. As the slopes over spur and groove are different, the alongshore variation of Fx depends on the depth.

In the alongshore, both theoretical model and D3D-FLOW + SWAN produce similar results for depths of 15 and 8 m, both in shape and in order of magnitudes. The alongshore variation of Fy shows that maximum absolute values occur at the transition between spur and groove and zero values are noticed over the top of spur and over the groove. The alongshore wave forces are function of the alongshore slope, whose general shape is unchangeable with the current schematic representation. Therefore, the expected shape of alongshore wave forces is the same all over the SAG zone, although the values can change according to the spur and wave heights. The maximum Fy are found on locations where the alonghore gradient of depth is maximum, precisely at the transition between spur and groove.

The cross-shore view of the depth-averaged wave forces close to the top of the spur calculated by the theoretical analysis and D3D-FLOW + SWAN is presented in Figure 4.20. The overall shape and values of both alongshore and cross-shore directions is similar for both methods. Regarding the alongshore wave forces, very low values were calculated, consistent with very low alongshore gradients of depth. The cross-shore wave forces shows a decrease in the wave force as approaching shallow waters, which was expected in the shoaling zone.

As it is further described in Chapter 5.3, wave forces are primarily balanced by pressure gradients both in the cross-shore and in the alongshore gradient. The mismatch between those is mostly balanced by viscous forces and friction in case of shore-normal shoaling waves. The resulting flow pattern is characterized by two circulation cells over spur and grooves, as it is elaborated further in Chapter 5.5.

The current MSc thesis assumes wave forces as the main driving mechanisms for flow circulation. The verification with theoretical analysis shows that D3D-FLOW + SWAN does a reasonable job representing them in SAG formations, matching the expected theoretical behavior.

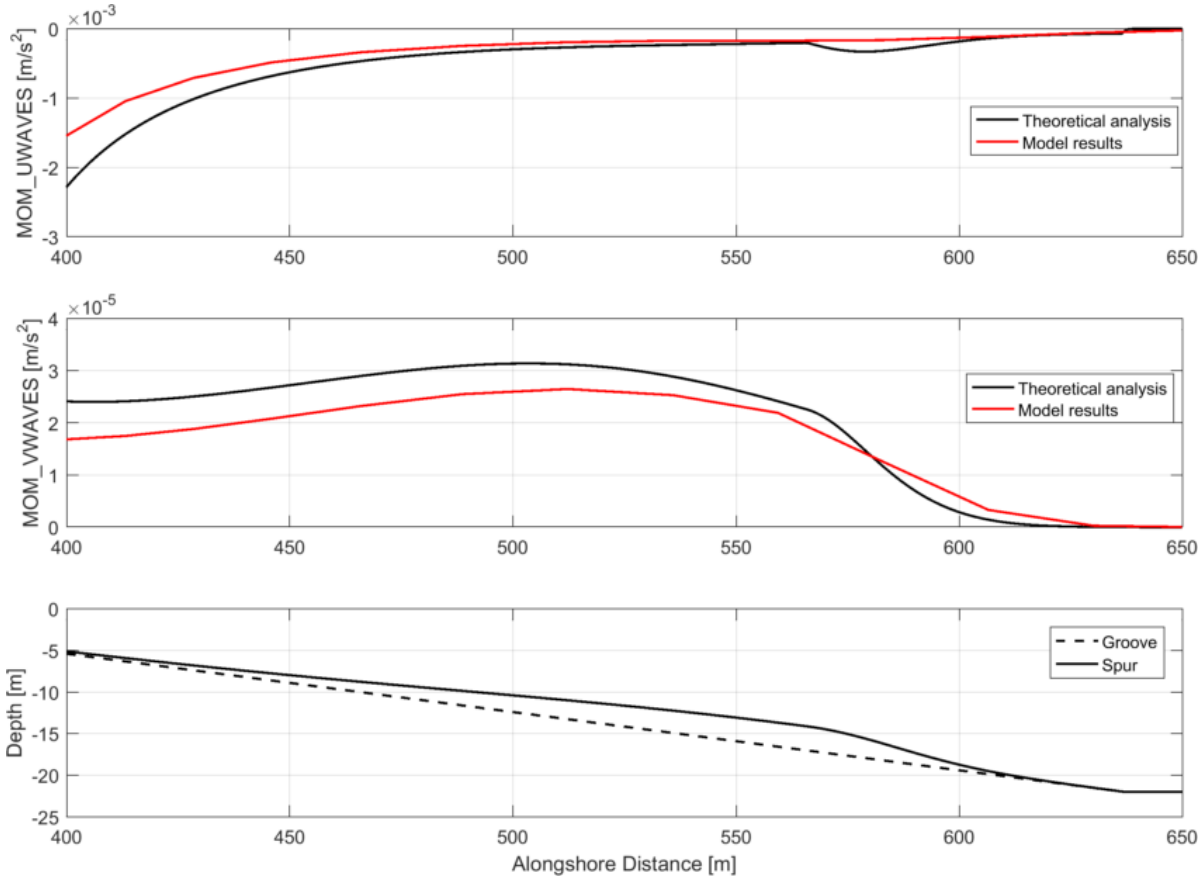

Figure 4.20: D3D-FLOW + SWAN and theoretical derivation results for wave forces MOM_UWAVES and MOM_VWAVES close to the top of spur and cross-shore depth profile.

4.4. OPTIMIZATION

This MSc thesis used numerical modelling for the investigation of wave hydrodynamics over SAG formations. In order to accomplish with a large variety of scenarios reproducing the wide range of SAG formations and sea states, the model setup was optimized to reduce the computational time keeping accuracy.

This optimization was performed using the Base Configuration from Rogers et al. (2013) through variations of the parameters shown below,:

- Number of SAG structures (see Figure 3.5);
- Time step;
- Time length of the simulation;
- Sponge layers (see Figure 3.4); and
- Number of alongshore grids in groove (see Figure 3.5); and

The brief description of how each parameter was defined is provided below.

It is important to mention that in the calibration section (Chapter 4.2) the results presented used the already optimized model setup (Table 4.7).

4.4.1. NUMBER OF SAG STRUCTURES

The initial simulations with schematic bathymetry reproducing the SAG formations showed significant border effects within the transition zone between alongshore uniform bathymetry and the introduction of SAG structures (Figure 3.4 and 3.5). Initially, 20 SAG structures were used to ensure that central SAG structure, that is the one effectively used for all the analyses, have accurate results.

The optimum number of SAG structures was found through stepwise decrease of the initial number of 20 SAG structures, and with analysis of the model results for the calibration case. 14 SAG structures was concluded to be the optimum number for the Research Simulations part.

4.4.2. TIME STEP

Sensitivity analyses with increasing time steps were performed to obtain the optimum time step that still ensures accurate results. This was done through stepwise increase of the initial time step of 0.01 min. This initial time step was estimated with Courant number calculations up to a maximum of around 10 (Deltares, 2016).

The time step of 0.01 min (0.6 s) was concluded to be adequate for the Research Simulations part.

4.4.3. TIME LENGTH OF SIMULATION (SPIN-UP PERIOD)

Although D3D-FLOW + SWAN results were generated throughout the time length of the simulation, the results effectively used for the analyses were considered only at the last time step calculated by the model.

The required simulation time length was optimized through an evaluation of the spin-up period of the simulations, i.e., a comparative analysis of the results with lower spin-up periods was carried out for the calibration case. The spin-up period of 3 h was concluded to be sufficiently good for the Research Simulations part. For the runs with wind activated, the spin-up was studied and still concluded to be adequate.

4.4.4. SPONGE LAYERS

The dimensions of the sponge layers both in the alongshore and cross-shore directions (Figure 3.4) were optimized through sensitivity analysis, aiming to reduce computational time. In the alongshore, this analysis considered mainly SWAN border effects, since D3D-FLOW was showed to be affected even further inside the grid, within the first SAG formations. The cross-shore sponge layer is basically the offshore flat zone with depth of 22 m before the fore reef. Alongshore and cross-shore sponge layers with 800 and 500 m m were concluded to prevent SWAN border effects.

4.4.5. NUMBER OF ALONGSHORE GRIDS IN GROOVE

The construction of the alongshore model grid was performed with a script whose fundamental variable is the number of grids to be considered in the alongshore axis of a groove, as explained in Chapter 3.2.5. The numbers of alongshore grids in the spur, in the sponge layers and in the transition zones are defined as function of the number of grids in the groove and considering the smoothness recommendations for D3D-FLOW (up to 20% variation in spacing according to Deltares (2016)).

Several number of grids on the groove were tested and comparative analysis was done. 4 grid lines - or 3 grids - were considered to perform well and were retained for the Research Simulations part.

4.4.6. OVERALL OPTIMIZATION PARAMETERS

Table 4.7 summarizes the optimum model setup parameters for the model runs:

Table 4.7: Optimized model setup parameters

Number of SAG structures	**Time step**	**Time length of simulation**	**Alongshore sponge layer**	**Cross-shore sponge layer**	**Number of alongshore grids in groove**
-	s	h	m	m	-
14	0.6	3	800	500	3

5

RESULTS

This chapter presents the modelling results achieved by this MSc Thesis. The conventions for the results were explained in Chapter 4.1.

As covered in Chapter 3.2.4, initially a Base Case simulation was performed, followed by variations of that input parameters to investigate the influence of short wave parameters, SAG geometry and alongshore forcing, as well as the importance of long waves. The most important parameters influencing the flow were retained for the permutation runs, where those parameters were varied together.

Chapter 5.1 covers the Base Case results, providing a thorough analysis of the 3D hydrodynamics on top of spurs and grooves. This includes the wave propagation, 3D and 2DH flow, surface and bottom flow, and the mechanisms by which momentum is balanced as a result of wave forcing.

In Chapter 5.2, the influence of the varying parameters is provided. The analysis of the 3D velocity profile on top of spur and grooves for changing conditions is shown, including variations of short wave parameters, SAG geometry and alongshore forcing, and the influence of long waves.

The mechanisms associated with the changes in 3D velocity profile are covered in Chapter 5.3, through analysis of the momentum balance terms for each varying parameter.

Next, indicators for the flow are proposed related both to flow pattern and to potential implications of the hydrodynamics on the coral growth aspects, including a quantification of how flow is sensitive to changing input conditions (Chapter 5.4).

Chapter 5.5 presents the overall flow patterns found for all the simulations performed - sensitivity and permutation -, with a description of the 3D velocity profile shapes found. The flow pattern expected to occur as a function of waves and SAG geometry is further discussed.

5.1. BASE CASE RESULTS

The Base Case model results were used to acquire insight in the wave and flow processes happening over SAG formations and in the resulting flow pattern. As it is further discussed in Chapter 5.5, the Base Case results are representative for the majority of simulated wave conditions on top of SAG formations. Although they show in general low Lagrangian velocities, the flow pattern has similarities with most of the other cases. Accordingly, the Base Case flow conditions were further adopted as reference for comparisons of observed flows in different conditions (Chapters 5.2 and 5.4).

The Base Case model setup parameters (Table 3.4) correspond to a typical SAG formation found in southern Moloka'i (Storlazzi et al., 2003; Rogers et al., 2013).

Initially, the results of the wave propagation are presented in Chapter 5.1.1, as waves are driving the flow conditions. The 3D Lagrangian velocity profiles, including cross-shore, alongshore and vertical currents, are provided in Chapter 5.1.2. The depth-averaged flow results, with cross-shore, alongshore and vertical Lagrangian currents, are further presented in Chapter 5.1.3. The flow conditions in the water surface and in the bottom, where corals live, are provided in Chapter 5.1.4, including bottom shear stress results. In Chapter 5.1.5, the cross-shore and alongshore momentum terms are presented so as to explain the flow conditions observed in the Base Case.

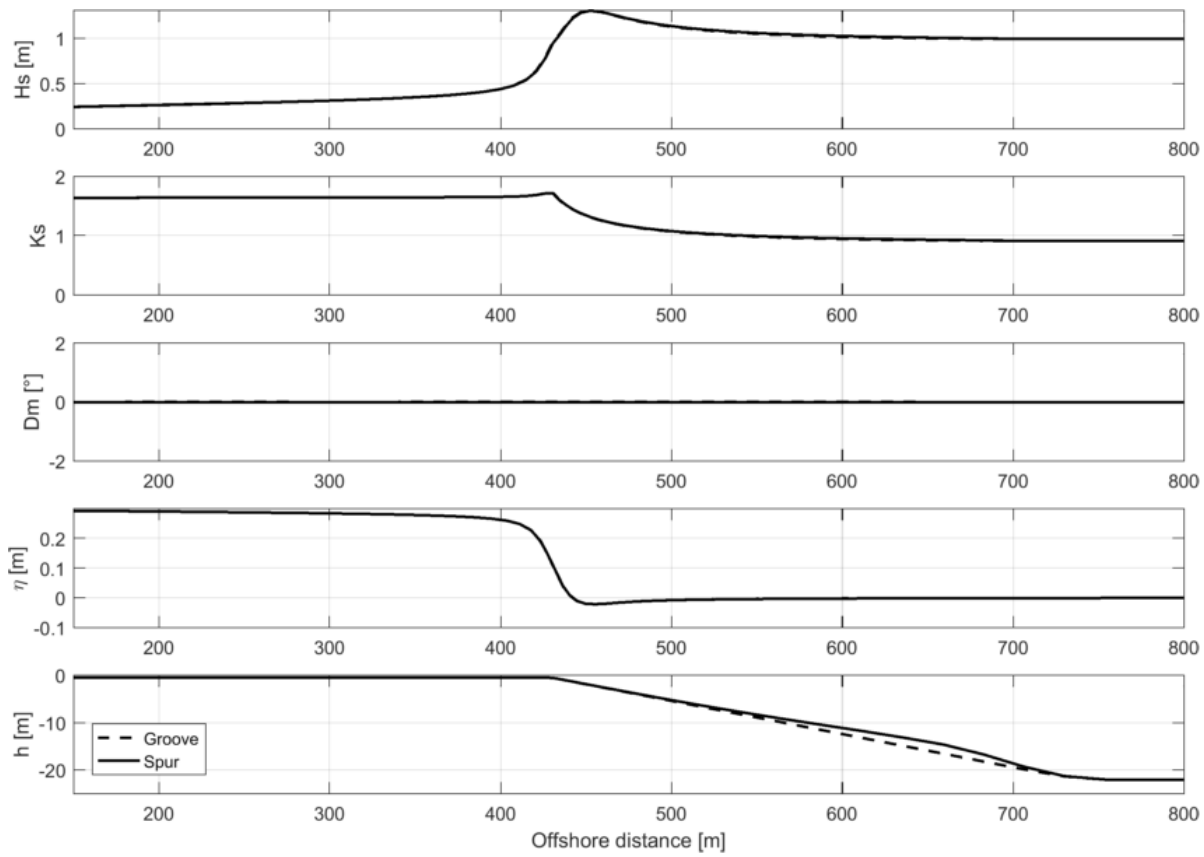

Figure 5.1: Cross-shore view of Base Case results for significant wave height Hs, shoaling coefficient Ks, mean wave angle D_m, setup η, and cross-shore depth profile over spur and groove.

5.1.1. WAVE PROPAGATION

The Base Case results for the wave propagation are shown in Figure 5.1. Waves approaching the SAG zone firstly gradually shoal, then start shoaling fastly (x ≈ 500 m), up to the point where they start breaking (x ≈ 450 m), where they rapidly decrease over the reef crest, and then gradually reduce over the reef flat. The shoaling coefficient, that was estimated with (2.7), shows that waves at a depth of 22 m (offshore limit) are increasing, thus they already passed the point where shoaling coefficient is minimum, as discussed in Chapter 2.4. The shoaling coefficient over the spur and groove is roughly similar, even with depth difference of up to 2 m (maximum spur height). The wave heights both over the spur and groove are similar, consistent with the findings from Chapter 4.2. Likewise, the mean wave directions over spur and groove are always equal to zero, corresponding to shore-normal waves that do not change the mean direction, representing waves for which diffraction overcome refraction effects.

For the part of the cross-shore profile where waves are shoaling (from x ≈ 800 m to x ≈ 450 m), the water level decrease relatively to the mean water level of 0 m. This set-down keeps pace with the shoaling coefficient, i.e., the set-down starts decreasing more when shoaling coefficients are growing faster up to the breaking zone, where it reaches its minimum value with O (1 cm). From that point further onshore, the set-up - increase of water level - is observed. The set-up grows faster where the wave breaking is faster, and then it increases more gradually, reaching a value of about 30 cm.

5.1.2. 3D VELOCITY PROFILE

The cross-shore view of the 3D Lagrangian velocities is presented in Figure 5.2, where four cross-sections are shown, corresponding to the groove, middle between groove and spur, spur, and middle between spur and groove (same locations as black and blue vertical lines in Figure 3.2). The arrows indicate the cross-shore and vertical current magnitude and direction, while the colours represent the strength of the alongshore currents.

This figure shows that all currents have relatively low magnitudes O (1 cm/s). The cross-shore currents

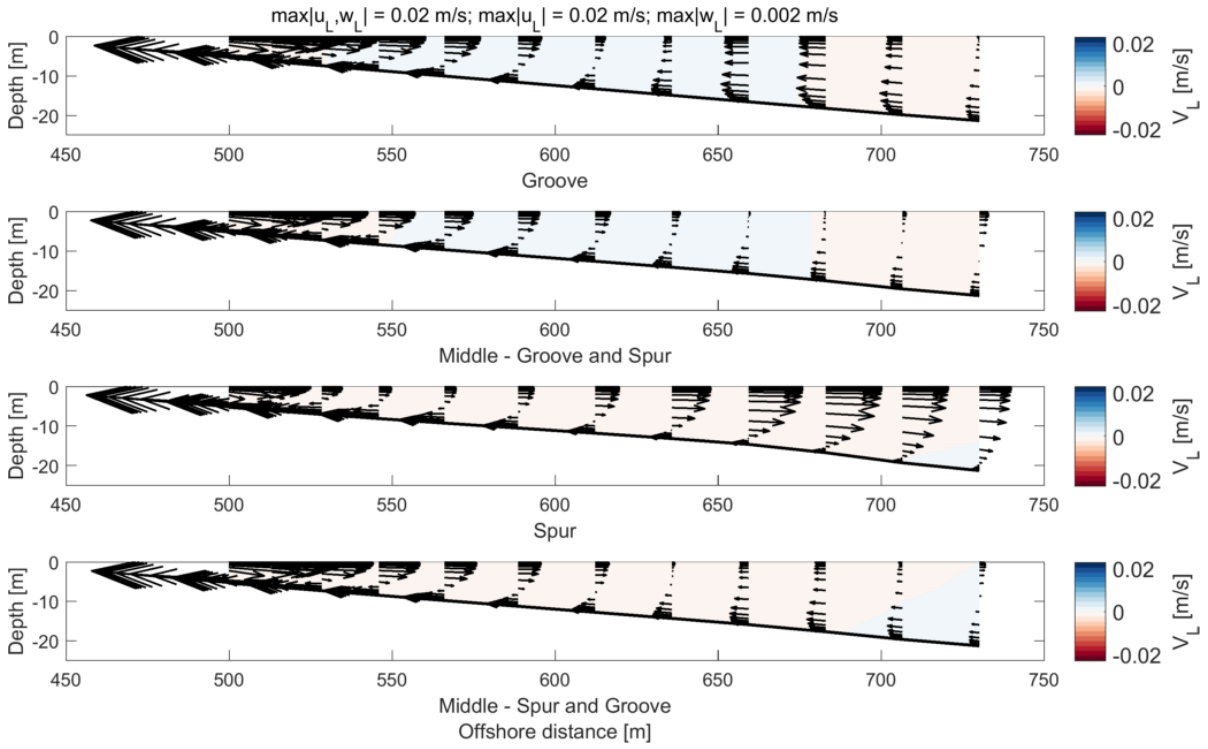

Figure 5.2: Cross-shore views of Base Case results for velocities u_L, v_L, w_L on top of groove, middle between groove and spur, spur, and middle between spur and groove. Blue and red colours indicate eastwards and westwards flows, respectively.

are dominant relatively to the alongshore and vertical velocities, and those last have the lowest values O (1 mm/s).

The groove plot shows that, in the offshore zone, currents are onshore, with maximum values a few metres above the bed. Those onshore currents firstly grow, peak at x ≈ 670 m, and at x ≈ 610 m the surface currents reverse sign, becoming offshore directed. From that point further onshore, both the onshore surface currents and the bottom offshore currents grow in absolute values as approaching shallower waters, although waves are still not breaking for x ≈ 500 m (see Figure 5.1).

As for the spur, in the offshore zone currents are offshore, with peak values at the water surface, decreasing further downwards, and reversing sign only in the lowest layers. These offshore currents grow and peak at x ≈ 670 m, coinciding with the point where onshore groove currents peak. After peaking, offshore currents start decreasing, and around x ≈ 610 m, the onshore bottom currents start growing and more layers in the water column become onshore directed. Those onshore currents located in the lowest layers continue increasing further onshore, while the offshore currents upper in the water column grows slowlier.

Middle cross-sections between spur and grooves resemble more the groove profile, as for those the currents in the offshore zone are onshore. All four cross-shore profiles have similarities, such as the presence of onshore bottom currents everywhere, and velocity profiles with offshore surface currents and onshore bottom velocities for x < 600 m. As it is shown in Chapter 5.1.3, this cross-shore location (x ≈ 600 m) is the approximate position where the depth-averaged flow over grooves become offshore, while the depth-averaged spur currents turn into onshore.

These persistent onshore current currents at the bed do not come from wave streaming, as the wave forces at the bottom do not show so (see Chapter 5.1.5) and as the wave boundary layer thickness is lower than the model vertical resolution (see Chapter 3.2.5). The velocity profile with onshore surface currents and offshore bottom velocities is found approaching the surf zone. As for the groove, the offshore surface currents are higher than the onshore bottom velocities, resulting in offshore depth-averaged flow. As for the spur, the onshore bottom currents are higher than the offshore surface currents, giving a depth-averaged flow in the onshore direction.

Sensitivity runs conducted to obtain insight in the importance of SAG formations as drivers of circulation also found this type of velocity profile, as briefly described below.

The first sensitivity run used alongshore uniform bathymetry with reef profiles without spurs, i.e., with

a cross-shore depth profile equivalent to the groove. The resulting velocity profiles showed an equivalent shape - onshore surface currents and offshore bottom velocities - of velocity profile for the whole shoaling part of the cross-shore profile, while with SAG formations this profile is found only for x < 60 m. For this first sensitivity run, results show nearly a depth-integrated compensation of Stokes Drift, different than with SAG formations, as shown later in Chapter 5.1.3, since the depth-averaged Lagrangian velocities for the alongshore uniform case have *O* (0.01 mm/s), much lower than the *O* (1 mm/s) found for the Base Case (Figure 5.10). The second sensitivity run with alongshore uniform bathymetry with spurs instead of grooves provided the very same results.

A third sensitivity run with alongshore uniform similar to groove profiles, but also with friction difference between groove and spur similar to the Base Case (Figure 3.7), was further carried out. The 3D velocity profie showed the same trend, with offshore surface velocities and onshore bottom currents. For this case, the depth-integrated compensation of stokes drift was also observed in the offshore zone, but with growing vertical imbalance (or depth-averaged Lagrangian current) as moving onshore, although still very small - *O* (0.1 mm/s).

The cross-shore profile of Eulerian and Stokes Drift velocities over spur and groove are shown in Figures 5.3 and 5.4. In these plots, the dashed lines indicate the locations of the alongshore sections, while the red lines represent the vertical profile of the cross-shore velocities relatively to each of the dashed lines. The Eulerian currents are nearly always offshore, except for the lowest layers over the groove in the offshore zone. The higher Eulerian velocities are found in the water surface, and further downwards they decrease up to zero at the bottom, consistent with the no-slip condition assumed as boundary condition (Deltares, 2016). As for the spur, those currents have a general increasing trend as moving onshore. As for the groove, the surface Eulerian currents start decreasing, and then at x ≈ 610 m the velocity profile becomes fully offshore, approximately at the same location where Lagrangian currents turn into offshore.

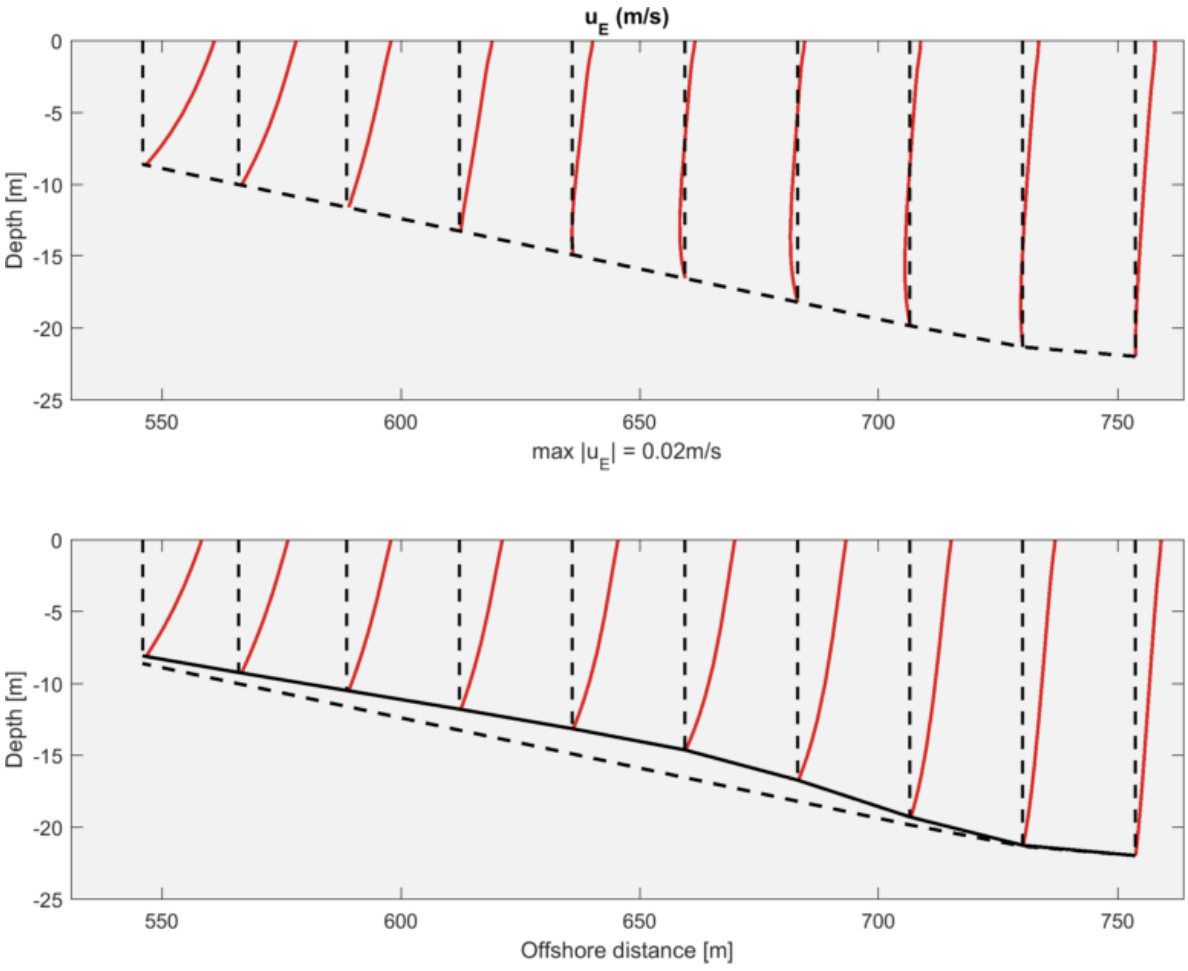

Figure 5.3: Cross-shore views of Base Case results for Eulerian u_E on top of groove and spur.

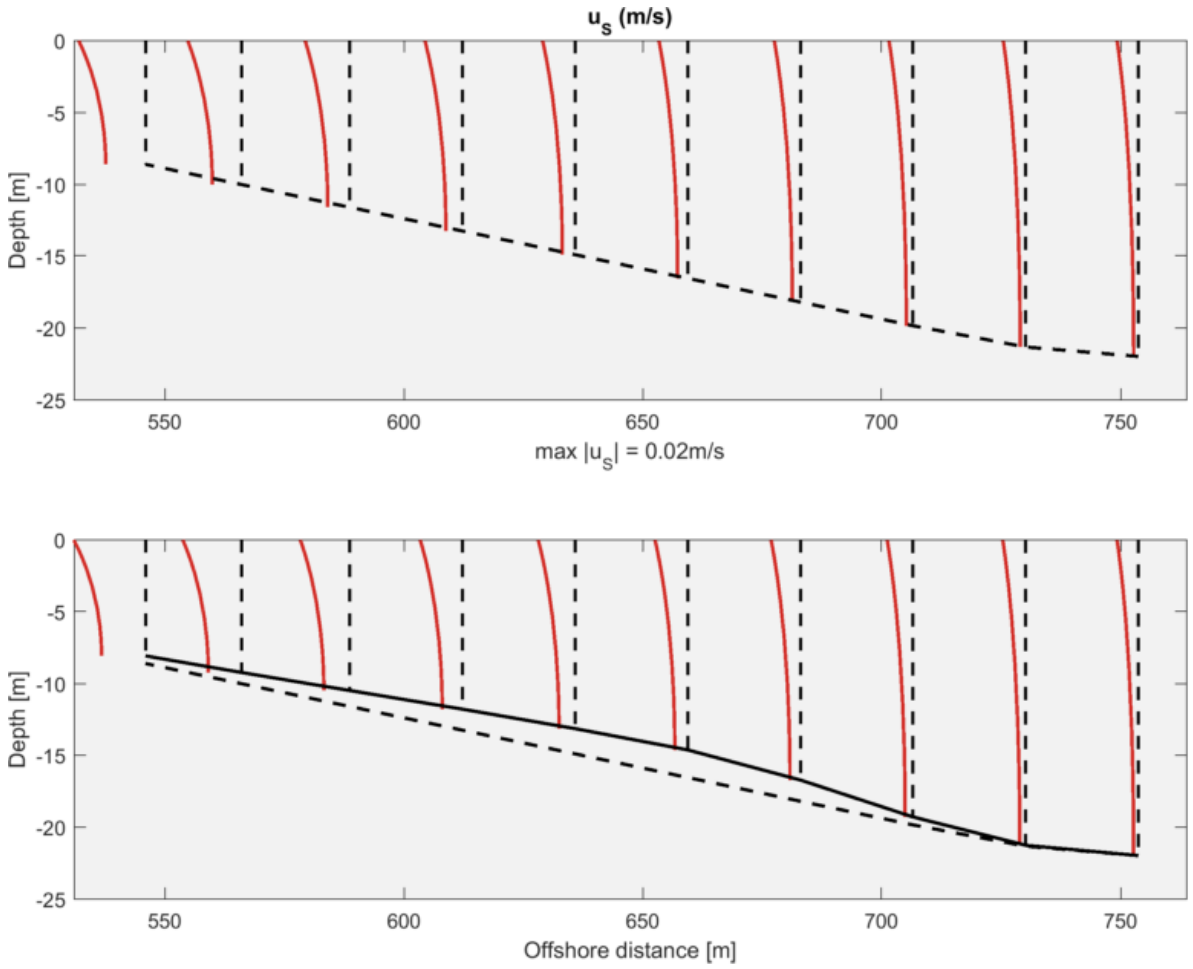

Figure 5.4: Cross-shore views of Base Case results for Stokes Drift velocities u_S on top of groove and spur.

The Stokes drift velocities have an overall shape that is similar for both spur and groove, consistent with (2.27). All currents are onshore, with lower values close to bottom and higher values close to the surface. The Stokes Drift velocities over the spur are higher than over the groove, as a result of higher shoaling waves over spurs. In general, Stokes Drift velocity values scale with the Eulerian velocities, thus Lagrangian velocities tend be very small as a result of the imbalance between those.

The alongshore views of the 3D Lagrangian velocities for depths of 20, 15, 10 and 5 m are shown in Figures 5.5, 5.6, 5.7 and 5.8, respectively. In those plots, the arrows represent the alongshore and vertical velocities, while colors give the cross-shore flow. Those plots show again that alongshore and vertical velocities are lower than the cross-shore currents. As for the depth of 20 m, water flows towards the groove, while for a depth of 15 m the convergence becomes towards the spur. As for the depth of 10 m, the vertical flow becomes as important as the alongshore, and at a depth of 5 m it becomes even more important.

The alongshore currents over the groove look approximately zero and with reduced values over the spur comparatively to the rest of the alongshore section. This is consistent with lower alongshore wave forcing as a result of low alongshore depth gradient, as explained in Chapter 4.3.

The cross-shore velocities shown in these plots provide the same trend as explained for Figure 5.2, with onshore groove currents in the whole water column for depths of 20 and 15 m, that then become offshore in the majority of the water colum for depths of 10 and 5 m. As for the spur, the offshore currents that are higher at the water surface and reverse at the bottom appear in depths of 20 and 15 m, while the velocity profile with stronger onshore currents near the bottom together with weaker offshore surface velocities is evident for depths of 10 and 5 m.

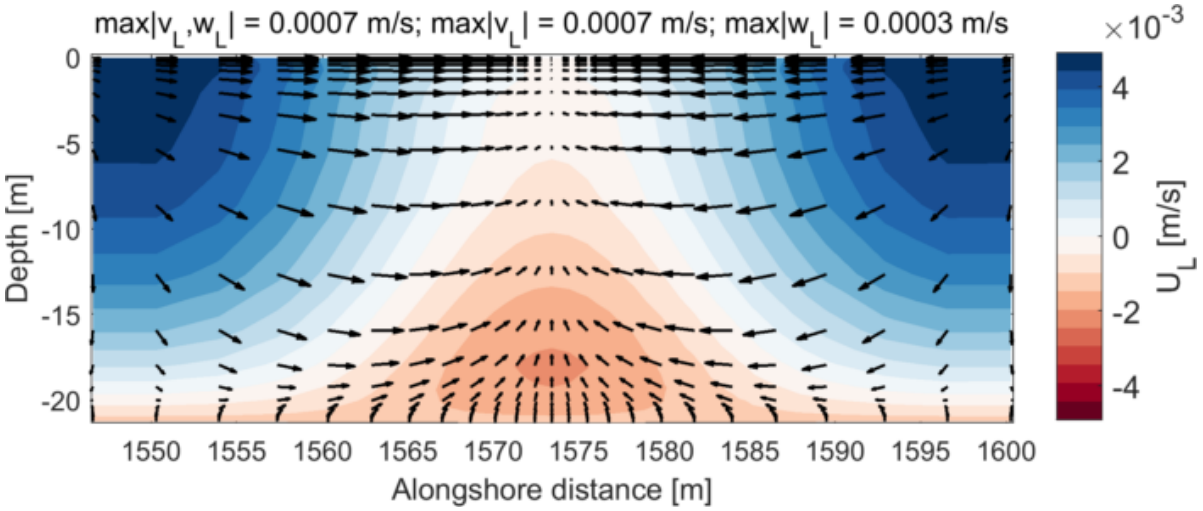

Figure 5.5: Alongshore view of Base Case results for velocities u_L, v_L, w_L at depths of around 20 m. Blue and red colours indicate offshore and onshore flows, respectively.

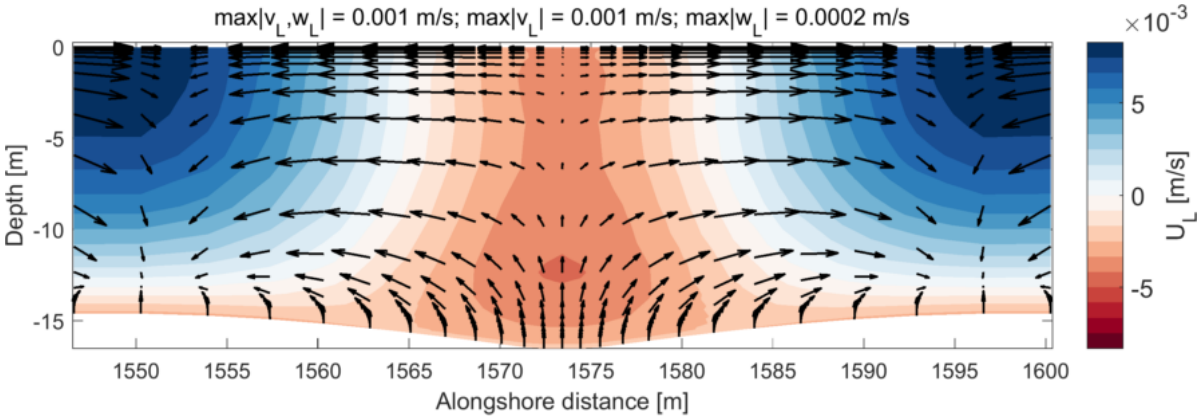

Figure 5.6: Alongshore view of Base Case results for velocities u_L, v_L, w_L at depths of around 15 m. Blue and red colours indicate offshore and onshore flows, respectively.

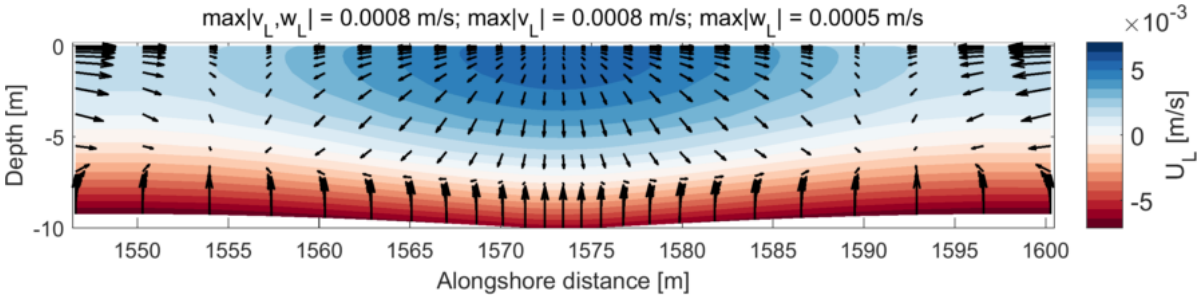

Figure 5.7: Alongshore view of Base Case results for velocities u_L, v_L, w_L at depths of around 10 m. Blue and red colours indicate offshore and onshore flows, respectively.

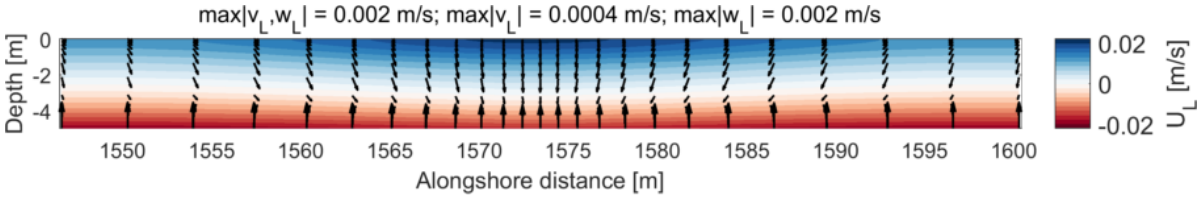

Figure 5.8: Alongshore view of Base Case results for velocities u_L, v_L, w_L at depths of around 5 m. Blue and red colours indicate offshore and onshore flows, respectively.

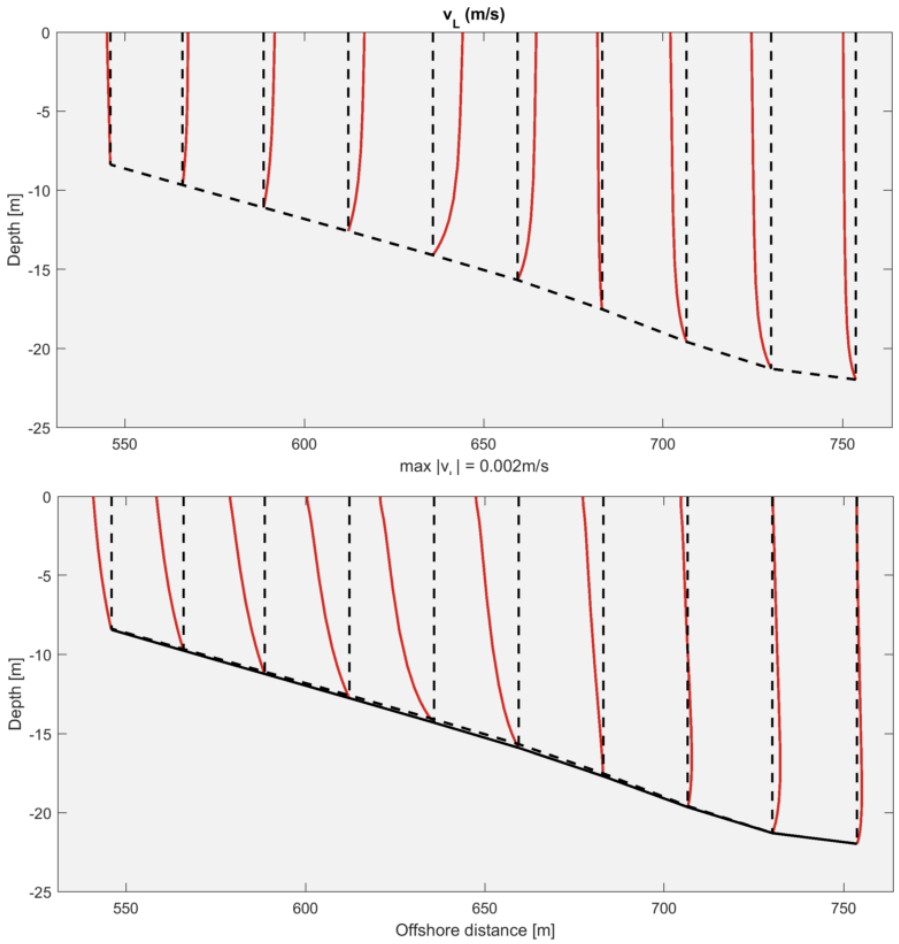

Figure 5.9: Cross-shore views of Base Case results for Lagrangian velocities v_L on cross-sections in the mid points between groove and spur (top), and spur and groove (bottom).

The cross-shore view of alongshore Lagrangian velocities for cross-shore sections between spur and groove is presented in Figure 5.9. The dashed lines give the locations of the alongshore sections, while the red lines provide the vertical profile of alongshore velocities relatively to each of the dashed lines. The red lines on the RHS of the dashed lines represent the eastwards currents, with westwards currents being on the left. The cross-shore sections on top of middle points between spur and groove were preferred due to the higher alongshore velocities observed.

This plot shows that the alongshore currents have in general a nearly logarithmic profile, and that the middle section between groove and spur (top plot) has alongshore velocities with opposite sign than the middle section between spur and groove (bottom plot). Maximum alongshore currents appear to happen at x around 600 m, close to the aforementioned reversing point of cross-shore currents.

5.1.3. DEPTH-AVERAGED FLOW

The map of cross-shore and alongshore depth-averaged Lagrangian currents is shown in Figure 5.10. This plot is very similar to the results shown in the calibration section (4.7) for the Base Configuration from Rogers et al. (2013). Depth-averaged velocities show the predominance of cross-shore currents compared to the alongshore, although they have O (1 mm/s). Cross-shore currents show two circulation cells, with onshore flow over the groove and offshore flow over the spur for the offshore zone (x > 600 m) and the reversing pattern further onshore. Lagrangian currents are in general higher in the offshore zone and for a given alongshore cross-section, the maximum currents are always found either over the spur or groove.

The cross-shore profile of the cross-shore, alongshore and vertical depth-averaged Lagrangian currents U_L, V_L, and W_L is shown in Figure 5.12. The top plot with U_L over spur and groove shows clearly the aforementioned circulation cells, as detailed below:

- Spur: cross-shore currents grows and peak at x ≈ 680 m, then decrease back and reverse sign at x ≈ 600

m. Subsequently they decrease, and stabilize at x ≈ 560 m, then start decreasing fast from x ≈ 500 m, where wave shoaling is also faster (Figure 5.1), up to a minimum value at the breaking point (x ≈ 440 m); and

- Groove: cross-shore currents decrease up to a minimum at x ≈ 680 m, then increase back and reverse sign at x ≈ 600 m, and subsequently increase and stabilize at x ≈ 560 m, then start increasing fast from x ≈ 500 m up to a maximum value in the breaking point (x ≈ 440 m).

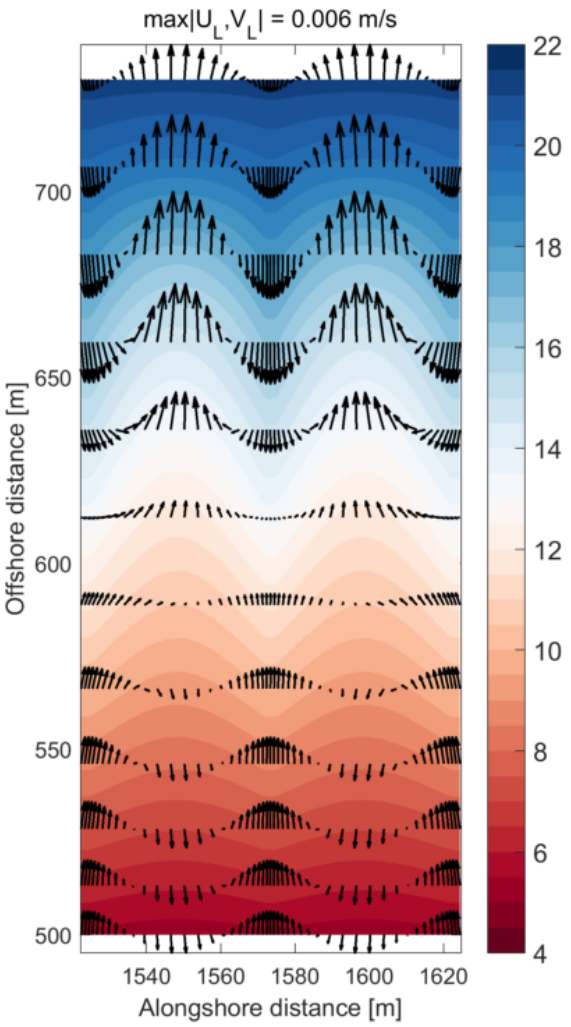

Figure 5.10: Map view of Base Case results for depth-averaged Lagrangian velocities U_L and V_L.

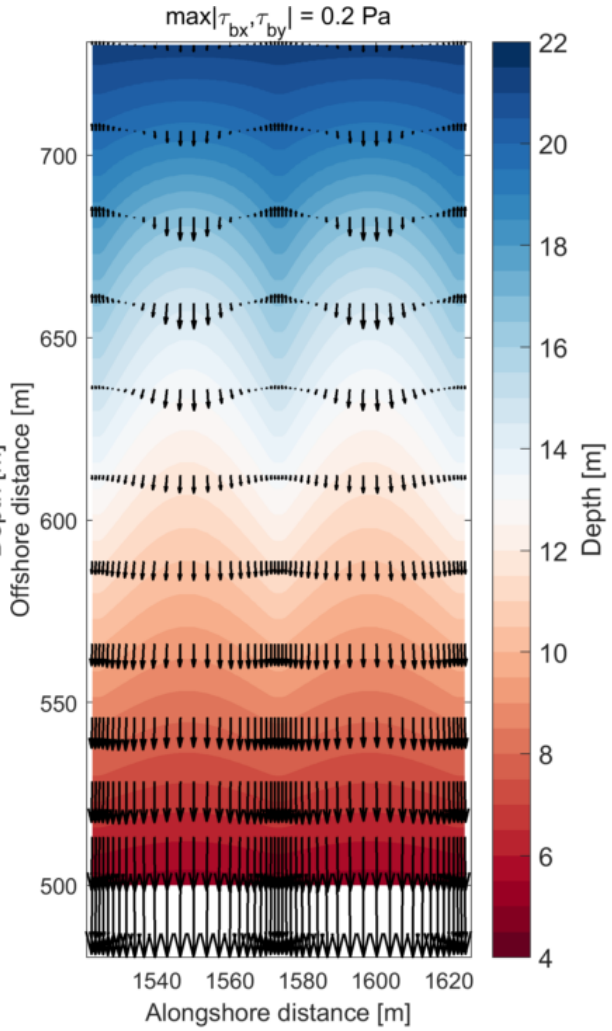

Figure 5.11: Map view of Base Case results for the cross-shroe and alongshore bottom shear stresses τ_{bx} and τ_{by}.

The depth-averaged cross-shore currents show a remarkable pattern of two circulation cells, one in the offshore zone with offshore spur and onshore groove flows, and the other in the onshore zone with reversed behaviour. These circulation cells are referred to as SAG circulation cells, as covered in Chapter 2.3. As it is further discussed in Chapter 5.5, this pattern is commonly found for shoaling shore-normal waves with SAG wavelengths sufficiently long ($\lambda_{SAG} \geq 50$ m).

The alongshore depth-averaged currents V_L over the mid cross-shore profiles between spur and groove (Figure 5.12) show that from offshore up to x ≈ 700 m the currents converge towards the groove, as they have opposite velocity signs. From x ≈ 700 m to 540 m, the convergence becomes towards the spur. Those trends were also shown in Figures 5.5 and 5.6. This convergence trend also appears in the breaking zone, with convergence to the groove, whose currents are offshore, resembling rip currents, although with much lower velocity magnitudes. This type of alongshore profile was also observed for most of the simulations, but it was not further explored due to the relatively lower velocities compared to the cross-shore currents. The importance of the alongshore currents compared to cross-shore velocities is further discussed in Chapter 5.4.

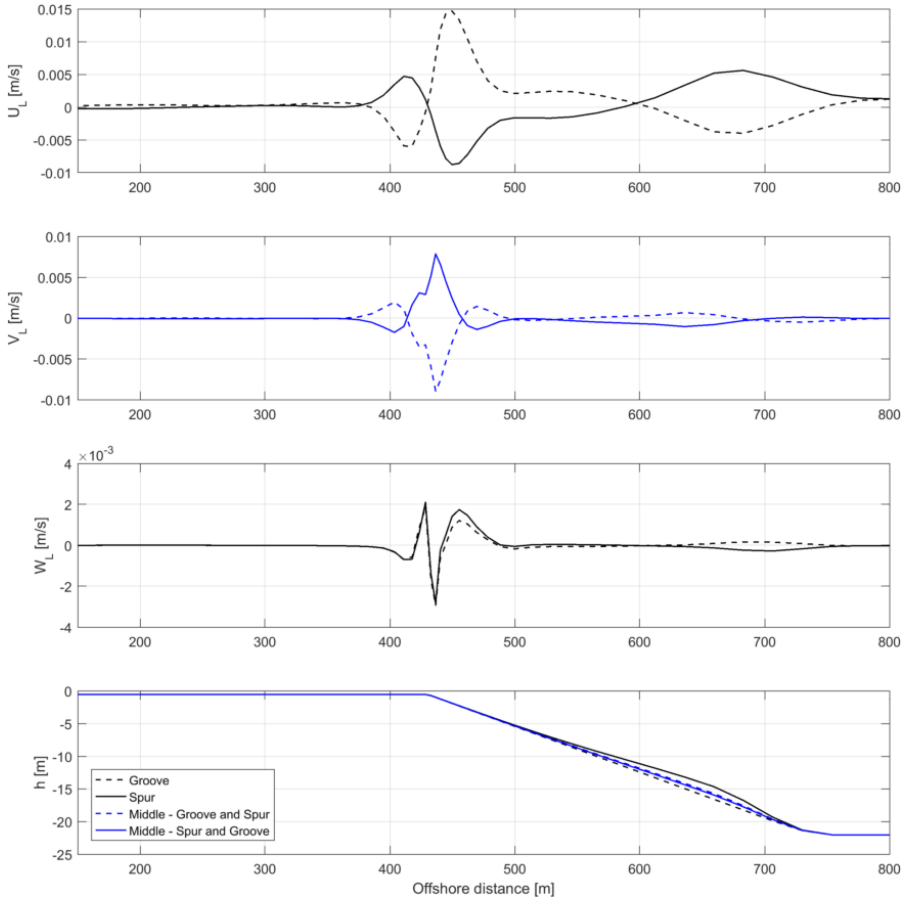

Figure 5.12: Cross-shore view of Base Case results for depth-averaged Lagrangian velocities U_L, V_L and W_L over spur and groove.

The vertical depth-averaged current W_L on top of spur and groove shows very low values for the whole cross-shore profile. From the offshore border up to x ≈ 600 m, vertical currents are upwards over the groove and downards over the spur (Figure 5.5), consistent with alongshore currents converging to the groove due to continuity. The cross-shore profile of depth-averaged vertical currents was also not further explored due to their relatively much lower values found for all simulated cases.

5.1.4. SURFACE AND BOTTOM FLOW

As this MSc thesis deals with hydrodynamics in coral reef environments, bottom currents and shear stresses are important indicators to evaluate the implications of hydrodynamics to coral growth aspects. On the other hands, surface currents might become important in case of surface flows, such as river plumes.

The map of cross-shore and alongshore Lagrangian velocities integrated over the top 0.5 m in the water column ($U_{L0.5m-surface}$ and $V_{L0.5m-surface}$) is presented in Figure 5.13. This figure shows that all surface currents are directed offshore, except for the groove offshore zone, also shown in Figure 5.2. Groove cross-shore surface currents start decreasing, peaking at x ≈ 680 m, then decrease up to reversing at x ≈ 600 m, and then keep increasing as approaching the surfzone. Spur cross-shore surface currents start increasing, peaking at x ≈ 680 m, then decrease without reversing and then increase slowly again as approaching the surfzone. As for the groove, the surface currents follow the same qualitative behaviour as the cross-shore depth-averaged currents. As for the spur, the surface flow is always offshore, thus different than the oscillating depth-averaged velocities.

As for the Eulerian and Stokes Drift surface currents ($U_{E0.5m-surface}$ and $U_{S0.5m-surface}$), Figure 5.15 shows that the point where Lagrangian surface currents are onshore over the groove (x > 600 m) coincides with very low values of Eulerian surface velocities. Stokes Drift surface velocities are slightly higher for the spur, with a general decrease up to the breaking point, where they increase, following the aforementioned trend for wave height. Eulerian surface currents are always offshore for both spur and groove.

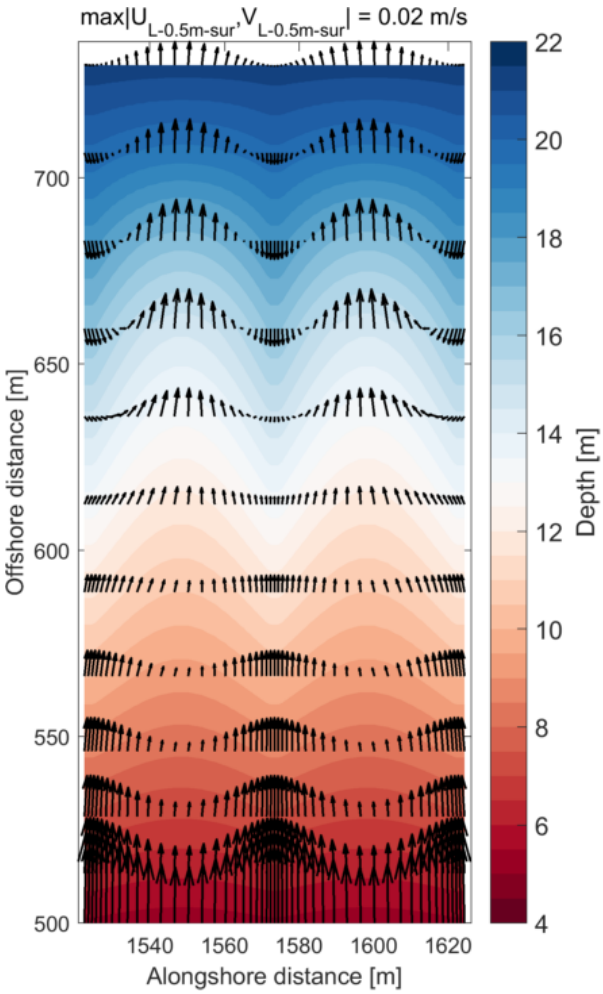

Figure 5.13: Map view of Base Case results for surface Lagrangian velocities $U_{L-0.5m-sur}$ and $V_{L-0.5m-sur}$.

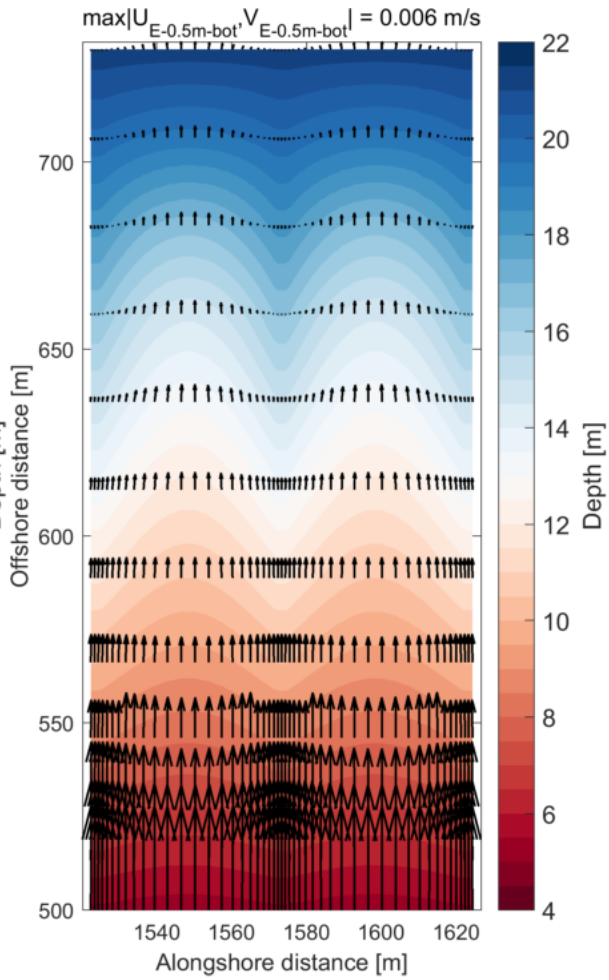

Figure 5.14: Map view of Base Case results for bottom Eulerian velocities $U_{E-0.5m-bot}$ and $V_{EL-0.5m-bot}$.

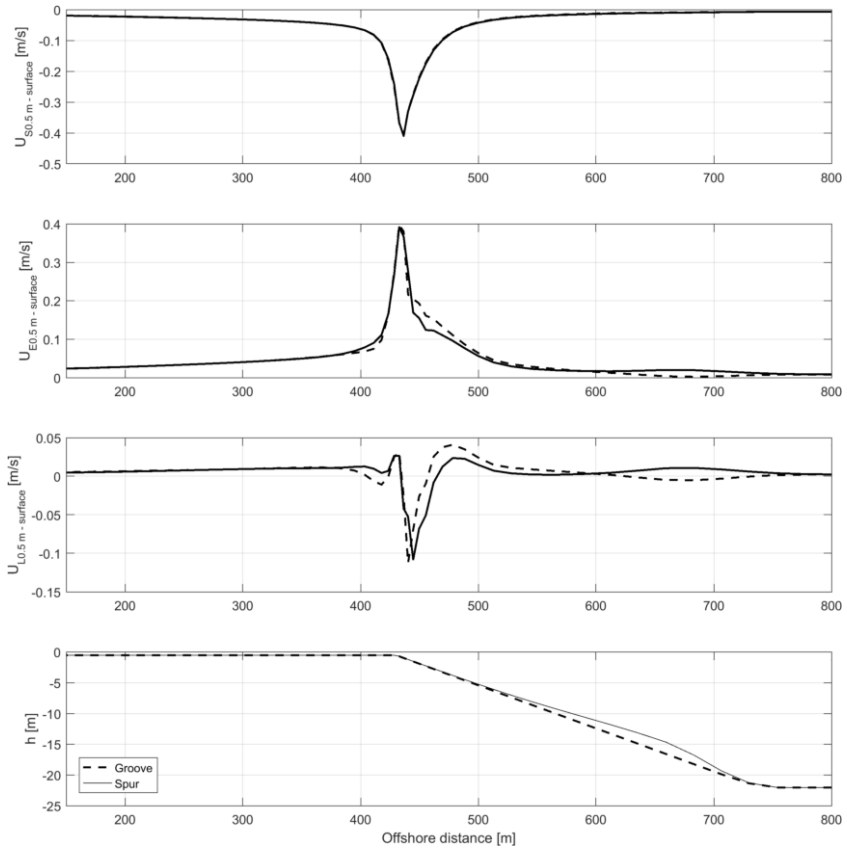

Figure 5.15: Cross-shore view of Base Case results for cross-shore surface velocities $U_{S-0.5m-sur}$, $U_{E-0.5m-sur}$ and $U_{L-0.5m-sur}$ over spur and groove.

The map of cross-shore and alongshore Eulerian velocities integrated over the lowest 0.5 m in the water column ($U_{L0.5m-bottom}$ and $V_{L0.5m-bottom}$) is presented in Figure 5.14. This plot shows that all currents are directed offshore, except for x > 650 m over the groove. These currents have very low values, with O (1 mm/s), and in general the spur velocities are higher than the groove ones.

Figure 5.16 shows that in the SAG zone Eulerian bottom currents are never higher in absolute values than Stokes Drift velocities, resulting in Lagrangian currents always directed onshore. Lagrangian bottom velocities over spur and groove look very similar, although slightly higher over spur, following the Stokes Drift trend.

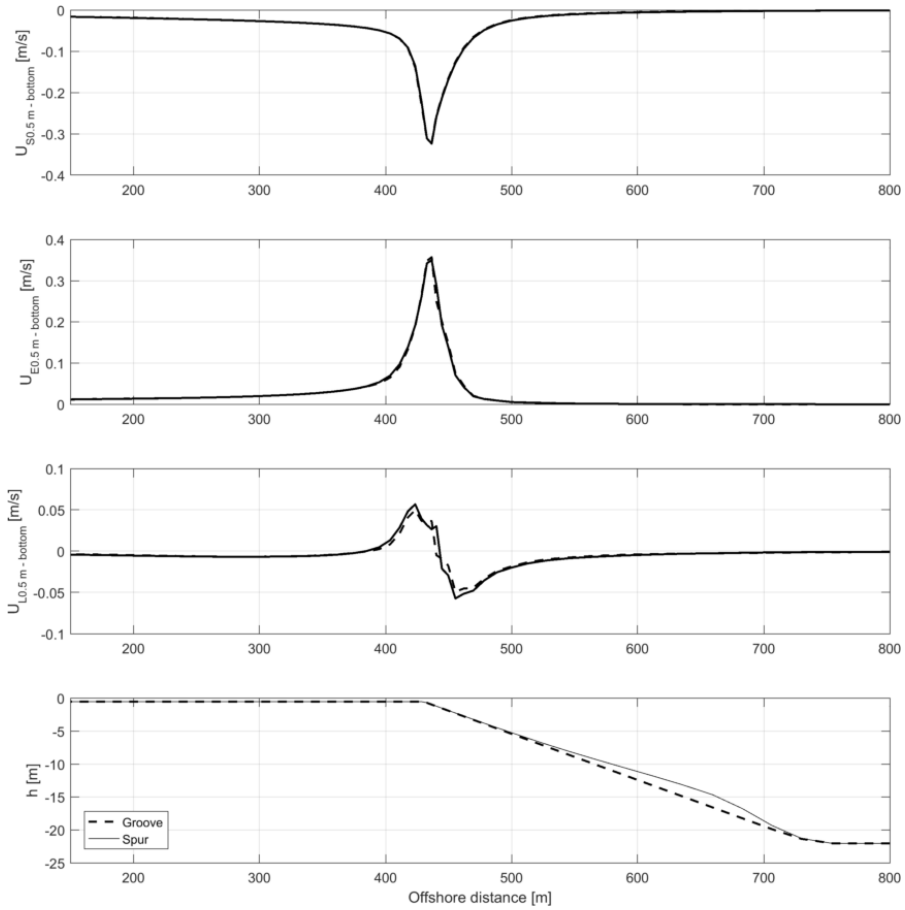

Figure 5.16: Cross-shore view of Base Case results for cross-shore bottom velocities $U_{S-0.5m-bot}$, $U_{E-0.5m-bot}$ and $U_{L-0.5m-bot}$ over spur and groove.

The bottom shear stresses, shown in Figure 5.11, have in general the same overall shape than the Eulerian bottom currents. This is consistent with the D3D-FLOW model formulation that uses the lowest layer Eulerian velocities for the bottom shear stress, as discussed in Chapter 3.1.4. Shear stress values in the SAG zone have O (0.1 Pa), being higher over the spurs than over grooves. The same order of magnitude and higher values over spurs were found for SAG formations on Palmyra Atoll (Rogers et al., 2015), as discussed in Chapter 4.3.

5.1.5. MOMENTUM BALANCE

The analysis of how momentum is balanced in SAG formations is fundamental to the understanding of the flow pattern observed, and how it changes to different input conditions. The nomenclature for the momentum terms in the 3D momentum conservation equation (3.4) solved by D3D-FLOW was presented in Chapter 4.1.

The cross-shore view of the cross-shore momentum terms over spur and groove is shown in Figure 5.17, where dashed lines indicate the location of the alongshore sections and each of momentum terms is represented by a single colour, relatively to each of the dashed lines.

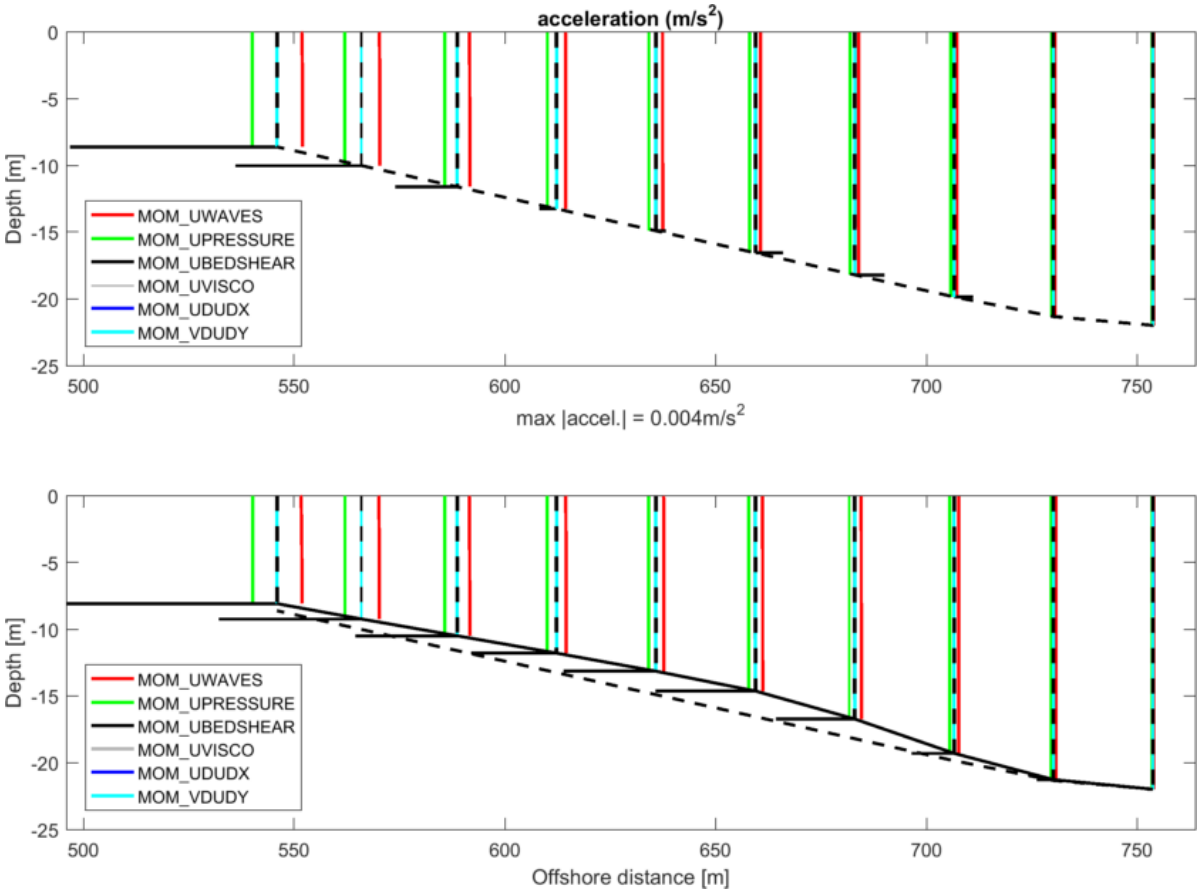

Figure 5.17: Cross-shore views of Base Case results for cross-shore momentum terms on top of groove and spur. MOM_UWAVES, MOM_UPRESSURE, MOM_UBEDSHEAR, MOM_UVISCO, MOM_UDUDX and MOM_VDUDY represent the wave forces, pressure gradient, bottom shear stress, horizontal viscous forces, streamwise and lateral advective accelerations, respectively.

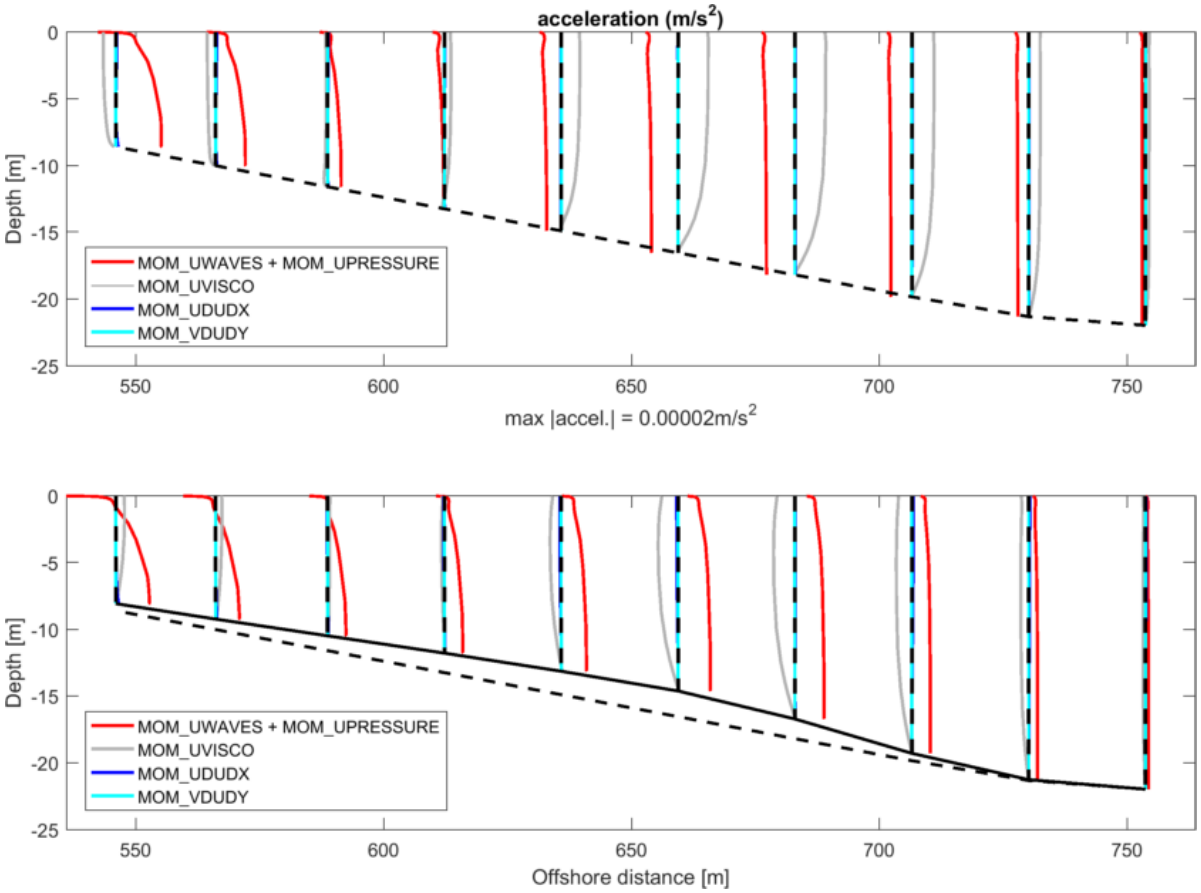

Figure 5.18: Cross-shore views of Base Case results for cross-shore momentum terms on top of groove and spur - imbalance between pressure gradient and wave forces. MOM_UWAVES, MOM_UPRESSURE, MOM_UVISCO, MOM_UDUDX and MOM_VDUDY represent the wave forces, pressure gradient, horizontal viscous forces, streamwise and lateral advective accelerations, respectively.

This plot shows that in general the momentum terms grow as approaching shallower waters, consistent with higher wave forcing as moving onshore, as shown in Figure 4.20. The main terms involved in the balance are the pressure gradient (green) and wave forces (red) along the whole water column, and friction over the bottom (black). Pressure gradients are by definition vertically homogenous. Wave forces are not invariant in the vertical, but changes in the vertical are low, consistent with no breaking waves and to a limited effect of Stokes Drift divergence. Friction values over the spur are, as already said, higher over the spurs.

Wave forces are mainly balanced by pressure gradient. The other terms that balance the mismatch between those forces have lower order of magnitudes. Figure 5.18 shows an equivalent plot as Figure 5.17, but focusing on the imbalance between wave forces and pressure gradient (red) and the role of the remainder momentum terms, excluding the bottom shear stress for scaling purposes. This plot shows that the horizontal turbulent stresses are the main forcing balancing the mismatch between those, especially for higher depths.

Although the vertical turbulent stresses are not shown in the plot - it is not provided as output from D3D-FLOW as discussed in Chapter 4.1 -, they likely become more important in shallower waters, mixing more the cross-shore velocities along the vertical. Both the streamwise (blue) and lateral (cyan) advective terms are low, with a negigible role in the Base Case momentum balance.

The mismatch between pressure gradient (vertically homogeneous) and wave force has variations in the vertical, showing that the wave forces are not invariant in the vertical, with a remarkable onshore momentum flux in the top layer that grows moving onshore. As for the water surface, sensitivity runs neglecting the dissipation by whitecapping showed that even for the Base Case there is a small fraction of whitecapping. As for the vertical variation in the wave force, it can be explained by the divergence of the Stokes Drift, also part of the wave force, as discussed in Chapter 3.1.4. A simulation without considering the divergence of Stokes Drift as part of the wave force ouput (but still including it in the momentum conservation equation) was conducted, with results reported in Appendix H. Results show that the Stokes Drift divergence is the responsible for the vertically heterogeneous wave force.

Comparing Figures 5.18 and 5.2, it can be noticed that the imbalance between wave forces and pressure gradient and the horizontal turbulent forces have similar trends to the velocity profile: an increase from offshore, peaking at x ≈ 650 m, further decrease and reversing at x ≈ 600 m, both over spur and groove, but with opposite signs. In general, negative mismatch and positive horizontal viscous forces correlate with onshore velocities, while positive imbalance and negative horizontal turbulent forces connect to offshore velocities. As moving further onshore, with the likely increase of vertical turbulent forces, the velocity profile switches to the aforementioned shape with bottom onshore velocities and top offshore velocities, although with heterogeneous shape between spur and groove. The imbalance between wave forces and pressure gradient in the top layer as moving onshore gets larger over the spur, correlating with the lower offshore spur surface velocities.

Equivalent plots to Figures 5.17 and 5.18 for the alongshore momentum terms over middle cross-shore sections between spur and groove are shown in Figures 5.19 and 5.20. Momentum terms on the RHS of dashed lines indicate eastwards accelerations, with westwards accelerations being on the left. The first plot (Figure 5.19) shows that wave forces are mainly balanced by pressure gradients, similar to the cross-shore momentum balance.

In the offshore zone (x > 725 m), very low forces are shown, which can be justified by wave forcing being zero in alongshore uniform bathymetries, similar to Fy over the groove in Figures 4.18 and 4.19. Subsequently, both the driving wave forces and pressure gradients increase, and Figure 5.19 shows that the imbalance between those is one order of magnitude lower than in the cross-shore, resulting in low alongshore velocities. The logarithmic shape of the horizontal turbulent stresses has an overall similar shape to the velocity profile, shown in Figure 5.9. The locations where the imbalance between wave force and pressure is low (x ≈ 680 m for both top and bottom plots, and x ≈ 540 m for the top plot) connect to the locations where alongshore velocities are approximately null. The same trends from the cross-shore direction with positive imbalance and negative horizontal turbulent stresses correlating with eastwards velocities, and vice-versa are also observed in the alongshore direction.

5.2. INFLUENCE OF VARYING PARAMETERS

This section presents the results of the sensitivity runs, described in Chapter 3.2.4. Variations of the Base Case scenario were tested with one parameter being modified at a time.

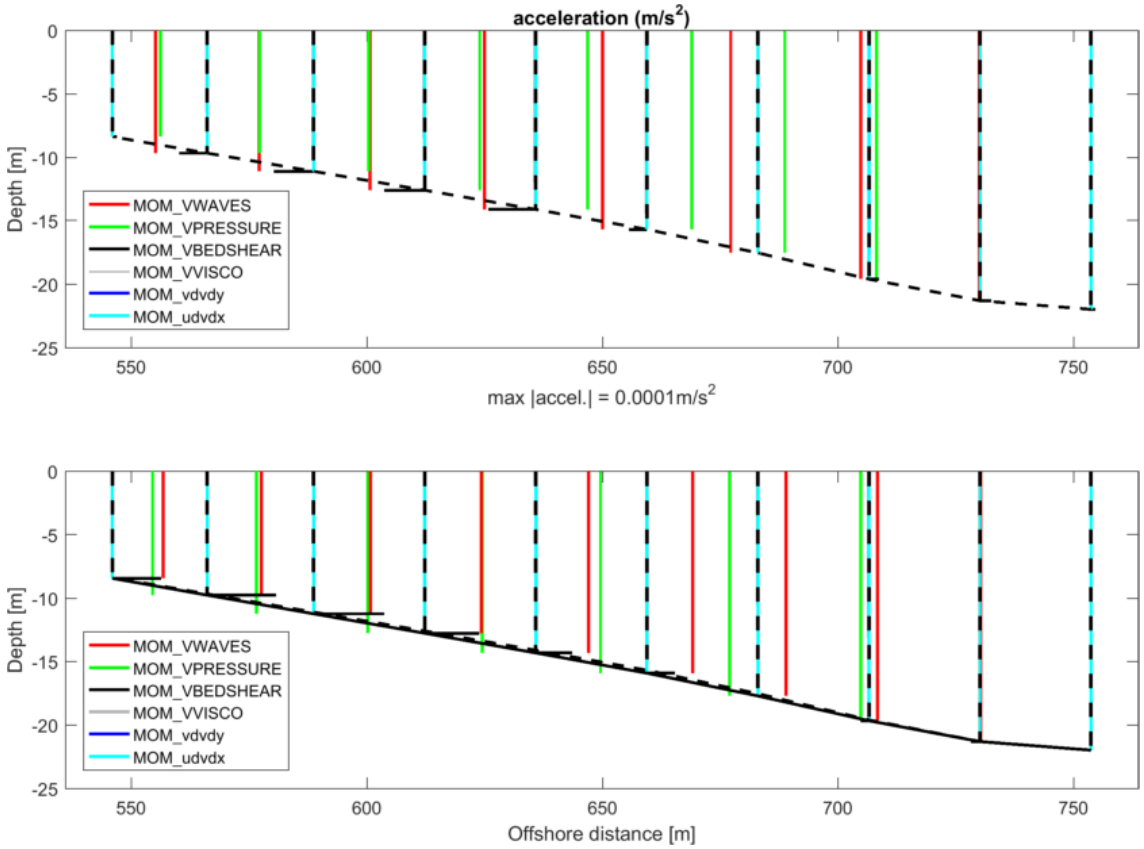

Figure 5.19: Cross-shore views of Base Case results for alongshore momentum terms on cross-sections in the middle between groove and spur (top), and spur and groove (bottom). MOM_VWAVES, MOM_VPRESSURE, MOM_VBEDSHEAR, MOM_VVISCO, MOM_VDVDY and MOM_UDVDX represent the wave forces, pressure gradient, bottom shear stress, horizontal viscous forces, streamwise and lateral advective accelerations, respectively.

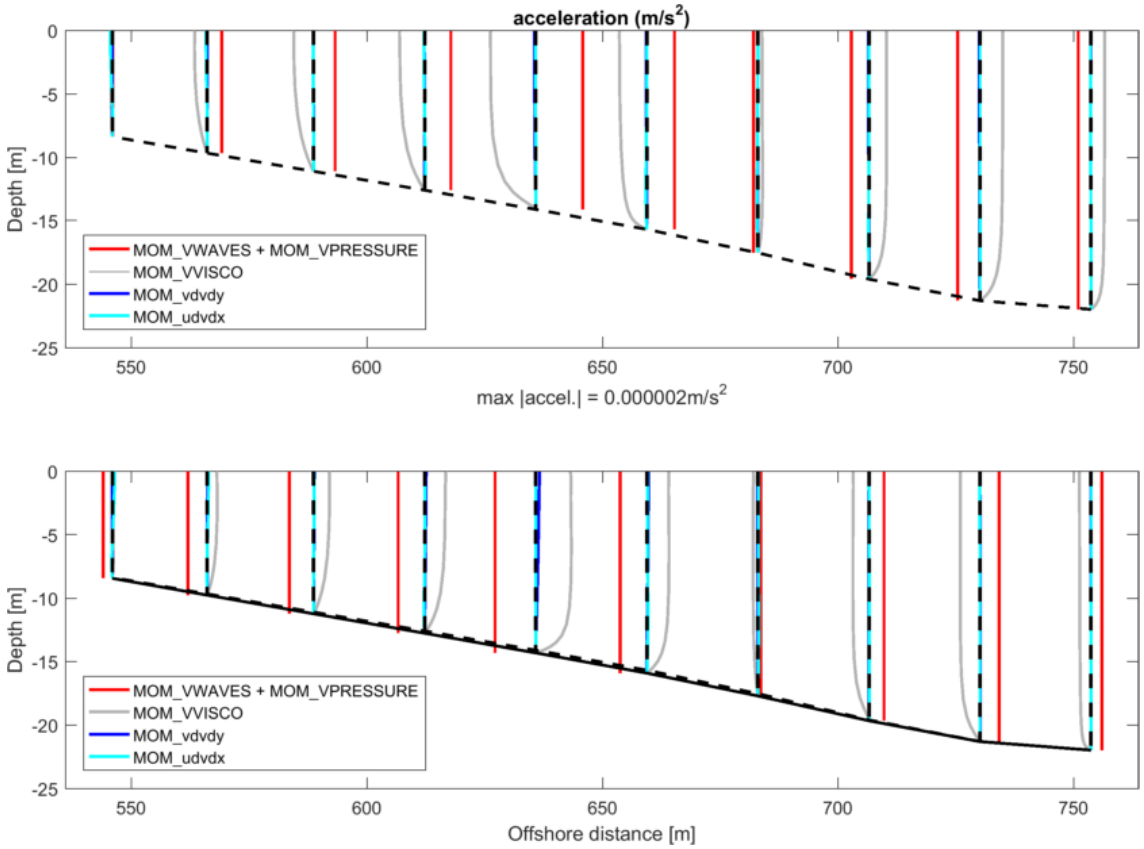

Figure 5.20: Cross-shore views of Base Case results for alongshore momentum terms on cross-sections in the middle between groove and spur, and spur and groove - imbalance between pressure gradient and wave force. MOM_VWAVES, MOM_VPRESSURE,MOM_VVISCO, MOM_VDVDY and MOM_UDVDX represent the wave forces, pressure gradient, horizontal viscous forces, streamwise and lateral advective accelerations, respectively.

The effects of variations of short wave parameters (Chapter 5.2.1), SAG geometry (Chapter 5.2.2) and alongshore forcing (Chapter 5.2.3), and the influence of long waves (Chapter C.1.4) are studied through comparisons of 3D cross-shore Lagrangian velocity profiles on top of spurs and grooves. The cross-shore velocities were chosen due to their dominance over alongshore and vertical velocities for most cases. Similar plots for the alongshore are presented in Appendix C.

In all the velocity profiles presented below, the dashed lines represent the locations of alongshore sections, while the coloured lines provide the velocities relatively to each of those dashed lines. Reddish colours correspond to higher values of each variable, while lower values are blueish.

5.2.1. INFLUENCE OF SHORT WAVE PARAMETERS

The description of the investigated short wave parameters and range of parameters was covered in Chapter 3.2.3. The two wave parameters under research are listed below:

- Significant Wave Height (Hs_0); and
- Wave Steepness ($\frac{Hs_0}{Lp_0}$).

The results for each of the parameters are provided below.

WAVE HEIGHT

The cross-shore profiles of cross-shore Lagrangian velocities u_L on top of spur and grooves for varying Hs are shown in Figure 5.21. With increasing wave heights, there is an overall strengthening of the currents involved in the SAG circulation cells, i.e., an increase of spur offshore and groove onshore velocities in the offshore circulation cell, and of the groove offshore and spur onshore currents in the onshore circulation cell. In other words, the increase of wave heights result in a significant enhancement of SAG circulation.

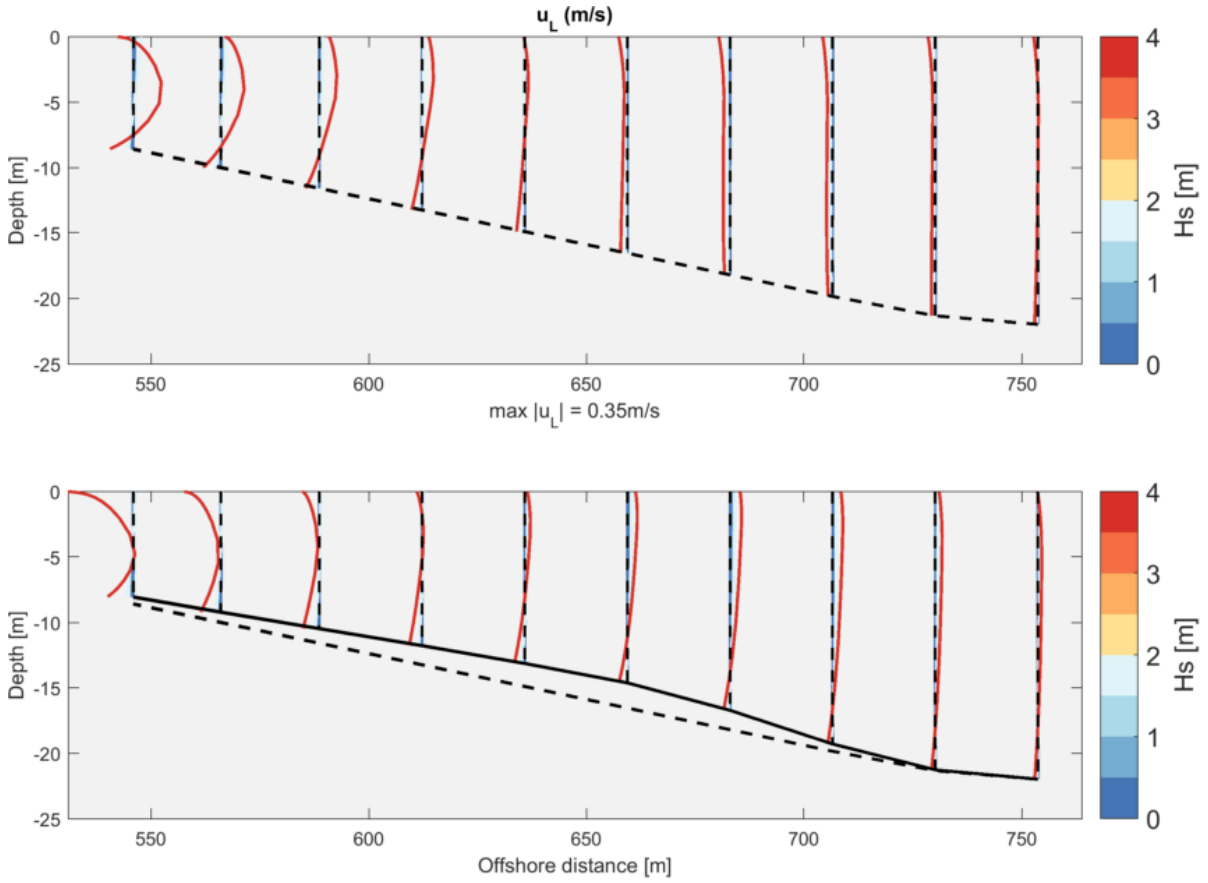

Figure 5.21: Cross-shore views of results for cross-shore Lagrangian velocity u_L over spur and groove for varying significant wave height Hs.

The velocity profiles for Hs = 4 m shows that as approaching shallower waters there is a change in the velocity profile shape, that turns into parabolic. As for the groove, there are onshore surface velocities, that reverse to offshore and peak in the mid water column, then reversing back to onshore close to the bottom. As for the spur, the similar velocity shape is observed with all currents shifting towards onshore, resulting in onshore velocities nearly along the whole water column. Those shapes suggest early breaking wave heights, that effectively changes the velocity profile into a typical wave-induced current profile in the surfzone, with roller on top and undertow in the mid water column, related to mixing by the vertical turbulent stresses.

WAVE PERIOD

The cross-shore profiles of cross-shore Lagrangian velocities u_L on top of spur and grooves for varying Tp are shown in Figure 5.22. Two types of behaviours are observed depending on range of Tp, as described below.

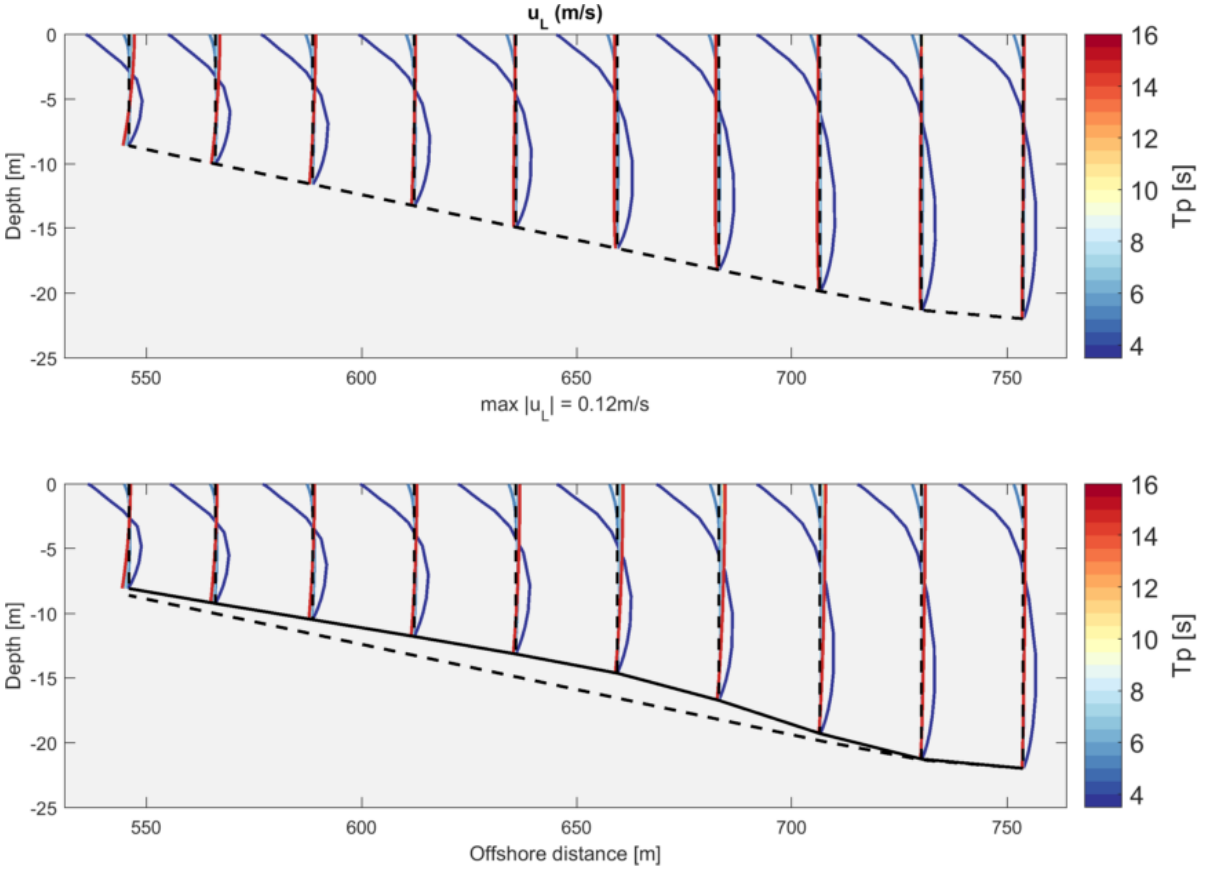

Figure 5.22: Cross-shore views of results for cross-shore Lagrangian velocity u_L over spur and groove for varying peak wave period Tp .

As for Tp between 7 and 15 s, increasing wave periods leads to the enhancement of SAG circulation, similarly to increasing Hs. This amplification looks limited comparatively to the case of higher wave heights.

As for Tp lower than 7 s, decreasing wave periods leads to velocity profiles with onshore surface and offshore bottom currents, that becomes more parabolic as moving onshore, consistent with higher vertical turbulent mixing. These lower periods suggest steepness-induced breaking - whitecapping - ever since the start of the offshore limit of the model. The velocity profile for Tp ≈ 4 s (dark blue) looks similar for both spur and groove, and it presents velocities much higher than all the other cases, suggesting that the breaking forces lead to higher velocities. The velocity profile for Tp ≈ 5 s (light blue) has a roughly similar shape than Tp ≈ 4 s, but with much lower velocities, consistent with lower $\frac{Hs}{Lo}$ resulting in lower breaking forces.

5.2.2. INFLUENCE OF SAG GEOMETRY

The description of the investigated SAG geometry parameters and evaluated range was covered in Chapter 3.2.3. The seven SAG geometry parameters under research are listed below:

- Spur height (h_{spr});

- Spur wavelength (λ_{SAG});
- Ratio of groove width and spur wavelength ($\frac{W_{grv}}{\lambda_{SAG}}$);
- Cross-shore slope (β_f);
- Reef flat width (W_{reef});
- Ratio of groove and spur friction coefficient ($\frac{C_{D-grv}}{C_{D-spr}}$); and
- Cross-shore position of maximum spur height (z_μ).

The results for each of the parameters are provided below.

SPUR HEIGHT

The cross-shore profiles of cross-shore Lagrangian velocities u_L on top of spur and groove for varying h_{spr} are shown in Figure 5.23. Overall, growing spur heighs lead to a significant enhancement of SAG circulation, with effect very similar to the wave heights (Figure 5.21).

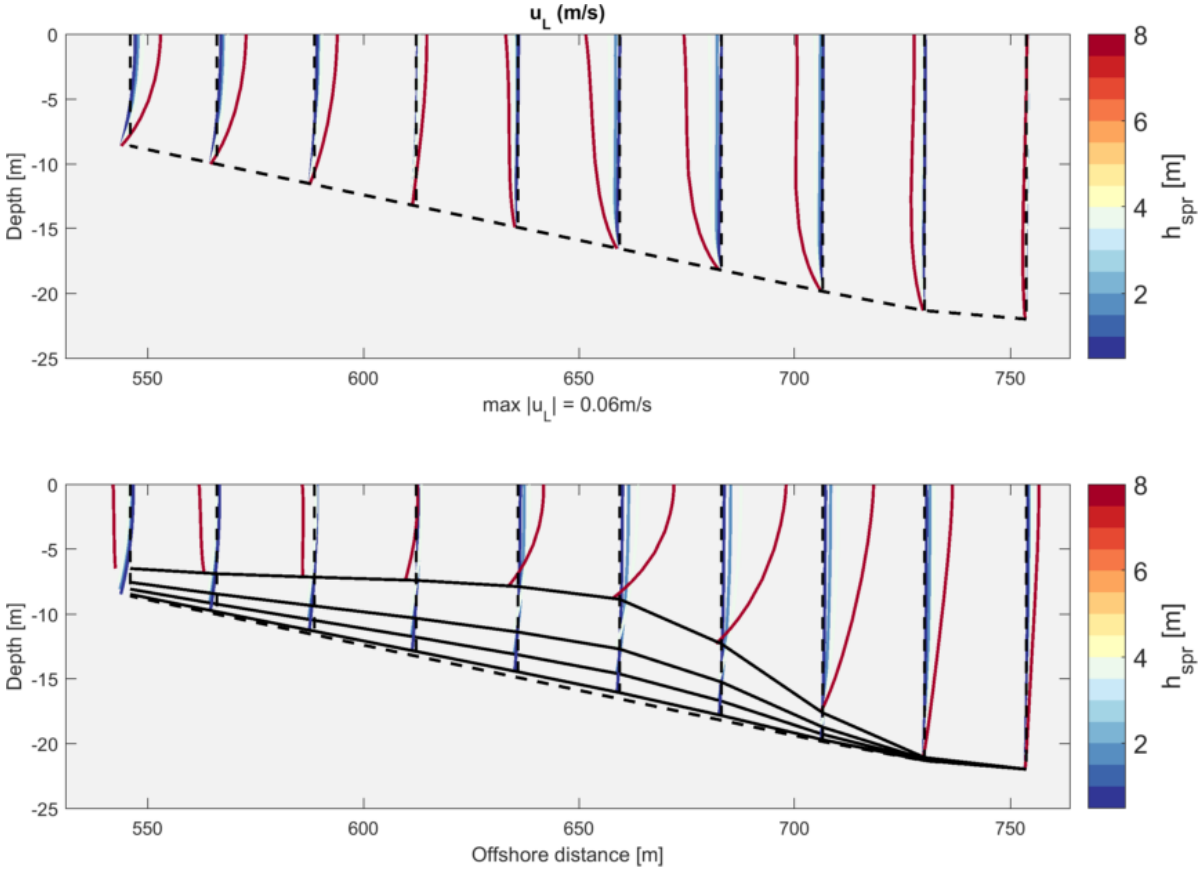

Figure 5.23: Cross-shore views of results for cross-shore Lagrangian velocity u_L over spur and groove for spur height h_{spr} .

The spur height of 8 m results have a spur velocity profile in the onshore zone that is vertically homogenous, with onshore currents along the whole water column. The lower depths in that region, that occur as a function of larger spur heights, result in the strenghtening of the onshore currents that now occupy the whole water column.

SAG WAVELENGTH

The cross-shore profiles of cross-shore Lagrangian velocities u_L on top of spur and grooves for varying λ_{SAG} are shown in Figure 5.24. Two types of velocity profiles occur depending on the λ_{SAG}, as described below.

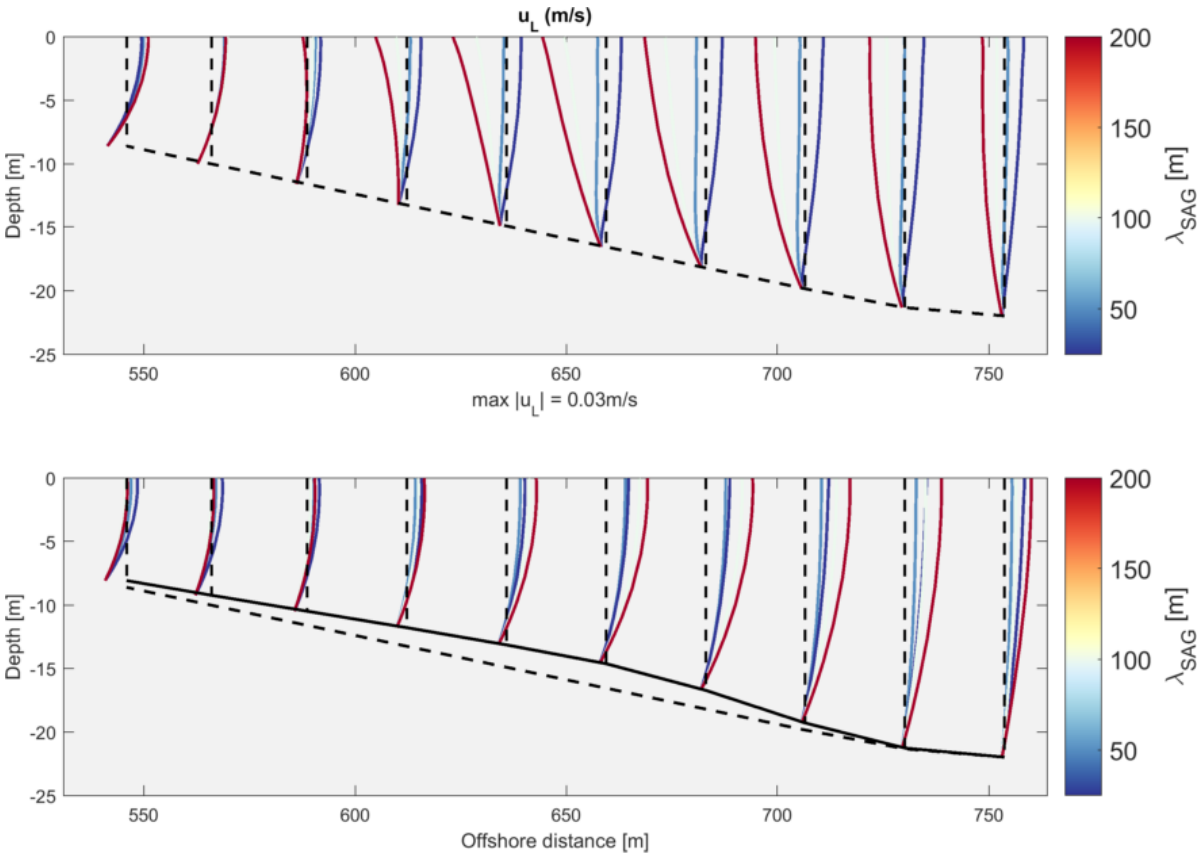

Figure 5.24: Cross-shore views of results for cross-shore Lagrangian velocity u_L over spur and groove for varying spur wavelength λ_{SAG}.

As for $\lambda_{SAG} \geq 50$ m, there is an enhancement of SAG circulation with increasing λ_{SAG}. This strengthening is moderate comparatively to the Hs or h_{spr} effects.

As for $\lambda_{SAG} = 25$ m (dark blue), the SAG circulation is affected in the offshore zone, with a shifting of the groove velocities towards offshore, while the spur currents get stronger than for $\lambda_{SAG} = 50$ m. In the onshore, the SAG circulation remains nearly the same. Therefore, in terms of shape of velocity profile, the low SAG wavelength changes only the offshore circulation cell, but the onshore part remains the same.

GROOVE WIDTH

The cross-shore profiles of cross-shore Lagrangian velocities u_L on top of spur and grooves for varying W_{grv} for a fixed λ_{SAG} (or simply $\frac{W_{grv}}{\lambda_{SAG}}$) are shown in Figure 5.25. Overall, effects on the velocity profile are limited, with a slight trend to undermine the SAG circulation for growing $\frac{W_{grv}}{\lambda_{SAG}}$.

CROSS-SHORE SLOPE

The cross-shore profiles of cross-shore Lagrangian velocities u_L on top of spur and grooves for $\tan\beta_f = 0.02$ (the mildest) and $\tan\beta_f = 0.50$ (the steepest) are shown in Figures 5.26 and 5.27. The mildest slope produced results similar in shape to the case where $\lambda_{SAG} = 25$ m, and as it is further discussed in Chapter 5.4, an overall flow strength similar to the Base Case ($\tan\beta_f = 0.07$). The steepest slope has a distinct shape, with offshore surface currents over the spur and groove for the entire SAG cross-shore profile.

In terms of SAG circulation,the lowest slope shows only the onshore circulation cell, with offshore groove- and onshore spur currents in a depth-averaged sense. Intermediate slopes resulted in flow profile similar to the Base Case, with similar SAG circulation. The most extreme slope provided results similar to the Base Case in the depth-averaged sense, but with offshore groove surface currents in the offshore zone. In general, increasing $\tan\beta_f$ does not enhance much circulation in a depth-averaged sense, but affects vastly the surface and bottom currents, as further covered in Chapter 5.4.

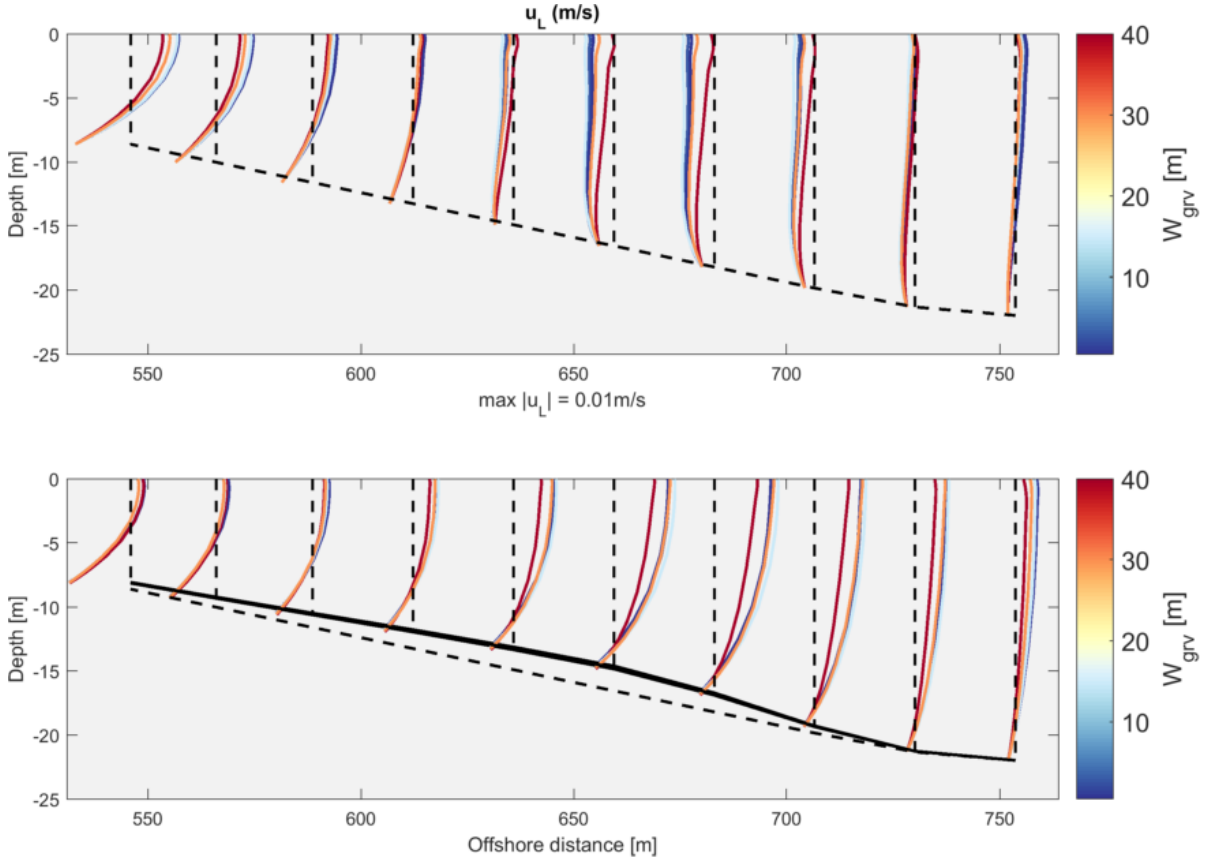

Figure 5.25: Cross-shore views of results for cross-shore Lagrangian velocity u_L over spur and groove for varying groove width W_{grv}.

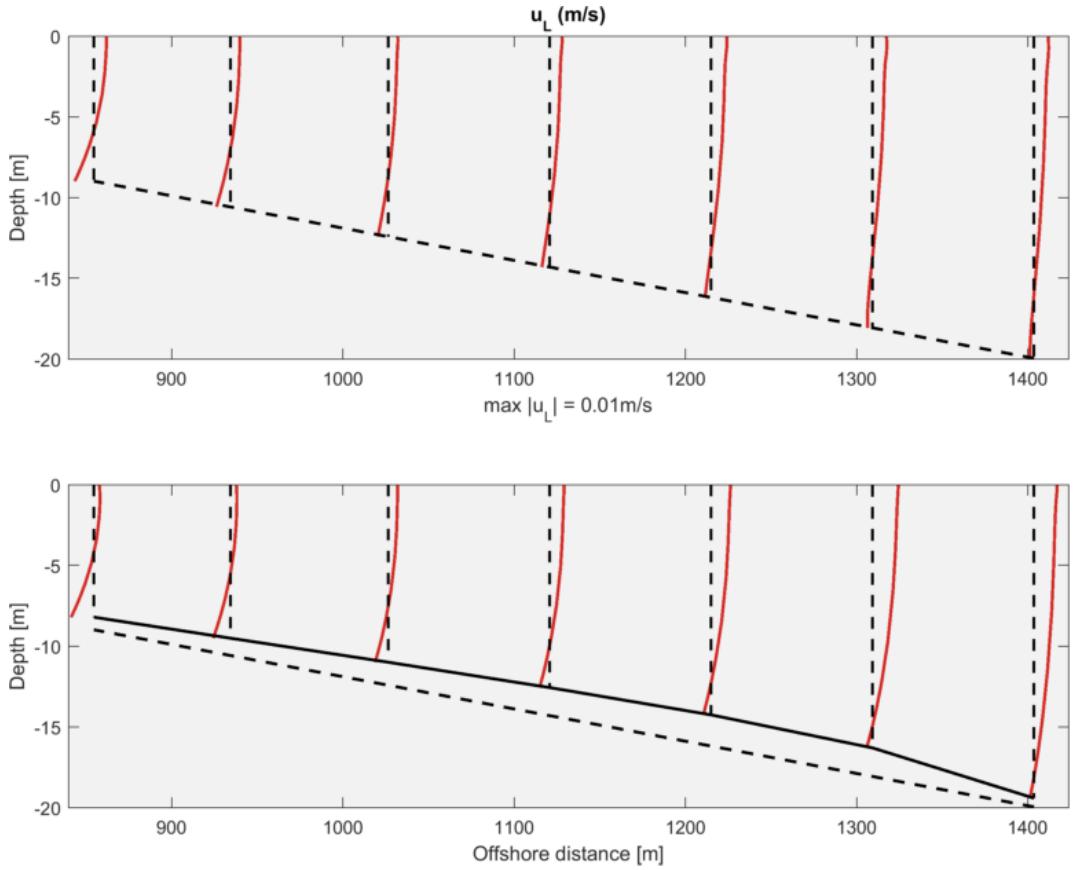

Figure 5.26: Cross-shore views of results for cross-shore Lagrangian velocity u_L over spur and groove for mild slope ($\tan\beta_f = 0.02$).

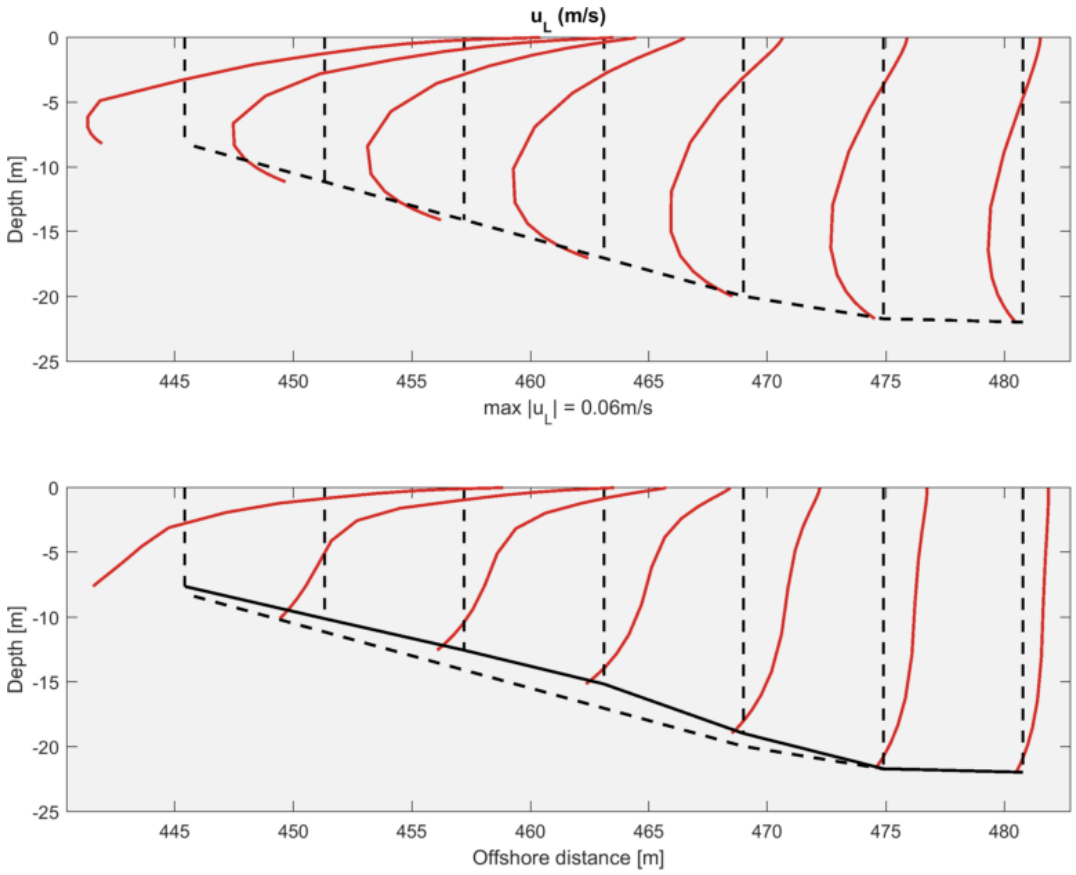

Figure 5.27: Cross-shore views of results for cross-shore Lagrangian velocity u_L over spur and groove for steep slope ($\tan\beta_f = 0.50$).

REEF FLAT WIDTH

The variations of W_{reef} - 50 and 1000 m - were found to produce no difference on the 3D cross-shore velocity profile, i.e., those two reef flat widths provide results similar to Base Case (W_{reef} = 300 m), shown in Figure 5.2. This means that the large-scale circulation on the reef flat does not seem to exert an important role for the hydrodynamics in the SAG zone.

FRICTION COEFFICIENT RATIO

The cross-shore profiles of cross-shore Lagrangian velocities u_L on top of spur and grooves for varying $\frac{C_{D-grv}}{C_{D-spr}}$ are shown in Figure 5.28. Overall, the effects on the velocity profile look limited, with a slight shifting of the currents over spur and groove towards offshore. This results in oscillating trends to enhance and undermine SAG circulation with decreasing $\frac{C_{D-grv}}{C_{D-spr}}$.

POSITION OF MAXIMUM SPUR HEIGHT

The cross-shore profiles of cross-shore Lagrangian velocities u_L on top of spur and grooves for varying z_μ are shown in Figure 5.29. In general, for decreasing z_μ there is a significant strengthening of the SAG circulation, comparable in order of magnitude to the effects of increasing Hs. Decreasing z_μ also leads to a shifting of the SAG circulation towards onshore, i.e., the offshore and onshore circulation cells are transferred onshore, closer to the z_μ. The amplification and shifting of SAG circulation are later shown for the cases with long waves (Figures 5.31, D.1, and D.3), and are further quantified in Chapter 5.4.

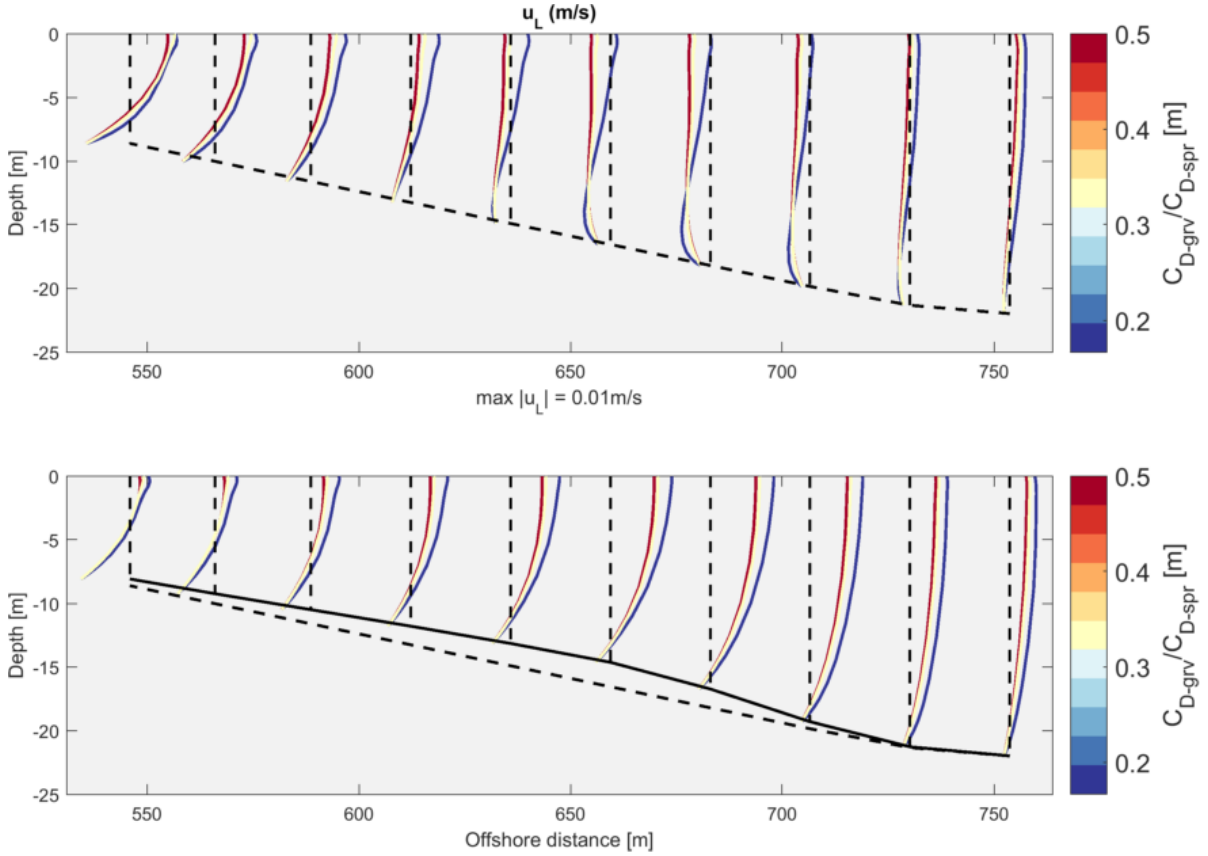

Figure 5.28: Cross-shore views of results for cross-shore Lagrangian velocity u_L over spur and groove for varying ratio of groove and spur friction coefficient $\frac{C_{D-grv}}{C_{D-spr}}$.

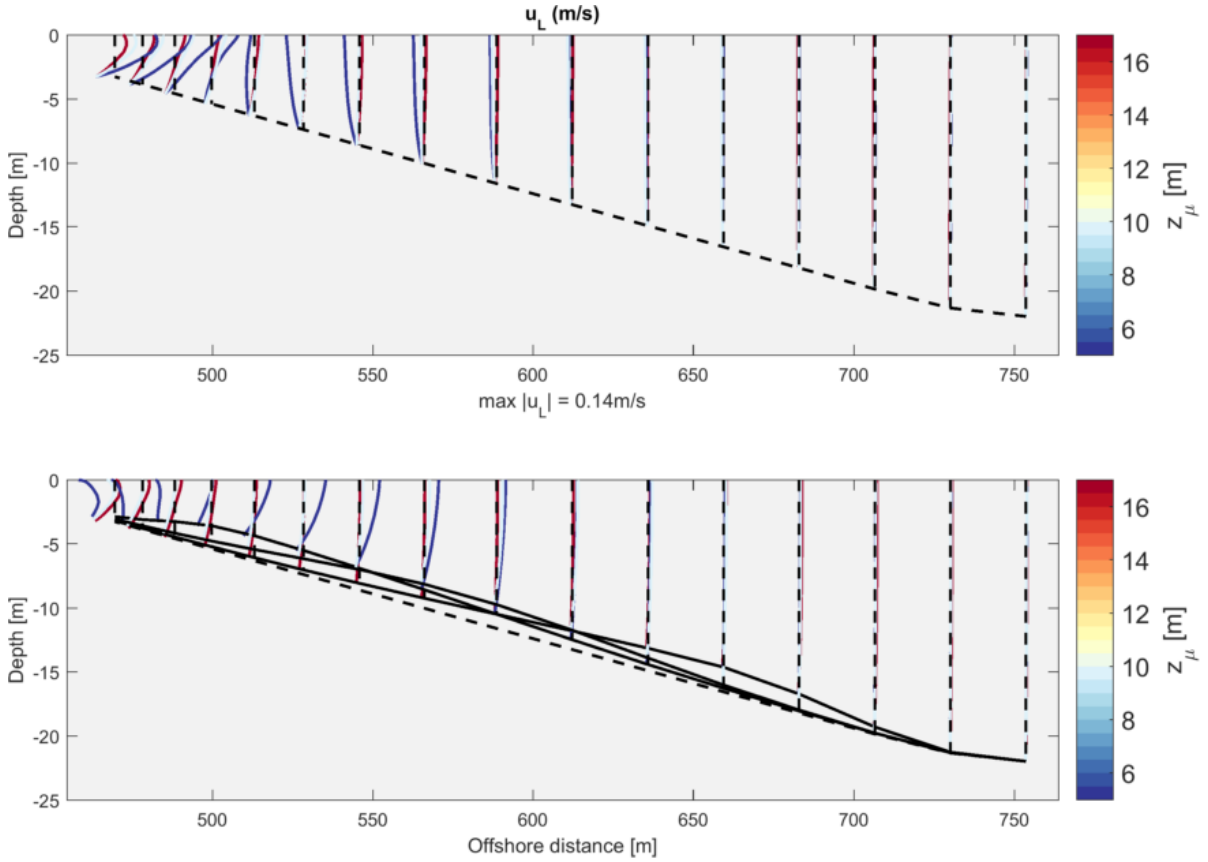

Figure 5.29: Cross-shore views of results for cross-shore Lagrangian velocity u_L over spur and groove for varying vertical position of maximum spur height z_μ.

5.2.3. INFLUENCE OF ALONGSHORE CURRENT

To investigate the changes in 3D circulation, varying alongshore wind speeds U_{10} were used. The cross-shore profiles of cross-shore Lagrangian velocities u_L on top of spur and grooves for varying U_{10} are shown in Figure 5.30. Overall, the strength of the changes introduced by alongshore forcing is low, but there is a modification of velocity profile shape.

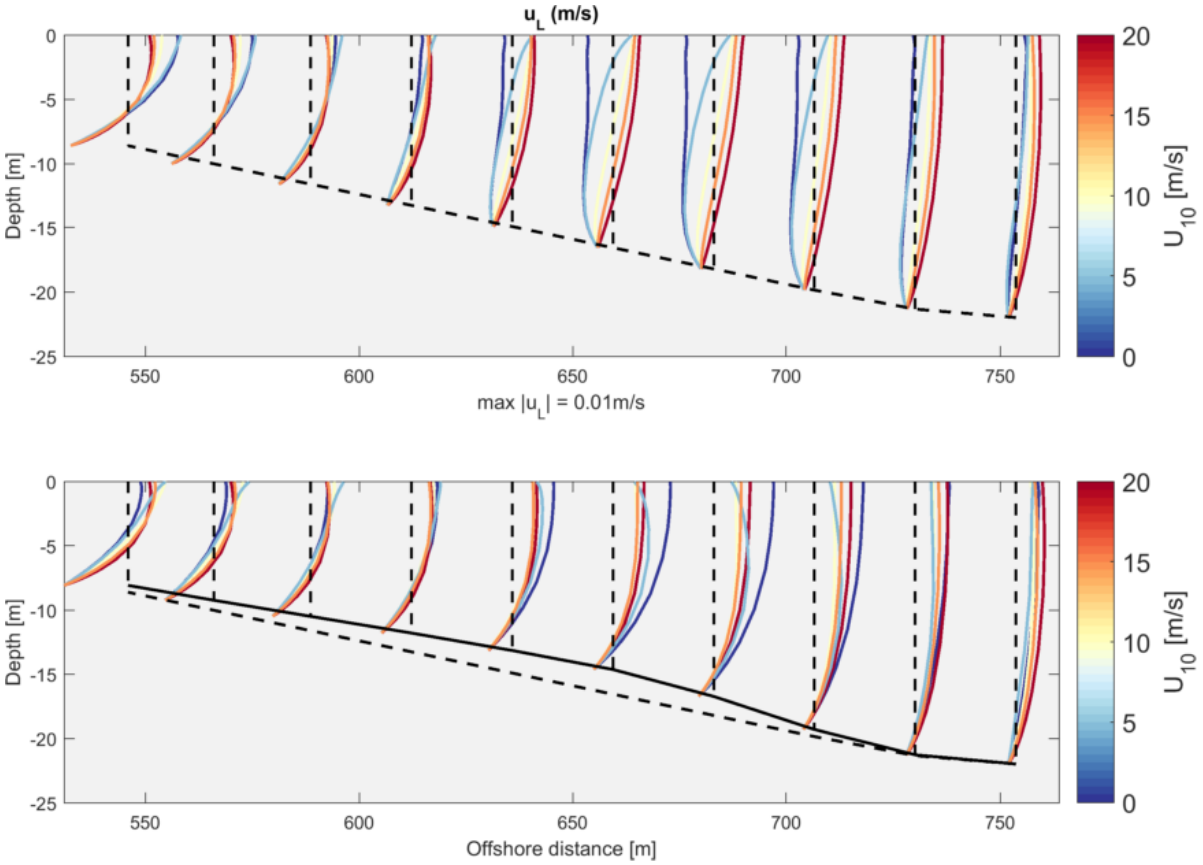

Figure 5.30: Cross-shore views of results for cross-shore Lagrangian velocity u_L over spur and groove for varying alongshore wind speed U_{10}.

As for the groove, increasing alongshore wind action leads to a shifting towards offshore of the currents, happening only in the offshore zone (x > 600 m). The shifting further reverses to onshore for shallower waters. As for the spur, the velocity shifting is directed onshore, occuring especially for x > 600 m.

Two types of velocity profiles occur depending on the U_{10}. As for $U_{10} \leq 10$ m/s, the velocity profile is similar to the Base Case, except for the offshore groove surface currents in the offshore zone. As for $U_{10} \geq 15$ m/s, the velocity profile is similar to the case with $\lambda_{SAG} = 25$ m (Figure 5.30), i.e., the velocity profile is similar to the Base Case, except for the offshore currents found on top of the groove. Therefore, in terms of shape of velocity profile, the wind forcing changes only the SAG offshore circulation cell, but the onshore part remains the same.

5.2.4. IMPORTANCE OF LONG WAVES

The importance of long wave forcing was studied assuming the Base Case setup with varying peak spur heights z_μ, as described in Chapter 3.2.4. D3D-FLOW + XBeach surfbeat mode were used for those simulations. This section covers only the results for the Base Case setup (Hawaiian style, with $z_\mu = 17$ m). As the remainder results have conceptually the same behaviour, they are presented in Appendix D.

With long wave forcing, velocities vary in the wave group timescale. The mean velocities over the last 2 h of each simulation were used for the analysis of 3D velocity profiles. The Fourier type of output from D3D-FLOW was used to obtain those currents for all layers (Deltares, 2016). As for the calculation of the significant long wave height Hs_{long}, the mean variance of the water level σ^2 over the last 20 min from XBeach was used, with the formula below (5.1):

$$Hs_{long} = 4\sqrt{\sigma^2} \tag{5.1}$$

The significant long wave height Hs_{long} and the mean cross-shore depth-averaged velocity $\hat{U}_L$ for the SAG Hawaiian style (z_μ = 17 m) are shown in Figure 5.31. The result for Hs_{long} shows an increasing Hs_{long} from offshore to onshore, with peaking in the reef crest and further breaking. The zone around x ≈ 450 m, that is slightly offshore of the reef crest, is characterized by a lower Hs_{long} peak, suggesting partial reflection of long waves, coherent with the estimations from the dimensionless normalized bed slope parameters proposed by van Dongeren et al. (2007). All Hs_{long} were lower than 30 cm, and in the SAG zone they are generally lower than 10 cm. The results for $\hat{U}_L$ show cross-shore profiles very similar to Figure 5.12, with the aforementioned SAG circulation. With decreasing z_μ (Appendix D), the aforementioned shifting towards onshore and strengthening of the circulation cells zones can easily be noticed.

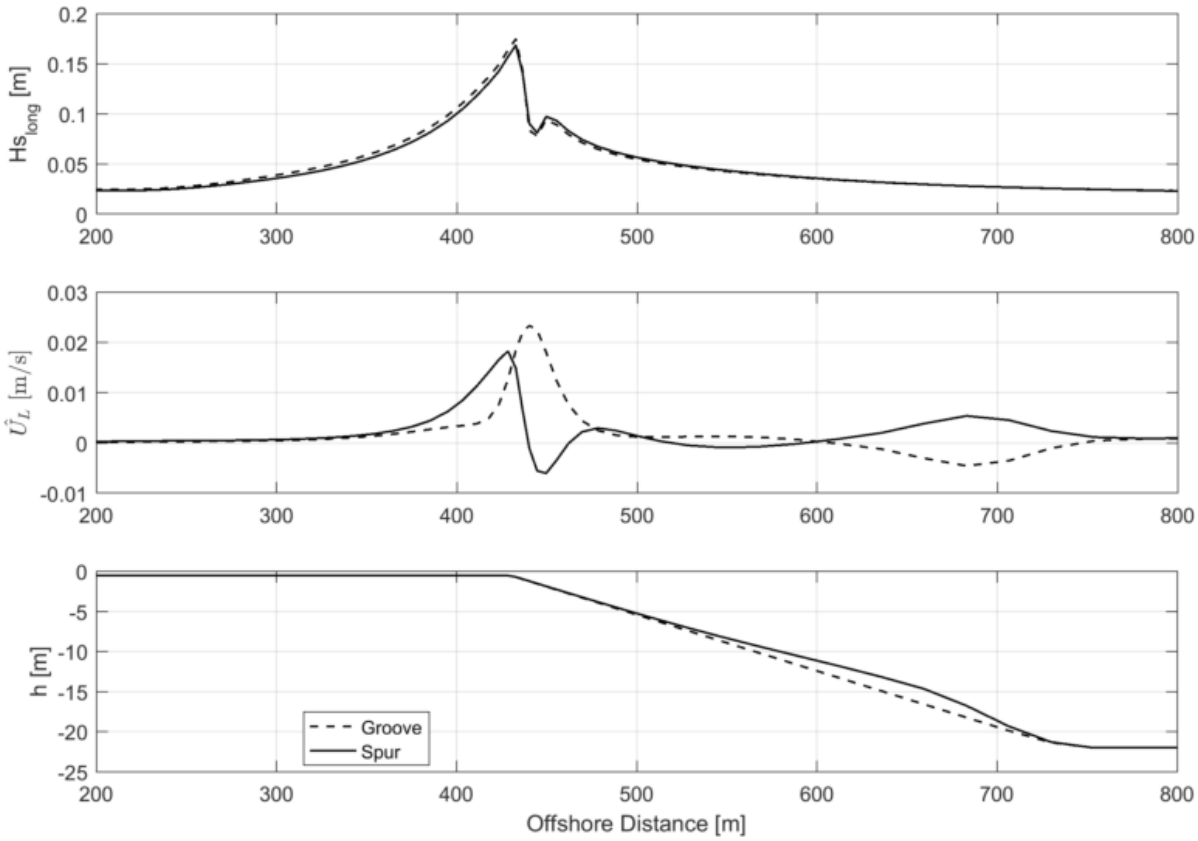

Figure 5.31: Cross-shore views of D3D-FLOW + XBeach surfbeat Base Case (Hawaiian type with z_μ = 17 m) results for significant long wave height Hs, cross-shore depth-averaged Lagrangian velocity $\hat{U}_L$ and cross-shore depth profile over spur and groove.

The cross-shore profiles of cross-shore Lagrangian velocities $\hat{u_L}$ on top of spur and grooves - for cases with (red) and without (blue) long waves - are shown in Figure 5.32 for the Hawaiian style (z_μ = 17 m). The velocity profile shape remains nearly the same for all the SAG types with long wave forcing (Appendix D).

Overall, the strength of the changes introduced by long wave forcing in the mean flow is low, with minor modifications in the mean velocity profile for the three SAG types. As for the Hawaiian SAG style, there is a very slight overall shifiting of the surface velocities towards onshore. As for the Intermediate and Buttress SAG types (Appendix D), there is a slight shifting towards onshore of the groove surface currents, towards offshore of the spur surface currents.

The changes in the mean large-scale circulation with long waves are primarily focused in the reef flat, and, similarly to the reef flat width, they do not seem to interfere in the hydrodynamics of the SAG zone.

The study of the intrawave motion - i.e., the flow within the long wave period - was evaluated by statistically analyzing the time series of the depth-averaged spur velocities at the peak spur height depth for each of the SAG type (Appendix D). The conclusion from this study was that the intrawave flow seems to be as important as the mean flow. Accordingly, the transport of matter might be affected, thus that intrawave motion

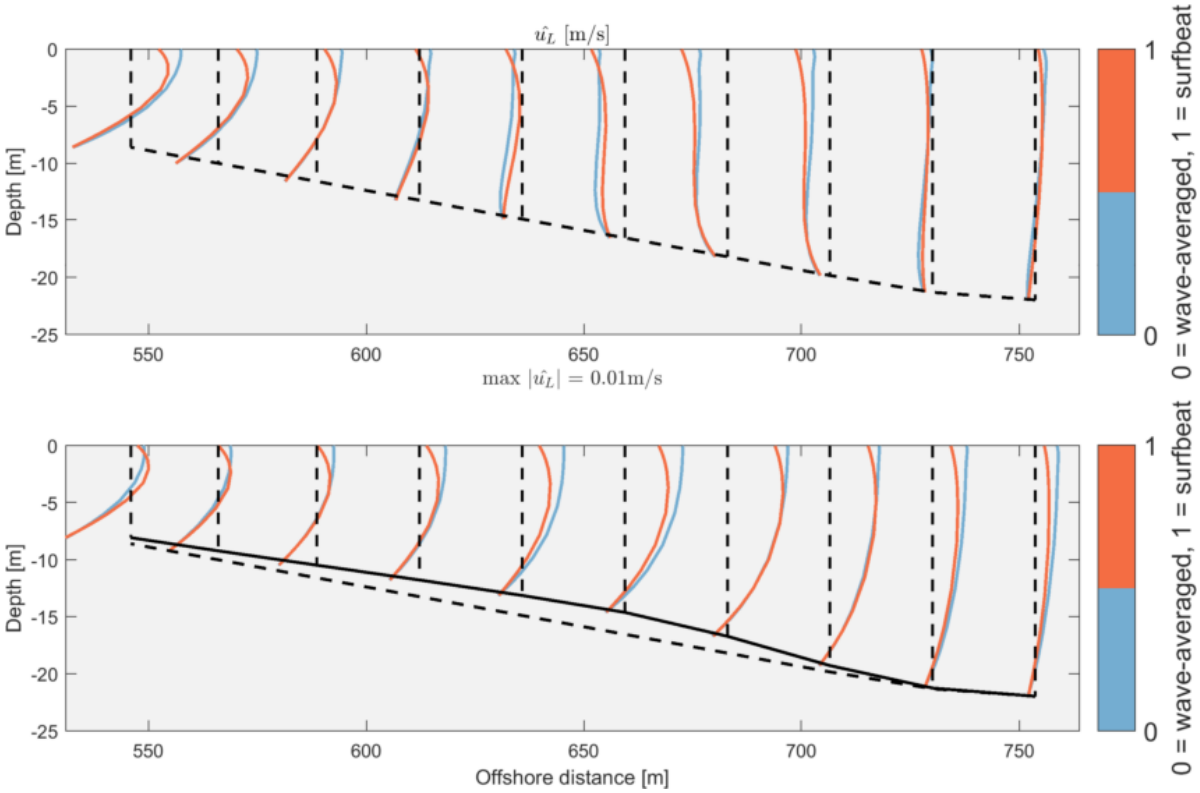

Figure 5.32: Cross-shore views of D3D-FLOW + SWAN and D3D-FLOW + XBeach surfbeat Base Case (Hawaiian type with z_μ = 17 m) results for cross-shore Lagrangian velocity $\hat{uL}$ over spur and groove.

might be relevant in the context of coral growth and health. Further research on the SAG flow within the long wave period is recommended as a next step.

5.3. MECHANISMS AND EFFECTS

In the last sections, the effects of different input parameters were evaluated through changes in the cross-shore Lagrangian velocity profile. In order to understand the mechanisms for those changes, the analysis of the momentum terms for each of the sensitivity runs were carried out. The nomenclature for the momentum terms under investigation was described in Chapter 4.1.

In the current analysis, the spatial mean along the cross-shore SAG zone of the depth-averaged momentum terms over the spur was considered for the cross-shore direction. As for the alongshore direction, a mid point between spur and groove was taken for the momentum terms, due to the relatively higher currents found there. Only cross-shore zone region where the spur height is greater than 0.4 m was assumed, so as to capture the circulation mechanisms occurring in the core of the SAG zone. The depth-averaged momentum terms were preferred for that analysis, instead of the RMS values, after sensitivity analysis showed that the overall representation is more consistent for the former ones. Besides all the momentum terms, the spatial mean of the depth-averaged imbalance between wave forces and pressure gradient was also calculated, given that it is insightful in the understanding of how momentum is balanced, as discussed in Chapter 5.1.5.

The results of the spatial mean along the SAG zone of the depth-averaged cross-shore momentum terms for the aforementioned varying input parameters are shown in Figure 5.33, while for the alongshore momentum terms they are provided in Figure 5.34.

Overall, the results show that wave forcing (red) and pressure gradients (green) have similar orders of magnitude, and that growing wave forces lead to increasing imbalance between those (yellow). Friction (black) values involve the maximum acceleration in the cross-shore, consistent with the fact that they act in a thin layer in the model parameterization, as discussed in Chapter 4.3. In the alongshore, they generally have lower values, with order similar to the wave forcing, except for the situations in which alongshore currents are enhanced - steeper slopes and alongshore wind, as further discussed in Chapter 5.4. In general, the mismatch between pressure gradient and wave forces is mostly balanced by friction and horizontal turbulent stresses,

with the advective terms - streamwise (blue) and lateral (cyan) - playing a minor role.

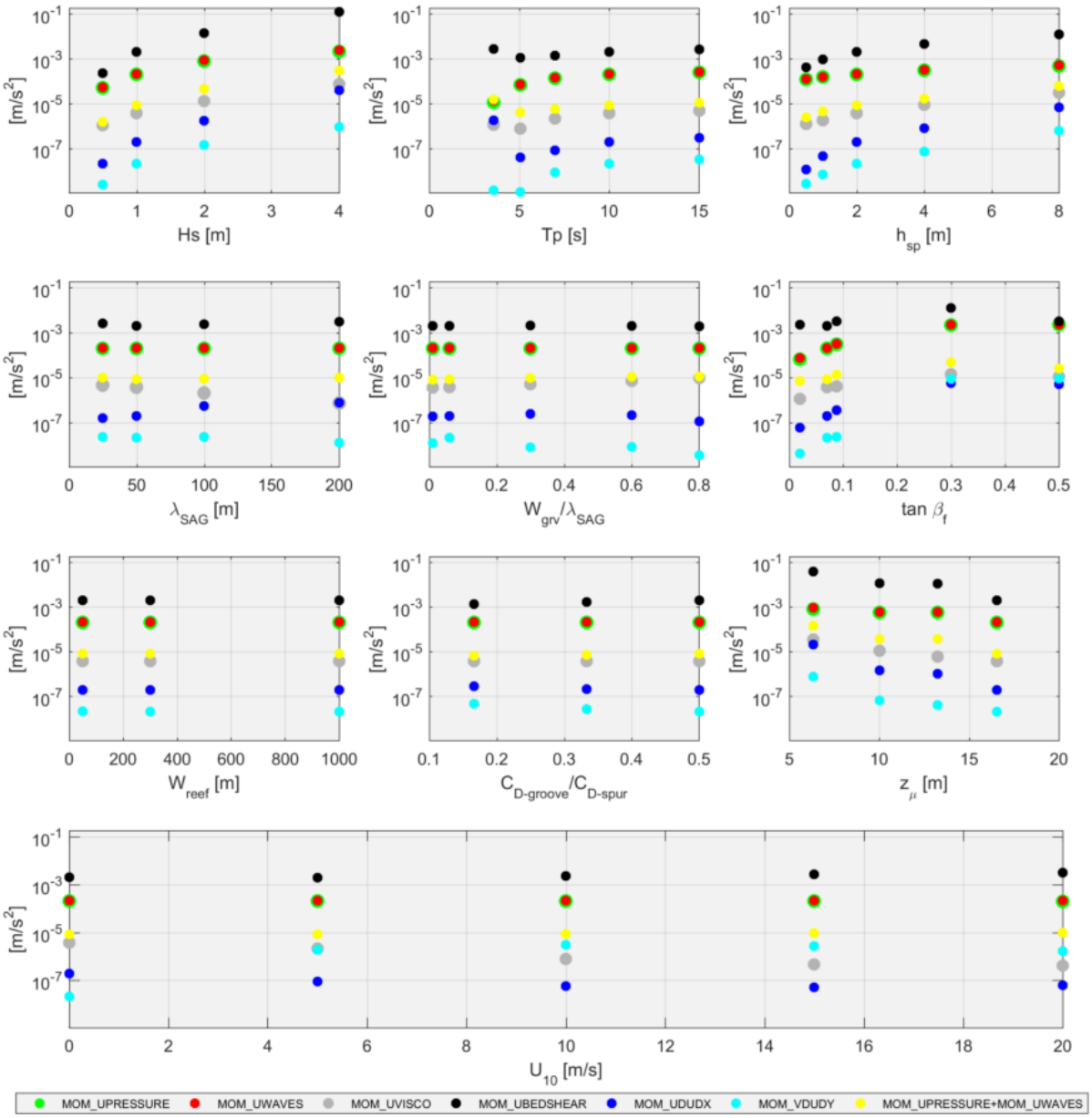

Figure 5.33: Results of the spatial mean along the SAG cross-shore section of the cross-shore momentum terms on top of the spur. MOM_UWAVES, MOM_UPRESSURE, MOM_UBEDSHEAR, MOM_UVISCO, MOM_UDUDX and MOM_VDUDY represent the wave forces, pressure gradient, bottom shear stress, horizontal viscous forces, streamwise and lateral advective accelerations, respectively.

The specifics of how momentum is balanced for each varying parameter is addressed below through comparison with the Base Case momentum balance (Chapter 5.1.5) and resulting flow pattern (Chapter 5.1.2). For the Base Case, wave forcing is mainly balanced by pressure gradient, and the mismatch between those is mainly balanced by horizontal turbulent stresses and bottom friction. The Base Case velocity profile shape was shown to be correlated with the vertical distribution of the imbalance and of the viscous forces.

5.3.1. SHORT WAVE PARAMETERS

WAVE HEIGHT

Wave heights are directly associated to wave forces (2.19 and 2.20), as energy is primarily a function of wave height (2.2). With growing wave heights, pressure gradients grow accordingly, as well as the imbalance between them. The way this mismatch is balanced is approximately constant, i.e., friction, horizontal turbulent

stresses and advective aceleration grow at the same pace as the wave forcing. This happens in both cross-shore and alongshore directions.

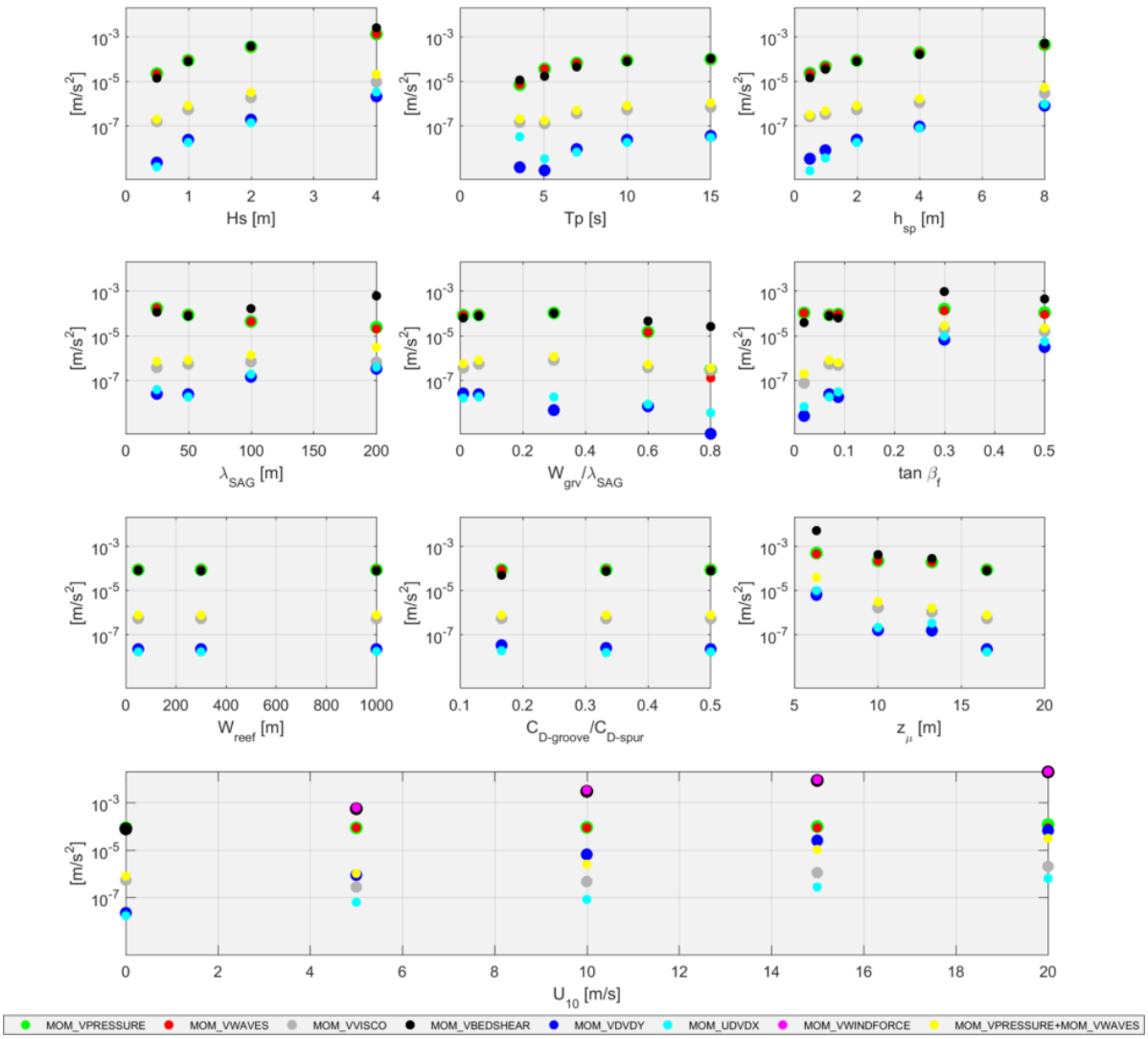

Figure 5.34: Results of the spatial mean along the SAG cross-shore section of the alongshore momentum terms on mid point between spur and groove. MOM_VWAVES, MOM_VPRESSURE, MOM_VBEDSHEAR, MOM_VVISCO, MOM_VDVDY, MOM_UDVDX, and MOM_VWINDFORCE represent the wave forces, pressure gradient, bottom shear stress, horizontal viscous forces, streamwise and lateral advective accelerations, and wind forces, respectively.

These mechanisms result in the flow pattern observed in Figure 5.21, that basically has the same shape as the Base Case, but with growing SAG circulation. Also in the alongshore an overall amplification of the strength of the flow is observed. The similar flow pattern both in cross-shore and alongshore is consistent with the overall similar way that momentum balanced, resulting in the same velocity profile.

The incoming Hs of 4 m showed depth-induced breaking over the onshore part of the SAG zone , resulting in a velocity profile with onshore surface flow and undertow with maximum values at mid depth. In cases of wave breaking, the aforementioned SAG circulation no longer holds, since the velocity profile shape changes.

WAVE PERIOD

Wave periods have influence in the wave forces (2.19 and 2.20) by affecting the wave propagation. Larger wave periods are associated with higher shoaling (2.7), thus increasing wave forces.

As for $Tp \geq 5$ s, increasing wave periods result in higher wave forcing, pressure gradients and imbalance between those. Comparatively to the wave heights, the wave forcing grows less, as well as all other terms. Similarly to the wave heights, the relative importance of the terms balancing the mismatch is constant, i.e., friction, horizontal turbulent stresses and advective aceleration grow at the same pace as the wave forcing.

Therefore, the resulting velocity profile from growing wave periods in that range provides moderate strengthening of SAG circulation comparatively to the wave heights.

As for $Tp < 5$ s, although the wave forcing and pressure gradient have the same trend as the other range of wave periods (lower wave forcing for lower Tp), the dissipation due to whitecapping is present, resulting in higher mismatch between those because of vertical imbalance in the wave momentum flux. Friction, horizontal viscous forces and streamwise advective acceleration get stronger to balance the flow. The streamwise advective acceleration is directly related to mass balance, suggesting that in breaking situations more water mass is exchanged.

These two behaviours are observed both in cross-shore and alongshore directions, with similar consequences for the alongshore flow, with moderate strengthening of currents for $Tp \geq 5$ s and different behaviour for $Tp < 5$ s, although for this particular last case the friction does not increase.

Again, breaking waves resulted in changes in the SAG circulation - with whitecapping, the velocity profile shape found on the Base Case no longer exists. The difference between breaking due to depth or steepness is that for the former the SAG circulationn is still found in the shoaling zone, while for the last there is no longer SAG circulation, since waves do not shoal but break ever since offshore.

5.3.2. SAG GEOMETRY

SPUR HEIGHT

The spur heights influence the waves by changing the shoaling pattern as result of different depths (2.7). Growing spur heights lead to higher waves over the spur, and with higher cross-shore and alongshore gradients of depth, the wave forcing increases, consistent with (2.19 and 2.20). Those forces are primarily balanced by pressure gradients, that grow accordingly. Similarly to the wave heights and periods, the relative importance of the terms balancing the mismatch is constant, i.e., friction, horizontal turbulent stresses and advective aceleration grow at the same pace as the wave forcing. This happens in both cross-shore and alongshore directions. Therefore, the resulting velocity profile from growing wave spur heights provides a significant strengthening of SAG circulation.

SAG WAVELENGTH

The SAG wavelengths do not interfere on the wave heights over spurs. As in the cross-shore direction the depth profile is the same, the resulting wave forcing does not change with different SAG wavelengths. In the alongshore, with longer SAG wavelengths the depth gradient decreases, resulting in lower wave forcing.

In the cross-shore, an increase of the streamwise advective term is observed with longer SAG wavelengths, as well as horizontal turbulent stresses. This decrease in horizontal viscous forces can be understood as mainly function of the alongshore gradient of cross-shore velocities, i.e., with longer SAG wavelengths those forces tend to decrease as alongshore gradients are lower. The increase in the streamwise advective terms is connected to the fact that those circulation cells found for the Base Case (Figure 5.10) are amplified due to more mass flux for longer SAG wavelengths.

The cross-shore flow pattern resulting from changing SAG wavelengths show two velocity profiles (Figure 5.24), one with full SAG circulation ($\lambda_{SAG} \geq 50$ m), and another one only with the SAG onshore circulation ($\lambda_{SAG} = 25$ m), while with spur and groove offshore currents in the offshore zone. This suggests that the higher horizontal turbulent stresses for shorter SAG wavelengths transfer more momentum in the alongshore between spur and groove, especially in the offshore zone, resulting in offshore currents both over spur and groove, undermining the offshore SAG circulation.

In the alongshore, although wave forcing decreases for longer SAG wavelengths, the imbalance between those increases, likely related to proportionally higher pressure gradients observed for longer SAG wavelengths. There is also a significant increase of advective terms, compatible with amplified circulation cells with growing SAG wavelength. This results in a more important alongshore circulation for longer SAG wavelengths.

GROOVE WIDTH

The groove width does not interfere on the wave heights over spurs. In the cross-shore, the wave forcing also does not change, as similar cross-shore slopes are observed (2.19). The overall effects on the cross-shore circulation with changing groove widths is minor, consistent with relatively similar momentum terms. The slight trend to undermine SAG circulation is possibly linked to growing horizontal turbulent stresses likely induced by higher alongshore gradients of cross-shore currents close to the spur for higher groove widths, similarly to what discussed in the last item.

In the alongshore the currents are in general lower for growing groove widths, consistent with the decrease of momentum terms due to overall lower alongshore gradients.

CROSS-SHORE SLOPE

The cross-shore slope has an important role in the wave forcing. Steeper profiles tend to have higher cross-shore wave forcing, due to higher cross-shore gradient of radiation stresses (2.19). As for $\tan\beta_f < 0.10$, more likely found on SAG formations (Duce et al., 2016), all other terms grow accordingly, resulting in relatively similar flow conditions, with a slight increase of strength of SAG circulation. The steepest slopes ($\tan\beta_f > 0.10$) present much higher advective terms, consistent with dominant alongshore currents.

REEF FLAT WIDTH

The reef flat width was found to produce no important difference in the flow profile over the SAG zone. Thus the momentum balance both in the cross-shore and alongshore directions looks equivalent for different reef flat widths.

FRICTION COEFFICIENT RATIO

The friction ratio between spurs and groove $\frac{C_{D-grv}}{C_{D-spr}}$ was shown to have a limited role. Likewise, the momentum balance for different friction ratios show similar overall momentum terms both in the cross-shore and alongshore. In the cross-shore, the friction gets larger for increasing ratios of friction. As the friction coefficient over the spur remains the same for all cases, lower groove friction coefficients lead to lower spur friction. As the vertical turbulent stresses distribution is unknown (Chapter 4.1), the mechanism by which those stresses are affected by different friction coefficients requires further investigations (Chapter 6.3).

POSITION OF MAXIMUM SPUR HEIGHT

The position of peak spur height is related to the zonation of the circulation cells. With decreasing z_μ, an amplification of the flow strength was observed. In general, gradients of depth located further onshore involve higher wave forcing due to higher waves found on that zone. Those forces are primarily balanced by pressure gradients, that grow accordingly. Similarly to the wave heights, periods and spur heights, the relative importance of the terms balancing the imbalance is constant, i.e., friction, horizontal turbulent stresses and advective aceleration grow at the same pace as the wave forcing. This happens in both cross-shore and alongshore directions. Therefore, the resulting velocity profile from lower z_μ provides a significant strengthening of SAG circulation.

5.3.3. ALONGSHORE CURRENTS

The alongshore forcing was shown to have an important role on the SAG offshore circulation cell, even without changes in the geometry or wave forcing.

In the alongshore direction, the wind force is fully balanced by friction. Growing wind forcing are associated with the increase of horizontal turbulent stresses and advective acceleration, mainly the streamwise one. With growing horizontal turbulent stresses, the momentum is transfered in the alongshore, resulting in more offshore currents over spurs and grooves. As those stresses are relatively more important in the offshore zone, the change in velocity shape occurs in the offshore zone. In the cross-shore, the lateral advective term gets more important with increasing wind action, consistent with dominant alongshore currents.

5.3.4. OVERALL MECHANISMS AND EFFECTS

The summary of the most important aforementioned effects in the cross-shore velocity profile due to changing input conditions and associated mechanisms is provided in Table 5.1.

Table 5.1: Important effects in the cross-shore velocity profile and associated mechanism – Wave, SAG Geometry and Alongshore Currents. The ratio of groove width and SAG wavelength $\frac{W_{grv}}{\lambda_{SAG}}$, the reef flat width W_{reef} and the presence of long waves were shown to play a minor role.

Type	Symbol	Main effects	Mechanism
Wave parameters	Hs_0	Significant enhancement of SAG circulation	Growing of all momentum terms for increasing Hs
		Undermining of offshore SAG circulation - wave-induced current profile with onshore flow near surface and undertow approaching the bottom	Depth-induced breaking ($\frac{H}{h} = 0.78$)
	$\frac{Hs_0}{Lp_0}$	Undermining of offshore SAG circulation - wave-induced current profile with onshore flow near surface and undertow approaching the bottom	Steepness-induced breaking ($\frac{H}{L} = \frac{1}{7}$)
	Tp	Enhancement of SAG circulation	Growing of all momentum terms for increasing Tp
	h_{spr}	Significant enhancement of SAG circulation	Growing of all momentum terms for increasing h_{spr}
	λ_{SAG}	Enhancement of SAG circulation	Growing of streamwise advective term for increasing λ_{SAG}
		Undermining of offshore SAG circulation by shifting of velocities towards offshore	Growing of horizontal turbulent stresses for decreasing λ_{SAG}
SAG geometry	$\tan\beta_f$	Enhancement of SAG circulation	Growing of all momentum terms for increasing $\tan\beta_f$
	$\frac{C_{D\text{-}grv}}{C_{D\text{-}spr}}$	Undermining of offshore SAG circulation by shifting of velocities towards offshore	Decreasing of vertical turbulent stress over groove for decreasing $\frac{C_{D\text{-}grv}}{C_{D\text{-}spr}}$
	z_μ	Significant enhancement of SAG circulation	Growing of all momentum terms for decreasing z_μ
Alongshore forcing	U_{10}	Undermining of offshore SAG circulation by shifting of velocities towards offshore	Growing of alongshore horizontal turbulent stresses for increasing U_{10}

5.4. FLOW INDICATORS

This MSc thesis addresses the flow pattern found on SAG formations and the implications of that flow in the context of coral health and grow. This section introduces indicators for the flow related to those, aiming to quantify how flow is sensitive to changing input conditions. Those indicators were built based on the knowledge acquired from the Base Case results (Chapter 5.1) and from the mechanisms and resulting effects on the 3D velocity profles (Chapter 5.2), summarized in Table 5.1.

5.4.1. DEFINITION OF INDICATORS

Four types of flow indicators are proposed, described below:

- Flow pattern: related to the overall characterization of the flow pattern to be expected in SAG formations;
- Flow strength: related to how depth-averaged currents are amplified;
- Impact for plumes: related to the strength of the surface currents; and
- Impact for coral reefs: related to the strength of bottom currents and shear stresses .

The definitions of the indicators is provided in Table 5.2. The discussion about what they represent is detailed below.

Table 5.2: Indicators to quantify importance of Wave, SAG Geometry and Alongshore Currents.

Symbol	**Type**	**Definition**	**Dominant parameters influencing indicator**
h_{cr}	Flow pattern	Depth where Lagrangian depth-averaged flow reverses from offshore to onshore over spur	Tp, $\tan\beta_f$ and z_μ
$\frac{\langle\lvert V_{spr}\rvert\rangle}{\langle\lvert U_{spr}\rvert\rangle}$	Flow pattern	Ratio of mean along SAG zone of alongshore flow over mid SAG and cross-shore flow over spur	λ_{SAG}, $\tan\beta_f$ and U_{10}
$\frac{U_{spr\text{-}max}}{U_{spr\text{-}max\text{-}BC}}$	Flow strength	Normalized maximum offshore Lagrangian depth-averaged velocity over spur in the offshore zone	Hs, h_{spr}, λ_{SAG}, and z_μ
$\frac{\langle\lvert U_{sur}\rvert\rangle}{\langle\lvert U_{sur\text{-}BC}\rvert\rangle}$	Impact for plumes	Normalized mean along SAG zone Lagrangian surface (top 0.5 m) velocity over spur	Hs, $\tan\beta_f$, h_{spr} and z_μ
$\frac{\langle\lvert U_{bot}\rvert\rangle}{\langle\lvert U_{bot\text{-}BC}\rvert\rangle}$	Impact for coral	Normalized mean along SAG zone of Eulerian bottom (lowest 0.5 m) velocity over spur	Hs, $\tan\beta_f$, h_{spr} and z_μ
$\lvert\tau_{bx\text{-}z\mu}\rvert$	Impact for coral	Cross-shore bottom shear stress at peak spur height for both spur and groove	Hs, h_{spr} and z_μ

For the characterization of the flow, the first indicator (h_{cr}) is the depth where Lagrangian depth-averaged cross-shore flow reverses offshore to onshore, for example x ≈ 600 m in Figure 5.12. This point represents in

most cases the approximate location where both spur and groove currents reverse, thus with very low cross-shore transport capacity. It represents the nodal point where material brought by groove currents, regardless if from onshore or offshore, would converge to, potentially resulting in longer retention.

Exception cases for which h_{cr} does not represent that concept happen when SAG circulation no longer holds (5.1), for example with low SAG wavelenghts (λ_{SAG} = 25 m), and alongshore forcing ($U_{10} \geq 15 m/s$). For those exceptions, h_{cr} represents simply the start of the onshore SAG circulation.

The second indicator for the flow pattern ($\frac{\langle|V_{spr}|\rangle}{\langle|U_{spr}|\rangle}$) represents the importance of the alongshore currents with regard to the cross-shore flow. As discussed by Storlazzi and Jaffe (2008), the transport systems in coral reef might oscillate between alongshore and cross-shore dominance depending on the main forcing, e.g. strong alongshore flow from wind versus large storm waves. Similarly, Rogers et al. (2013) used Uc (4.1) to represent the strength of cross-shore with regard to the alongshore flow.

The flow strength was represented by $\frac{U_{spr-max}}{U_{spr-max-BC}}$, that is the normalized offshore Lagrangian cross-shore velocity peak over spur in the offshore SAG circulation zone. This flow strength was preferred to a spatial averaging due to the fact that it actually represents an observed velocity in a notable point of the cross-shore velocity profile. In the Base Case, $U_{spr-max-BC}$ happens at x ≈ 670 m, as shown in Figure 5.12.

The indicator related to impact for plumes, namely the normalized spatial mean of the absolute values of Lagrangian surface currents over spurs ($\frac{\langle|U_{sur}|\rangle}{\langle|U_{sur-BC}|\rangle}$), represents the cross-shore strength of surface transport. Although this indicator does not give the surface flow direction, it provides in most cases the transport capacity of materials towards offshore. Exceptions occur in case of wave breaking (whitecapping or depth-induced breaking), for which the surface flow over the spur turns into onshore.

The first indicator associated with impacts for corals relates the normalized mean Eulerian cross-shore velocities over the bottom, representing the overall strength of the flow felt by corals. It aims to provide predictive capability about the most important parameters influencing the flow right over them.

The second indicator related to corals, that is the spur and groove bottom shear stress at the peak spur height, provides insight into the flow motion and forces over spurs and grooves. This indicator might help understand the relative difference between hydrodynamics aspects over spur and groove. The bottom shear stress at a specific location, instead of a spatial average, with units of stresses, rather than being dimensionless, was preferred to this indicator so as to provide information about the actual stress involved in the SAG hydrodynamics.

5.4.2. RESULTS OF INDICATORS

The figures relating each indicator with the changing short wave parameters, SAG geometry and alongshore forcing are shown in Appendix E, except for the result of the last indicator $\left|\tau_{\text{bx-z}\mu}\right|$. Table 5.2 summarizes the parameters that influence the most each of the indicators, as described below.

The h_{cr} is mostly influenced by the wave period, cross-shore slope, and depth for peak spur height. Swell periods (Tp ≥ 7 s) have practically constant h_{cr}, while lower wave periods might be associated with whitecapping and reverse the flow still in deeper waters. Steeper slopes extend the offshore Lagrangian flow towards onshore, providing significant influence even for the range where SAG formations are commonly found ($\tan\beta_f < 0.10$). Depths for peak spur heights seem directionally proportional to h_{cr}.

The importance of alongshore flow was shown to be mostly influenced by U_{10}, λ_{SAG} and $\tan\beta_f$. Growing wind speeds provided increasing importance of the alongwshore flow. A wind speed of 5 m/s gives an alongshore flow in average 5 times higher than in the cross-shore, while with wind magnitude of 10 m/s it jumps to more than 20 times higher, resulting in an extreme alongshore dominance. The steeper slopes presented stronger alongshore flows, but in the more likely SAG slope range the influence is negligible. The SAG wavelength presented similar values for $\lambda_{SAG} \leq 100$ m, but alongshore currents became more than 50% of the cross-shore with λ_{SAG} = 200 m.

The flow strength $\frac{U_{spr-max}}{U_{spr-max-BC}}$ was shown to be more influenced by Hs, h_{spr}, λ_{SAG}, and z_μ. The biggest influences were found for Hs, h_{spr} and z_μ. Growing Hs leads to stronger flows in a linear trend, while the same trend is found for h_{spr}, with a parabolic shape. The peak spur depth z_μ was found to be inversely proportional to the amplification. Growing λ_{SAG} results in stronger flows, although with lower influence.

The strength of the surface flow ($\frac{\langle|U_{sur}|\rangle}{\langle|U_{sur-BC}|\rangle}$) is mostly affected by Hs, that presents the highest amplification of the surface flow (up to 20). The spur height h_{spr}, slope $\tan\beta_f$ and peak spur location z_μ also showed an important influence (up to 7). All parameters are proportional to the surface flow, except for the z_μ, similarly to the flow strength.

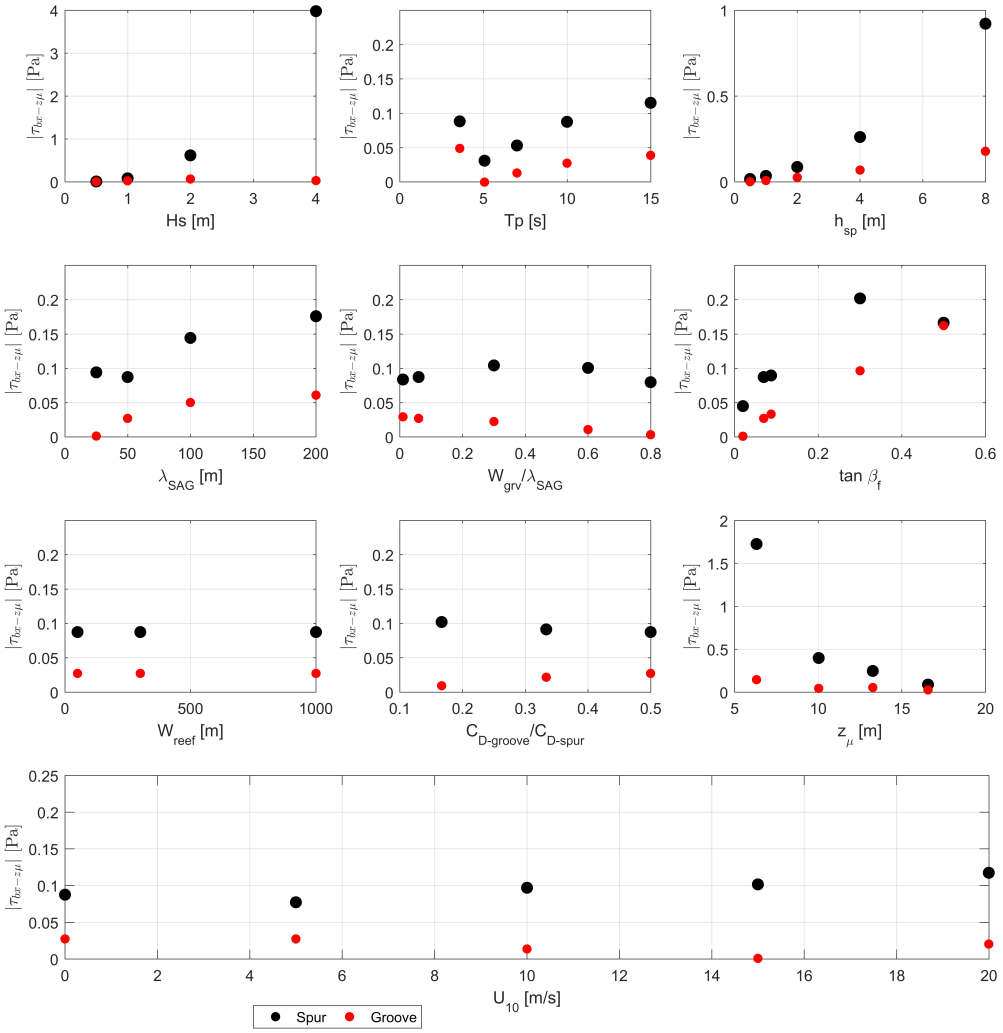

Figure 5.35: Results of $\tau_{\text{bx-z}\mu}$ for the sensitivity simulations with varying short wave parameters, SAG geometry and alongshore forcing.

The strength of the bottom flow ($\frac{\langle|U_{sur}|\rangle}{\langle|U_{sur-BC}|\rangle}$) presents a behaviour very similar to the strength of the surface flow, with biggest influence from Hs (amplification of up to 15), followed by slope $\tan\beta_f$ and peak spur location z_μ (amplification of up to 6). The spur height h_{spr} also matters to the bottom flow, but the amplification seems lower than the other parameters (up to 3), and also lower than for its influence in the surface and depth-averaged flows ($\frac{U_{spr-max}}{U_{spr-max-BC}}$ and $\frac{\langle|U_{sur}|\rangle}{\langle|U_{sur-BC}|\rangle}$, respectively).

The bottom shear stress over spurs and groove for varying short wave parameters, SAG geometry and alongshore forcing are presented in Figure 5.35. In general, bottom shear stresses are higher over the spur than over the groove, similar to the Base Case (Figure 5.11). The parameters affecting the most the $|\tau_{bx-z\mu}|$ are the Hs, h_{spr} and z_μ. Growing Hs and h_{spr} and decreasing z_μ lead to increasing bottom shear stresses. For those sensitivity runs, the highest shear stress found at peak spur height was 4 Pa. The shear stresses for the Buttress SAG type presented a shear stress of about 2 Pa, that are 10 times higher than the Hawaiian style for the same location (h ≈ 6 m).

5.4.3. OVERALL RESULTS

Overall, the most important parameters affecting the indicators were Hs, Tp, h_{spr}, λ_{SAG}, and z_μ. The cross-shore slope was also an important parameter, but with less significant influence for $\tan\beta_f < 0.10$, more likely

for SAG zones. As expected, the alongshore flow grows significantly with growing alongshore forcing. Alongshore winds tend to switch the dominance to the alongshore direction. Therefore, in situations of stronger wind speeds, the SAG circulation would be minor compared to the alongshore flow. As covered in Chapter 1.2, this MSc thesis does not address specifically the flow forced by alongshore currents, but its influence on the wave-induced flow.

The parameters Hs, Tp, h_{spr}, λ_{SAG}, and z_μ were retained for the permutation runs, i.e., for simulations where they were varied together.

5.5. FLOW PATTERN IN SAG FORMATIONS

The previous sections dealt with results from the sensitivity runs, i.e., with runs that varied one parameter at a time from the Base Case setup (Table 3.4). The parameters Hs, Tp, h_{spr}, λ_{SAG}, and z_μ were further varied together, with range of values shown in Table 3.3. The remainder model input parameters for the permutation runs were assumed to be the same as the Base Case.

The results of the permutation runs were evaluated in terms of shape of cross-shore spur and groove velocity profiles. Firstly, a description of the types of SAG current patterns is addressed (Chapter 5.5.1), followed by an evaluation of which kind of flow pattern to be expected for a given SAG formation (Chapter 5.5.2).

5.5.1. TYPES OF FLOW

The overall flow patterns encountered for all the simulations performed - sensitivity and permutation -, are summarized in Table 5.3. A classification of the velocity profile shapes was proposed, with Types A, B and C, including a few subtypes, that are elaborated below.

Type A is the flow pattern found for the Base Case (5.2), i.e., the aforementiond case with SAG circulation - offshore flow over spur and onshore over groove in the offshore zone that further onshore reverses, thus with two SAG circulation cells. This definition includes both surface and depth-averaged flows.

Type B is the velocity profile shape that for the spur has the same features as Type A, i.e., depth-averaged and surface offshore flow that further reverses at $h \approx h_{cr}$. As for the groove, the onshore part of the flow is the same as Type A, i.e., with depth-averaged and surface offshore flows. The offshore part of the flow has an offshore surface flow over the location where $U_{spr-max}$ is found, thus differing from Type A. Two subtypes were proposed: Type B.1 - with depth-averaged offshore flow over spurs in the offshore zone -, and Type B.1 - with depth-averaged onshore flow over spurs in the offshore zone -, detailed below.

Type B.2 also has the SAG circulation, i.e., in depth-averaged terms the same circulation cells from Type A happen. Examples from Type B.2 found on the sensitivity runs includes the cases with $U_{10} \leq 10$ m/s, $\tan\beta_f = 0.50$ and $\frac{C_{D-grv}}{C_{D-spr}} = 1/6$.

As for Type B.1, the offshore SAG circulation is lost, and only the onshore SAG circulation remains. Examples from Type B.1 found on the sensitivity runs include the cases with $\lambda_{SAG} = 25$ m, $U_{10} > 10$ m/s and $\tan\beta_f = 0.02$.

Type C is defined as the flow profile for which whitecapping happens every since offshore depths, resulting in onshore flow close to the surface and offshore down in the water column. Subtypes of C relate the direction of the depth-averaged flow over spur and groove in the offshore zone. Type C.1 has onshore flow over spur, while for Type C.2 this flow is offshore. Types C.1.1 and C.2.1 have offshore flow over the groove, while for Type C.1.2 and Type C.2.2 it is onshore. These subtypes were proposed as an indication of how the breaking forces and SAG dominance interact, as explored further.

In the sensitivity runs, examples from Type C include the cases with $Tp < 6$ s. As for $Tp \approx 4$ s, Type C.1.1 is observed, while for $Tp \approx 5$ s, it switches to Type C.2.1.

The cases in which breaking due to depth were not treated as a different type, since the SAG circulation was found to occur up to the breaking point.

Types A, B and C were concluded to represent reasonably the overall variation of all the simulations carried out in the current research.

5.5.2. PREDICTION OF FLOW PATTERN

The analysis of results reported so far showed that the flow pattern is a function of wave processes on top of SAG formations. The influence of wave and SAG geometry parameters on the SAG hydrodynamics was evaluated through analysis of the mechanisms by which they influence the momentum balance. Although the flow pattern expected to occur as function of waves and SAG geometry cannot be straightforwardly provided,

Table 5.3: Cross-shore flow patterns.

Type	Subtype	Flow over spur	Flow over groove
A	-	Offshore flow in deeper region, that reverses further in shallower region - both depth-averaged and surface currents	Onshore flow in deeper region, that reverses further in shallower region – both depth-averaged and surface currents
		Example in Figure 5.36	
B	-	Offshore flow in deeper region, that reverses further in shallower region - both depth-averaged and surface currents	Surface offshore flow in deeper region, and depth-averaged and surface offshore flow in shallower region
	1		Depth-averaged offshore flow in deeper region
		Example in Figure 5.37	
	2		Depth-averaged onshore flow in deeper region
		Example in Figure 5.38	
C	-	Onshore surface flow and undertow lower in the water column due to whitecapping	
	1.1	Depth-averaged onshore flow in deeper region	Depth-averaged offshore flow in deeper region
		Example in Figure 5.39	
	1.2		Depth-averaged onshore flow in deeper region
		Example in Figure 5.40	
	2.1	Depth-averaged offshore flow in deeper region	Depth-averaged offshore flow in deeper region
		Example in Figure 5.41	
	2.2		Depth-averaged onshore flow in deeper region
		Example in Figure 5.42	

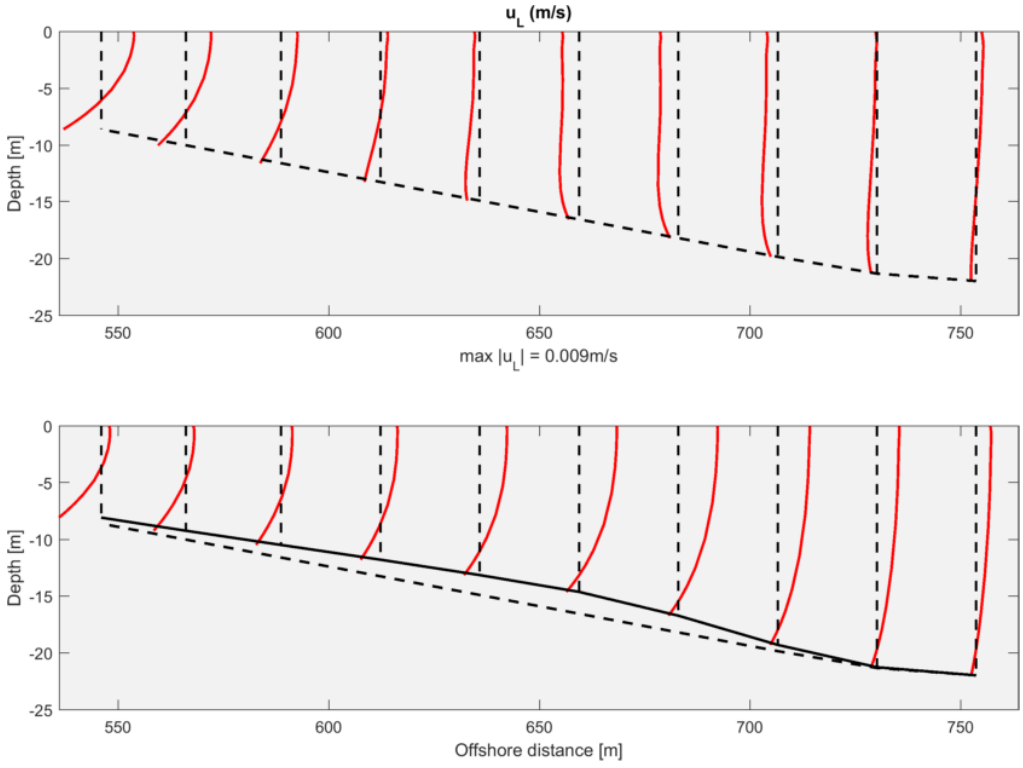

Figure 5.36: Type A of cross-shore flow pattern - Hs = 1 m, $\frac{Hs_0}{Lp_0}$ = 0.006 (Tp = 10 s), h_{spr} = 2 m, λ_{SAG} = 50 m and z_μ = 17 m.

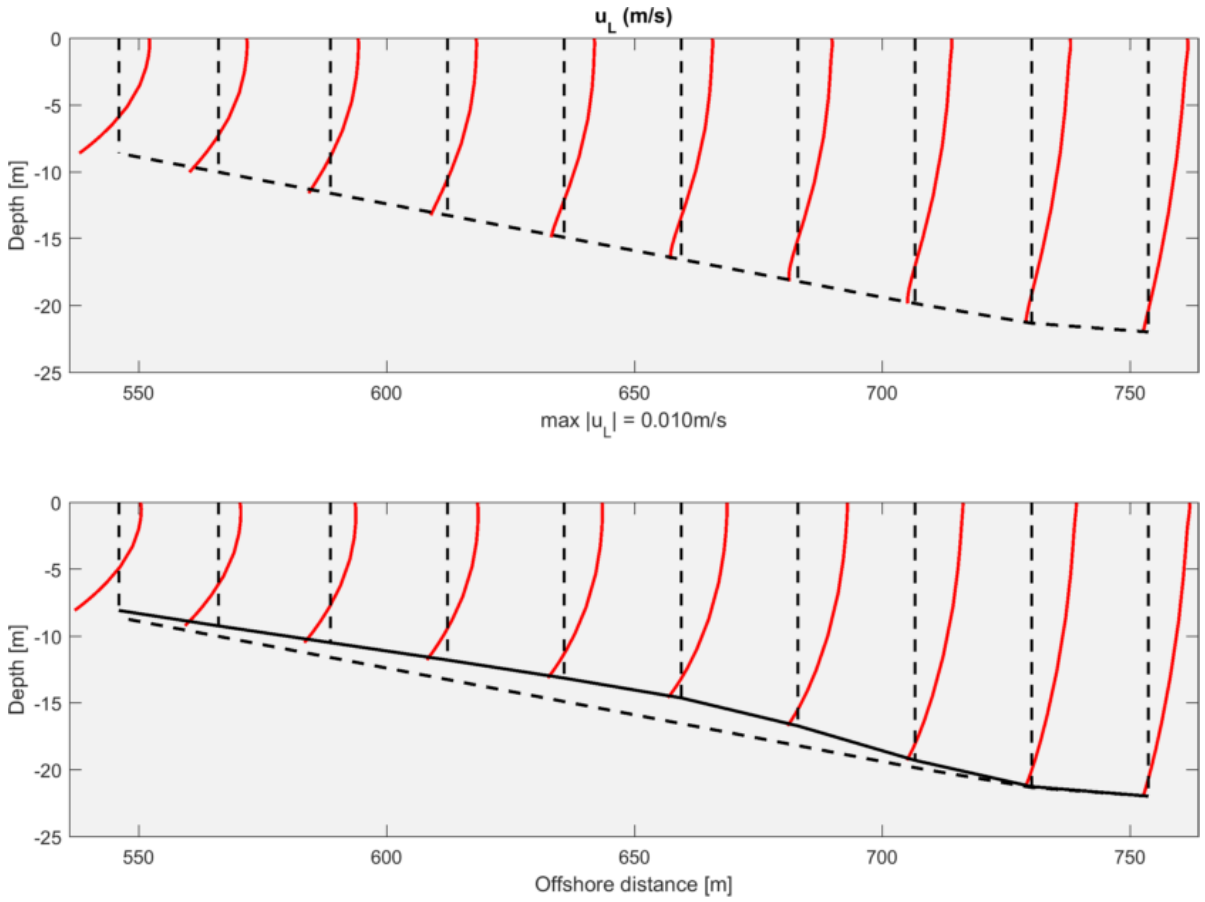

Figure 5.37: Type B.1 of cross-shore flow pattern - Hs = 1 m, $\frac{Hs_0}{Lp_0}$ = 0.006 (Tp = 10 s), h_{spr} = 2 m, λ_{SAG} = 25 m and z_μ = 17 m.

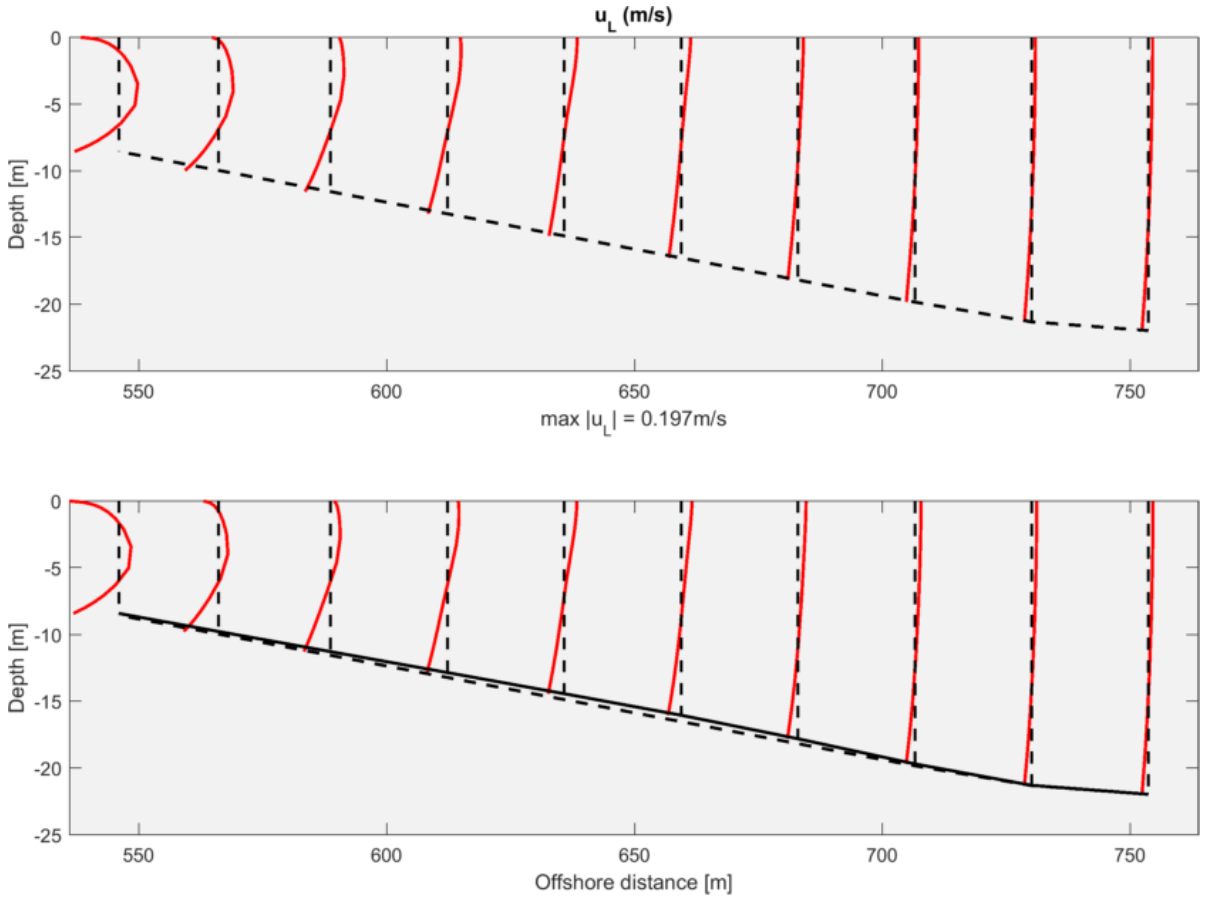

Figure 5.38: Type B.2 of cross-shore flow pattern - Hs = 4 m, $\frac{Hs_0}{Lp_0}$ = 0.006 (Tp = 20 s), h_{spr} = 0.5 m, λ_{SAG} = 25 m and z_μ = 17 m.

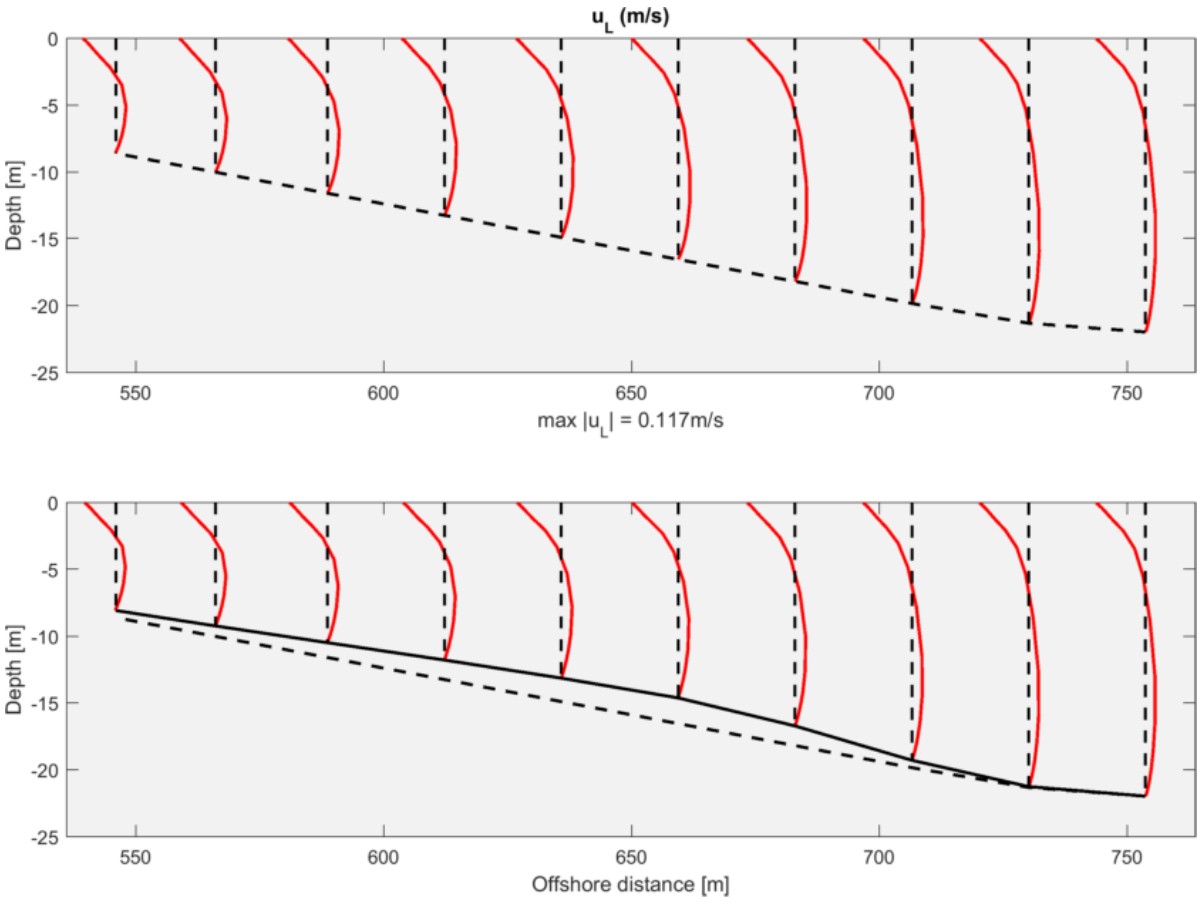

Figure 5.39: Type C.1.1 of cross-shore flow pattern - Hs = 1 m, $\frac{Hs_0}{Lp_0}$ = 0.050 (Tp = 4 s), h_{spr} = 2 m, λ_{SAG} = 50 m and z_μ = 17 m.

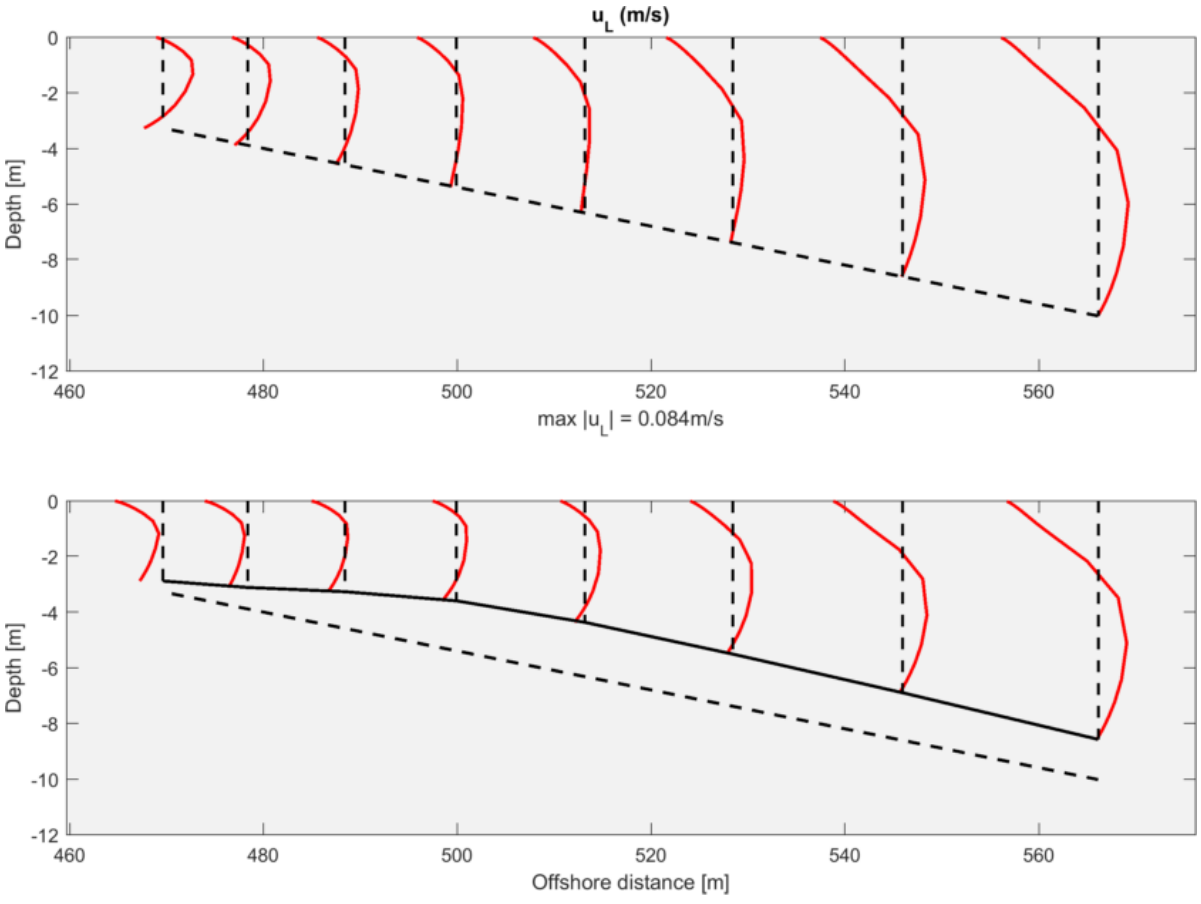

Figure 5.40: Type C.1.2 of cross-shore flow pattern - Hs = 1 m, $\frac{Hs_0}{Lp_0}$ = 0.050 (Tp = 4 s), h_{spr} = 2 m, λ_{SAG} = 25 m and z_μ = 5 m.

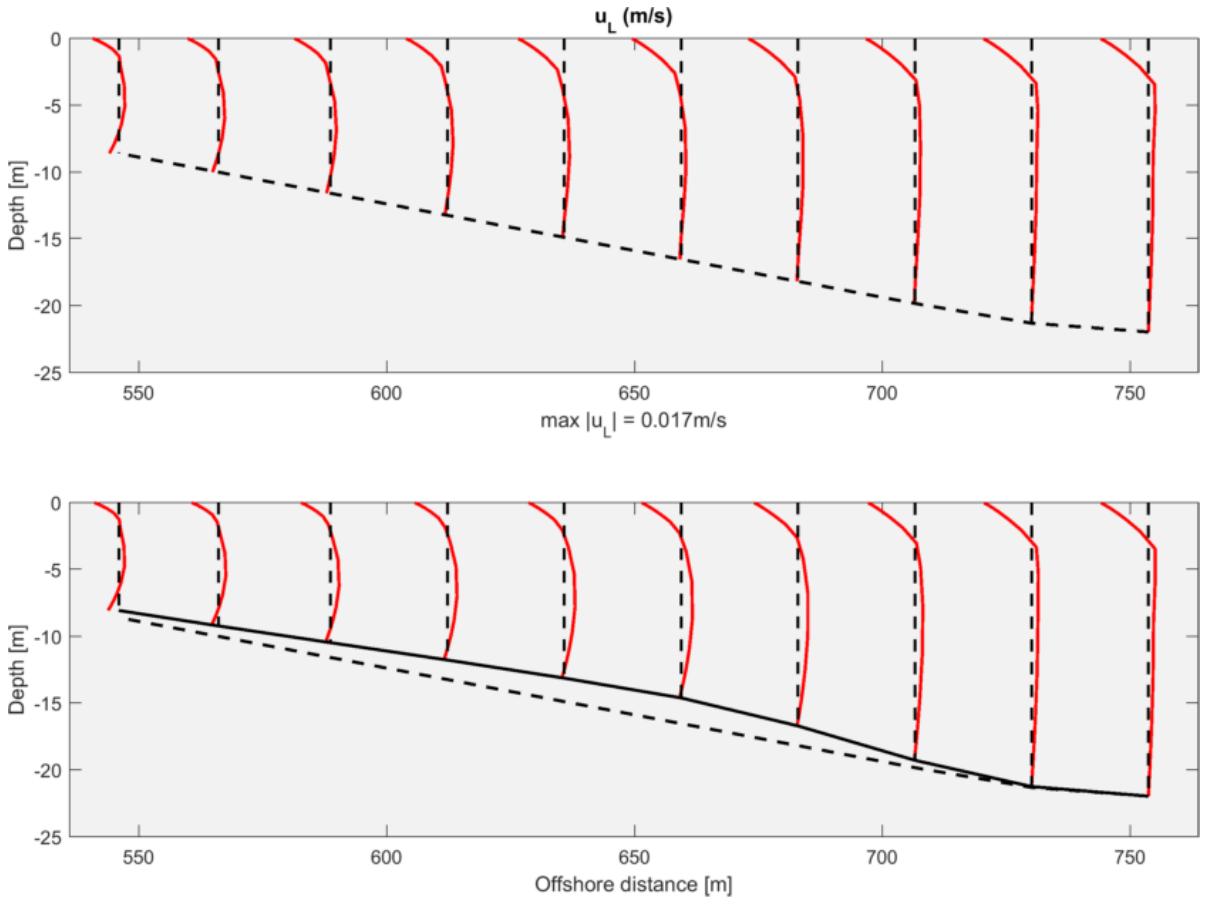

Figure 5.41: Type C.2.1 of cross-shore flow pattern - Hs = 1 m, $\frac{Hs_0}{Lp_0}$ = 0.025 (Tp = 5 s), h_{spr} = 2 m, λ_{SAG} = 50 m and z_μ = 17 m.

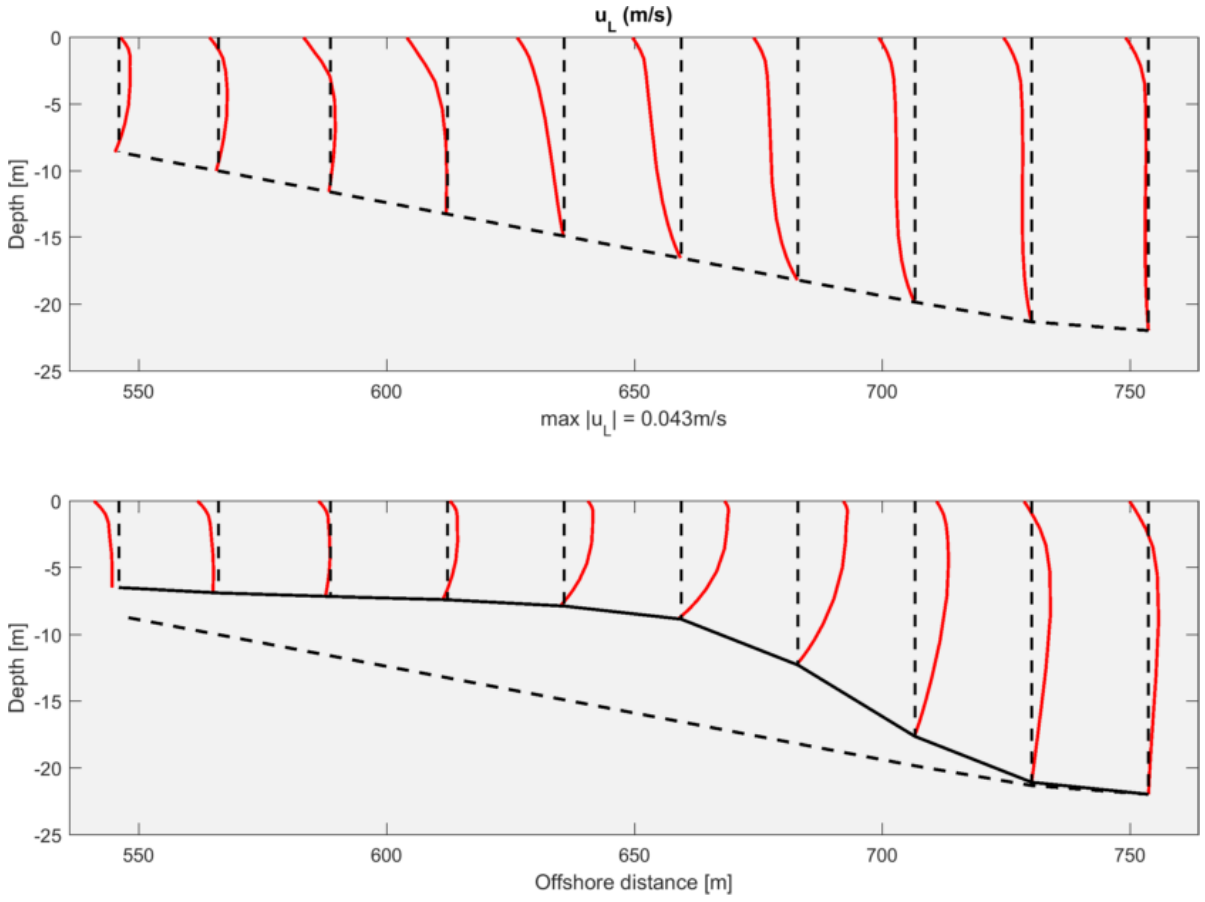

Figure 5.42: Type C.2.2 of cross-shore flow pattern - Hs = 1 m, $\frac{Hs_0}{Lp_0}$ = 0.025 (Tp = 5 s), h_{spr} = 8 m, λ_{SAG} = 100 m and z_μ = 17 m.

the insights from the sensitivity runs (Table 5.1) were found to be coherent with the velocity profiles found for the permutation runs.

With higher $\frac{Hs}{Lo}$, there is more potential for whitecapping ever since depths of 20 m, resulting in Type C. Type C.1 is in general correlated with higher $\frac{Hs}{Lo}$ and lower h_{spr} and λ_{SAG} comparatively to Type C.2, suggesting that higher amount of breaking forces lead to depth-averaged onshore flow over the spur in the deeper region. On the other hand, Type C.2 is correlated with higher h_{spr} and λ_{SAG} and lower $\frac{Hs}{Lo}$, indicating that the increasing of SAG structure (h_{spr} and λ_{SAG}) results in offshore flow over spur. Accordingly, Type C.1 can be thought of as whitecapping dominated, while C.2 is SAG dominated.

The distinction between Types C.1.1 and C.1.2, as well as C.2.1 and C.2.2, correlates with the SAG wavelength. Types C.1.2 and C.2.1 were found only for shorter SAG wavelengths. In general, for shorter SAG wavelengths the currents over the spur and groove in the offshore zone have the same sign. This is consistent with the growing horizontal turbulent stresses mixing momentum in the alongshore, as discussed in Chapter 5.3.

Apart from the whitecapping cases, SAG formations were concluded to experience velocity profiles with Types A and B. The distinction between Types A and B is again correlated with the SAG wavelength, as Type B was only found for shorter SAG wavelengths. As for Type B, the offshore currents are observed over the spur and at least the surface flow is also offshore, suggesting that the higher viscous forces in lower SAG wavelenghts mix momentum between spur and groove in deeper waters. The comparison between Types B.1 and B.2 shows that B.1 in general occurs for lower wave heights, and vice-versa. Higher wave heights were previously observed to increase the SAG circulation character, consistent with Type B.2 occuring for higher wave heights

Type A represents the SAG circulation, i.e., the existence of two circulation cells where spur and groove have velocities with opposite sign. It is the case found for most of the simulations. The previous findings suggest that for all cases without whitecapping for sufficiently big SAG wavelength, Type A occurs. Similarly, without whitecapping, at least the onshore circulation cell - with offshore groove and onshore spur currents - was showed to occur.

The current analysis aimed to provide insights into the prediction of flow profile through results of the analysis of the mechanism by which momentum is balanced in SAG formations. It is important to reinforce that the final velocity profile to expect is a function of the specifics of the case. The type of flow for every simulation performed in the current research is presented in the list of simulations provided in Appendix A.

6

DISCUSSION

This chapter provides a discussion about the significance of the results shown in Chapter 5. Firstly (Chapter 6.1), the interpretation of the findings from Chapter 5 are put into perspective regarding the types of SAG formations and expected dominant wave climate, that were previously covered in Chapter 2. Next, an evaluation about the implications of the SAG hydrodynamics for corals, sediments and nutrients is elaborated in Chapter 6.2. Finally, the limitations of this study, mainly connected to model uncertainties, are addressed in Chapter 6.3.

6.1. FLOW OVER SAG FORMATIONS

SAG formations are present in the fore slope of coral reef environments, with examples found worldwide, especially in low latitudes. They consist of elevated rhythmic shore-normal ridges of corals, separated by sediment covered channels, and are more commonly found in environments with shore-normal waves. SAG geometry properties are highly variable both between and within reefs.

As the dataset of measured SAG geometry properties is still very limited, it is not straightforward to generalize the knowledge acquired from the model results with regard to a representative SAG formation. This MSc thesis hypothesizes that sheltered locations have SAG development closer to the reef flat (Buttress type), while in more exposed locations their development migrate to deeper areas (Hawaiian).

The model results show that SAG bathymetries have different cross-shore current pattern between spur and groove, with reversed Lagrangian currents on top of them. The comparison between model results for alongshore uniform and SAG bathymetries shows that their introduction is associated with the creation of an alongshore imbalance that results in circulation cells.

The circulation cells consist essentially of reversed values of cross-shore currents over spur and groove: in the offshore cell, currents are onshore over the groove, while offshore over the spur, and the vertical distribution for both shows vertically monotonic currents, except for the bottom, at which velocities are always onshore; as for the onshore cell, the velocity profile shows offshore surface velocities and onshore bottom currents for both spur and groove, but with resulting depth-averaged offshore and onshore over groove and spur, respectively. This pattern - counter-rotating cells - was also observed by Rogers et al. (2013) in a depth-averaged sense.

Those circulation cells were observed for all cases without breaking waves, namely, shoaling waves over SAG formations are associated the development of those cells. The observation of the onshore circulation cell occurred for all the simulated cases without wave breaking. This cell extends from the breaking point up to the location where spur currents reverse, and is characterized by depth-averaged groove offshore and spur onshore currents. The offshore circulation cell was not present for the cases with strong alongshore wind and with shorter SAG wavelengths. The occurrence of alongshore winds is site and time specific, and results in other dominant effect, discussed further below.

Regarding the SAG wavelengths, the compilation of reported SAG structures (Figure 2.10) shows that mean SAG wavelengths can vary significantly. The shorter SAG wavelengths would tend to have only the onshore SAG circulation cell, since in the offshore zone both spur and groove currents remain offshore due to enhanced mixing by horizontal viscous forces. The increase of SAG wavelengths with higher depths was reported both by Storlazzi et al. (2003) and Duce et al. (2016). Their higher values in deeper waters suggest a

more likely existence of two circulation cells. However, with the schematic bathymetry assumed in the current research, the effect of varying SAG wavelengths for a same reef remains unknown, and needs further investigation.

The circulation cells were evaluated in term of strength and zonation. The strength of those cells - considering surface, depth-averaged and bottom velocities - was shown to be dependent mainly on the wave height, the spur height and on the SAG shape (location of peak spur height). Higher wave and spur heights together with lower peak spur height depths tend to present stronger circulation cells. Higher incoming waves are more expected to occur in environments with higher peak spur height depths (Storlazzi et al., 2003), while lower peak spur height depths are associated with lower incoming waves. Therefore, the strength of the flow in a way could be expected to converge for different SAG shapes due to those compensating mechanisms.

In terms of cells zonation, the reef slope and again the SAG shape have higher influences on the narrowing or widening of the circulation cells. Steeper slopes tend to widen the offshore circulation cell, while narrowing the onshore one. The research from Duce et al. (2016) with extensive measurement showed less likely development of SAG in steeply sloping ($\tan\beta_f > 0.10$). Therefore, the widening of the offshore circulation cell is less probable. As for the shape, lower peak spur height depths tend to have a narrower onshore circulation cell, suggesting that the location where spur currents reverse are close to the cross-shore position where SAG development is more noticeable.

The circulation cells reported so far consist of cross-shore transport system, i.e., with dominance of cross-shore velocities over the alongshore or vertical currents involved. While the vertical velocities were shown to be relatively low for all simulated cases, there are situations in which the cross-shore dominance switches to alongshore, as discussed below.

An initial evaluation of the oblique waves influence in the SAG flow is addressed in Appendix F. Although oblique waves might not be the dominant waves in SAG formations, waves at relatively low angles (15 degrees) already switch the dominance from a cross-shore to an alongshore transport system. For those cases, the onshore circulation cell remains and gets wider and stronger, although with alongshore velocities much higher. Even with the shore-normal waves being dominant, alternations of shore-normal and at least low angle waves are expected to occur in SAG bathymetries, such as measured in Palmyra Atoll (Rogers et al., 2015). For those cases, the onshore circulation cell would be persistent, while the offshore cell would oscillate.

As for the alongshore forcing, the alongshore dominance gets stronger proportionally to the input forcing. In situation of high alongshore forcing (e.g., strong alongshore winds), alongshore currents might become extremely higher than the cross-shore velocities involved in the circulation cells. Still, the onshore cells are persistent regardless of the wind speed, while the offshore cell progressively gets undermined with higher winds.

The situations without circulation cells at any point are connected with steepness-induced breaking waves. For those cases, the wave dissipation leads to velocity profile with onshore surface currents and undertow lower in the water depth. Similarly, for the situations with depth-induced breaking, the SAG circulation cell as elaborated above ceases existing. The difference between the former and the last is that for the last SAG circulation cells still occurs outside the breaking zone, thus the breaking role is to shift the onshore start of the onshore cell. As for the former, the steepness-induced breaking was showed to occur ever since the offshore start of the SAG bathymetries, thus no circulation cell was observed.

6.2. IMPLICATIONS OF SAG HYDRODYNAMICS

This section discusses the general implications of the calculated SAG hydrodynamics in terms of coral health and growth.

In general the results found on this research show the existence of two circulation cells, one located in deeper waters with offshore spur and onshore groove currents, and the other in shallower waters with reversed signs. The boundary between those cells means a convergence point for the groove currents, resulting in a nodal point where nutrients would tend to converge to, potentially resulting in longer retention. Its location close to the peak spur height suggests that in the long-term this preferential drift spot for nutrients could contribute to the SAG development.

The coral development is usually though to be dependent on the increasing water motion, associated with more mass transfer and nutrient uptake, possibly enhancing photsynthetic production (Falter et al., 2004; Rogers et al., 2013). In that sense, results show that the bed shear stresses over spurs are in general higher than over grooves, consistent with a higher potential of coral development in the ridge rather than in the channel.

The higher shear stresses over spur could also be associated with a higher potential for sediment transport. The relatively higher alongshore currents over spurs would tend to transport sediments to the grooves, where they would more likely deposit, due to a lower alongshore current and lower shear stress to resuspend them. In a way, this behaviour can also be connected to an enhanced coral development over spurs, due to a resulting lower suspended sediment concentration over them.

In cases of extreme wave heights, the bottom shear stresses over spurs were found to grow in parabolic shape. Similarly, bottom shear stresses over spur also increase with parabolic shape with decreasing peak spur height depths. Extreme bottom shear stresses could result in coral breakage, undermining SAG development. This finding is consistent with presence of Buttress type of SAG in less exposed locations, such as the Caribbean Sea, rather than the Hawaiian type with peak spur heights at depths of around 17 m, with rougher wave climate.

Similarly to the strength of the flow, the bottom shear stresses experienced by Hawaiian and Buttress SAG types tend to converge due to differential wave climate. This suggests that there is a range of hydrodynamics ideal conditions for coral development, where minimum shear stresses are needed for mass exchanges and nutrient uptake, and extreme values would result in coral breakage.

The Lagrangian velocity profile both over spurs and grooves showed persistent onshore bottom currents all over the SAG zone. Consequently, the bottom material would tend to slowly migrate from the outer slope to the reef flat, potentially carrying nutrients. On the other hand, material coming from the reef flat would be transported through the groove, that in a depth-averaged sense would carry the material up to the boundary of the circulation cells, where it could be potentially be retained, as discussed above.

For the cases without offshore circulation cells (oblique waves, strong alongshore forcing and short SAG wavelengths), material could continue further offshore towards the outer reef slope. This zone usually has steeper profiles, with a higher potential to gravitational transport downslope.

6.3. LIMITATIONS

This MSc thesis applied numerical modelling to reproduce the hydrodynamics of spurs-and-grooves formations. This section discusses the uncertainties related to the model (Chapter 6.3.1) and to the modelling aproach (Chapter 6.3.2) adopted in the current research to answer the research questions.

6.3.1. MODEL LIMITATIONS

The uncertainties associated with the use of D3D-FLOW coupled with SWAN/XBeach are firstly related to the equations solved by them, that do not resolve the wave phase, but represent its effects averagely. This means that wave forces are not solved within the wave period, but they are calculated with LWT formulation for radiation stresses (2.14, 2.15 and 2.16). The GLM formulation solves the wave-forced flow for Lagrangian velocities, and D3D-FLOW parameterizes bottom friction as function of the Eulerian velocities, thus assuming Stokes drift present at every cell. Also, Stokes Drift velocity is represented by LWT equation (2.27), instead of being function of the result of mass flux and Eulerian velocities (2.29).

The wave forces are calculated based on the wave parameters given by SWAN/XBeach. These models solve the wave action balance equation (3.2), that represents the spatial propagation of the wave energy, including processes such as refraction. The wave energy is assumed to propagate through wave rays, that by definition do not cross each other. Without propagation of energy across them, the diffraction is not considered by that equation.

As described in Chapter 4.2, the model was calibrated with results from another model that does consider the phase of the wave. During the calibration, it was noticed that shore-normal waves on top of SAG formations lead to extreme concentration of wave energy due to refraction that could not be smeared out by diffraction. Reasonable results concerning both wave propagation and flow pattern were obtained running SWAN with refraction deactivated. The results of sensitivity runs with and without refraction indicated that for all cases with refraction there was a high alongshore gradient of wave between spur and groove, not compatible with previous measurements (Rogers et al., 2015) and modelling (Rogers et al., 2013). Next, all simulated cases neglected refraction based on that assumption.

Although it is likely that diffraction overcomes refraction effects for SAG formations, there are situations in which this dominance might be undermined, e.g. with longer SAG wavelengths (Rogers et al., 2013). Also, in cases of oblique waves, even with diffraction being dominant, the wave directions on top of SAG may change towards more shore-normal waves. Those effects were not considered in the current research, and need further investigation.

The current research concluded that both long waves, primarily important as approaching the reef flat, and the reef flat width to have negligible influence in the hydrodynamics of SAG zone. Although the model calibration presented reasonable agreement in the SAG zone, the non-linear degree of waves in the surfzone grows, and this effect is not accurately represented by wave-averaged models (Figure 3.1). The model limitation to accurately reproduce the reef flat flow results in a less precise prediction of the interaction in terms of mass flux between them, and further research seems warranted.

Another model limitation is related to the fact that it does not provide as output neither the vertical diffusion of momentum nor the Fourier output for momentum terms that would be required for cases with long waves.

6.3.2. MODEL APPROACH LIMITATIONS

As for the modelling approach, the use of schematic bathymetry introduces simplifications with unknown influence on the hydrodynamics. For example, the SAG wavelength is generally reported to decrease as moving onshore. In the representation done in this research (Figure 3.2), the alongshore shape remains the same regardless of the bathymetry. Besides, although the shape was varied in function of the location of the peak spur height, the cross-shore shape was always assumed to be the aforementioned Gaussian skewed shape. The complexity of specific SAG formations is expected to exert important local effects, possibly associated with alongshore gradients of depth enhancing secondary currents.

As covered in Chapter 3.2.5, the wave-current interaction was not part of the current investigation. Although in general the current values involved in the SAG zone are low, the extreme wave heights or the Buttress SAG types tend to experience higher velocities. Further research especially for those extreme cases are recommended.

The alongshore forcing was evaluated with alongshore wind action. The wind is parameterized as a stress imposed on the water surface, that is mixed along the water column, generating alongshore currents. Although the effects on the velocity profile were treated as coming from a generic alongshore forcing, it is expected that the obtained results are representative only for the wind action.

7

CONCLUSIONS AND RECOMMENDATIONS

This chapters provides the conclusions (Chapter 7.1) of the current research, that specifically address the research questions described in Chapter 1.2, and the recommendations (Chapter 7.2) for the next step of the investigation of the SAG hydrodynamics.

7.1. CONCLUSIONS

The primary objective of this MSc thesis is to describe the flow patterns and to identify what are the dominant processes involved in the flow within SAG formations.

Shore-normal shoaling waves on top of SAG formations drive two circulations cells, the first in deeper waters with offshore spur and onshore groove depth-averaged velocities, and the second in shallower depths with offshore groove and onshore spur depth-averaged currents. This pattern is referred to as SAG offshore and onshore circulation cells, that are essentially zones with reversed values of cross-shore currents. In the offshore cell, the cross-shore velocity profile shows vertically monotonic currents - onshore to grooves and offshore to spurs -, except for the bottom, at which velocities are always onshore. In the onshore cell, the velocity profile shows offshore surface velocities and onshore bottom currents for both spur and groove, with resulting depth-averaged offshore groove and onshore spur velocities.

In terms of processes, the wave forcing is mostly balanced by pressure gradients both in the cross-shore and alongshore, and the mismatch between those is balanced by horizontal turbulent forces, that are higher in deeper waters, and friction, larger in shallower waters. Variations of this pattern are associated with changes in the velocity profile, that fundamentally depend on the wave, SAG geometry and alongshore forcing parameters.

7.1.1. FIRST SUBOBJECTIVE - HORIZONTAL AND VERTICAL FLOWS

The first subobjective of this research is to characterize the horizontal and vertical flows involved in SAGs.

Shore-normal waves, that are more most commonly found in SAG formations, drive the aforementioned circulation cells. In general the alongshore currents for the same cross-shore position converge towards either spur or groove, but with relatively lower strength than the cross-shore velocities found in the circulation cells. The vertical flows have much lower velocities than both the alongshore and cross-shore flows.

7.1.2. SECOND SUBOBJECTIVE - ROLE OF SHORT WAVE VARIATION

The second subobjective of this thesis is to determine the role of short wave variation in the SAG flow.

The waves are main driving of the SAG flow, and as such wave parameters - wave height, period and direction - play a fundamental role in the SAG hydrodynamics. The only parameter without noticeable influence was the directional spreading.

Wave heights are the most important parameter associated with the flow strength. Higher waves induce significantly stronger circulation cells, primarily due to the higher wave forcing involved in the momentum balance, that lead to an overall growing of the remainder balancing terms. When wave heights start breaking due to depth limitation, the SAG circulation cell is lost, and the velocity profile shape starts having onshore surface and undertow with maximum values at mid depth.

Wave periods have moderate influence on the velocity values found on SAG circulation cells. Although higher wave periods enhance the wave forcing due to higher shoaling, the overall increase in the wave forcing and the remainder balancing terms is not significant comparatively to the wave height. When the wave steepness reaches the breaking limit in the offshore start of the SAG profile, the whitecapping results in changes of the velocity profile similarly to the case of depth-induced breaking waves, but in this case the parabolic shape is less prominent due to lower vertical mixing.

The role of varying wave directions and directional spreadings could not be accurately evaluated due to uncertainties related to the importance of refraction and diffraction using a phase-averaged model. An initial assessment of their importance with a model neglecting refraction, thus with unchangeable wave direction, was performed. Results showed that oblique waves result in alongshore transport systems, i.e., cross-shore currents become significantly lower than in the alongshore. In those cases, the SAG offshore cell is lost, and the onshore cell gets wider and stronger, mainly associated with the growing of lateral advective term in the momentum balance. On the other hand, the directional spreading was shown to have very low influence on the flow pattern.

7.1.3. THIRD SUBOBJECTIVE - ROLE OF SAG GEOMETRY

The third subobjective of this thesis is to determine the role of SAG geometry in the SAG flow.

The SAG geometry has a very important role associated with the resulting SAG hydrodynamics. Each of the geometry parameters has a specific kind of effect associated with different mechanisms. Overall, the spur height, SAG wavelength and the SAG shape provide the biggest influence on the hydrodynamics.

The spur heights have significant influence in the strength of SAG circulation cells. Higher spur heights are associated with stronger flows, due to the higher wave forcing as a result of higher waves over the spur and to higher cross-shore and alongshore gradients of depth. The higher wave forcing results in an overall growing of the remainder balancing terms, resulting in growing SAG cells velocities.

The SAG wavelengths moderately influence the strength of the flow, with longer SAG wavelengths resulting in not much stronger SAG circulation cells. Shorter SAG wavelengths do not present the offshore SAG circulation cell, due to higher alongshore mixing of momentum that gives offshore spur and groove currents in that zone. Longer SAG wavelengths result in larger circulation cells that have proportionally higher alongshore currents, consistent with more mass flux within them.

The shape of the SAG formations is, together with the wave heights, the most important parameter influencing the strength of the flow. SAG formations with peak spur height located further onshore (Buttress type) have SAG circulation with higher velocities involved, as a result of growing wave forces and remainder momentum balance terms enhanced by higher depth gradients situated in shallower waters. The zonation of the SAG circulation cells changes accordingly, i.e., lower peak spur height depths have circulation cells shifted onshore, with widening of the offshore cell.

The reef slope for the more likely range where SAG formations are found does not interfere significantly neither on the strength nor in the velocity profile shape. Instead, the zonation of SAG circulation cells is affected, with steeper slopes providing wider SAG offshore circulation cells.

On the other hand, the groove width, the differential roughness between spur and groove, and the reef flat widths were shown to have a minor role in the SAG hydrodynamics, without significant changes associated.

7.1.4. FOURTH SUBOBJECTIVE - ROLE OF SAG ALONGSHORE CURRENTS

The fourth subobjective of this thesis is to determine the role of driving alongshore currents in the SAG flow.

The alongshore forcing leads to an alongshore transport system. The degree of the alongshore dominance is directionally proportional to the alongshore forcing. In the cross-shore direction, the onshore SAG circulation cell was persistent, while the offshore cell can be undermined with large alongshore forcing.

7.1.5. FIFTH SUBOBJECTIVE - ROLE OF LONG WAVES

The fifth subobjective of this thesis is determine the role of long waves in the SAG flow.

Long waves were shown to result in negligible influence in the mean SAG hydrodynamics, associated with the low long wave forcing observed in the SAG zone. They are primarily more important as approaching and within the reef flat, and the water exchange between this and the SAG zones was concluded to have limited influence in the SAG flow, consistent with the reef flat width also not being relevant.

7.1.6. SIXTH SUBOBJECTIVE - IMPLICATIONS OF THE HYDRODYNAMICS

The sixth subobjective of this thesis is to discuss what the implications of the hydrodynamic aspects could be for corals, sediments and nutrients in the context of coral health and growth.

Several implications concerning the implications of the hydrodynamics were discussed, with main findings briefly summarized below:

- Bottom shear stresses are systematically higher over spurs than grooves. This indicates that there is a higher potential for coral development over them, associated with increasing water motion. Accordingly, sediment transport potential is higher over spurs, for which alongshore currents are higher than grooves, thus sediments would tend to drift towards the grooves, where they would more likely deposit due to lower shear stresses;
- The fact that Hawaiian and Buttress SAG types experience similar bottom shear stresses suggests the existence of a range of ideal hydrodynamics conditions for coral development;
- The boundary between SAG circulation cells might be a nodal point for which groove currents would carry material to, potentially enhancing coral development, consistent with its location close to the peak spur height; and
- With the bottom currents flowing persistently onshore both over spur and groove, bottom material slowly migrates from the outer slope through the SAG towards the reef flat.

7.2. RECOMMENDATIONS

Based on the limitations previously addressed (Chapter 6.3), the following recommendations for further research are elaborated:

1. **Investigate SAG hydrodynamics with 3D phase-resolver model**

   The main limitation of study is related to the fact that flow is not solved within the wave period, but averagely, introducing uncertainties in the wave forcing, Stokes Drift velocities and in the wave height. With wave-averaged models, the accuracy for the wave forcing and Stokes drift velocities gets lower in the surfzone due to nonlinear effects. Diffraction processes, that are not considered in wave-averaged models, are extremely important in the case of shore-normal waves propagating over SAG formations. This research assumed that diffraction overcomes refraction processes in all cases, resulting in very low alongshore gradient of wave height over spur and groove, consistent with previous research and measurement.

   The application of a 3D phase-resolver wave model, such as SWASH, is recommended as a next step. This type of model could verify both the diffraction dominance and the 3D velocity profiles obtained in the current research. Besides, the large-scale circulation on the reef flat, that was shown to be negligible for the flow within the SAG zone, could have its importance reevaluated, as this model has more powerful representation of nonlinear effects and long waves are also directly included. As a last point, the wave-current interaction, not part of the current research, is also implicitly included in its formulation.

2. **Investigate particle fate within SAG formations**

   The study used the hydrodynamics results to ponder over the implications of the flow pattern in terms of coral growth and health. Although those implications were debated taking into account hydrodynamics indicators, the discussion itself was purely qualitative. Further studies could use particle track models to observe the fate of material within SAG formations so as to obtain quantitative insight into coral growth and health aspects.

3. **Collect metocean field data over SAG formations**

   The only extensive set of measured metocean data on top of SAG formations made so far was in Palmyra Atoll (Rogers et al., 2015). Although this dataset is insightul into the dominant mechanisms, it provides information about specific SAG formations that are not necessarily representative of the vastness of SAG formations found worldwide.

   The collection of more metocean field data over SAG bathymetries is recommended in order to obtain more insight into their physics. Further studies could also benefit from this field data for calibration purposes.

4. **Create database of SAG geometries with more field data**

   Although SAG formations have been reported ever since the 50's, extensive quantitative morphologic studies are limited (e.g. Storlazzi et al. (2003); Duce et al. (2016)). The collection of more detailed bathymetric or aerial imagery data and the conduction of more extensive morphology characterization of SAG bathymetries are recommended. On the one hand, statistical analysis of SAG geometry parameters would allow their better representation in schematic bathymetry models. On the other hand, the representativity of the modelled scenario could be better evaluated, especially if also metocean data are simultaneously collected.

5. **Invesigate the role of tide in SAG hydrodynamics**

   Although the majority of coral reef environments are located in wave-dominated environments, the tidal flow effects might also be important in SAG. Next studies could evaluate the importance of alongshore forcing by tides, e.g., to determine for which conditions SAG circulation cells could be undermined.

6. **Conduct physical model experiment with SAG bathymetry**

   The calibration step results indicated diffraction processes to be dominant for shore-normal waves approaching SAG formations. The conduction of laboratory experiments to explore the diffraction and refraction dominance for varying SAG wavelengths could be a next step towards a validation of the hypotheses assumed in the current research. Similarly, physical modelling results could be used for further studies calibration of wave parameters and currents.

BIBLIOGRAPHY

Andrews, D. G. and McIntyre, M. E. (1978), 'An exact theory of nonlinear waves on a Lagrangian-mean flow', *J. Fluid Mech.* **89**, 609–646.

Bird, E. C. F. (2008), *Coastal geomorphology: an introduction*, 2 edn, John Wiley Sons Ltd, Melbourne.

Blanchon, P. and Jones, B. (1995), 'Marine-plantation terraces on the shelf around Grand Cayman: a result of stepped Holocene sea-level rise', *Journal of Coastal Research* **11**, 1–33.

Blanchon, P. and Jones, B. (1997), 'Hurricane control on shelf-edge-reef architecture around Grand Cayman', *Sedimentology* **44**(3), 479–506.

Booij, N., Ris, R. and Holthuijsen, L. (1999), 'A third-generation wave model for coastal regions, 1. Model description and validation', *Journal of Geophysical Research* **104**(C4), 7649—-7666.

Bouchon, C. (1981), 'Quantitative Study of the Scleractinian Coral Communities of a Fringing Reef of Reunion Island (Indian Ocean)', *Mar. Ecol. Prog. Ser.* **4**, 273–288.

Camoin, G., Ebren, P., Eisenhauer, Bard, E. and Faure, G. (2001), 'A 300 000-yr coral reef record of sea level changes, Mururoa atoll (Tuamotu archipelago, French Polynesia)', *Palaeogeography, Palaeoclimatology, Palaeoecology* **175**, 325–341.

Chapman, M. R. and Kramer, D. L. (2000), 'Movements of fishes within and among fringing coral reefs in Barbados', *Environmental Biology of Fishes* **57**, 11–24.

Choi, D. R. (1982), 'Coelobites (reef cavity-dwellers) as indicators of environmental effects caused by offshore drilling', *Bulletin of Marine Science* **32**(4), 880–889,.

Cloud, P. E. (1951), 'Preliminary report on geology and marine environments of Onotoa Atoll, Gilbert Islands', *Atoll Res Bull* **12**, 1–73.

Cloud, P. E. (1959), 'Geology of Saipan, Mariana Islands, Part 4 - Submarine topography and shallow-water ecology', *U. S. Geological Survey Prof Paper 280-K* pp. 361–445.

Cloud, P. E. J. (1954), 'Superficial aspects of modern organic reefs', *Sci. Mon.* **79**(4), 195–208.

Dean, R. G. and Dalrymple, R. A. (2001), *Coastal processes with Engineering Applications*, Cambridge University Press.

Deltares (2016), Delft3D-FLOW Simulation of multi-dimensional hydrodynamic flows and transport phenomena, including sediments. User Manual, Hydro-Morphodynamics, Technical report, Delft.

do Nascimento Araujo, P. V. and do Amaral, R. F. (2016), 'Mapping of coral reefs in the continental shelf of Brazilian Northeast through remote sensing', *Journal of Integrated Coastal Zone Management* **16**(1), 5–20.

Dollar, S. (1982), 'Wave Stress and Coral Community Structure in Hawaii', *Coral Reefs* **1**, 71–81.

Duce, S., Vila-Concejo, A., Hamylton, S., Bruce, E. and Webster, J. M. (2014), 'Spur and groove distribution, morphology and relationship to relative wave exposure, Southern Great Barrier Reef, Australia', *Journal of Coastal Research* **70**, 115–120.

Duce, S., Vila-Concejo, A., Hamylton, S., Webster, J., Bruce, E. and Beaman, R. (2016), 'A morphometric assessment and classification of coral reef spur and groove morphology', *Geomorphology* **265**, 68–83.

Emery, K. O., Tracey, J. I. and Ladd, H. S. (1959), 'Submarine geology and topography in the Northern Marshalls', *Trans. AGU* **30**(1), 55–58.

Falter, J. L., Atkinson, M. J. and Merrifield, M. A. (2004), 'Mass-transfer limitation of nutrient uptake by a wave-dominated reef flat community', *Limnol. Oceanogr.* **49**(5), 1820—-1831.

Gischler, E. (2010), 'Indo-Pacific and Atlantic spurs and grooves revisited: the possible effects of different Holocene sea-level history, exposure, and reef accretion rate in the shallow fore reef', *Facies* **56**, 173–177.

Goreau, T. F. (1959), 'The ecology of Jamaican coral reefs, 1 — Species composition and zonation', *Ecology* **40**, 67–90.

Guilcher, A. (1988), *Coral reef geomorphology*, Wiley, Chichester.

Holthus, P. and Maragos, J. (1995), Marine ecosystem classification for the Tropical Island Pacific, *in* J. Marago, M. Peterson, L. Eldredge, J. Bardach and H. Takeuchi, eds, 'Marine and Coastal Biodiversity in the Tropical Island Pacific Region', East West Center, Hawaii, pp. 239–278.

Hopley, D. (2011), *Encyclopedia of Modern Coral Reefs*, Springer.

Jensen, B. L., Sumer, B. M. and Fredsoe, J. (1989), 'Turbulent oscillatory boundary layers at high Reynolds numbers', *Journal of Fluid Mechanics* **206**, 265–297.

Kamphuis, J. (2010), *Introduction to coastal engineering and management*, 2 edn, World Scientific. ISBN 9789812834843, Singapore.

Kan, H., Hori, N. and Ichikawa, K. (1997), 'Formation of a coral reef-front spur', *Coral Reefs* **16**, 3–4.

Kan, H., Hori, N., Nakashima, Y. and Ichikawa, K. (1995), 'Narrow reef flat formation in a high-latitude fringing reef', *Coral Reefs* **14**, 123–130.

Kayanne, H., Hongo, C. and Yamano, H. (2015), Coral reef landforms in Japan, *in* 'Coral Reefs of Japan', pp. 14–19.

Kolijn, D. (2014), Effectiveness of a multipurpose artificial underwater structure as a coral reef canopy, Master's thesis, Delft University of Technology, Delft.

Ladd, H. S., Tracey, J. I., Wells, J. W. and Emery, K. O. (1950), 'Organic growth and sedimentation on an atoll', *J Geol* **58**, 410–425.

Lidz, B. H.and Reich, C. D. S. E. (2007), 'Systematic Mapping of Bedrock and Habitats along the Florida Reef Tract: Central Key Largo to Halfmoon Shoal (Gulf of Mexico)', *U. S. Geological Survey Professional Paper* p. 1751.

Longuet-Higgins, M. (1969), 'On the transport of mass by time-varying ocean currents', *Deep-Sea Research* **16**, 431–447.

Longuet-Higgins, M. and Stewart, R. (1964), 'Radiation stress and mass transport in gravity waves, with application to 'surf beats'', *Deep-Sea Research* **11**(4), 529—-562.

Lowe, R. J. and Falter, J. L. (2015), 'Oceanic Forcing of Coral Reefs', *Annual Review of Marine Science* **7**, 43–66.

Lowe, R. J., Leon, A. S., Symonds, G., Falter, J. L. and Gruber, R. (2015), 'The intertidal hydraulics of tide-dominated reef platforms', *J. Geophys. Res. Oceans* **120**, 4845—-4868.

Massey, T. C., Anderson, M. E., Smith, J. M., Gomez, J. and Jones, R. (2011), STWAVE: Steady-State Spectral Wave Model User's Manual for STWAVE, Version 6.0, Technical report, US Army Engineer Research and Development Center, Vickburg, MS.

Mei, C. C. (1983), *The applied dynamics of ocean surface waves*, Wiley, New York.

Mumbya, P. J. and Harborne, A. R. (1998), 'Development of a systematic classi®cation scheme of marine habitats to facilitate regional management and mapping of Caribbean coral reefs', *Biological Conservation* **88**, 155–163.

Munk, W. H. and Sargent, M. C. (1948), 'Adjustment of Bikini Atoll to Ocean Waves', *U. S. Geol. Sur. Prof. Paper 260-C* pp. 275–280.

Newell, N. D. (1954), 'Reefs and sedimentary processes of Raroia', *Atoll Res. Bull.* **36**, 1–35.

Newell, N. D., Rigby, K. J., Whiteman, A. J. and S., B. J. (1951), 'Shoal-water geology and environs, eastern Andros Island, Bahamas', *Bull Am Mus Nat Hist* **97**, 7–29.

Nunez-Lara, E., Arias-Gonzalez, J. E. and Legendre, P. (2005), 'Spatial patterns of Yucatan reef fish communities: Testing models using a multi-scale survey design', *Journal of Experimental Marine Biology and Ecology* **324**, 157–169.

Nwogu, O. and Demirbilek, Z. (2001), BOUSS-2D: A Boussinesq wave model for coastal regions andharbors - Report 1: Theoretical Background and User's Manual. ERDC. CHL TR-01-25, Technical report, US Army Engineer Research and Development Center, Vicksburg, MS.

Odum, H. T. and Odum, E. P. (1955), 'Trophic Structure and Productivity of a Windward Coral Reef Community on Eniwetok Atoll', *Ecological Monographs* **25**(3), 291:320.

Pearson, S. G. (2016), Predicting Wave-Induced Flooding on Low-Lying Tropical Islands Using a Bayesian Network, Master's thesis, Delft University of Technology, Delft.

Purdy, E. G. (1954), 'Reef configurations: cause and effect', *Atoll Res. Bull.* **36**, 1–35.

Quataert, E., Storlazzi, C., van Rooijen, A., Cheriton, O. and van Dongeren, A. (2015), 'The influence of coral reefs and climate change on wave-driven flooding of tropical coastlines', *Geophys. Res. Lett.* **42**, 6407—6415.

Rakitin, A. and Kramer, D. L. (1996), 'Effect of a marine reserve on the distribution of coral reef fishes in Barbados', *Mar Ecol Prog Ser* **131**, 97–113.

Roberts, H. H. (1974), Variability of reefs with regard to changes in wave power around an island, *in* '2nd International Coral Reef Symposium', Brisbane, Australia.

Roberts, H. H., Murray, S. P. and Suhayda, J. N. (1977), 'Evidence for strong currents and turbulence in a deep coral reef groove', *Limnol. Oceanogr.* **22**(1), 152–156.

Roberts, H. H., Murray, S. P. and Suhayda, J. N. (1980), 'Physical process in a fringing reef system', *J. Mar. Res.* **33**, 233—-260.

Roelvink, D. and Reniers, A. (2012), *A guide to modeling coastal morphology*, Vol. 12, World Scientific.

Roelvink, J., Reniers, A. J. H. M., van Dongeren, A., van Thiel de Vries, J. S. M., Lescinski, J. and McCall, R. (2010), XBeach Model Description and Manual, Technical report, Unesco-IHE, Deltares and Delft University of Technology, Delft.

Roelvink, J.and Reniers, A., van Dongeren, A., van Thiel de Vries, J. S. M., McCall, R., and Lescinski, J. (2009), 'Modelling storm impacts on beaches, dunes and barrier islands', *Coastal Engineering* **56**(11-12), 1133–1152.

Rogers, J. S., Monismith, S. G., Dunbar, R. B. and Koweek, D. (2015), 'Field observations of wave-driven circulation over spur and groove formations on a coral reef', *Journal of Geophysical Research: Oceans* **120**, 145–160.

Rogers, J. S., Monismith, S. G., Feddersen, F. and Storlazzi, C. D. (2013), 'Hydrodynamics of spur and groove formations on a coral reef', *Journal of Geophysical Research: Oceans* **118**, 3059–3073.

Rosman, J. H. and Hench, J. L. (2011), 'A framework for understanding drag parameterizations for coral reefs', *Journal of Geophysical Research,* **116**(C08025), 1–15.

Sheppard, C. R. C. (1981), 'The Groove and Spur Structures of Chagos Atolls and their Coral Zonation', *Estuarine, Coastal and Shelf Science* **12**, 549–560.

Shinn, E. A. (1963), 'Spur and groove formation on the Florida reef tract', *J Sed Petrol* **33**, 291–303.

Shinn, E. A., Hudson, J. H., Robbin, D. M. and Lidz, B. (1981), Spurs and grooves revisited: construction versus erosion Looe Key Reef, Florida, *in* 'Proceedings of the Fourth International Coral Reef Symposium', Vol. 1, Manila, pp. 475–483.

Smit, P., G.S.Stelling, Roelvink, D., van Thiel de Vries, J., McCall, R., van Dongeren, A., Zwinkels, C. and Jacobs, R. (2014), XBeach: Non-hydrostatic model. Validation, verification and model description, Technical report, Delft University of Technology and Deltares, Delft.

Sneh, A. and Friedman, G. M. (1980), 'Spur and groove patterns on the reefs of the northern gulfs of the Red Sea', *J Sed Petrol* **50**, 981–986.

Stearn, C. W., Scoffin, T. P. and Martindale, W. (1977), 'Calcium carbonate budget of a fringing reef on the west coast of Barbados', *Bulletin of Marine Science* **27**(3), 479–510.

Storlazzi, C. D. and Jaffe, B. E. (2008), 'The relative contribution of processes driving variability in flow, shear, and turbidity over a fringing coral reef: West Maui, Hawaii', *Estuarine and Coastal Shelf Science* **77**, 549 – 564.

Storlazzi, C. D., Logan, J. B. and Field, M. E. (2008), Shape of the South Moloka'i Fringing Reef: Trends and Variation, *in* M. E. Field, S. A. Cochran, J. B. Logan and C. D. Storlazzi, eds, 'The Coral Reef of South Moloka'i, Hawai'i', U.S. Geological Survey, Reston, Virginia, pp. 33–36.

Storlazzi, C., Logan, J. and Field, M. (2003), 'Quantitative morphology of a fringing reef tract from high-resolution laser bathymetry: Southern Molokai, Hawaii', *GSA Bulletin* **115**(11), 1344—-1355.

Tracey, J. I., Ladd, H. S. and Hoffmeister, J. E. (1948), 'Reefs of Bikini, Marshall Islands', *Bulletin of the Geological Society of America* **59**, 861–878.

van Dongeren, A., Battjes, J., Janssen, T., van Noorloos, J., Steenhauer, K., Steenbergen, G. and Reniers, A. (2007), 'Shoaling and shoreline dissipation of low-frequency waves', *Journal of Geophysical Research* **112**, 1 –15.

van Mierlo, F. (2014), Numerical modelling of wave penetration in ports, Master's thesis, Delft University of Technology, Delft.

Weydert, P. (1979), 'Direction of growth of the spurs on an outer barrier reef tract - the example of the Grand Recif of Tulear (Madagascar)', *Marine Geology* **30**, 9–19.

Wood, R. and Oppenheimer, C. (2000), 'Spur and groove morphology from a Late Devonian reef', *Sedimentary Geology* **133**, 185–193.

Yahel, G., Post, A. F., Fabricius, Katharina; Marie, D., Vaulot, D. and Genin, A. (1998), 'Phytoplankton distribution and grazing near coral reefs', *Limnology and Oceanography* **43**(4), 551–663.

Zijlema, M., Stelling, G. S. and Smit, P. B. (1969), 'SWASH: An operational public domain code for simulating wave fields and rapidly varied flows in coastal waters', *Coastal Engineering* **56**(10), 992–1012.

A

LIST OF SIMULATIONS - SENSITIVITY AND PERMUTATION RUNS

This appendix presents the input parameters for the simulations carried out in the current research.

The sensitivity runs - variations of the Base Case for short wave parameters, SAG geometry and forcing alongshore flow, with one parameter at a time - are presented in Table A.1.

The permutation runs - simultaneous variations of the incoming significant wave height Hs_0, incoming wave steepness $\frac{Hs_0}{Lp_0}$, spur height h_{spr}, SAG wavelength λ_{SAG} and vertical position of maximum spur height z_μ - are shown in Table A.3

Table A.1: List of simulations - Sensitivity runs - Part 1/2.

ID	Incoming Significant Wave Height	Incoming Wave Steepness	Peak Wave Direction	Directional Spreading	Spur Height	SAG Wavelength	Ratio of Groove Width and SAG Wavelength	SAG Cross-shore Slope	Reef Flat Width	Ratio of Friction Coefficient	Maximum Spur Height Depth	Alongshore Wind Speed	Flow Type
	Hs_0	$\frac{Hs_0}{Lp_0}$	Dp_0	m	h_{spr}	λ_{SAG}	$\frac{W_{grv}}{\lambda_{SAG}}$	$\tan\beta_f$	W_{reef}	$\frac{C_{D\text{-}grv}}{C_{D\text{-}spr}}$	z_μ	U_{10}	
	m	-	°	-	m	m	-	-	m	-	m	m/s	-
Base Case	1	0.006	0	30	2	50	0.06	0.07	300	0.5	17	0	A
S01	0.5	0.003	0	30	2	50	0.06	0.07	300	0.5	17	0	A
S02	2	0.013	0	30	2	50	0.06	0.07	300	0.5	17	0	A
S03	4	0.026	0	30	2	50	0.06	0.07	300	0.5	17	0	A
S04	1	0.003	0	30	2	50	0.06	0.07	300	0.5	17	0	A
S05	1	0.013	0	30	2	50	0.06	0.07	300	0.5	17	0	A
S06	1	0.025	0	30	2	50	0.06	0.07	300	0.5	17	0	C.2.1
S07	1	0.050	0	30	2	50	0.06	0.07	300	0.5	17	0	C.1.1
S08	1	0.006	15	30	2	50	0.06	0.07	300	0.5	17	0	B.1
S09	1	0.006	30	30	2	50	0.06	0.07	300	0.5	17	0	B.1
S10	1	0.006	0	2	2	50	0.06	0.07	300	0.5	17	0	A
S11	1	0.006	0	6	2	50	0.06	0.07	300	0.5	17	0	A
S12	1	0.006	0	30	0.5	50	0.06	0.07	300	0.5	17	0	A
S13	1	0.006	0	30	4	50	0.06	0.07	300	0.5	17	0	A
S14	1	0.006	0	30	8	50	0.06	0.07	300	0.5	17	0	A
S15	1	0.006	0	30	2	25	0.06	0.07	300	0.5	17	0	B.1
S16	1	0.006	0	30	2	100	0.06	0.07	300	0.5	17	0	A
S17	1	0.006	0	30	2	200	0.06	0.07	300	0.5	17	0	A
S18	1	0.006	0	30	2	50	0.01	0.07	300	0.5	17	0	A

ID	Incoming Significant Wave Height	Incoming Wave Steepness	Peak Wave Direction	Directional Spreading	Spur Height	SAG Wavelength	Ratio of Groove Width and SAG Wavelength	SAG Cross-shore Slope	Reef Flat Width	Ratio of Friction Coefficient	Maximum Spur Height Depth	Alongshore Wind Speed	Flow Type
	Hs_0	$\frac{Hs_0}{Lp_0}$	Dp_0	m	h_{spr}	λ_{SAG}	$\frac{W_{grv}}{\lambda_{SAG}}$	$\tan\beta_f$	W_{reef}	$\frac{C_{D\text{-}grv}}{C_{D\text{-}spr}}$	z_μ	U_{10}	
	m	-	°	-	m	m	-	-	m	-	m	m/s	-
S19	1	0.006	0	30	2	50	0.30	0.07	300	0.5	17	0	A
S20	1	0.006	0	30	2	50	0.60	0.07	300	0.5	17	0	A
S21	1	0.006	0	30	2	50	0.80	0.07	300	0.5	17	0	A
S22	1	0.006	0	30	2	50	0.06	0.02	300	0.5	17	0	B.1
S23	1	0.006	0	30	2	50	0.06	0.09	300	0.5	17	0	A
S24	1	0.006	0	30	2	50	0.06	0.30	300	0.5	17	0	A
S25	1	0.006	0	30	2	50	0.06	0.50	300	0.5	17	0	B.2
S26	1	0.006	0	30	2	50	0.06	0.07	50	0.5	17	0	A
S27	1	0.006	0	30	2	50	0.06	0.07	1000	0.5	17	0	A
S28	1	0.006	0	30	2	50	0.06	0.07	300	0.17	17	0	B.2
S29	1	0.006	0	30	2	50	0.06	0.07	300	0.33	17	0	A
S30	1	0.006	0	30	2	50	0.06	0.07	300	0.5	5	0	A
S31	1	0.006	0	30	2	50	0.06	0.07	300	0.5	10	0	A
S32	1	0.006	0	30	2	50	0.06	0.07	300	0.5	13.5	0	A
S33	1	0.006	0	30	2	50	0.06	0.07	300	0.5	17	5	B.2
S34	1	0.006	0	30	2	50	0.06	0.07	300	0.5	17	10	B.2
S35	1	0.006	0	30	2	50	0.06	0.07	300	0.5	17	15	B.1
S36	1	0.006	0	30	2	50	0.06	0.07	300	0.5	17	20	B.1

Table A.3: List of simulations - Permutation runs.

ID	Incoming Significant Wave Height	Incoming Wave Steepness	Spur Height	SAG Wavelength	Maximum Spur Height Depth	Flow Type
	Hs_0	$\frac{Hs_0}{Lp_0}$	h_{spr}	λ_{SAG}	z_μ	
	m	-	m	m	m	-
P001	0.5	0.006	0.5	25	17	B.1
P002	0.5	0.006	0.5	50	17	A
P003	0.5	0.006	0.5	100	17	A
P004	0.5	0.006	0.5	200	17	A
P005	0.5	0.006	1	25	17	B.1
P006	0.5	0.006	1	50	17	A
P007	0.5	0.006	1	100	17	A
P008	0.5	0.006	1	200	17	A
P009	0.5	0.006	2	25	17	B.1
P010	0.5	0.006	2	100	17	A
P011	0.5	0.006	2	200	17	A
P012	0.5	0.006	4	25	17	B.1
P013	0.5	0.006	4	50	17	A
P014	0.5	0.006	4	100	17	A
P015	0.5	0.006	4	200	17	A
P016	0.5	0.006	8	25	17	B.1
P017	0.5	0.006	8	50	17	A
P018	0.5	0.006	8	100	17	A
P019	0.5	0.006	8	200	17	A
P020	0.5	0.025	0.5	25	17	C.2.1
P021	0.5	0.025	0.5	50	17	C.2.1
P022	0.5	0.025	0.5	100	17	C.2.2
P023	0.5	0.025	0.5	200	17	C.2.2
P024	0.5	0.025	1	25	17	C.2.1
P025	0.5	0.025	1	50	17	C.2.1
P026	0.5	0.025	1	100	17	C.2.2
P027	0.5	0.025	1	200	17	C.2.2
P028	0.5	0.025	2	25	17	C.2.1
P029	0.5	0.025	2	50	17	C.2.1
P030	0.5	0.025	2	100	17	C.2.2
P031	0.5	0.025	2	200	17	C.2.2
P032	0.5	0.025	4	25	17	C.2.1
P033	0.5	0.025	4	50	17	C.2.1
P034	0.5	0.025	4	100	17	C.2.2
P035	0.5	0.025	4	200	17	C.2.2
P036	0.5	0.025	8	25	17	C.2.1
P037	0.5	0.025	8	50	17	C.2.1
P038	0.5	0.025	8	100	17	C.2.2
P039	0.5	0.025	8	200	17	C.2.2
P040	1	0.006	0.5	25	17	B.1
P041	1	0.006	0.5	100	17	A
P042	1	0.006	0.5	200	17	A
P043	1	0.006	1	25	17	B.1
P044	1	0.006	1	50	17	A
P045	1	0.006	1	100	17	A
P046	1	0.006	1	200	17	A
P047	1	0.006	4	25	17	B.1

Table A.3: List of simulations - Permutation runs.

ID	Incoming Significant Wave Height	Incoming Wave Steepness	Spur Height	SAG Wavelength	Maximum Spur Height Depth	Flow Type
	Hs_0	$\frac{Hs_0}{Lp_0}$	h_{spr}	λ_{SAG}	z_μ	
	m	-	m	m	m	-
P048	1	0.006	4	100	17	A
P049	1	0.006	4	200	17	A
P050	1	0.006	8	25	17	B.1
P051	1	0.006	8	100	17	A
P052	1	0.006	8	200	17	A
P053	1	0.025	0.5	25	17	C.2.1
P054	1	0.025	0.5	50	17	C.2.1
P055	1	0.025	0.5	100	17	C.2.2
P056	1	0.025	0.5	200	17	C.2.2
P057	1	0.025	1	25	17	C.2.1
P058	1	0.025	1	50	17	C.2.1
P059	1	0.025	1	100	17	C.2.2
P060	1	0.025	1	200	17	C.2.2
P061	1	0.025	2	25	17	C.2.1
P062	1	0.025	2	100	17	C.2.2
P063	1	0.025	2	200	17	C.2.2
P064	1	0.025	4	25	17	C.2.1
P065	1	0.025	4	50	17	C.2.1
P066	1	0.025	4	100	17	C.2.2
P067	1	0.025	4	200	17	C.2.2
P068	1	0.025	8	25	17	C.2.1
P069	1	0.025	8	50	17	C.2.2
P070	1	0.025	8	100	17	C.2.2
P071	1	0.025	8	200	17	A
P072	1	0.050	0.5	25	17	C.1.2
P073	1	0.050	0.5	50	17	C.1.1
P074	1	0.050	0.5	100	17	C.1.1
P075	1	0.050	0.5	200	17	C.1.1
P076	1	0.050	1	25	17	C.1.2
P077	1	0.050	1	50	17	C.1.1
P078	1	0.050	1	100	17	C.1.1
P079	1	0.050	1	200	17	C.1.1
P080	1	0.050	2	25	17	C.1.2
P081	1	0.050	2	100	17	C.1.1
P082	1	0.050	2	200	17	C.1.1
P083	1	0.050	4	25	17	C.1.2
P084	1	0.050	4	50	17	C.1.1
P085	1	0.050	4	100	17	C.1.1
P086	1	0.050	4	200	17	C.1.1
P087	1	0.050	8	25	17	C.1.2
P088	1	0.050	8	50	17	C.1.1
P089	1	0.050	8	100	17	C.1.1
P090	1	0.050	8	200	17	C.1.1
P091	2	0.006	0.5	25	17	B.1
P092	2	0.006	0.5	50	17	A
P093	2	0.006	0.5	100	17	A
P094	2	0.006	0.5	200	17	A

Table A.3: List of simulations - Permutation runs.

ID	Incoming Significant Wave Height	Incoming Wave Steepness	Spur Height	SAG Wavelength	Maximum Spur Height Depth	Flow Type
	Hs_0	$\frac{Hs_0}{Lp_0}$	h_{spr}	λ_{SAG}	z_μ	
	m	-	m	m	m	-
P095	2	0.006	1	25	17	B.1
P096	2	0.006	1	50	17	A
P097	2	0.006	1	100	17	A
P098	2	0.006	1	200	17	A
P099	2	0.006	2	25	17	B.1
P100	2	0.006	2	100	17	A
P101	2	0.006	2	200	17	A
P102	2	0.006	4	25	17	B.1
P103	2	0.006	4	50	17	A
P104	2	0.006	4	100	17	A
P105	2	0.006	4	200	17	A
P106	2	0.006	8	25	17	B.1
P107	2	0.006	8	50	17	A
P108	2	0.006	8	100	17	A
P109	2	0.006	8	200	17	A
P110	2	0.025	0.5	25	17	C.2.1
P111	2	0.025	0.5	50	17	C.2.2
P112	2	0.025	0.5	100	17	C.2.2
P113	2	0.025	0.5	200	17	C.2.2
P114	2	0.025	1	25	17	C.2.1
P115	2	0.025	1	50	17	C.2.2
P116	2	0.025	1	100	17	C.2.2
P117	2	0.025	1	200	17	C.2.2
P118	2	0.025	2	25	17	C.2.1
P119	2	0.025	2	50	17	C.2.2
P120	2	0.025	2	100	17	C.2.2
P121	2	0.025	2	200	17	A
P122	2	0.025	4	25	17	B.1
P123	2	0.025	4	50	17	A
P124	2	0.025	4	100	17	A
P125	2	0.025	4	200	17	A
P126	2	0.025	8	25	17	B.1
P127	2	0.025	8	50	17	A
P128	2	0.025	8	100	17	A
P129	2	0.025	8	200	17	A
P130	2	0.050	0.5	25	17	C.1.2
P131	2	0.050	0.5	50	17	C.1.1
P132	2	0.050	0.5	100	17	C.1.1
P133	2	0.050	0.5	200	17	C.1.1
P134	2	0.050	1	25	17	C.1.2
P135	2	0.050	1	50	17	C.1.1
P136	2	0.050	1	100	17	C.1.1
P137	2	0.050	1	200	17	C.1.1
P138	2	0.050	2	25	17	C.1.2
P139	2	0.050	2	50	17	C.1.1
P140	2	0.050	2	100	17	C.1.1
P141	2	0.050	2	200	17	C.1.1

Table A.3: List of simulations - Permutation runs.

ID	Incoming Significant Wave Height	Incoming Wave Steepness	Spur Height	SAG Wavelength	Maximum Spur Height Depth	Flow Type
	Hs_0	$\frac{Hs_0}{Lp_0}$	h_{spr}	λ_{SAG}	z_μ	
	m	-	m	m	m	-
P142	2	0.050	4	25	17	C.2.1
P143	2	0.050	4	50	17	C.1.1
P144	2	0.050	4	100	17	C.1.1
P145	2	0.050	4	200	17	C.1.1
P146	2	0.050	8	25	17	C.2.1
P147	2	0.050	8	50	17	C.2.1
P148	2	0.050	8	100	17	C.2.2
P149	2	0.050	8	200	17	C.2.2
P150	4	0.006	0.5	25	17	B.2
P151	4	0.006	0.5	50	17	B.2
P152	4	0.006	0.5	100	17	A
P153	4	0.006	0.5	200	17	A
P154	4	0.006	1	25	17	B.2
P155	4	0.006	1	50	17	A
P156	4	0.006	1	100	17	A
P157	4	0.006	1	200	17	A
P158	4	0.006	2	25	17	B.2
P159	4	0.006	2	100	17	A
P160	4	0.006	2	200	17	A
P161	4	0.006	4	25	17	B.2
P162	4	0.006	4	50	17	A
P163	4	0.006	4	100	17	A
P164	4	0.006	4	200	17	A
P165	4	0.006	8	25	17	A
P166	4	0.006	8	50	17	A
P167	4	0.006	8	100	17	A
P168	4	0.006	8	200	17	A
P169	4	0.025	0.5	25	17	C.2.1
P170	4	0.025	0.5	50	17	C.2.2
P171	4	0.025	0.5	100	17	A
P172	4	0.025	0.5	200	17	A
P173	4	0.025	1	25	17	-
P174	4	0.025	1	50	17	A
P175	4	0.025	1	100	17	A
P176	4	0.025	1	200	17	A
P177	4	0.025	2	25	17	B.1
P178	4	0.025	2	50	17	A
P179	4	0.025	2	100	17	A
P180	4	0.025	2	200	17	A
P181	4	0.025	4	25	17	B.2
P182	4	0.025	4	50	17	A
P183	4	0.025	4	100	17	A
P184	4	0.025	4	200	17	A
P185	4	0.025	8	25	17	A
P186	4	0.025	8	50	17	A
P187	4	0.025	8	100	17	A
P188	4	0.025	8	200	17	A

Table A.3: List of simulations - Permutation runs.

ID	Incoming Significant Wave Height	Incoming Wave Steepness	Spur Height	SAG Wavelength	Maximum Spur Height Depth	Flow Type
	Hs_0	$\frac{Hs_0}{Lp_0}$	h_{spr}	λ_{SAG}	z_μ	
	m	-	m	m	m	-
P189	4	0.050	0.5	25	17	C.1.2
P190	4	0.050	0.5	50	17	C.2.2
P191	4	0.050	0.5	100	17	C.2.2
P192	4	0.050	0.5	200	17	C.2.2
P193	4	0.050	1	25	17	C.2.1
P194	4	0.050	1	50	17	C.2.2
P195	4	0.050	1	100	17	C.2.2
P196	4	0.050	1	200	17	C.2.2
P197	4	0.050	2	25	17	C.2.1
P198	4	0.050	2	50	17	C.2.2
P199	4	0.050	2	100	17	C.2.2
P200	4	0.050	2	200	17	C.2.2
P201	4	0.050	4	25	17	C.2.1
P202	4	0.050	4	50	17	C.2.2
P203	4	0.050	4	100	17	C.2.2
P204	4	0.050	4	200	17	A
P205	4	0.050	8	25	17	C.2.2
P206	4	0.050	8	50	17	A
P207	4	0.050	8	100	17	A
P208	4	0.050	8	200	17	A
P209	6	0.006	0.5	25	17	B.2
P210	6	0.006	0.5	50	17	B.2
P211	6	0.006	0.5	100	17	A
P212	6	0.006	0.5	200	17	A
P213	6	0.006	1	25	17	B.2
P214	6	0.006	1	50	17	A
P215	6	0.006	1	100	17	A
P216	6	0.006	1	200	17	A
P217	6	0.006	2	25	17	B.2
P218	6	0.006	2	50	17	A
P219	6	0.006	2	100	17	A
P220	6	0.006	2	200	17	A
P221	6	0.006	4	25	17	A
P222	6	0.006	4	50	17	A
P223	6	0.006	4	100	17	A
P224	6	0.006	4	200	17	A
P225	6	0.006	8	25	17	A
P226	6	0.006	8	50	17	A
P227	6	0.006	8	100	17	A
P228	6	0.006	8	200	17	A
P229	6	0.025	0.5	25	17	A
P230	6	0.025	0.5	50	17	A
P231	6	0.025	0.5	100	17	A
P232	6	0.025	0.5	200	17	A
P233	6	0.025	1	25	17	A
P234	6	0.025	1	50	17	A
P235	6	0.025	1	100	17	A

Table A.3: List of simulations - Permutation runs.

ID	Incoming Significant Wave Height	Incoming Wave Steepness	Spur Height	SAG Wavelength	Maximum Spur Height Depth	Flow Type
	Hs_0	$\frac{Hs_0}{Lp_0}$	h_{spr}	λ_{SAG}	z_μ	
	m	-	m	m	m	-
P236	6	0.025	1	200	17	A
P237	6	0.025	2	25	17	A
P238	6	0.025	2	50	17	A
P239	6	0.025	2	100	17	A
P240	6	0.025	2	200	17	A
P241	6	0.025	4	25	17	A
P242	6	0.025	4	50	17	A
P243	6	0.025	4	100	17	A
P244	6	0.025	4	200	17	A
P245	6	0.025	8	25	17	A
P246	6	0.025	8	50	17	A
P247	6	0.025	8	100	17	A
P248	6	0.025	8	200	17	C.2.2
P249	6	0.050	0.5	25	17	C.1.2
P250	6	0.050	0.5	50	17	C.2.2
P251	6	0.050	0.5	100	17	C.2.2
P252	6	0.050	0.5	200	17	C.2.2
P253	6	0.050	1	25	17	C.2.2
P254	6	0.050	1	50	17	C.2.2
P255	6	0.050	1	100	17	C.2.2
P256	6	0.050	1	200	17	C.2.2
P257	6	0.050	2	25	17	C.2.2
P258	6	0.050	2	50	17	C.2.2
P259	6	0.050	2	100	17	C.2.2
P260	6	0.050	2	200	17	C.2.2
P261	6	0.050	4	25	17	C.2.2
P262	6	0.050	4	50	17	C.2.2
P263	6	0.050	4	100	17	A
P264	6	0.050	4	200	17	A
P265	6	0.050	8	25	17	C.2.2
P266	6	0.050	8	50	17	A
P267	6	0.050	8	100	17	A
P268	6	0.050	8	200	17	C.2.2
P269	0.5	0.006	0.5	25	10	B.1
P270	0.5	0.006	0.5	50	10	A
P271	0.5	0.006	1	25	10	B.1
P272	0.5	0.006	1	50	10	A
P273	0.5	0.006	2	25	10	B.1
P274	0.5	0.006	2	50	10	A
P275	0.5	0.006	4	25	10	B.1
P276	0.5	0.006	4	50	10	A
P277	0.5	0.025	0.5	25	10	C.2.1
P278	0.5	0.025	0.5	50	10	C.2.1
P279	0.5	0.025	1	25	10	C.2.1
P280	0.5	0.025	1	50	10	C.2.1
P281	0.5	0.025	2	25	10	C.2.1
P282	0.5	0.025	2	50	10	C.2.1

Table A.3: List of simulations - Permutation runs.

ID	Incoming Significant Wave Height	Incoming Wave Steepness	Spur Height	SAG Wavelength	Maximum Spur Height Depth	Flow Type
	Hs_0	$\frac{Hs_0}{Lp_0}$	h_{spr}	λ_{SAG}	z_μ	
	m	-	m	m	m	-
P283	0.5	0.025	4	25	10	C.2.1
P284	0.5	0.025	4	50	10	C.2.1
P285	1	0.006	0.5	25	10	B.1
P286	1	0.006	0.5	50	10	A
P287	1	0.006	1	25	10	B.1
P288	1	0.006	1	50	10	A
P289	1	0.006	2	25	10	B.1
P290	1	0.006	4	25	10	B.2
P291	1	0.006	4	50	10	A
P292	1	0.025	0.5	25	10	C.2.1
P293	1	0.025	0.5	50	10	C.2.1
P294	1	0.025	1	25	10	C.2.1
P295	1	0.025	1	50	10	C.2.1
P296	1	0.025	2	25	10	C.2.1
P297	1	0.025	2	50	10	C.2.1
P298	1	0.025	4	25	10	C.2.1
P299	1	0.025	4	50	10	C.2.1
P300	1	0.050	0.5	25	10	C.1.2
P301	1	0.050	0.5	50	10	C.1.2
P302	1	0.050	1	25	10	C.1.2
P303	1	0.050	1	50	10	C.1.2
P304	1	0.050	2	25	10	C.1.2
P305	1	0.050	2	50	10	C.1.2
P306	1	0.050	4	25	10	C.1.2
P307	1	0.050	4	50	10	C.1.1
P308	2	0.006	0.5	25	10	B.2
P309	2	0.006	0.5	50	10	A
P310	2	0.006	1	25	10	B.2
P311	2	0.006	1	50	10	A
P312	2	0.006	2	25	10	B.2
P313	2	0.006	2	50	10	A
P314	2	0.006	4	25	10	B.2
P315	2	0.006	4	50	10	A
P316	2	0.025	0.5	25	10	C.2.1
P317	2	0.025	0.5	50	10	C.2.1
P318	2	0.025	1	25	10	C.2.1
P319	2	0.025	1	50	10	C.2.1
P320	2	0.025	2	25	10	C.2.1
P321	2	0.025	2	50	10	C.2.1
P322	2	0.025	4	25	10	A
P323	2	0.025	4	50	10	C.2.1
P324	2	0.050	0.5	25	10	C.1.2
P325	2	0.050	0.5	50	10	C.1.1
P326	2	0.050	1	25	10	C.2.1
P327	2	0.050	1	50	10	C.1.1
P328	2	0.050	2	25	10	C.2.1
P329	2	0.050	2	50	10	C.2.1

Table A.3: List of simulations - Permutation runs.

ID	Incoming Significant Wave Height	Incoming Wave Steepness	Spur Height	SAG Wavelength	Maximum Spur Height Depth	Flow Type
	Hs_0	$\frac{Hs_0}{Lp_0}$	h_{spr}	λ_{SAG}	z_μ	
	m	-	m	m	m	-
P330	2	0.050	4	25	10	C.2.1
P331	2	0.050	4	50	10	C.2.1
P332	4	0.006	0.5	25	10	B.2
P333	4	0.006	0.5	50	10	B.2
P334	4	0.006	1	25	10	B.2
P335	4	0.006	1	50	10	A
P336	4	0.006	2	25	10	B.2
P337	4	0.006	2	50	10	A
P338	4	0.006	4	25	10	A
P339	4	0.006	4	50	10	A
P340	4	0.025	0.5	25	10	C.2.1
P341	4	0.025	0.5	50	10	C.2.2
P342	4	0.025	1	25	10	C.2.1
P343	4	0.025	1	50	10	C.2.2
P344	4	0.025	2	25	10	A
P345	4	0.025	2	50	10	C.2.2
P346	4	0.025	4	25	10	A
P347	4	0.025	4	50	10	A
P348	4	0.050	0.5	25	10	C.1.2
P349	4	0.050	0.5	50	10	C.2.2
P350	4	0.050	1	25	10	C.2.1
P351	4	0.050	1	50	10	C.2.2
P352	4	0.050	2	25	10	C.2.1
P353	4	0.050	2	50	10	C.2.2
P354	4	0.050	4	25	10	C.2.1
P355	4	0.050	4	50	10	C.2.1
P356	6	0.006	0.5	25	10	-
P357	6	0.006	0.5	50	10	B.2
P358	6	0.006	1	25	10	B.2
P359	6	0.006	1	50	10	A
P360	6	0.006	2	25	10	A
P361	6	0.006	2	50	10	A
P362	6	0.006	4	25	10	A
P363	6	0.006	4	50	10	A
P364	6	0.025	0.5	25	10	C.1.2
P365	6	0.025	0.5	50	10	C.2.2
P366	6	0.025	1	25	10	C.1.2
P367	6	0.025	1	50	10	A
P368	6	0.025	2	25	10	C.2.2
P369	6	0.025	2	50	10	A
P370	6	0.025	4	25	10	A
P371	6	0.025	4	50	10	A
P372	6	0.050	0.5	25	10	C.1.2
P373	6	0.050	0.5	50	10	C.1.2
P374	6	0.050	1	25	10	C.1.2
P375	6	0.050	1	50	10	C.2.2
P376	6	0.050	2	25	10	C.1.2

Table A.3: List of simulations - Permutation runs.

ID	Incoming Significant Wave Height	Incoming Wave Steepness	Spur Height	SAG Wavelength	Maximum Spur Height Depth	Flow Type
	Hs_0	$\frac{Hs_0}{Lp_0}$	h_{spr}	λ_{SAG}	z_μ	
	m	-	m	m	m	-
P377	6	0.050	2	50	10	C.2.2
P378	6	0.050	4	25	10	C.1.2
P379	6	0.050	4	50	10	C.2.2
P380	0.5	0.006	0.5	25	5	B.2
P381	0.5	0.006	0.5	50	5	C.2.1
P382	0.5	0.006	1	25	5	A
P383	0.5	0.006	1	50	5	A
P384	0.5	0.006	2	25	5	A
P385	0.5	0.006	2	50	5	A
P386	0.5	0.006	4	25	5	A
P387	0.5	0.006	4	50	5	A
P388	0.5	0.025	0.5	25	5	C.2.1
P389	0.5	0.025	0.5	50	5	C.2.1
P390	0.5	0.025	1	25	5	C.2.1
P391	0.5	0.025	1	50	5	C.2.1
P392	0.5	0.025	2	25	5	C.2.1
P393	0.5	0.025	2	50	5	C.2.1
P394	0.5	0.025	4	25	5	C.2.1
P395	0.5	0.025	4	50	5	C.2.1
P396	1	0.006	0.5	25	5	B.2
P397	1	0.006	0.5	50	5	A
P398	1	0.006	1	25	5	B.2
P399	1	0.006	1	50	5	A
P400	1	0.006	2	25	5	A
P401	1	0.006	4	25	5	A
P402	1	0.006	4	50	5	A
P403	1	0.025	0.5	25	5	C.2.1
P404	1	0.025	0.5	50	5	C.2.1
P405	1	0.025	1	25	5	C.2.1
P406	1	0.025	1	50	5	C.2.1
P407	1	0.025	2	25	5	C.2.1
P408	1	0.025	2	50	5	C.2.1
P409	1	0.025	4	25	5	C.2.1
P410	1	0.025	4	50	5	C.2.1
P411	1	0.050	0.5	25	5	C.1.2
P412	1	0.050	0.5	50	5	C.1.2
P413	1	0.050	1	25	5	C.1.2
P414	1	0.050	1	50	5	C.1.2
P415	1	0.050	2	25	5	C.1.2
P416	1	0.050	2	50	5	C.1.1
P417	1	0.050	4	25	5	C.2.1
P418	1	0.050	4	50	5	C.2.1
P419	2	0.006	0.5	25	5	B.2
P420	2	0.006	0.5	50	5	B.2
P421	2	0.006	1	25	5	B.2
P422	2	0.006	1	50	5	A
P423	2	0.006	2	25	5	B.2

Table A.3: List of simulations - Permutation runs.

ID	Incoming Significant Wave Height	Incoming Wave Steepness	Spur Height	SAG Wavelength	Maximum Spur Height Depth	Flow Type
	Hs_0	$\frac{Hs_0}{Lp_0}$	h_{spr}	λ_{SAG}	z_μ	
	m	-	m	m	m	-
P424	2	0.006	2	50	5	A
P425	2	0.006	4	25	5	A
P426	2	0.006	4	50	5	A
P427	2	0.025	0.5	25	5	C.2.1
P428	2	0.025	0.5	50	5	C.2.1
P429	2	0.025	1	25	5	C.2.1
P430	2	0.025	1	50	5	C.2.1
P431	2	0.025	2	25	5	C.2.1
P432	2	0.025	2	50	5	C.2.1
P433	2	0.025	4	25	5	A
P434	2	0.025	4	50	5	C.2.1
P435	2	0.050	0.5	25	5	C.1.2
P436	2	0.050	0.5	50	5	C.1.1
P437	2	0.050	1	25	5	C.2.1
P438	2	0.050	1	50	5	C.2.1
P439	2	0.050	2	25	5	C.2.1
P440	2	0.050	2	50	5	C.2.1
P441	2	0.050	4	25	5	C.2.1
P442	2	0.050	4	50	5	C.2.1
P443	4	0.006	0.5	25	5	B.2
P444	4	0.006	0.5	50	5	B.2
P445	4	0.006	1	25	5	B.2
P446	4	0.006	1	50	5	A
P447	4	0.006	2	25	5	B.2
P448	4	0.006	2	50	5	A
P449	4	0.006	4	25	5	B.2
P450	4	0.006	4	50	5	B.1
P451	4	0.025	0.5	25	5	C.2.1
P452	4	0.025	0.5	50	5	C.2.2
P453	4	0.025	1	25	5	C.2.1
P454	4	0.025	1	50	5	C.2.2
P455	4	0.025	2	25	5	A
P456	4	0.025	2	50	5	C.2.1
P457	4	0.025	4	25	5	A
P458	4	0.025	4	50	5	B.1
P459	4	0.050	0.5	25	5	C.1.2
P460	4	0.050	0.5	50	5	C.1.2
P461	4	0.050	1	25	5	C.2.1
P462	4	0.050	1	50	5	C.2.2
P463	4	0.050	2	25	5	C.2.1
P464	4	0.050	2	50	5	C.2.1
P465	4	0.050	4	25	5	C.2.1
P466	4	0.050	4	50	5	C.2.1
P467	6	0.006	0.5	25	5	-
P468	6	0.006	0.5	50	5	B.2
P469	6	0.006	1	25	5	-
P470	6	0.006	1	50	5	A

Table A.3: List of simulations - Permutation runs.

ID	**Incoming Significant Wave Height**	**Incoming Wave Steepness**	**Spur Height**	**SAG Wavelength**	**Maximum Spur Height Depth**	**Flow Type**
	Hs_0	$\frac{Hs_0}{Lp_0}$	h_{spr}	λ_{SAG}	z_μ	
	m	-	m	m	m	-
P471	6	0.006	2	25	5	B.2
P472	6	0.006	2	50	5	A
P473	6	0.006	4	25	5	A
P474	6	0.006	4	50	5	A
P475	6	0.025	0.5	25	5	C.1.2
P476	6	0.025	0.5	50	5	C.1.2
P477	6	0.025	1	25	5	C.1.2
P478	6	0.025	1	50	5	C.2.2
P479	6	0.025	2	25	5	C.1.2
P480	6	0.025	2	50	5	-
P481	6	0.025	4	25	5	-
P482	6	0.025	4	50	5	A
P483	6	0.050	0.5	25	5	C.1.2
P484	6	0.050	0.5	50	5	C.1.2
P485	6	0.050	1	25	5	C.1.2
P486	6	0.050	1	50	5	C.1.2
P487	6	0.050	2	25	5	C.1.2
P488	6	0.050	2	50	5	C.2.2
P489	6	0.050	4	25	5	C.1.2
P490	6	0.050	4	50	5	C.2.2

B

WAVE RESULTS - SENSITIVITY RUNS WITH AND WITHOUT REFRACTION

This appendix presents the results of the sensitivity runs with and without refraction. The objective of this investigation was to understand the effects of refraction for SAG formations in wave-averaged models that do not consider diffraction.

Plots of the cross-shore variation of the significant wave height Hs between spur and groove are provided for varying input conditions - short wave parameters and SAG geometry - both for runs with and without refraction. The alongshore forcing was not included in this analysis, as wave results do not change for different winds, that were not considered as source term for SWAN.

Overall, the results indicate that including refraction leads to extreme concentration of energy over spurs, resulting in high alongshore gradient of wave height between spurs (full lines) and grooves (dashed lines).

B.1. INFLUENCE OF VARYING PARAMETERS

B.1.1. INFLUENCE OF SHORT WAVE PARAMETERS

The four wave parameters under research are listed below:

- Significant Wave Height (Hs_0);
- Wave Steepness ($\frac{Hs_0}{Lp_0}$);
- Peak Wave Direction (Dp); and
- Directional Spreading (m in $\cos^m\theta$).

The results for each of the parameters are provided below.

WAVE HEIGHT

The cross-shore profiles of the significant wave height Hs on top of spurs and grooves for varying Hs are shown in Figure B.1, including runs with and without refraction.

WAVE PERIOD

The cross-shore profiles of the significant wave height Hs on top of spurs and grooves for varying Tp are shown in Figure B.2.

WAVE DIRECTION

The cross-shore profiles of the significant wave height Hs on top of spurs and grooves for varying Dp are shown in Figure B.3.

DIRECTIONAL SPREADING

The cross-shore profiles of the significant wave height Hs on top of spurs and grooves for varying m are shown in Figure B.4.

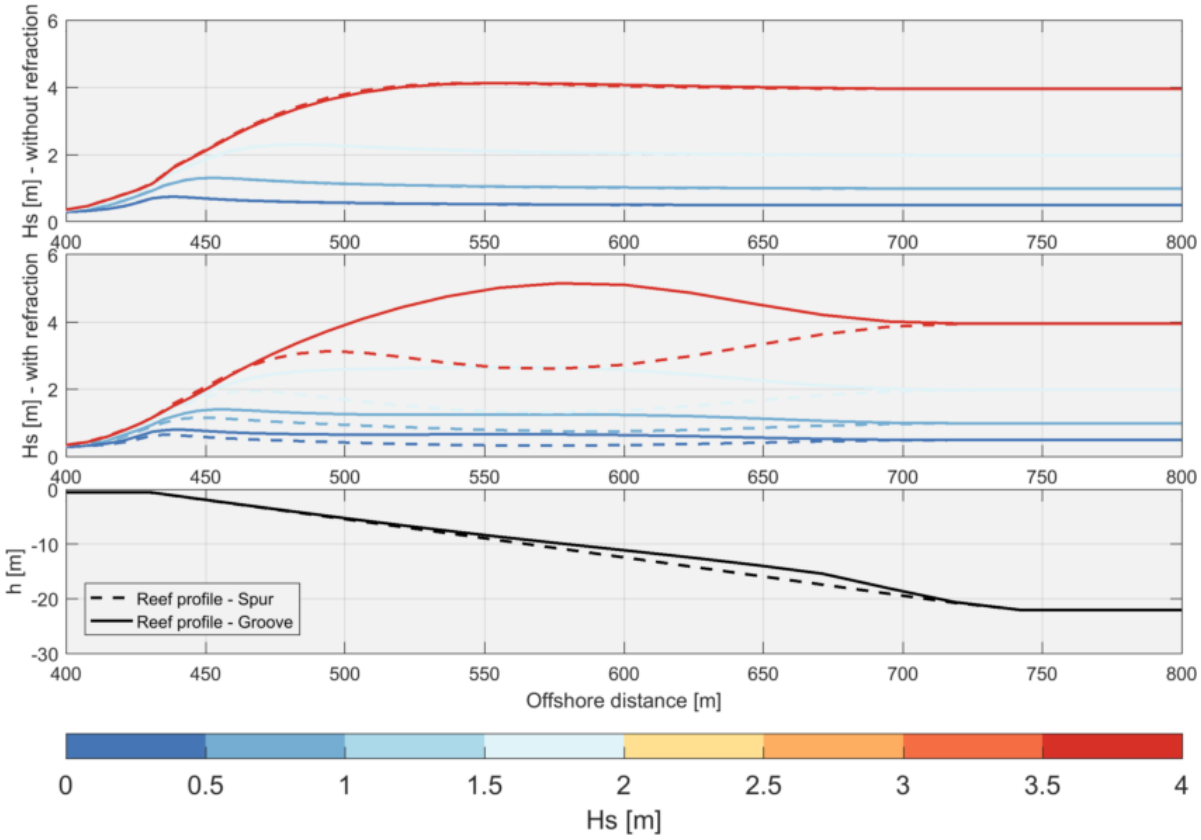

Figure B.1: Cross-shore views of results for significant wave height Hs over spur and groove for varying incoming Hs, including runs with and without refraction.

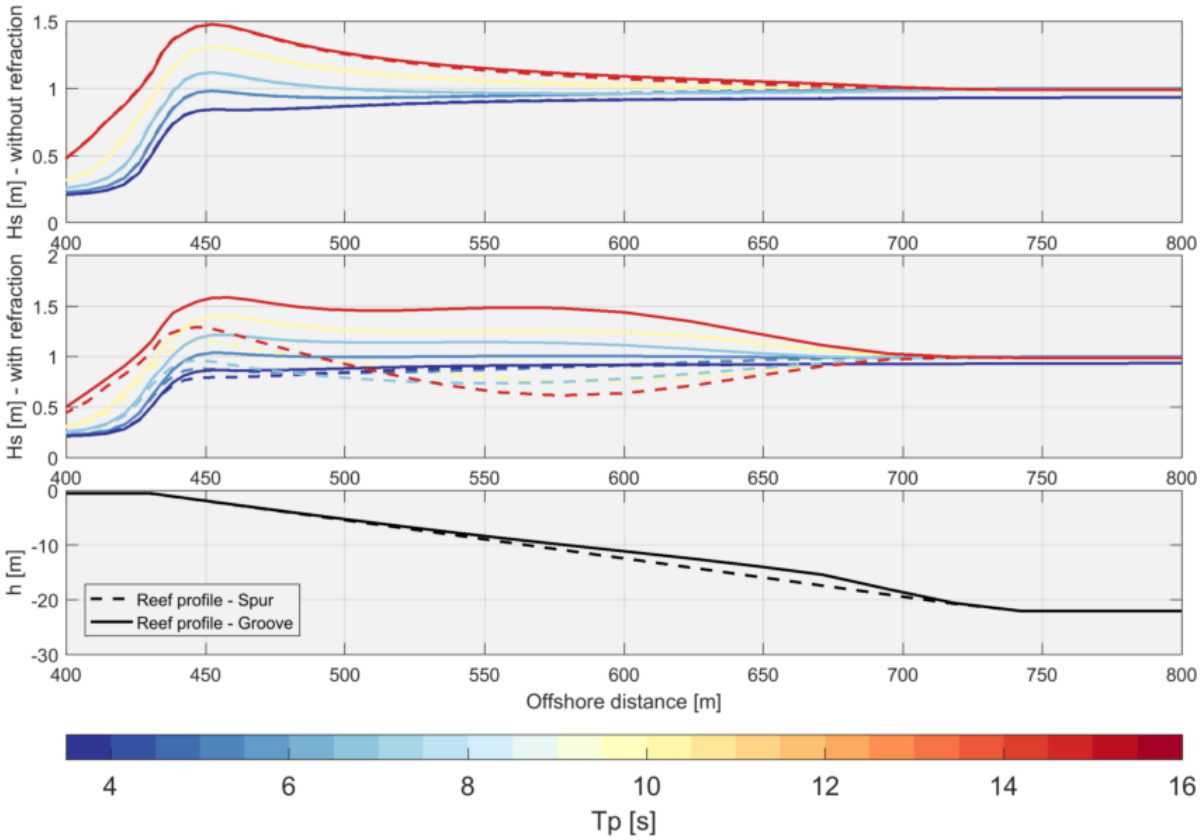

Figure B.2: Cross-shore views of results for alongshore Lagrangian velocity u_L over spur and groove for varying peak wave period Tp, including runs with and without refraction.

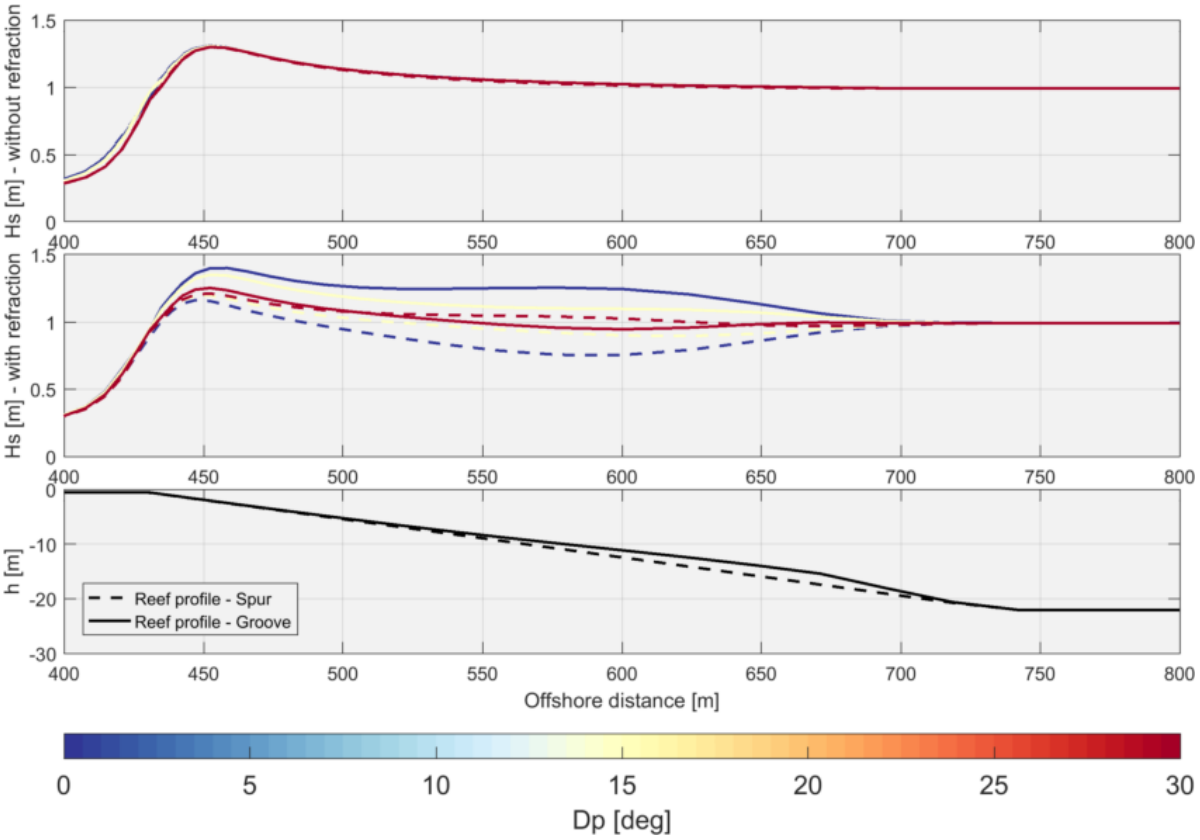

Figure B.3: Cross-shore views of results for significant wave height Hs over spur and groove for varying wave direction Dp, including runs with and without refraction.

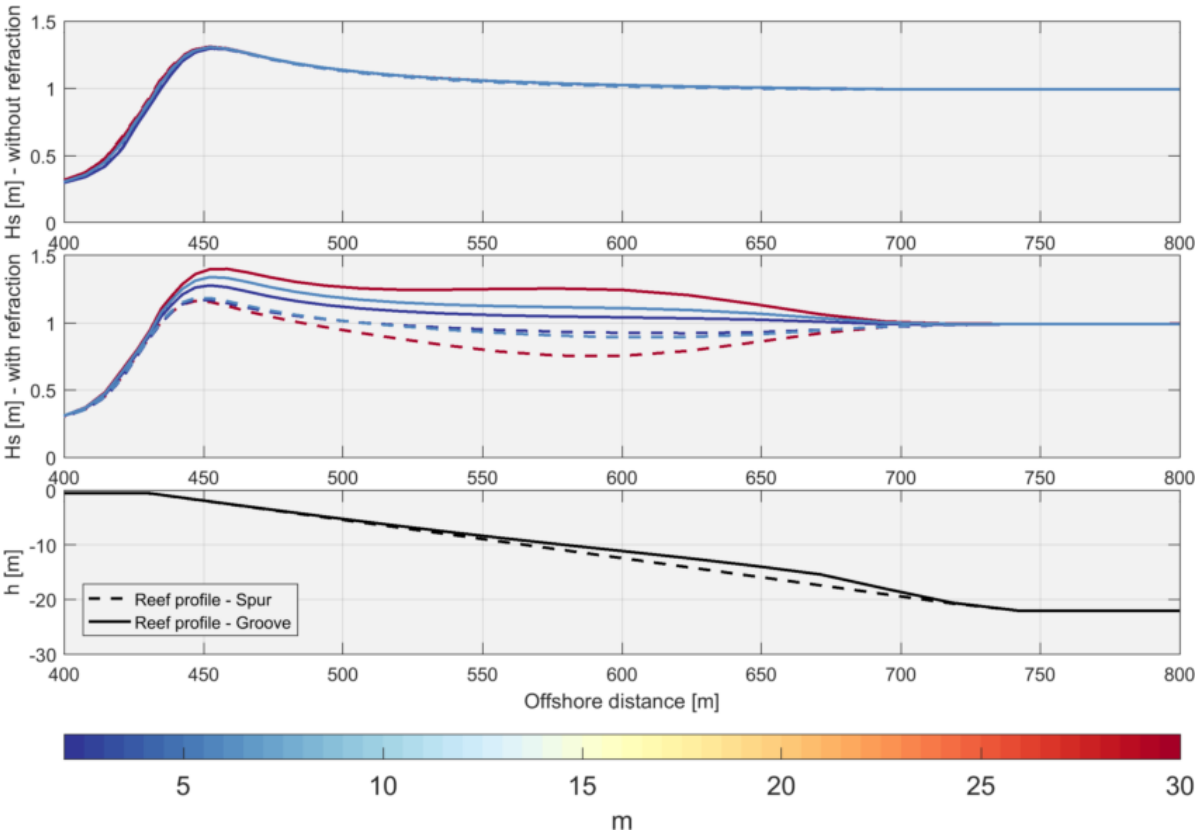

Figure B.4: Cross-shore views of results for significant wave height Hs over spur and groove for varying directional spreading m, including runs with and without refraction.

B.1.2. INFLUENCE OF SAG GEOMETRY

The five SAG geometry parameters under research with influence on SAG wave height are listed below:

- Spur height (h_{spr});
- Spur wavelength (λ_{SAG});
- Ratio of groove width and spur wavelength ($\frac{W_{grv}}{\lambda_{SAG}}$);
- Cross-shore slope (β_f);
- Cross-shore position of maximum spur height (z_μ).

The remainder parameters - ratio of friction coefficient and reef flat width - were not included in the analysis, since they have no influence on SWAN results.

The results for each of the parameters are provided below.

SPUR HEIGHT

The cross-shore profiles of the significant wave height Hs on top of spurs and grooves for varying h_{spr} are shown in Figure B.5.

SAG WAVELENGTH

The cross-shore profiles of the significant wave height Hs on top of spurs and grooves for varying λ_{SAG} are shown in Figure B.6.

GROOVE WIDTH

The cross-shore profiles of the significant wave height Hs on top of spurs and grooves for varying W_{grv} for a fixed λ_{SAG}, or simply $\frac{W_{grv}}{\lambda_{SAG}}$, are shown in Figure B.7.

CROSS-SHORE SLOPE

The cross-shore profiles of the significant wave height Hs on top of spurs and grooves for $\tan\beta_f = 0.02$ (the mildest) and $\tan\beta_f = 0.50$ (the steepest) are shown in Figures B.9 and B.10.

POSITION OF MAXIMUM SPUR HEIGHT

The cross-shore profiles of the significant wave height Hs on top of spurs and grooves for varying z_μ are shown in Figure B.8.

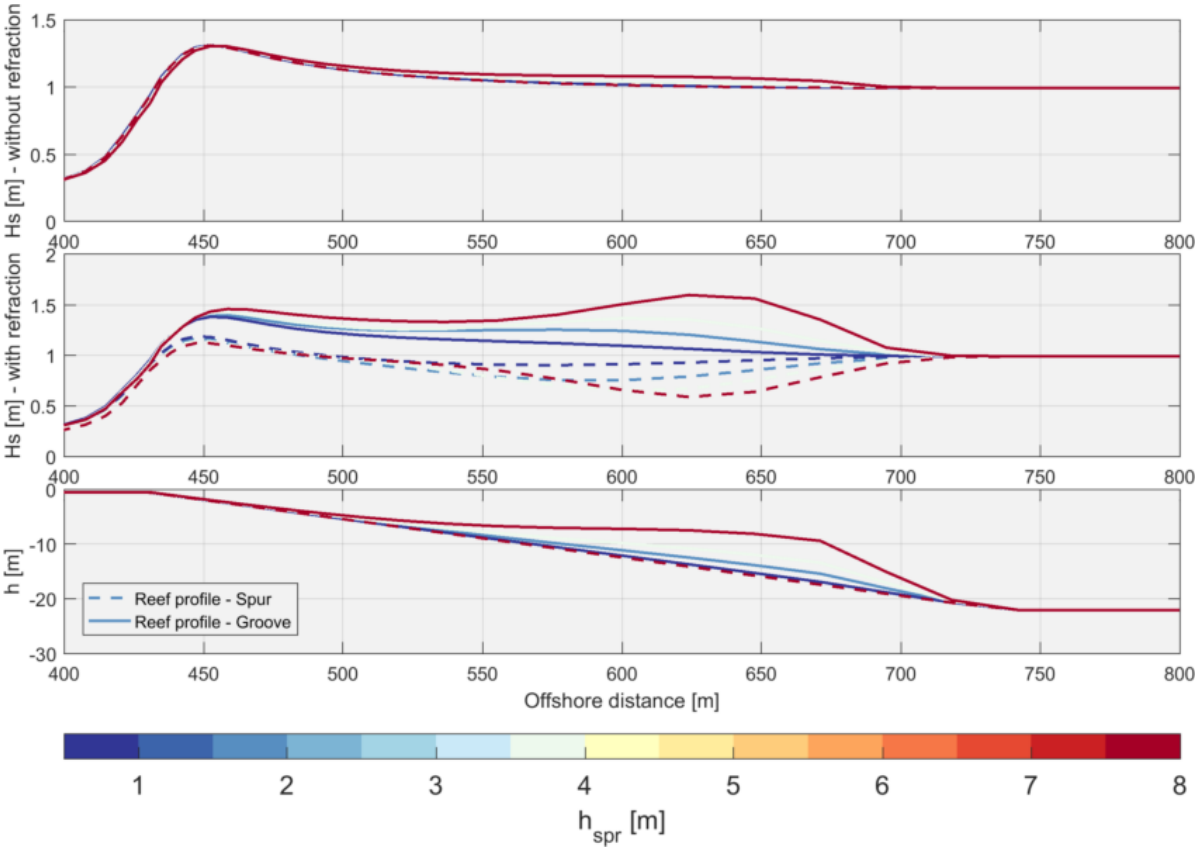

Figure B.5: Cross-shore views of results for significant wave height Hs over spur and groove for varying spur height h_{spr}, including runs with and without refraction.

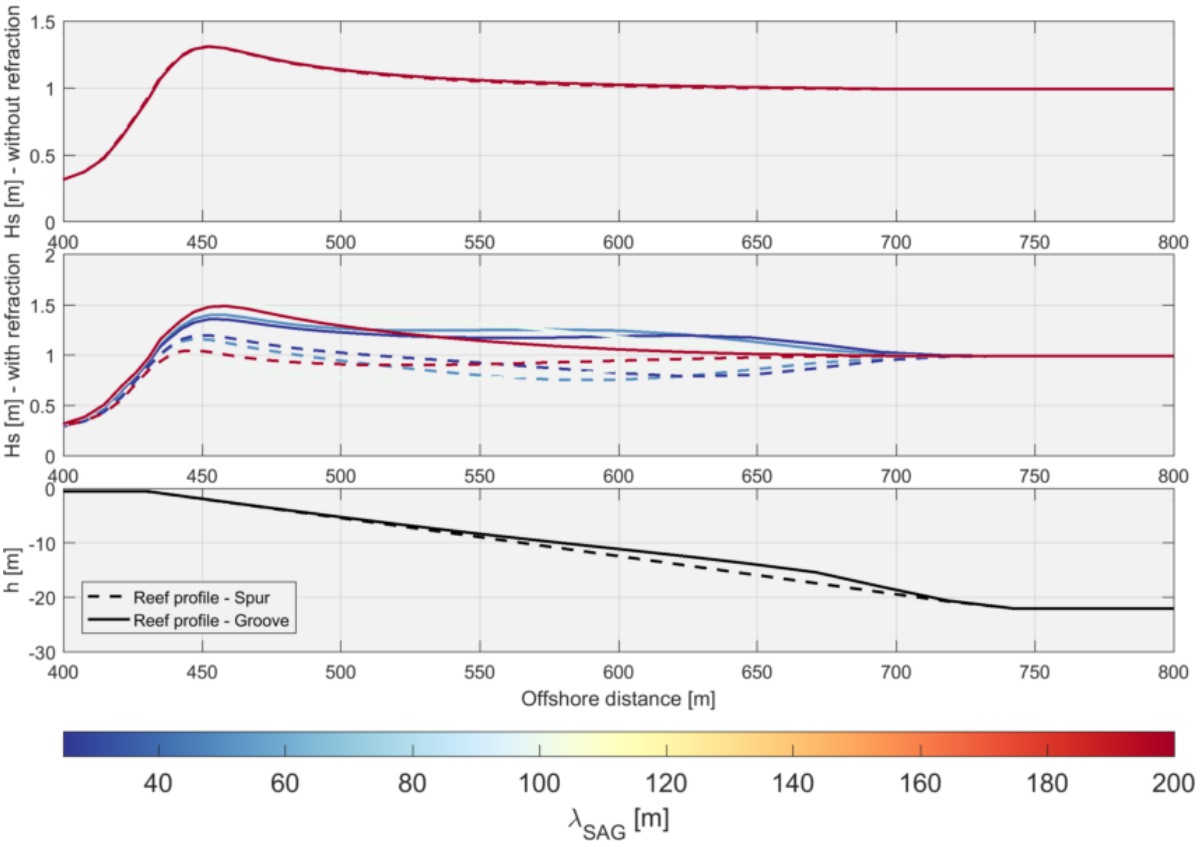

Figure B.6: Cross-shore views of results for significant wave height Hs over spur and groove for varying spur wavelength λ_{SAG}, including runs with and without refraction.

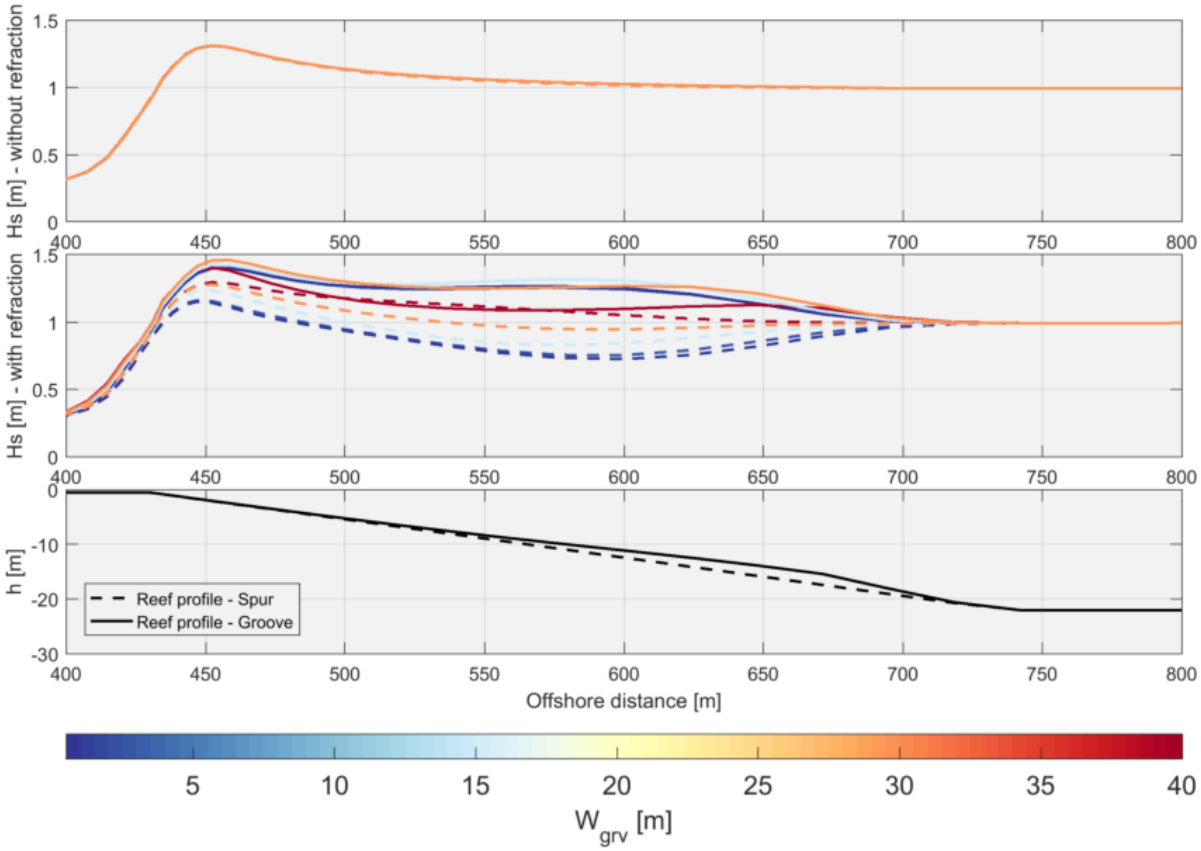

Figure B.7: Cross-shore views of results for significant wave height Hs over spur and groove for varying groove width W_{grv}, including runs with and without refraction.

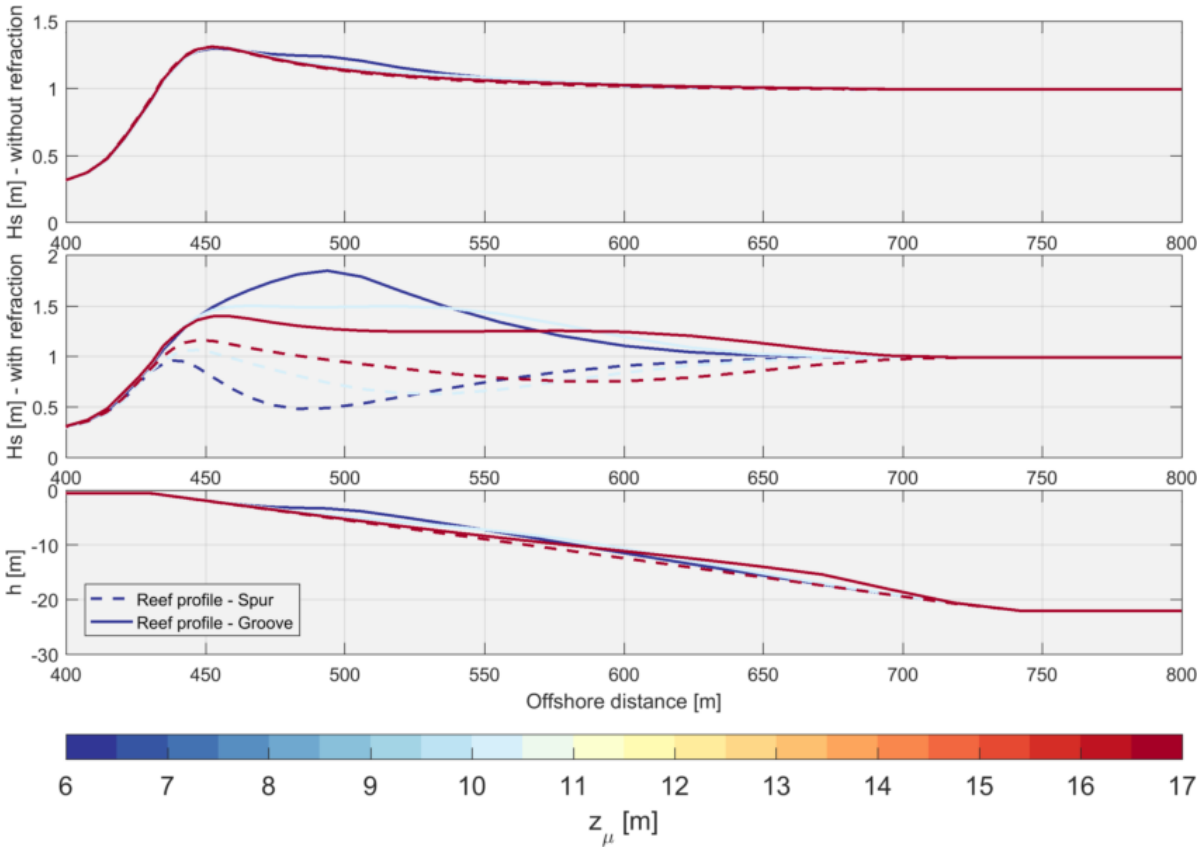

Figure B.8: Cross-shore views of results for alongshore Lagrangian velocity u_L over spur and groove for varying vertical position of maximum spur height z_μ, including runs with and without refraction.

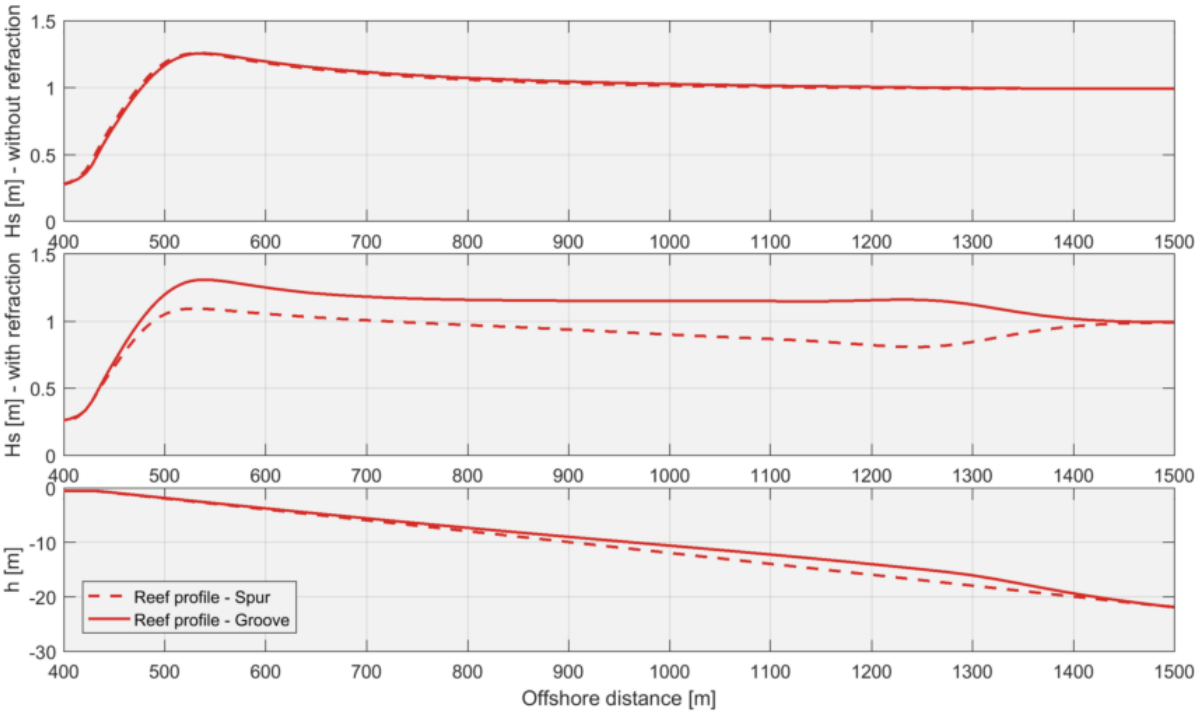

Figure B.9: Cross-shore views of results for significant wave height Hs over spur and groove for mild slope ($\tan\beta_f = 0.02$), including runs with and without refraction.

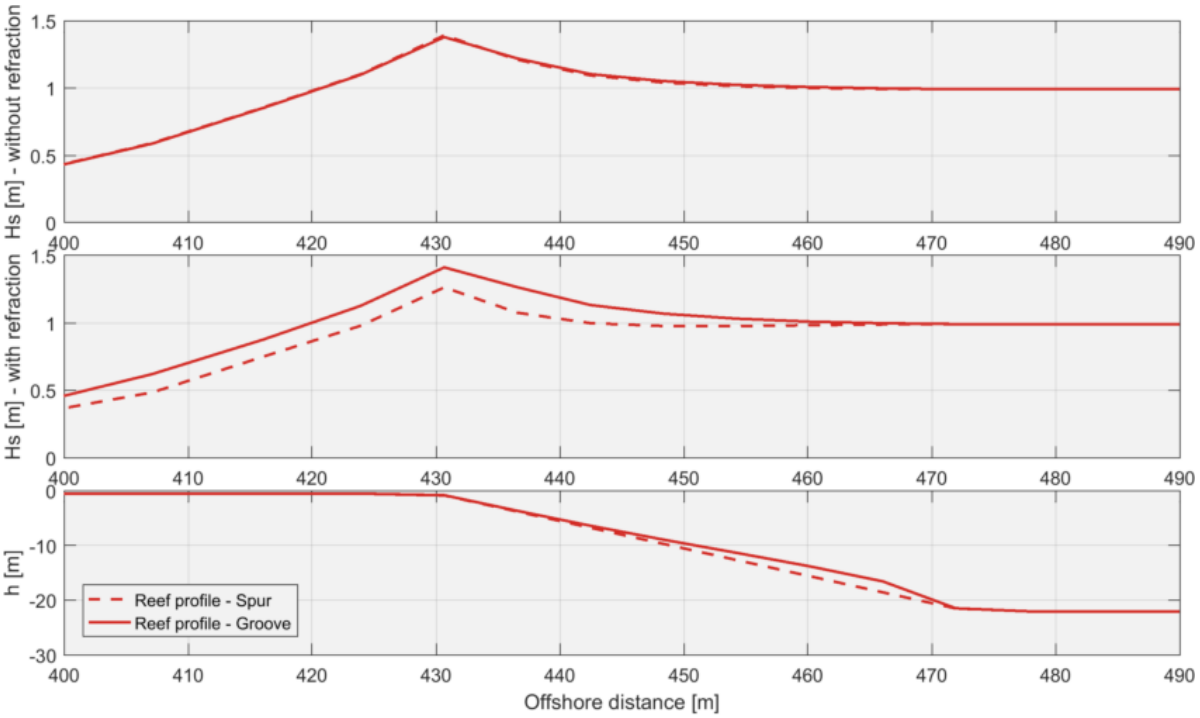

Figure B.10: Cross-shore views of results for significant wave height Hs over spur and groove for steep slope ($\tan\beta_f = 0.50$), including runs with and without refraction.

C

ALONGSHORE VELOCITIES - INFLUENCE OF VARYING PARAMETERS

This appendix presents the alongshore velocities results for varying input conditions on top of mid points between spurs and grooves. The discussion about the mechanisms and resulting effects for the alongshore currents is done in Chapter 5.3.

C.1. INFLUENCE OF VARYING PARAMETERS

In Chapter 5.2, the effects of variations of short wave parameters (Chapter 5.2.1), SAG geometry (Chapter 5.2.2), alongshore forcing (Chapter 5.2.3) and long wave forcing (Chapter C.1.4) were studied through comparisons of 3D cross-shore Lagrangian velocity profiles on top of spurs and grooves. This appendix presents similar plots for the alongshore velocities on top of mid points between spurs and grooves.

In all the velocity profiles presented below, the dashed lines represent the locations of alongshore sections, while the coloured lines provide the velocities relatively to each of those dashed lines. Reddish colours correspond to higher values of each variable, while lower values are blueish.

C.1.1. INFLUENCE OF SHORT WAVE PARAMETERS

The two wave parameters under research are listed below:

- Significant Wave Height (Hs_0); and
- Wave Steepness ($\frac{Hs_0}{Lp_0}$).

The results for each of the parameters are provided below.

WAVE HEIGHT

The cross-shore profiles of alongshore Lagrangian velocities u_L on top of mid points between spurs and grooves for varying Hs are shown in Figure C.1.

WAVE PERIOD

The cross-shore profiles of alongshore Lagrangian velocities u_L on top of mid points between spur and grooves for varying Tp are shown in Figure C.2.

C.1.2. INFLUENCE OF SAG GEOMETRY

The seven SAG geometry parameters under research are listed below:

- Spur height (h_{spr});
- Spur wavelength (λ_{SAG});
- Ratio of groove width and spur wavelength ($\frac{W_{grv}}{\lambda_{SAG}}$);

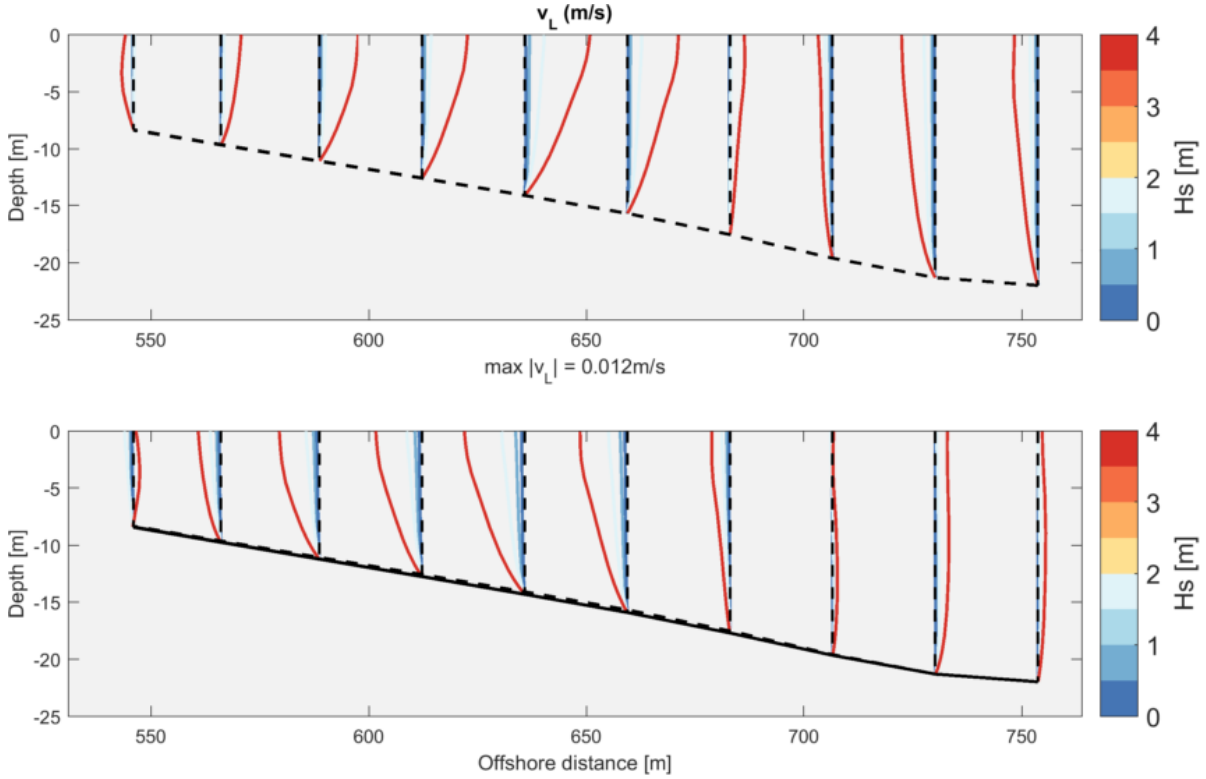

Figure C.1: Cross-shore views of results for alongshore Lagrangian velocity u_L on top of mid points between spurs and grooves for varying significant wave height Hs.

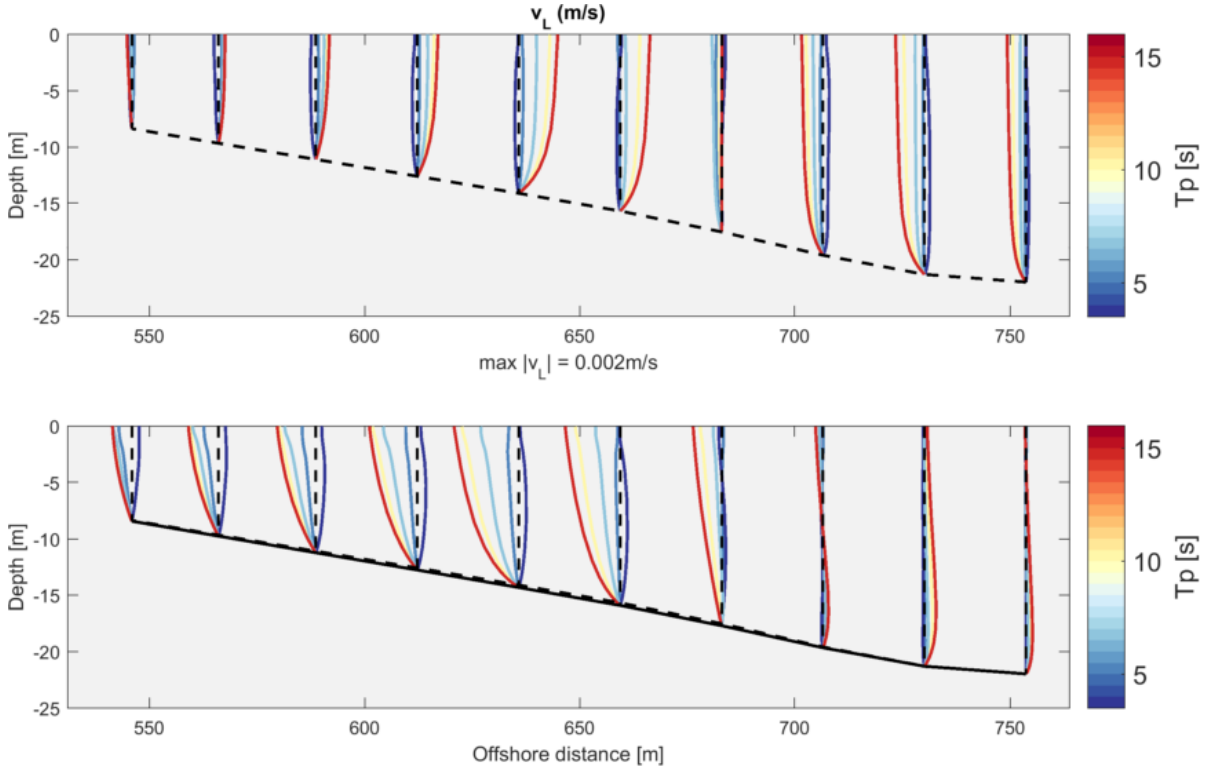

Figure C.2: Cross-shore views of results for alongshore Lagrangian velocity u_L on top of mid points between spurs and grooves for varying peak wave period Tp.

- Cross-shore slope (β_f);
- Reef flat width (W_{reef});
- Ratio of groove and spur friction coefficient ($\frac{C_{D-grv}}{C_{D-spr}}$); and
- Cross-shore position of maximum spur height (z_μ).

The results for each of the parameters are provided below.

SPUR HEIGHT
The cross-shore profiles of alongshore Lagrangian velocities u_L on top of mid points between spur and grooves for varying h_{spr} are shown in Figure C.3.

SAG WAVELENGTH
The cross-shore profiles of alongshore Lagrangian velocities u_L on top of mid points between spur and grooves for varying λ_{SAG} are shown in Figure C.4.

GROOVE WIDTH
The cross-shore profiles of alongshore Lagrangian velocities u_L on top of mid points between spur and grooves for varying W_{grv} for a fixed λ_{SAG}, or simply $\frac{W_{grv}}{\lambda_{SAG}}$, are shown in Figure C.5.

CROSS-SHORE SLOPE
The cross-shore profiles of alongshore Lagrangian velocities u_L on top of mid points between spur and grooves for $\tan\beta_f = 0.02$ (the mildest) and $\tan\beta_f = 0.50$ (the steepest) are shown in Figures C.7 and C.8.

REEF FLAT WIDTH
The variations of W_{reef} - 50 and 1000 m - were found to produce no difference on the 3D alongshore velocity profile, i.e., those two reef flat widths provide results similar to Base Case, (W_{reef} = 300 m).

FRICTION COEFFICIENT RATIO
The cross-shore profiles of alongshore Lagrangian velocities u_L on top of mid points between spur and grooves for varying $\frac{C_{D-grv}}{C_{D-spr}}$ are shown in Figure C.6.

POSITION OF MAXIMUM SPUR HEIGHT
The cross-shore profiles of alongshore Lagrangian velocities u_L on top of mid points between spur and grooves for varying z_μ are shown in Figure C.9.

C.1.3. INFLUENCE OF ALONGSHORE CURRENT
To investigate the changes in 3D circulation, varying alongshore wind speeds U_{10} were used. The cross-shore profiles of alongshore Lagrangian velocities u_L on top of mid points between spur and grooves for varying U_{10} are shown in Figure C.10.

C.1.4. IMPORTANCE OF LONG WAVES
The importance of long wave forcing was studied assuming the Base Case setup with varying peak spur heights z_μ, as described in Chapter 3.2.4. D3D-FLOW + XBeach surfbeat mode were used for those simulations. The mean alongshore depth-averaged velocity $\hat{U_L}$ for the SAG Hawaiian (z_μ = 17 m), Intermediate (z_μ = 10 m) and Buttress ($z_\mu \approx$ 5 m) styles are shown in Figure 5.31.

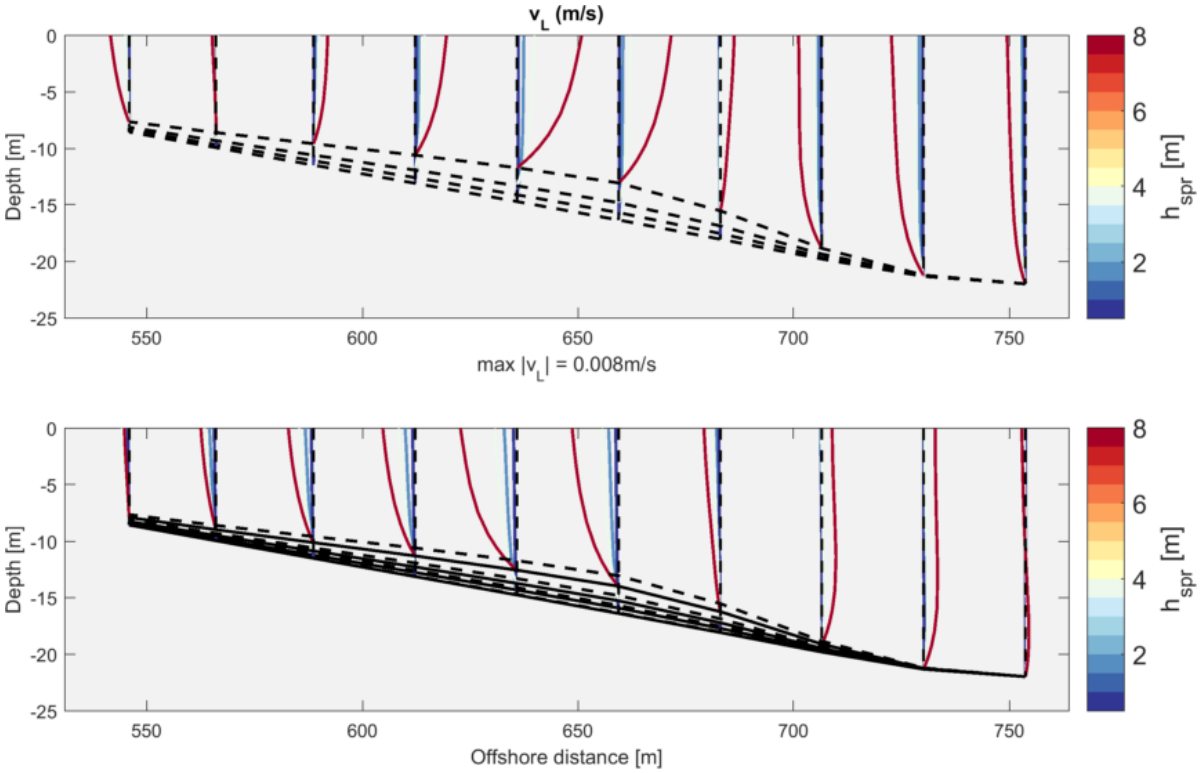

Figure C.3: Cross-shore views of results for alongshore Lagrangian velocity u_L on top of mid points between spurs and grooves for varying spur height h_{spr} .

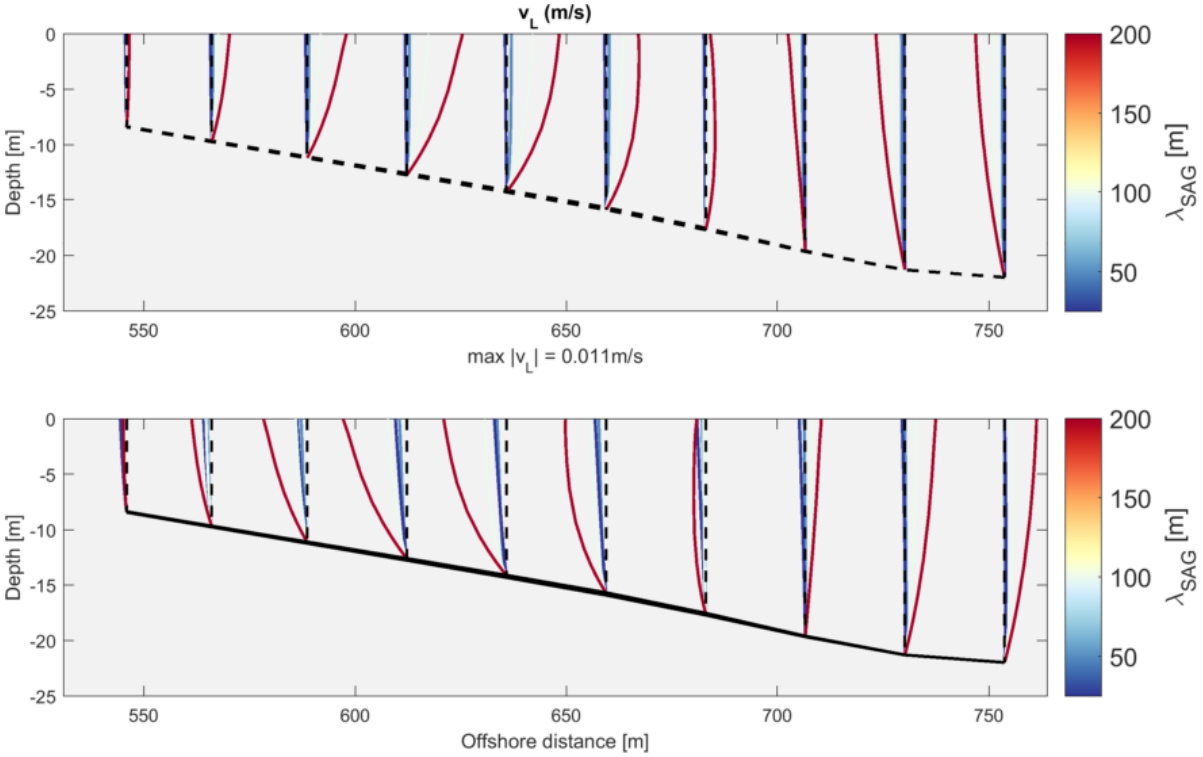

Figure C.4: Cross-shore views of results for alongshore Lagrangian velocity u_L on top of mid points between spurs and grooves for varying spur wavelength λ_{SAG}.

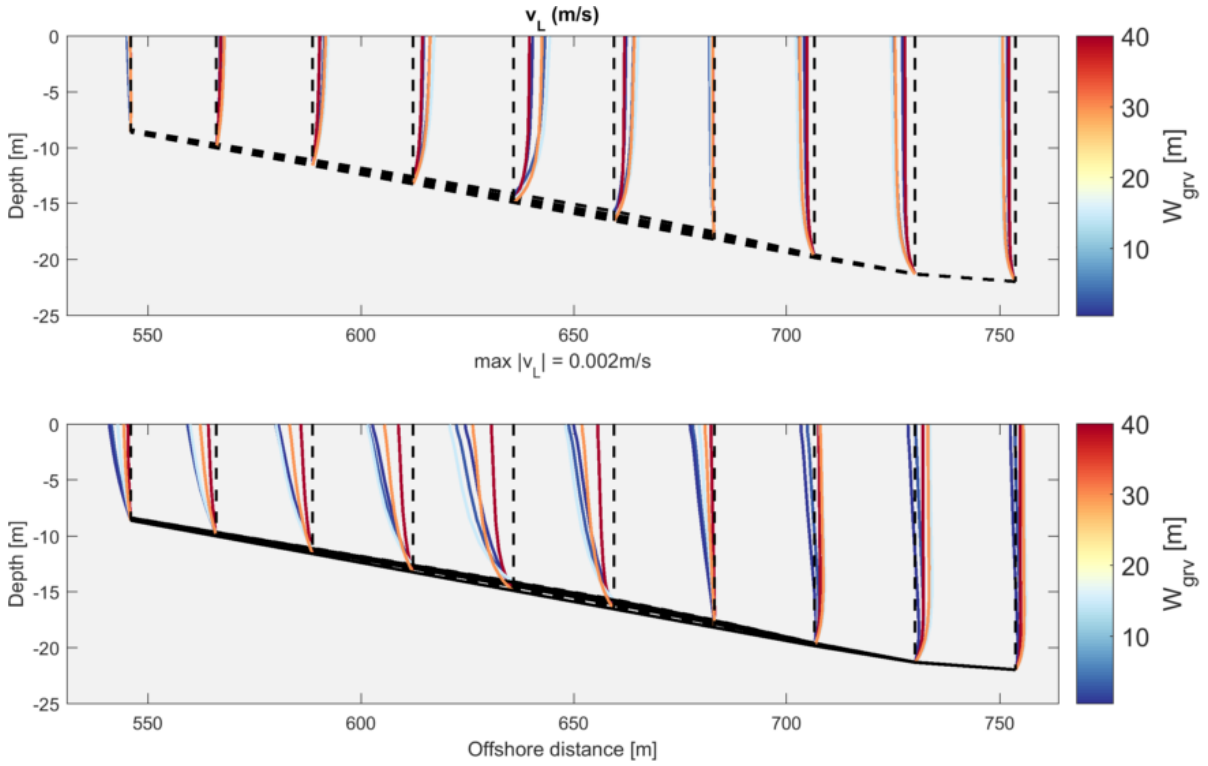

Figure C.5: Cross-shore views of results for alongshore Lagrangian velocity u_L on top of mid points between spurs and grooves for varying groove width W_{grv}.

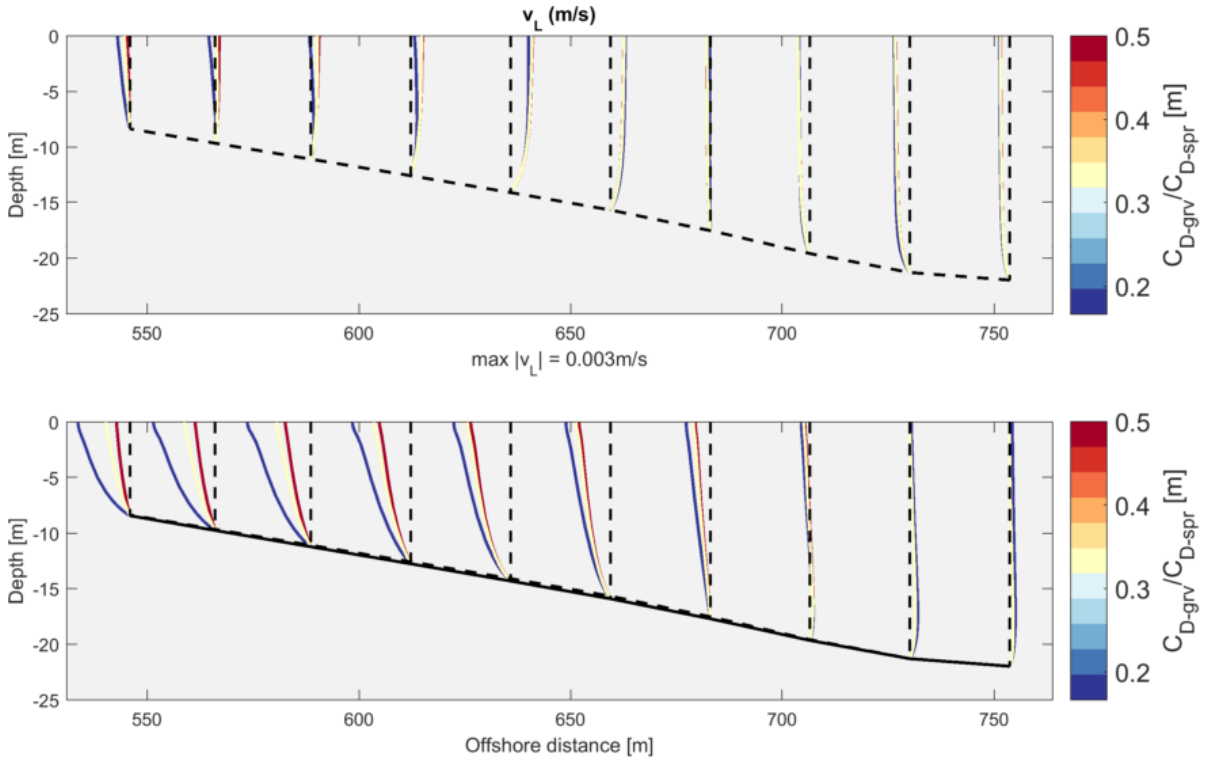

Figure C.6: Cross-shore views of results for alongshore Lagrangian velocity u_L on top of mid points between spurs and grooves for varying ratio of groove and spur friction coefficient $\frac{C_{D-grv}}{C_{D-spr}}$.

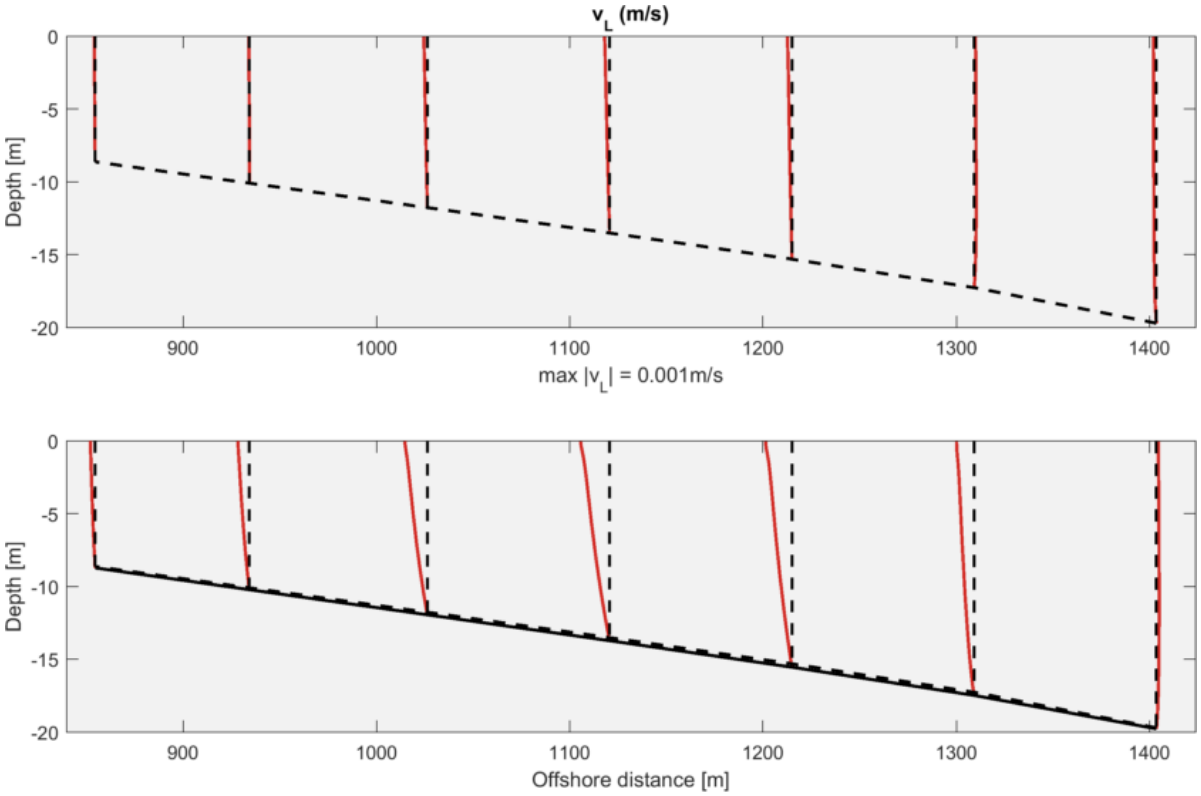

Figure C.7: Cross-shore views of results for alongshore Lagrangian velocity u_L on top of mid points between spurs and grooves for mild slope ($\tan\beta_f = 0.02$).

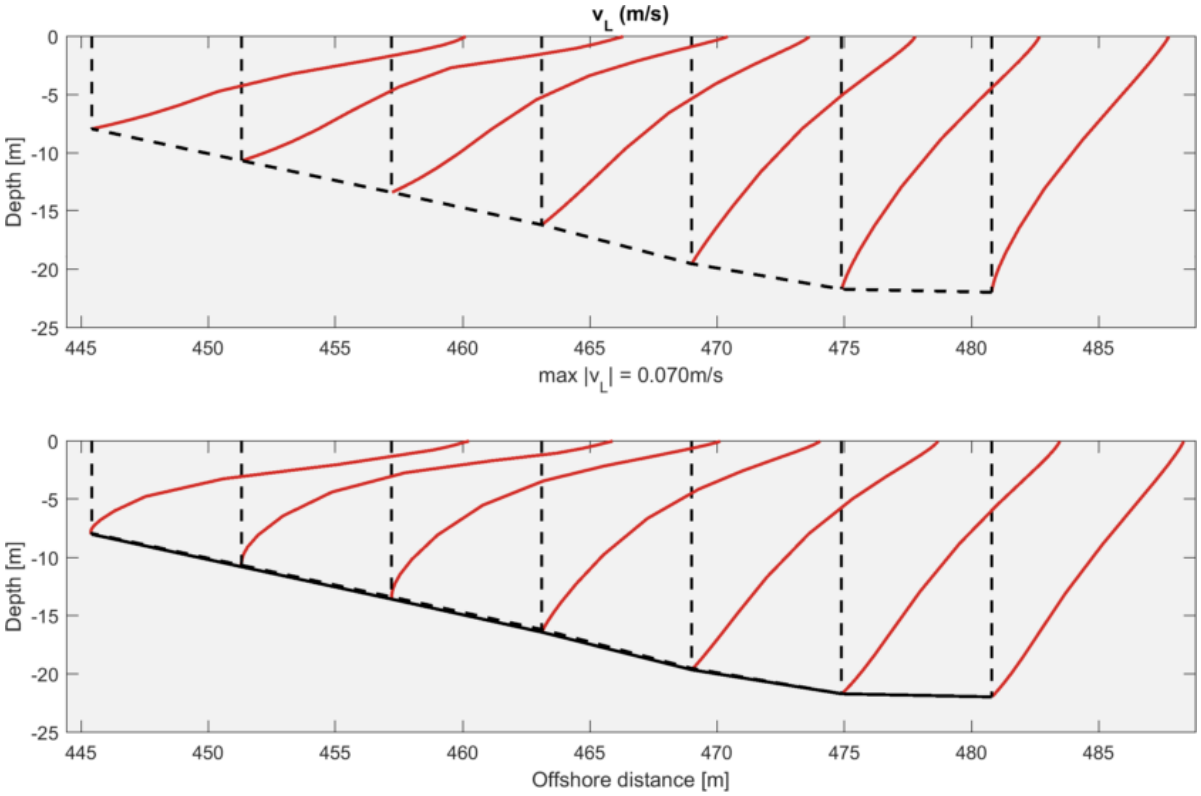

Figure C.8: Cross-shore views of results for alongshore Lagrangian velocity u_L on top of mid points between spurs and grooves for steep slope ($\tan\beta_f = 0.50$).

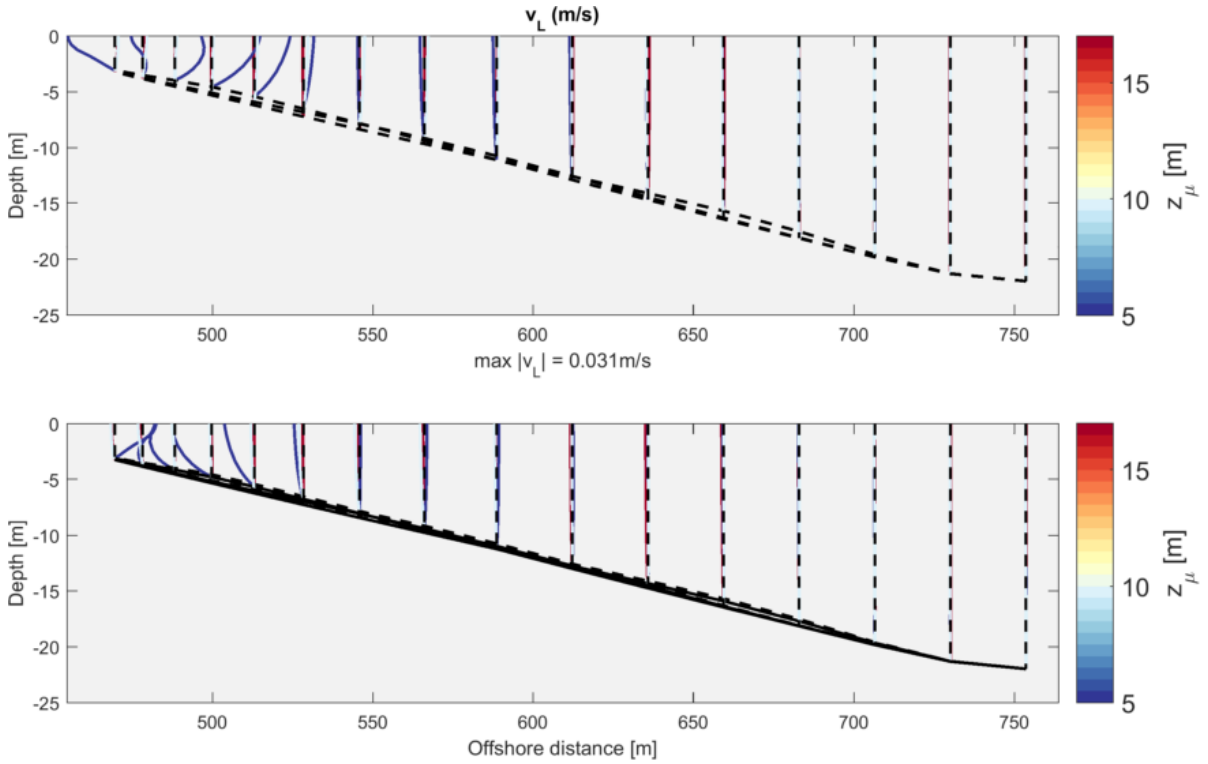

Figure C.9: Cross-shore views of results for alongshore Lagrangian velocity u_L on top of mid points between spurs and grooves for varying vertical position of maximum spur height z_μ.

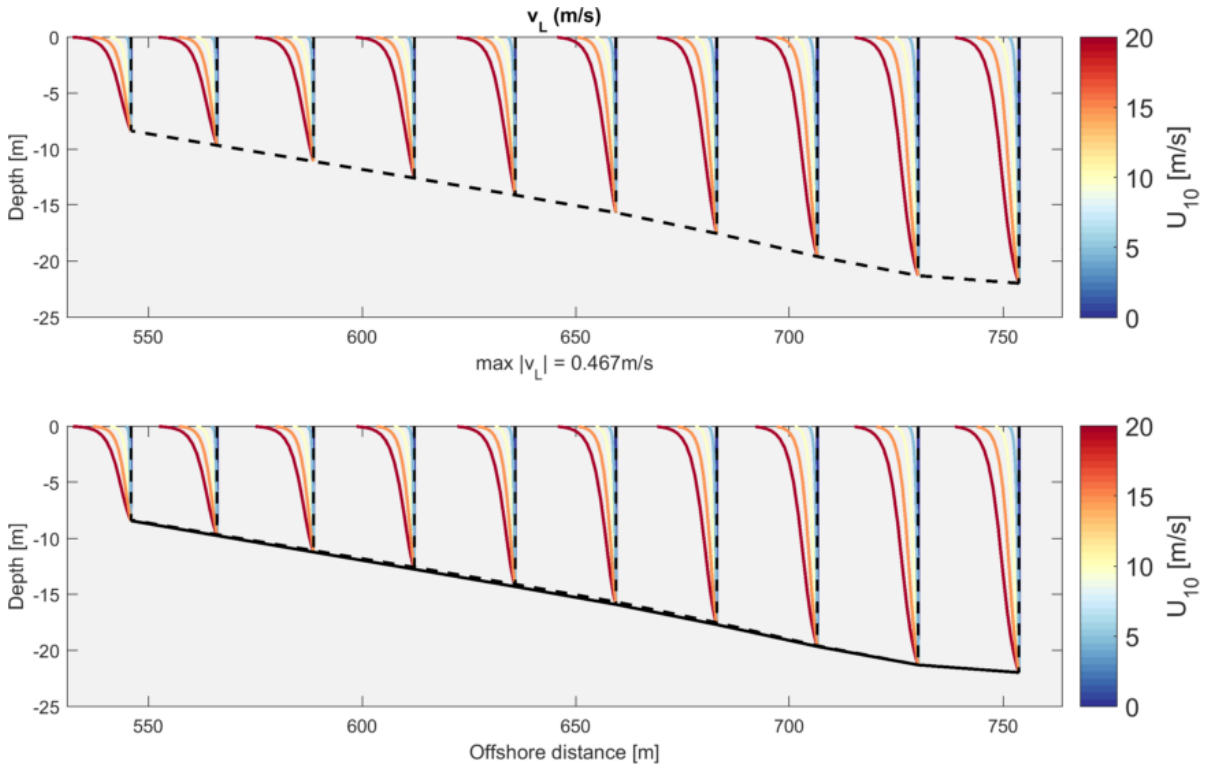

Figure C.10: Cross-shore views of results for alongshore Lagrangian velocity u_L on top of mid points between spurs and grooves for varying alongshore wind speed U_{10}.

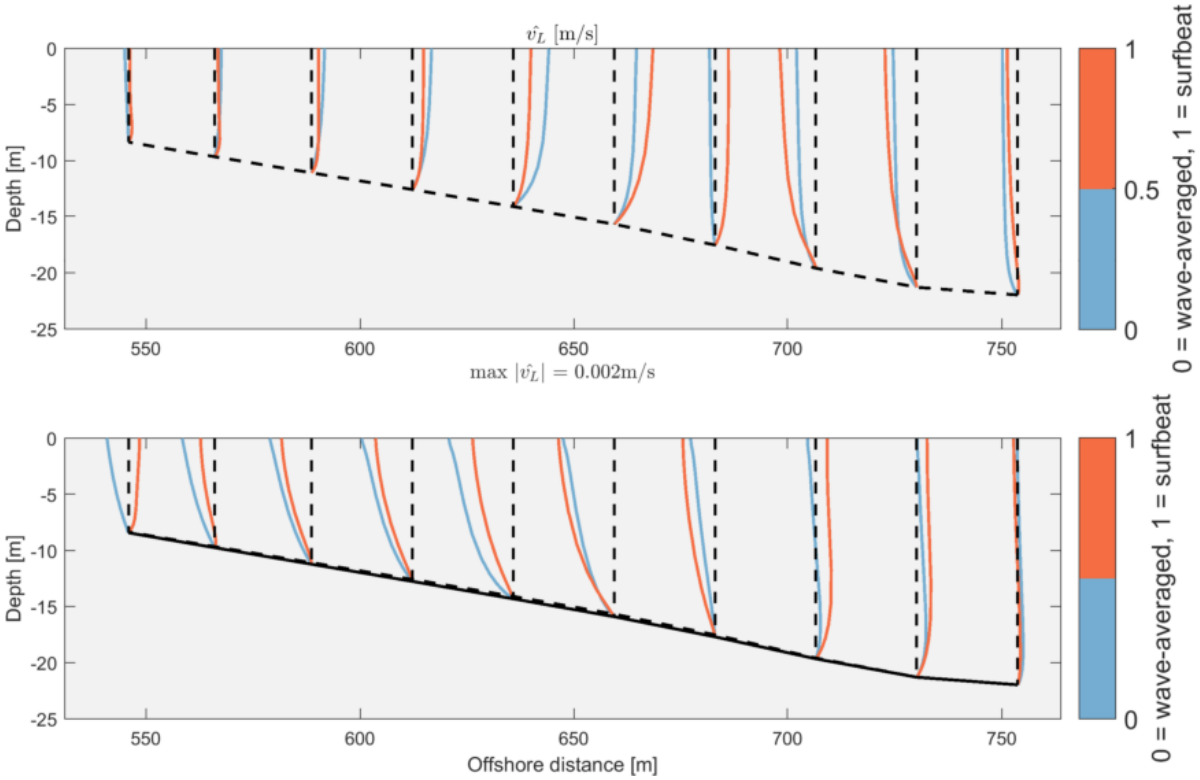

Figure C.11: Cross-shore views of D3D-FLOW + SWAN and D3D-FLOW + XBeach surfbeat Base Case (Hawaiian type with z_μ = 17 m) results for alongshore shore Lagrangian velocity $\hat{v_L}$ on top of mid points between spurs and grooves.

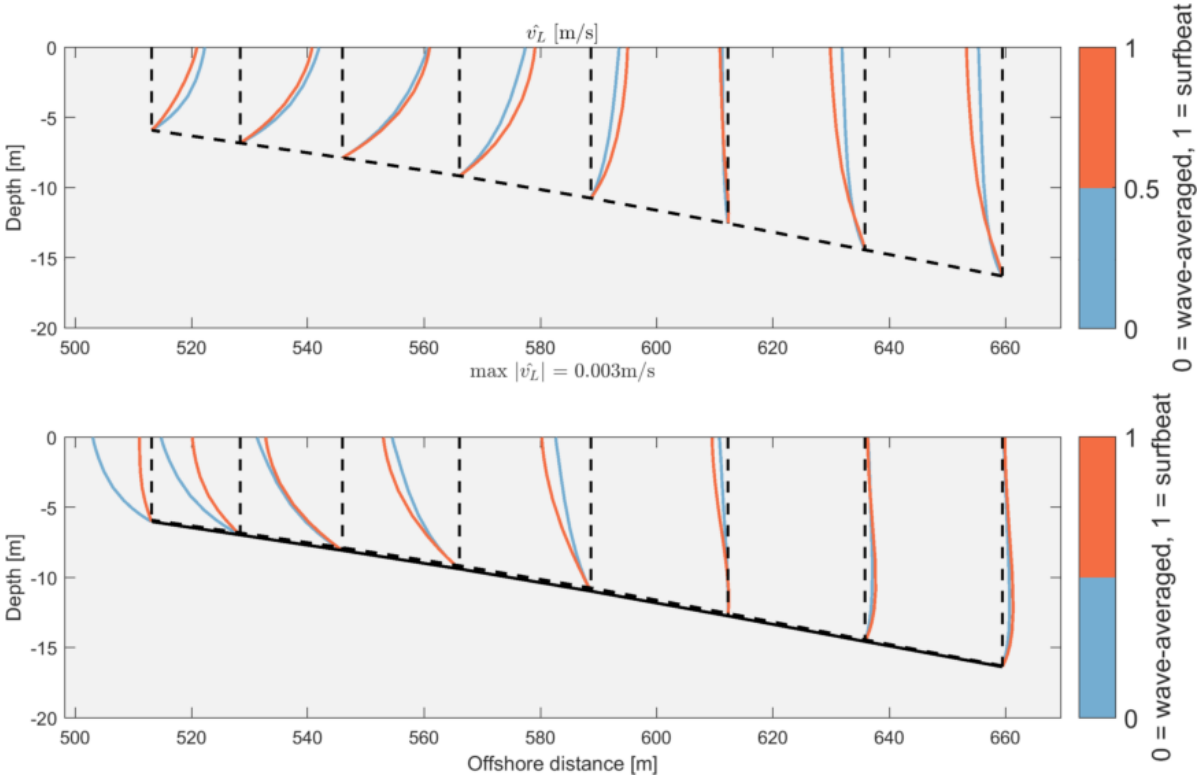

Figure C.12: Cross-shore views of D3D-FLOW + SWAN and D3D-FLOW + XBeach surfbeat Intermediate type (z_μ = 10 m) results for alongshore shore Lagrangian velocity $\hat{v_L}$ on top of mid points between spurs and grooves.

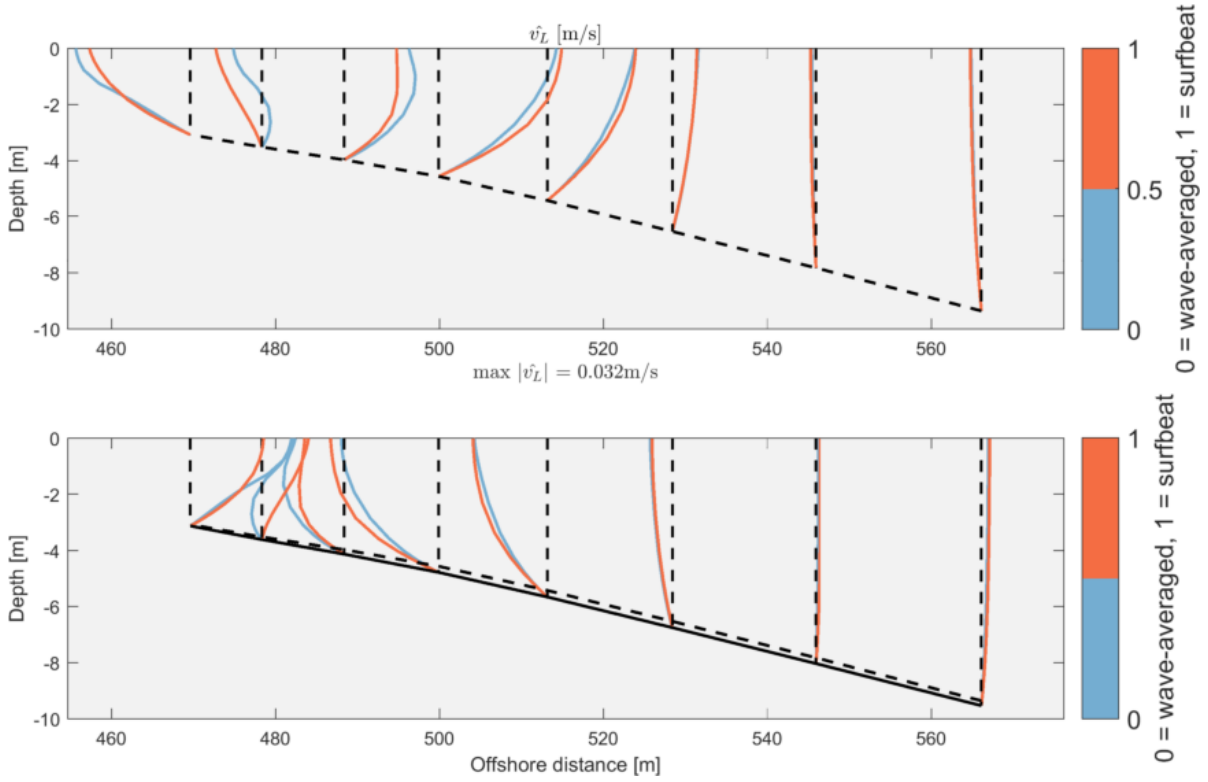

Figure C.13: Cross-shore views of D3D-FLOW + SWAN and D3D-FLOW + XBeach surfbeat Buttress type ($z_\mu \approx 5$ m) results for alongshore shore Lagrangian velocity v_L^* on top of mid points between spurs and grooves.

D

RESULTS FOR D3D-FLOW + XBEACH

This appendix presents the mean results for the Intermediate and Buttress SAG types with long wave forcing (Section D.1) and the intrawave flow variation for all cases (Section D.2) .

The importance of long wave forcing was studied assuming the Base Case setup with varying peak spur heights z_μ. D3D-FLOW + XBeach surfbeat mode were used for those simulations.

D.1. SIGNIFICANT LONG WAVE HEIGHT AND MEAN FLOW

Plots of significant long wave height and the mean cross-shore depth-averaged velocities were reported in CHapter C.1.4 for the Base Case (Hawaiann SAG style).

The significant long wave height Hs_{long} and the mean cross-shore depth-averaged velocity $\hat{U}_L$ for Intermediate style (z_μ = 10 m) and Buttress SAG style ($z_\mu \approx$ 5 m) are shown in Figures D.1 and D.3.

The cross-shore profiles of cross-shore Lagrangian velocities $\hat{u_L}$ on top of spur and grooves for cases with (red) and without (blue) long waves are shown in Figures D.2 and D.4, for Intermediate style (z_μ = 10 m) and Buttress style ($z_\mu \approx$ 5 m), respectively.

The discussion about the results presented below is shown in Chapter C.1.4.

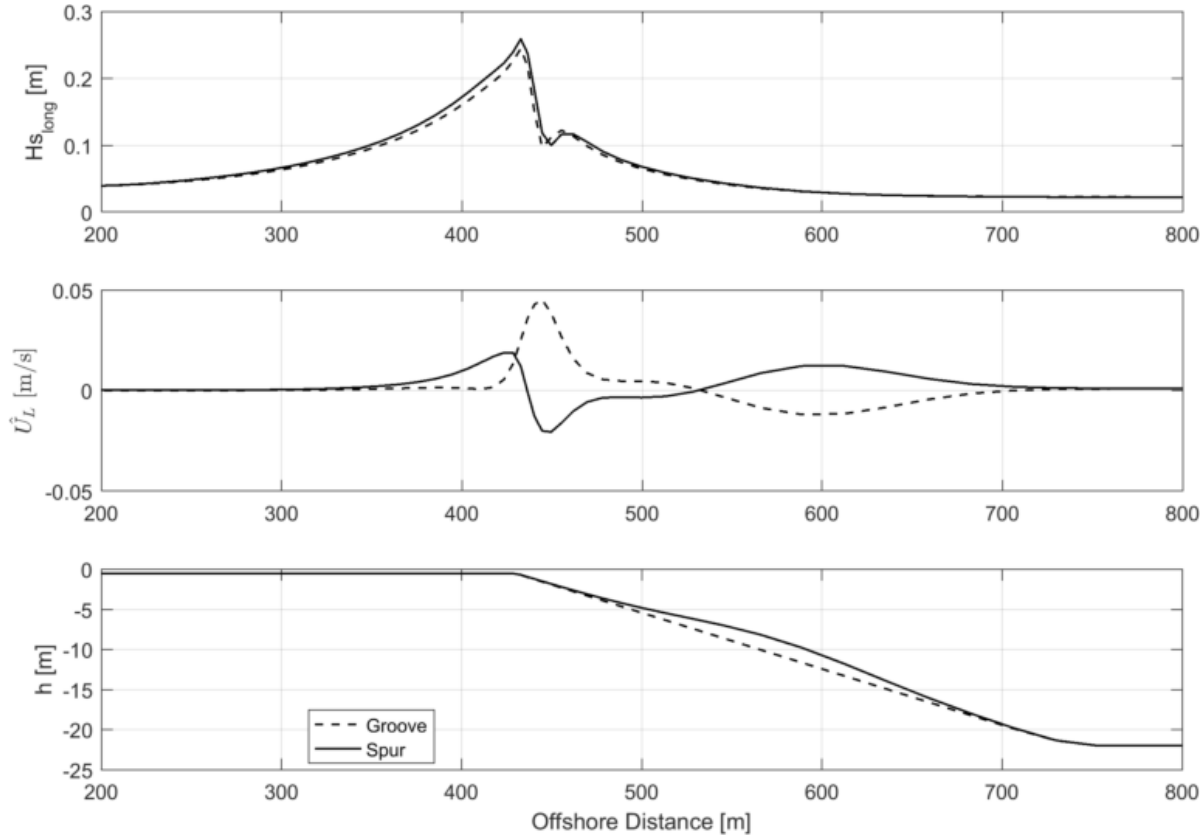

Figure D.1: Cross-shore views of D3D + XBeach surfbeat Intermediate type (z_μ = 10 m)) results for significant long wave height Hs, cross-shore depth-averaged Lagrangian velocity $\hat{U}_L$ and cross-shore depth profile over spur and groove.

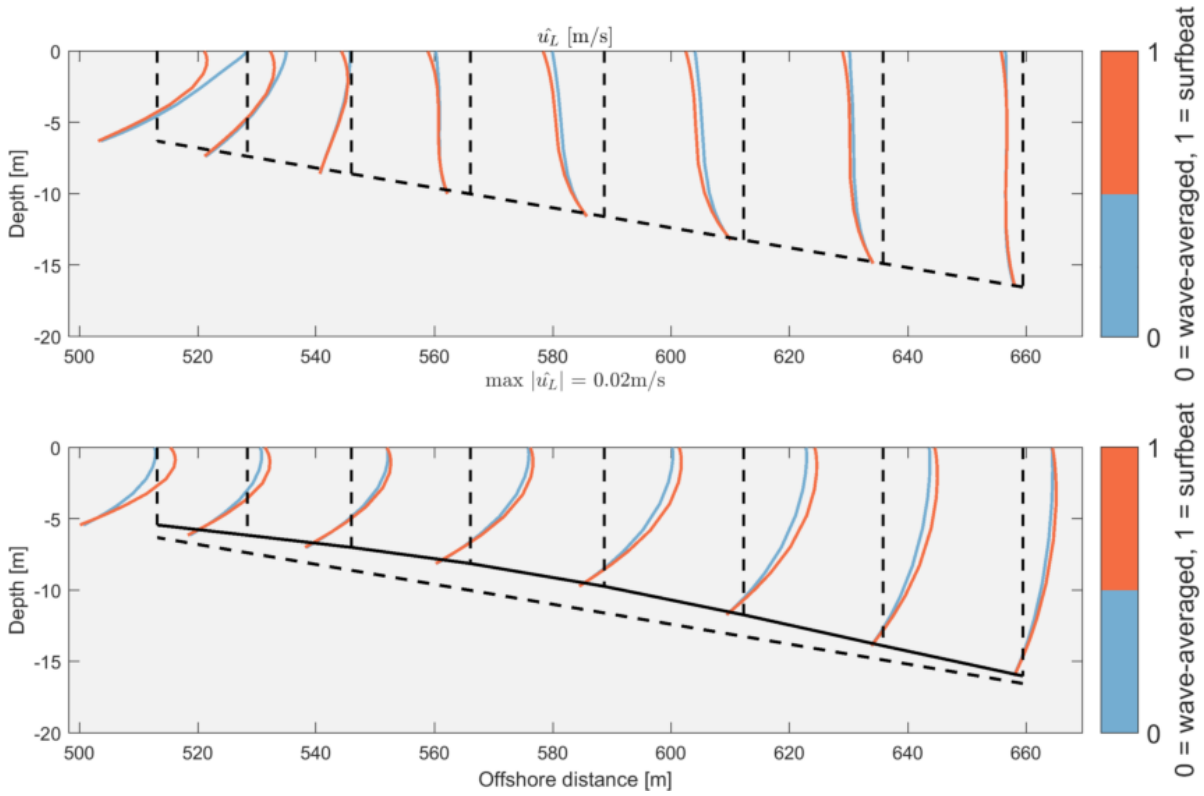

Figure D.2: Cross-shore views of D3D-FLOW + SWAN and D3D-FLOW + XBeach surfbeat Intermediate type (z_μ = 10 m) results for cross-shore Lagrangian velocity $\hat{u_L}$ over spur and groove.

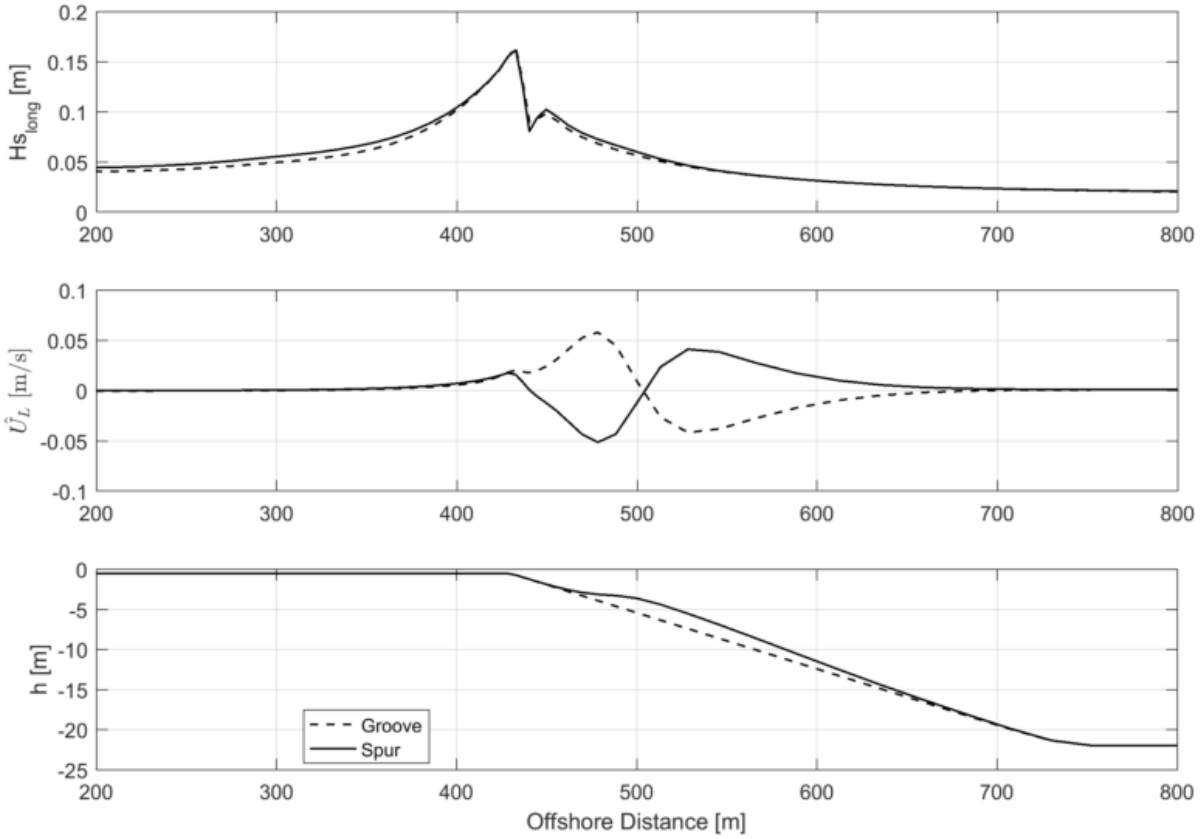

Figure D.3: Cross-shore views of D3D + XBeach surfbeat Buttress type ($z_\mu \approx 5$ m) results for significant long wave height Hs, cross-shore depth-averaged Lagrangian velocity $\hat{U}_L$ and cross-shore depth profile over spur and groove.

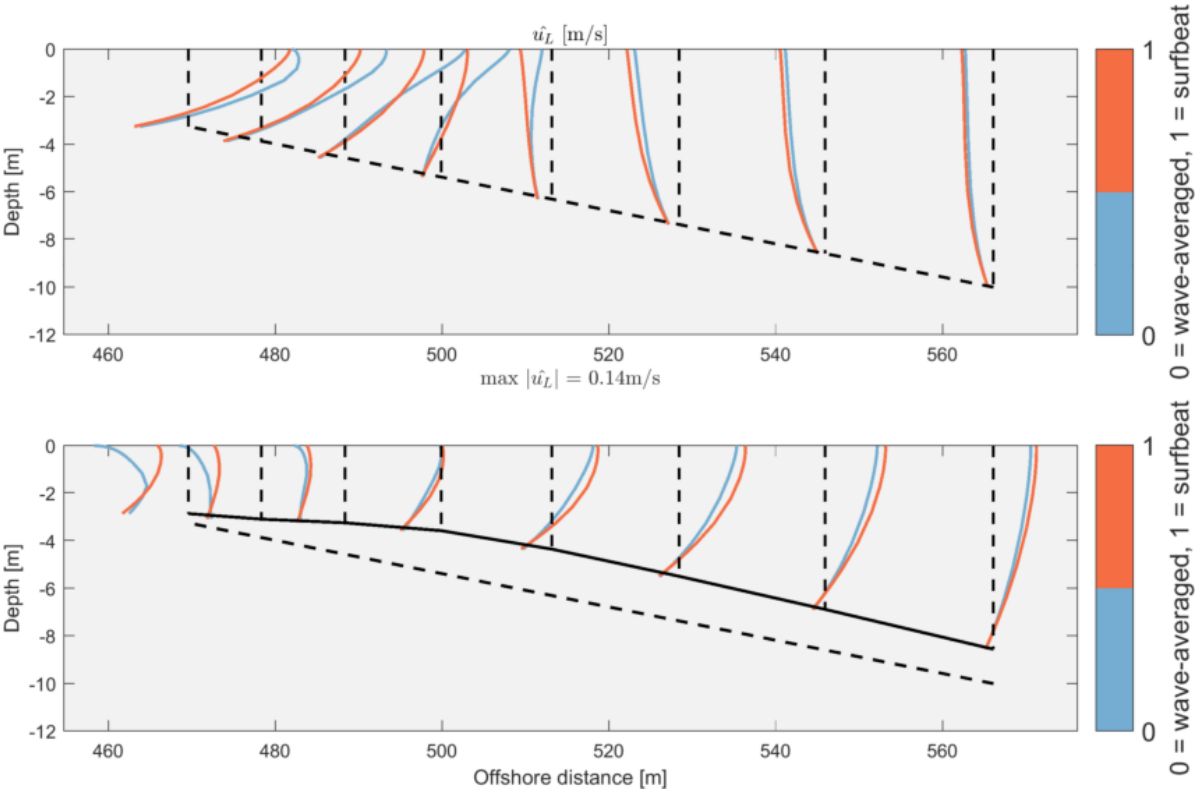

Figure D.4: Cross-shore views of D3D-FLOW + SWAN and D3D-FLOW + XBeach surfbeat Buttress type ($z_\mu \approx 5$ m) results for cross-shore Lagrangian velocity $\hat{u_L}$ over spur and groove.

D.2. INTRAWAVE FLOW

The intrawave flow - i.e., the flow within the long wave period - was evaluated by statistically analyzing the time series of the depth-averaged spur velocities at the peak spur height depth for each of the SAG type. Figures D.5, D.6 and D.7 present the velocity time series plot for the depth-averaged Lagrangian velocities for the Hawaiannn, Intermediate and Buttress types, respectively.

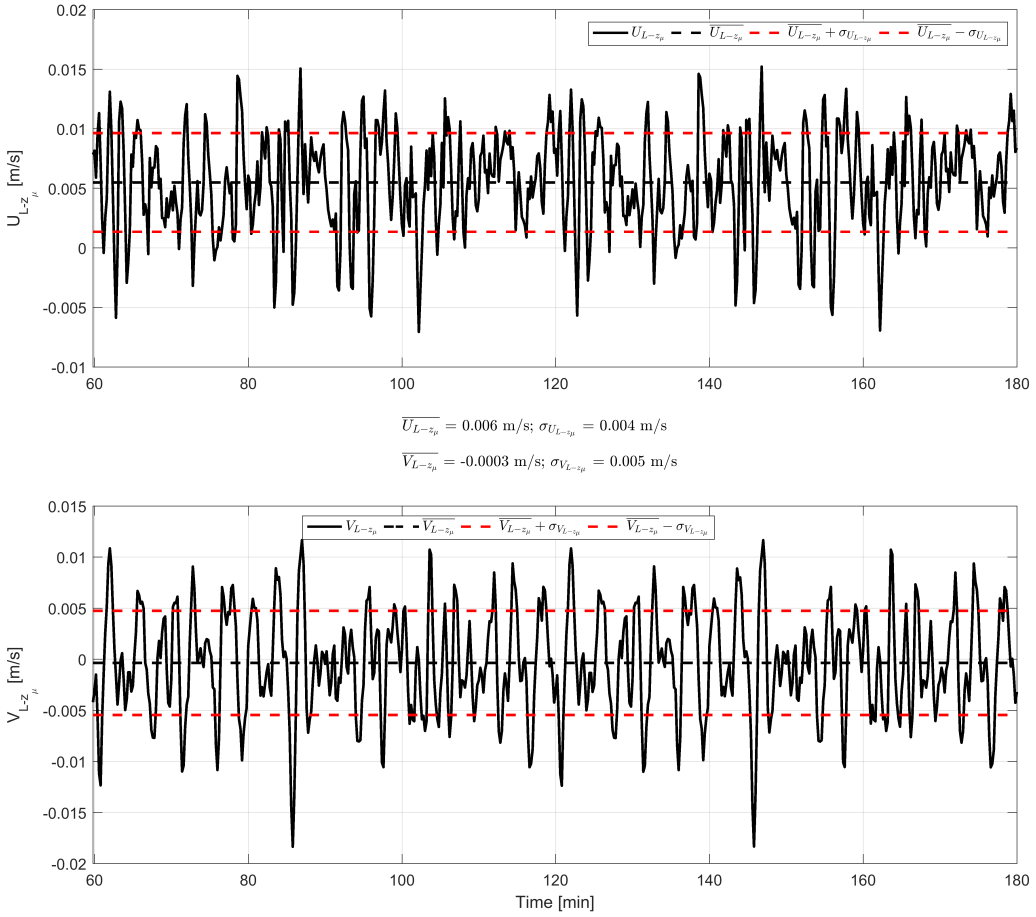

Figure D.5: Time series for cross-shore and alongshore depth-averaged Lagrangian velocities (U_L and V_L) of D3D + XBeach surfbeat run with Hawaiann type (z_μ = 17 m).

Results show that the intrawave variations of the flow are significant, with standard deviation being equal or higher than the mean velocities both for the cross-shore and alongshore velocities. The alongshore velocities oscillate around a zero value, with standard variations one order of magnitude higher than the mean alongshore flow. This null mean alongshore flow was shown to be the point where pressure gradient and wave force balance for the Base Case at the peak spur height depth (Figure 5.19). The standard deviation of cross-shore and alongshore flow have similar order of magnitude.

Overall, the intrawave flow seems to be as important as the mean flow. Accordingly, the transport of matter might be affected, thus that intrawave motion may be relevant in the context of coral growth and health. Further research on the SAG flow within the long wave period is recommended as a next step.

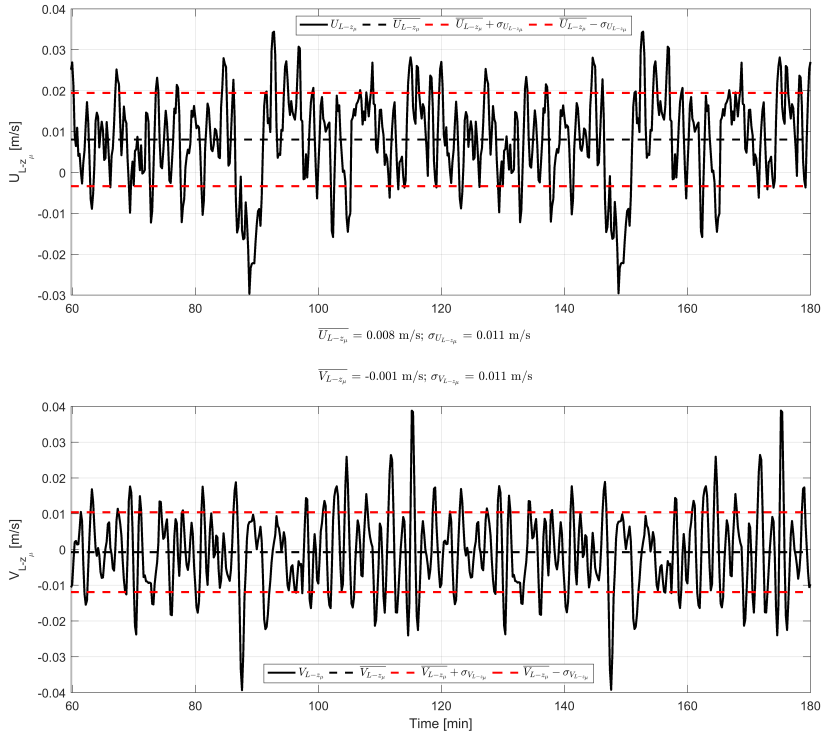

Figure D.6: Time series for cross-shore and alongshore depth-averaged Lagrangian velocities (U_L and V_L) of D3D + XBeach surfbeat run with Intermediate type (z_μ = 10 m).

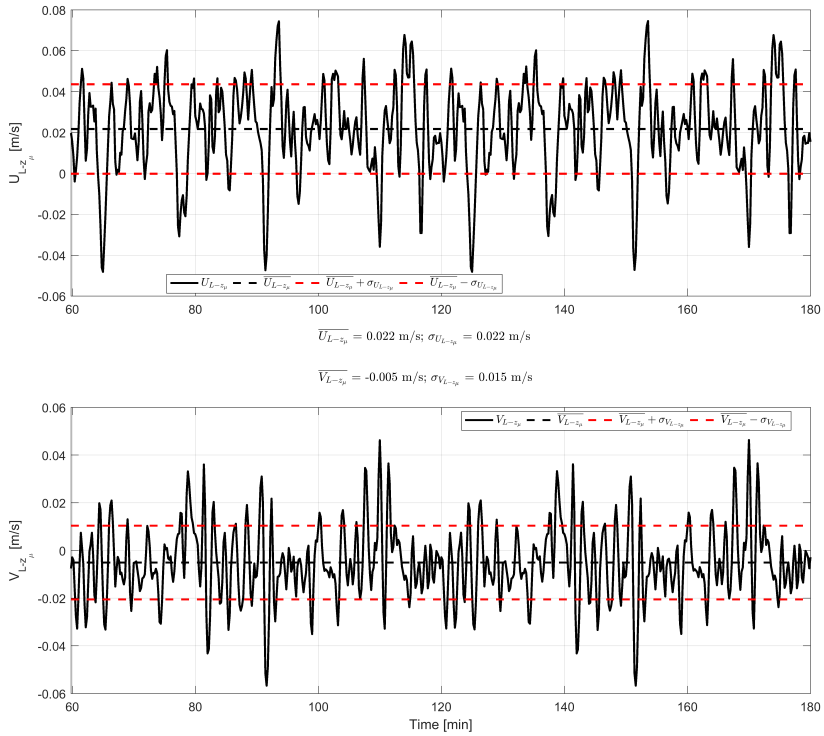

Figure D.7: Time series for cross-shore and alongshore depth-averaged Lagrangian velocities (U_L and V_L) of D3D + XBeach surfbeat run with Buttress type ($z_\mu \approx 5$ m).

E

RESULTS OF INDICATORS FOR VARYING WAVE PARAMETERS, SAG GEOMETRY AND ALONGSHORE FORCING

This appendix presents the results for the indicators for the flow characterization and for evaluations on the implications of that flow considering coral health aspects.

The results for h_{cr}, $\frac{\langle|V_{sp}|\rangle}{\langle|U_{sp}|\rangle}$, $\frac{U_{spr-max}}{U_{spr-max-BC}}$, $\frac{\langle|U_{sur}|\rangle}{\langle|U_{sur-BC}|\rangle}$, and $\frac{\langle|U_{bot}|\rangle}{\langle|U_{bot-BC}|\rangle}$ for varying short wave parameters, SAG geometry and alongshore forcing are presented in Figures E.1, E.2, E.3, E.4 and E.5.

The discussion about these results presented below is shown in Chapter 5.4.2.

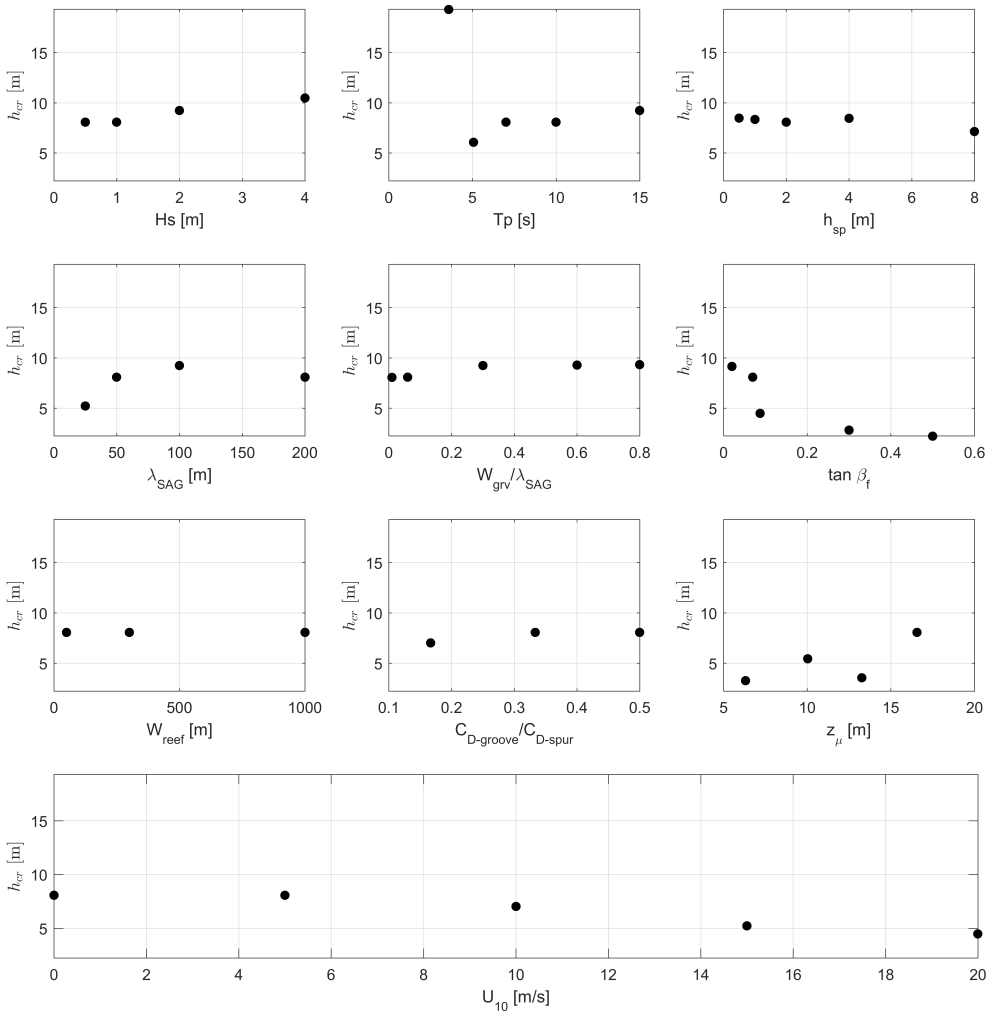

Figure E.1: Results of h_{cr} for the sensitivity simulations with varying short wave parameters, SAG geometry and alongshore forcing.

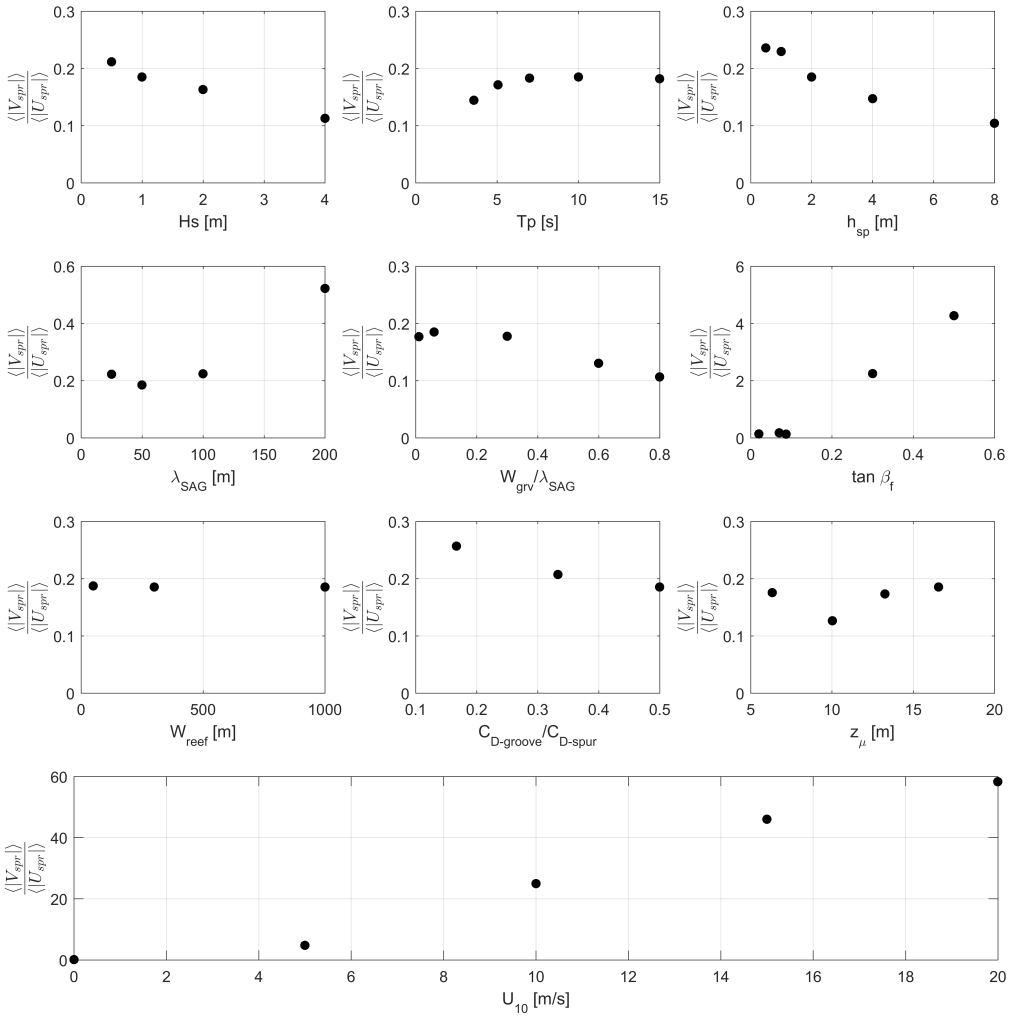

Figure E.2: Results of $\frac{V_{sp}}{U_{sp}}$ for the sensitivity simulations with varying short wave parameters, SAG geometry and alongshore forcing.

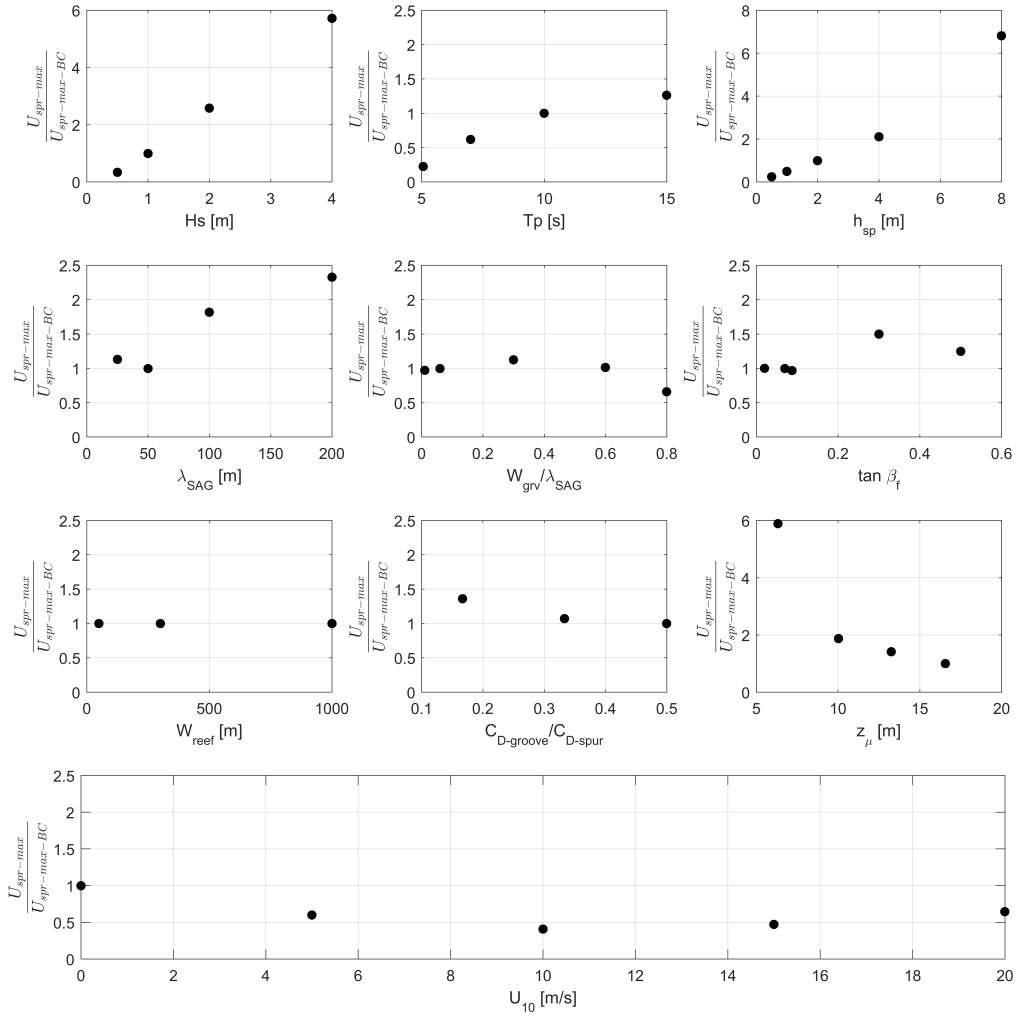

Figure E.3: Results of $\frac{U_{max}}{U_{max\text{-}BC}}$ for the sensitivity simulations with varying short wave parameters, SAG geometry and alongshore forcing.

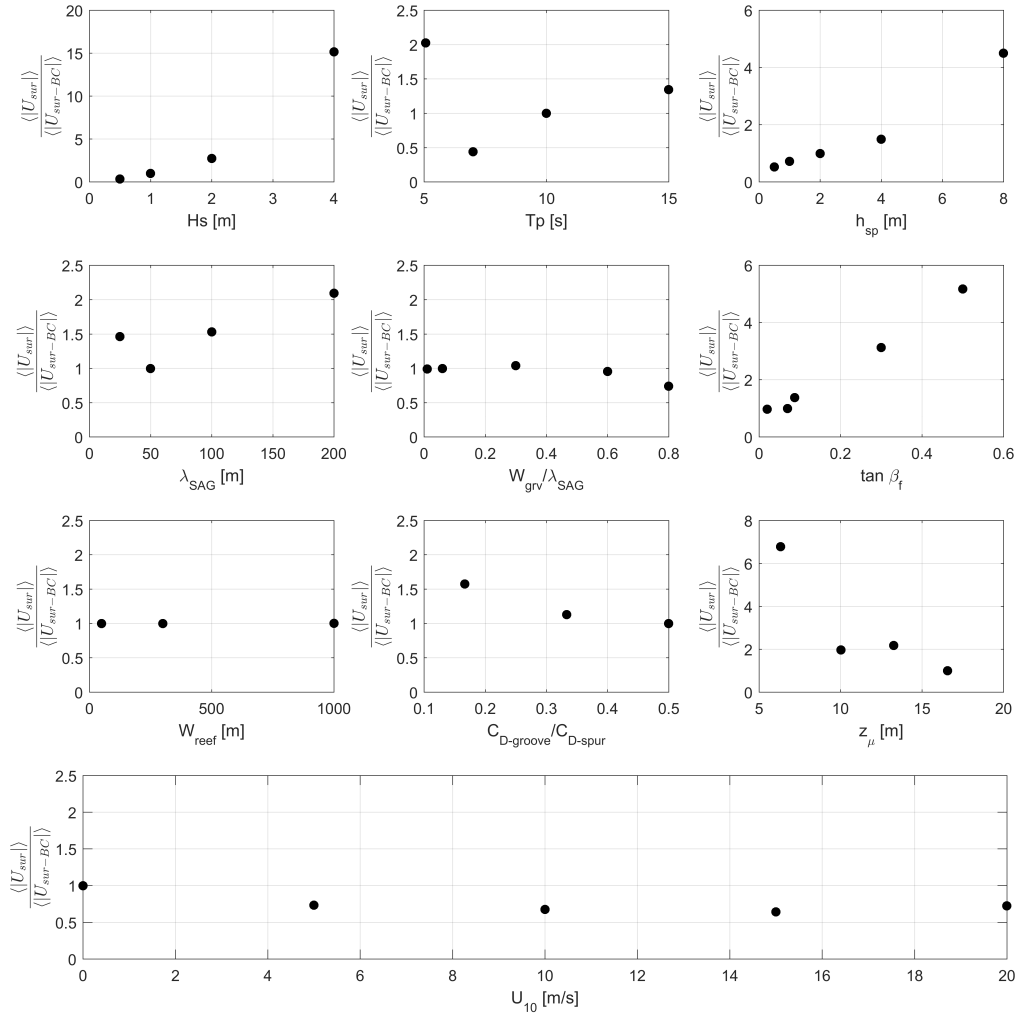

Figure E.4: Results of $\frac{U_{sur}}{U_{sur\text{-}BC}}$ for the sensitivity simulations with varying short wave parameters, SAG geometry and alongshore forcing.

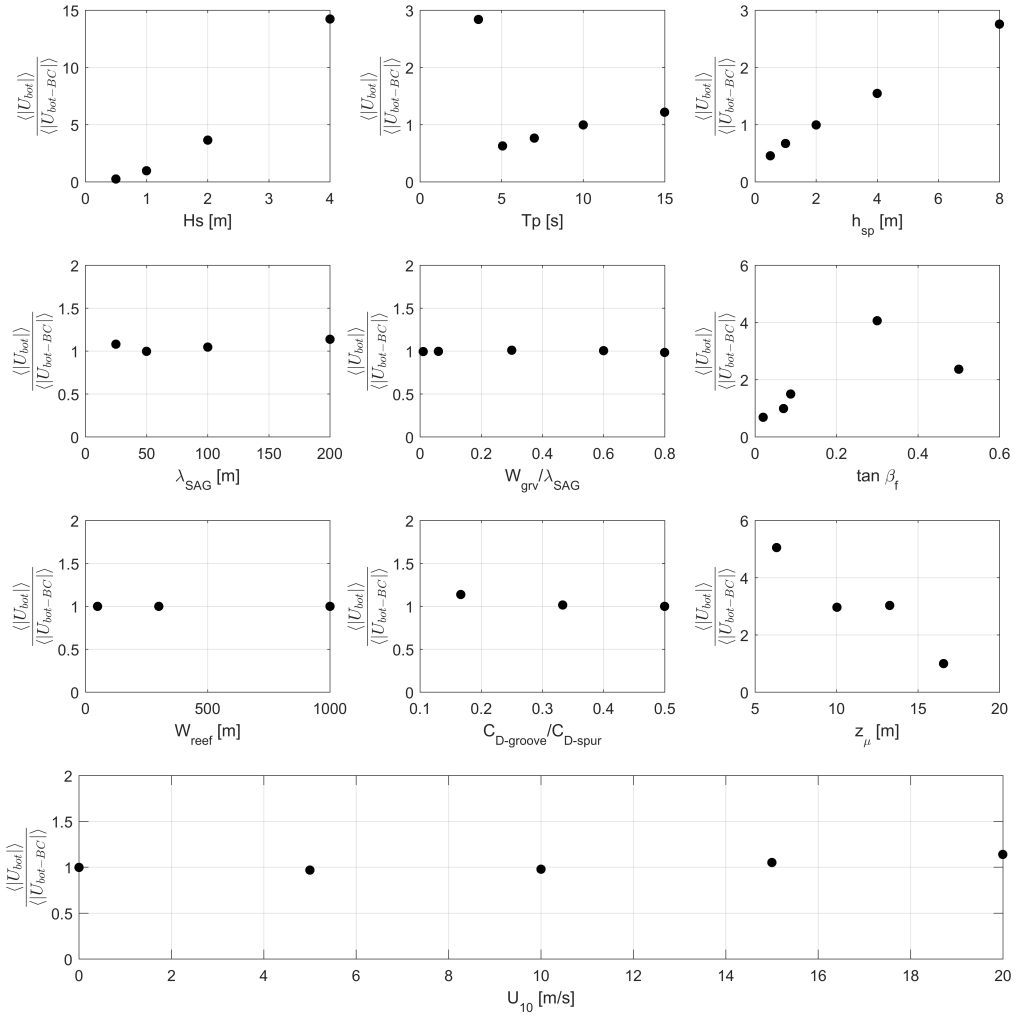

Figure E.5: Results of $\frac{U_{bot}}{U_{bot\text{-}BC}}$ for the sensitivity simulations with varying short wave parameters, SAG geometry and alongshore forcing.

F

ROLE OF VARYING WAVE ANGLES AND DIRECTIONAL SPREADINGS

This MSc thesis opted not to investigate the role of varying wave angles and directional spreadings due to the uncertainties related to the diffraction and refraction processes, as shown in Chapter 4.2.4.

In Palmyra Atoll, Rogers et al. (2015) showed that even for situations with oblique waves the wave heights over spur and groove look quite similar, possibly related to the low SAG wavelengths found there. Assuming that waves tend to have rougly similar heights over spur and groove with oblique waves, runs without refraction for oblique waves tend to provide reasonable wave forcing magnitudes. In terms of direction, those runs would tend to overestimate the alongshore forcing and subestimate the cross-shore wave forcing. In the SAG zone, the mean wave direction for runs with and without refraction have maximum differences of about 15 degrees. This maximum inaccuracy of about 15 degrees was accepted as reasonable for an initial evaluation of the wave angle and directional spreading importance. As it is also shown below, the velocity profile shape for oblique waves looks the same for different wave angles, suggesting that the innacuracy in the wave angle does not affect the flow pattern, adding consistency to this assumption.

The importance of the wave angle and directional spreading was evaluated similarly to the other parameters. Firstly, the cross-shore and alongshore velocity profiles were investigated (Chapter F.1). Next, the momentum balance terms were calculated (Chapter F.2) to understand the changes in the flow. The last step was to calculate the indicators for the flow, related both to flow pattern and to potential implications of the hydrodynamics on the coral growth aspects as explained in Chapter F.3.

Overall, oblique waves result in alongshore transport systems, i.e., cross-shore currents become significantly lower than in the alongshore. In those cases, the SAG offshore cell is lost, and the onshore cell gets wider and stronger, mainly associated with the growing of lateral advective term in the momentum balance. On the other hand, the directional spreading was shown to have very low influence on the flow pattern.

F.1. INFLUENCE OF VARYING PARAMETERS

This section presents the results of the sensitivity runs. The effects of variations of wave angles and directional spreadings are studied through comparisons of 3D cross-shore and alongshore Lagrangian velocity profiles on top of spurs and grooves.

In all the velocity profiles presented below, the dashed lines represent the locations of alongshore sections, while the coloured lines provide the velocities relatively to each of those dashed lines. Reddish colours correspond to higher values of each variable, while lower values are blueish.

F.1.1. WAVE DIRECTION

The cross-shore profiles of cross-shore Lagrangian velocities u_L on top of spur and grooves for varying Dp are shown in Figure F.1. As for the groove, all observed currents for oblique waves are offshore, and the presence of onshore velocities occurs only near the bottom. In general, those offshore currents grow and become more parabolic as approaching shallower waters. As for the spur, currents for oblique waves start offshore, decrease, switch to onshore still at higher depths, and then those onshore currents grow as approaching shallower waters.

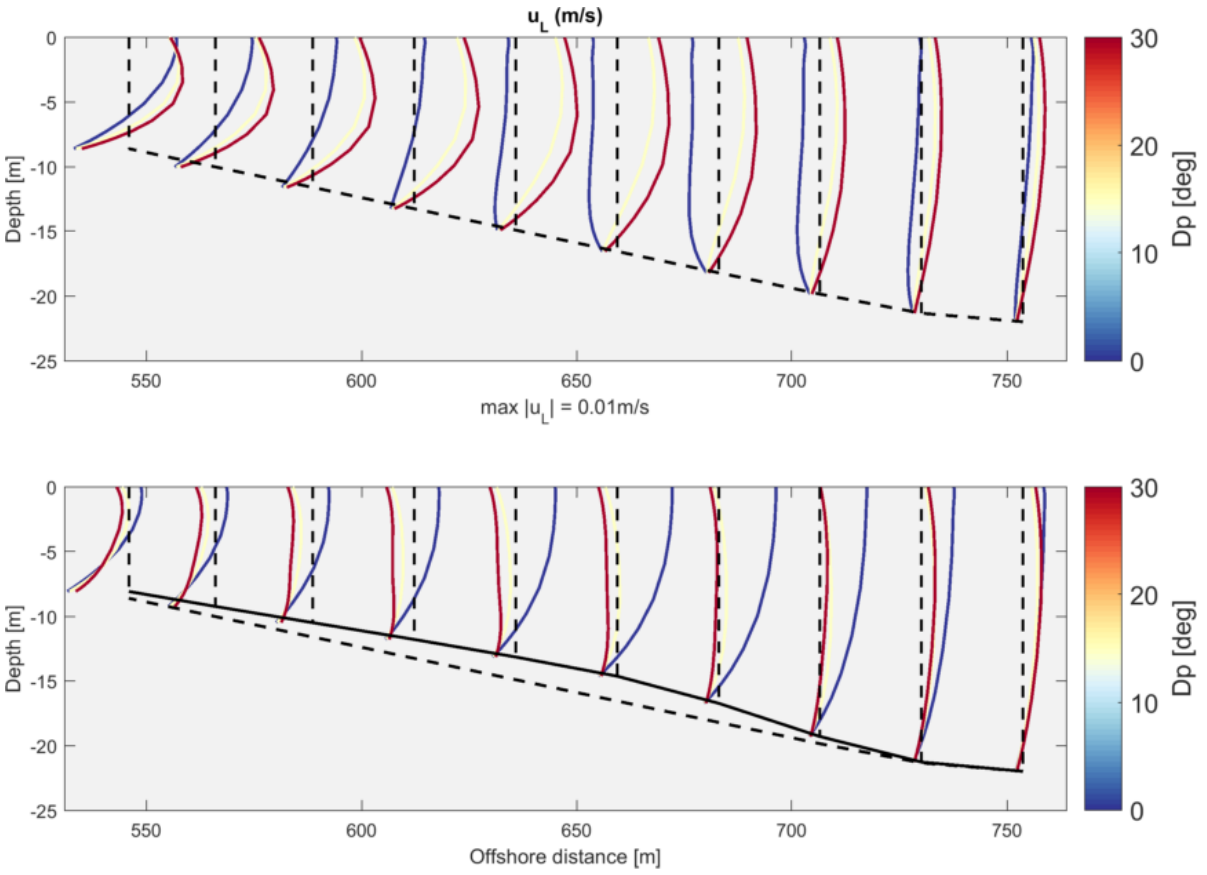

Figure F.1: Cross-shore views of results for cross-shore Lagrangian velocity u_L over spur and groove for varying wave direction Dp .

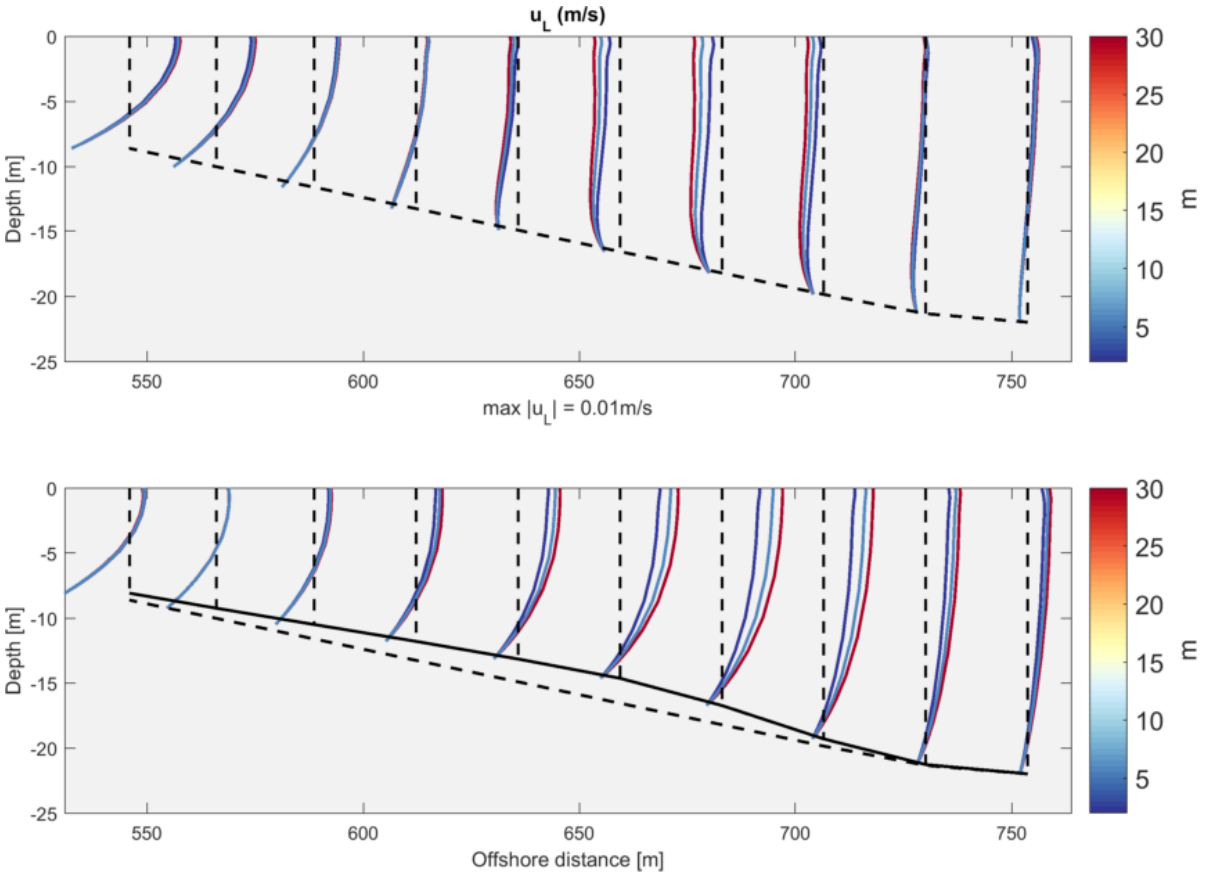

Figure F.2: Cross-shore views of results for cross-shore Lagrangian velocity u_L over spur and groove for varying directional spreading m .

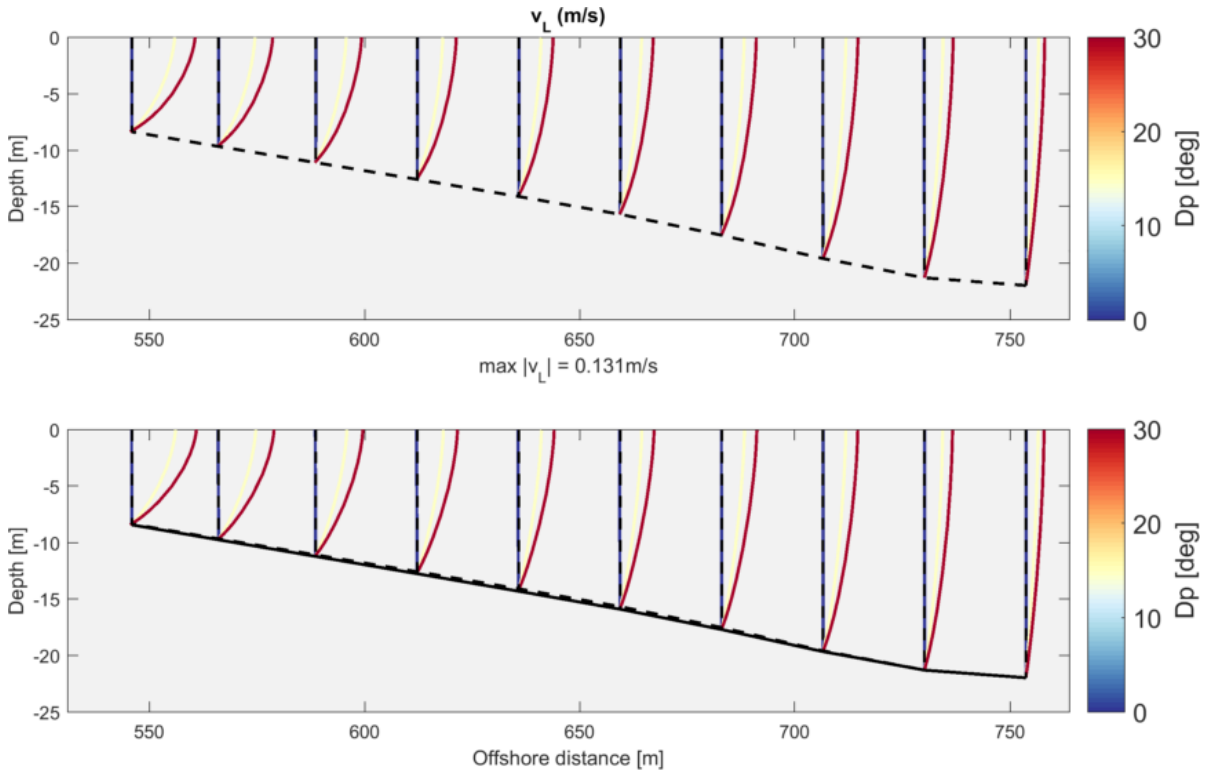

Figure F.3: Cross-shore views of results for alongshore Lagrangian velocity u_L on top of mid points between spurs and grooves for varying wave direction Dp .

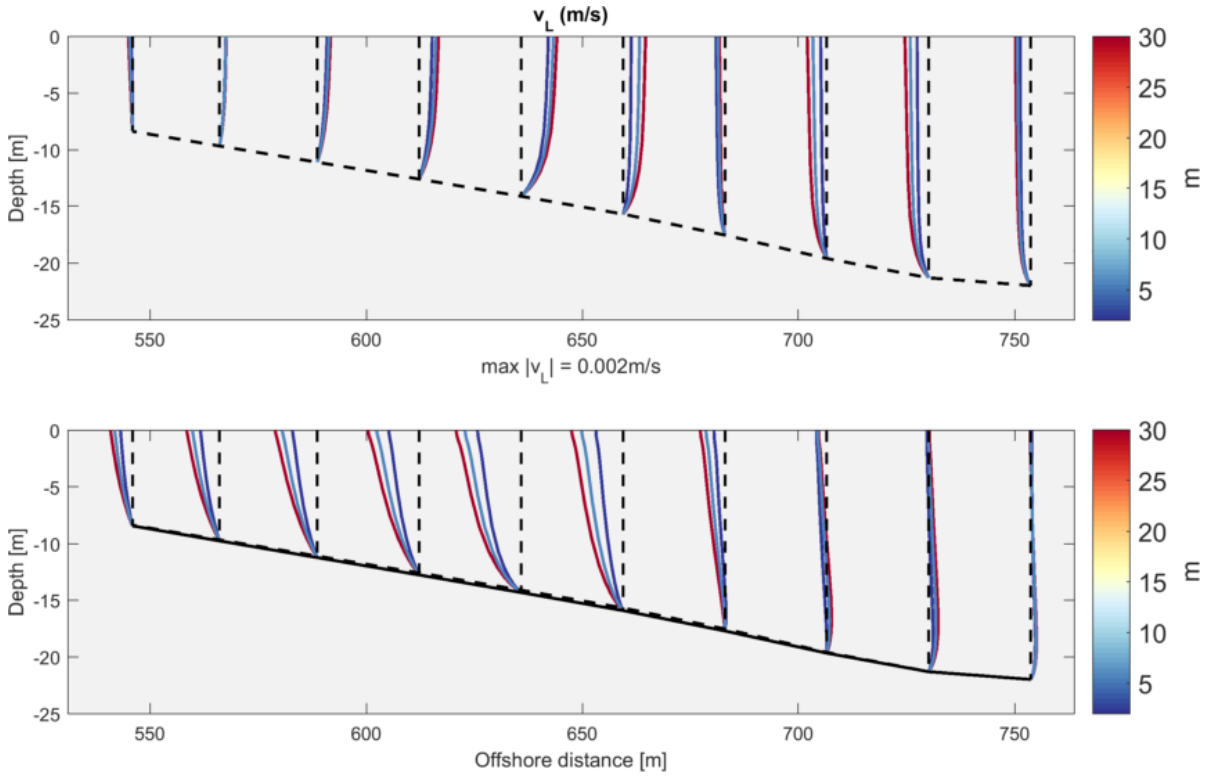

Figure F.4: Cross-shore views of results for alongshore Lagrangian velocity u_L on top of mid points between spurs and grooves for varying directional spreading m .

Overall, the SAG circulation is altered comparatively to shore-normal waves, with the disappearing of the offshore circulation cell, but with extending and strengthening of the second circulation cell. Differences

between runs with 30 and 15 degrees look minor, suggesting that the cross-shore flow pattern for oblique waves is persistent regardless of the wave angle.

The cross-shore profiles of alongshore Lagrangian velocities u_L on top of mid points between spur and grooves for varying Dp are shown in Figure F.3. In the alongshore, the difference of wave angles affect the alongshore strength of the flow: larger angles provide larger alongshore currents.

F.1.2. DIRECTIONAL SPREADING

The cross-shore profiles of cross-shore and alongshore Lagrangian velocities u_L on top of spur and grooves for varying m are shown in Figures F.2 and F.4. Overall, there is a very low weakening of the SAG circulation, consistent with lower cross-shore forcing due to wider wave directional bands. Results suggest that the directional sppreading is a minor parameter for SAG hydrodynamics.

F.2. MECHANISMS AND EFFECTS

In order to understand the mechanisms for the changes in SAG flow induced by varying wave angles and directional spreading, the analysis of the momentum terms for each of the sensitivity runs were carried out.

The spatial mean along the cross-shore SAG zone of the depth-averaged momentum terms over the spur was considered for the cross-shore direction. As for the alongshore direction, a mid point between spur and groove was taken for the momentum terms, due to the relatively higher currents found there. Only cross-shore zone region where the spur height is greater than 0.4 m was assumed, so as to capture the circulation mechanisms occurring in the core of the SAG zone. The depth-averaged momentum terms were preferred for that analysis, instead of the RMS values, after sensitivity analysis showed that the overall representation is more consistent for the former ones. Besides all the momentum terms, the spatial mean of the depth-averaged imbalance between wave forces and pressure gradient was also calculated, given that it is insightful in the understanding of how momentum is balanced, as discussed in Chapter 5.1.5.

The specifics of how momentum is balanced for each varying parameter is addressed below through comparison with the Base Case momentum balance (Chapter 5.1.5) and resulting flow pattern (Chapter 5.1.2). For the Base Case, wave forcing is mainly balanced by pressure gradient, and the mismatch between those is mainly balanced by horizontal turbulent stresses and bottom friction. The Base Case velocity profile shape was shown to be correlated with the vertical distribution of the imbalance and of the viscous forces.

The results of the spatial mean along the SAG zone of the depth-averaged cross-shore momentum terms for all varying input parameters, now including Dp and m, are shown in Figure F.5, while for the alongshore momentum terms they are provided in Figure F.6. The parameters already evaluated in Chapter 5.3 are repeated here for the evaluation of the overall relative importance of the wave angle and directional spreading.

F.2.1. WAVE DIRECTION

The wave directions are linked to the wave forcing direction. Oblique waves result in lower F_x and higher F_y , although the order magnitude keeps the same regardless of the wave angle. Therefore, the wave forcing, pressure gradients and imbalance between those have similar order of magnitude than the shore-normal case, regardless of the oblique wave direction.

Oblique waves have a different manner to balance the flow, with a significant growing of lateral advection, that becomes the main balancing term together with horizontal viscous forces. Likewise, the streamwise advection gets lower. This behaviour results in a complete undermining of the SAG offshore circulation cell, but also in a significant enhancement and widening of the SAG onshore circulation cell (offshore currents over groove and onshore over spur).

In the alongshore, besides the trends reported above, friction also gets mucher stronger, that become much higher than in the cross-shore, associated with the dominant alongshore currents in case of oblique waves.

F.2.2. DIRECTIONAL SPREADING

Overall, the directional spreading was shown to play a minor role in the velocity profile. Likewise, the changes in the momentum terms are low, with a slight increase of the terms for higher m, consistent with slightly lower cross-shore forcing due to wider wave directional bands.

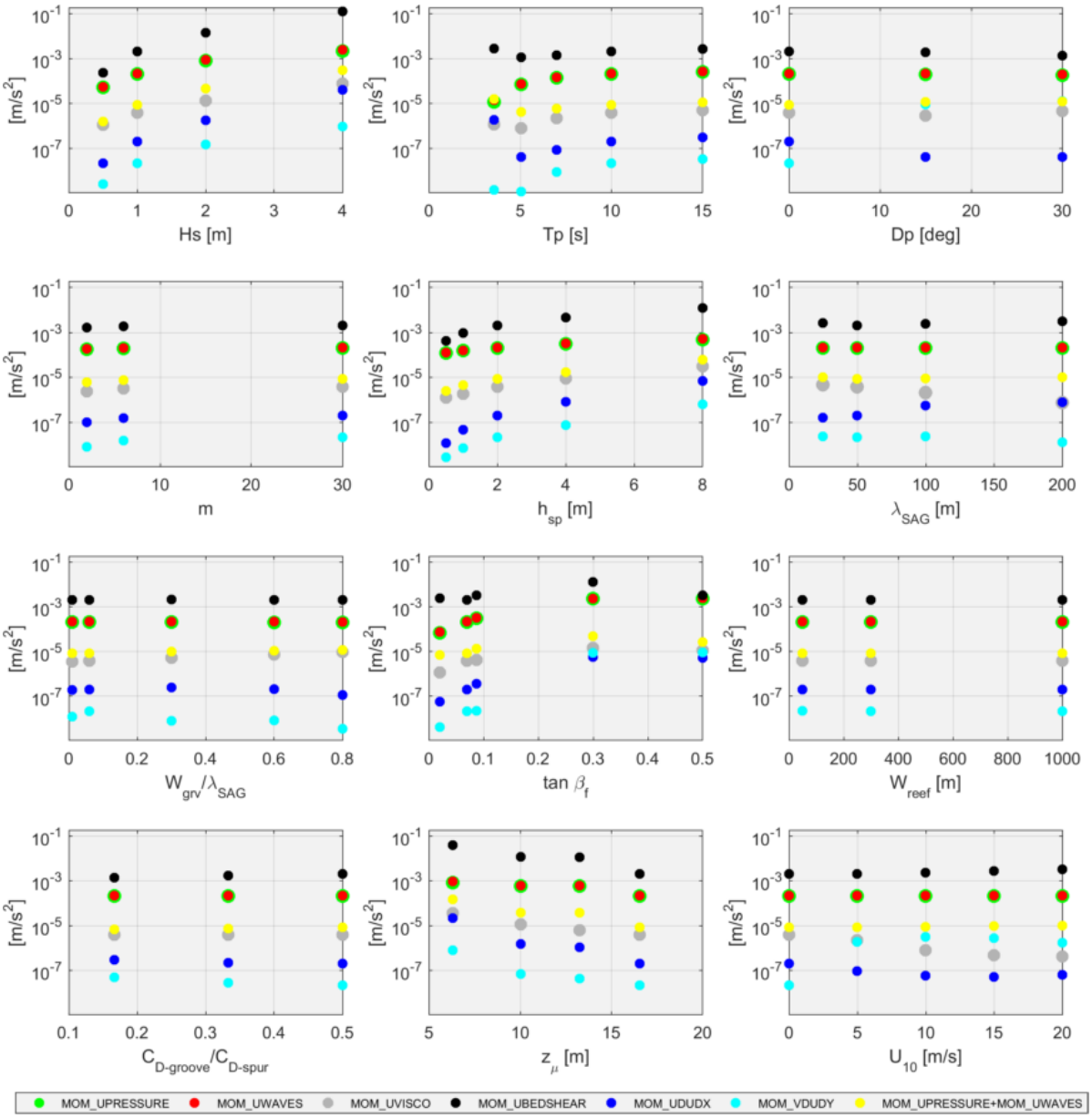

Figure F.5: Results of the spatial mean along the SAG cross-shore section of the cross-shore momentum terms *MOM_UDUDX*, *MOM_VDUDY*, *MOM_UPRESSURE*, *MOM_UWAVES*, *MOM_UVISCO*, *MOM_UBEDSHEAR*, *MOM_UPRESSURE* + *MOM_UWAVES* on top of the spur.

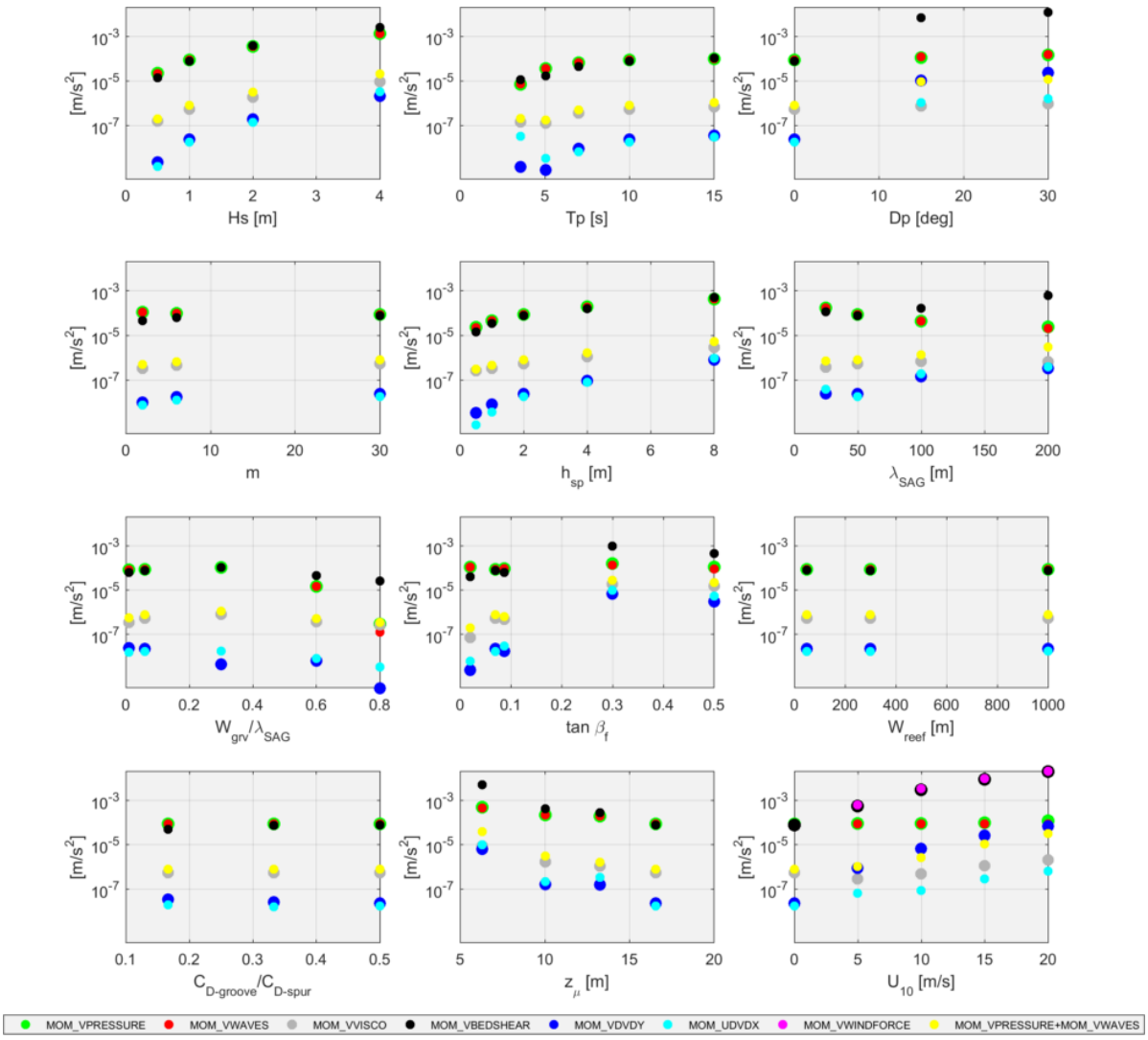

Figure F.6: Results of the spatial mean along the SAG cross-shore section of the alongshore momentum terms *MOM_VDVDY*, *MOM_UDVDX*, *MOM_VPRESSURE*, *MOM_VWAVES*, *MOM_VVISCO*, *MOM_VBEDSHEAR*, *MOM_VWINDFORCE* and *MOM_VPRESSURE* + *MOM_VWAVES* on mid point between spur and groove.

F.3. RESULTS OF INDICATORS

The figures relating each indicator to each of the short wave, SAG geometry parameters and alongshore forcing, but now including the changing wave angle and directional spreading are presented below (Figures F.7, F.8, F.9, F.10, F.11 and F.12). The parameters that were already addressed in Chapter 5.4 are repeated in those figures to evaluate the overall relative importance of wave direction and directional spreading.

The results show that:

- h_{cr} is influenced by the wave angle, i.e., more oblique waves tend to move the reversing point of Lagrangian currents to the offshore zone;
- The importance of alongshore flow was shown to be mostly influenced by Dp. In case of oblique waves, the alongshore flow became extremely more important than the cross-shore flow - for Dp = 15 degrees, the alongshore flow is more than 20 times higher the cross-shore velocities;
- The parameters relating the flow strength ($\frac{U_{spr-max}}{U_{spr-max-BC}}$, $\frac{\langle|U_{sur}|\rangle}{\langle|U_{sur-BC}|\rangle}$ and $\frac{\langle|U_{sur}|\rangle}{\langle|U_{sur-BC}|\rangle}$) are not sensitive neither to Dp nor to m; and
- The bottom shear stress at the peak spur height depth is not influenced neither by Dp nor by m.

Overall, the alongshore flow grows significantly with growing alongshore forcing. Oblique waves are important in the SAG dynamics by making the transport system dominated by alongshore motion. However, SAG formations are more commonly found on environments with dominance of shore-normal waves, as previously discussed in Chapter 2.

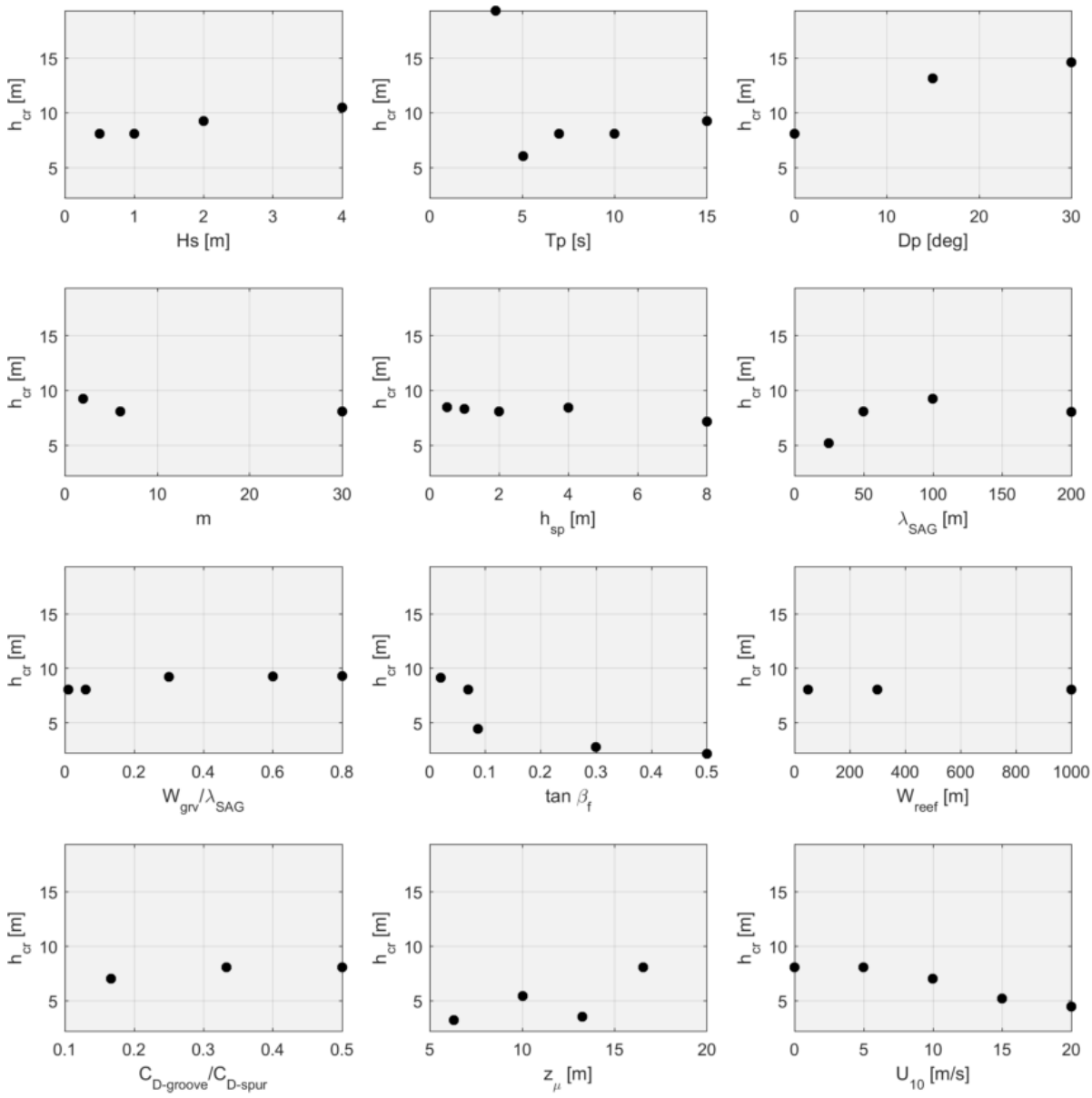

Figure F.7: Results of h_{cr} for the sensitivity simulations with varying wave angle and directional spreading.

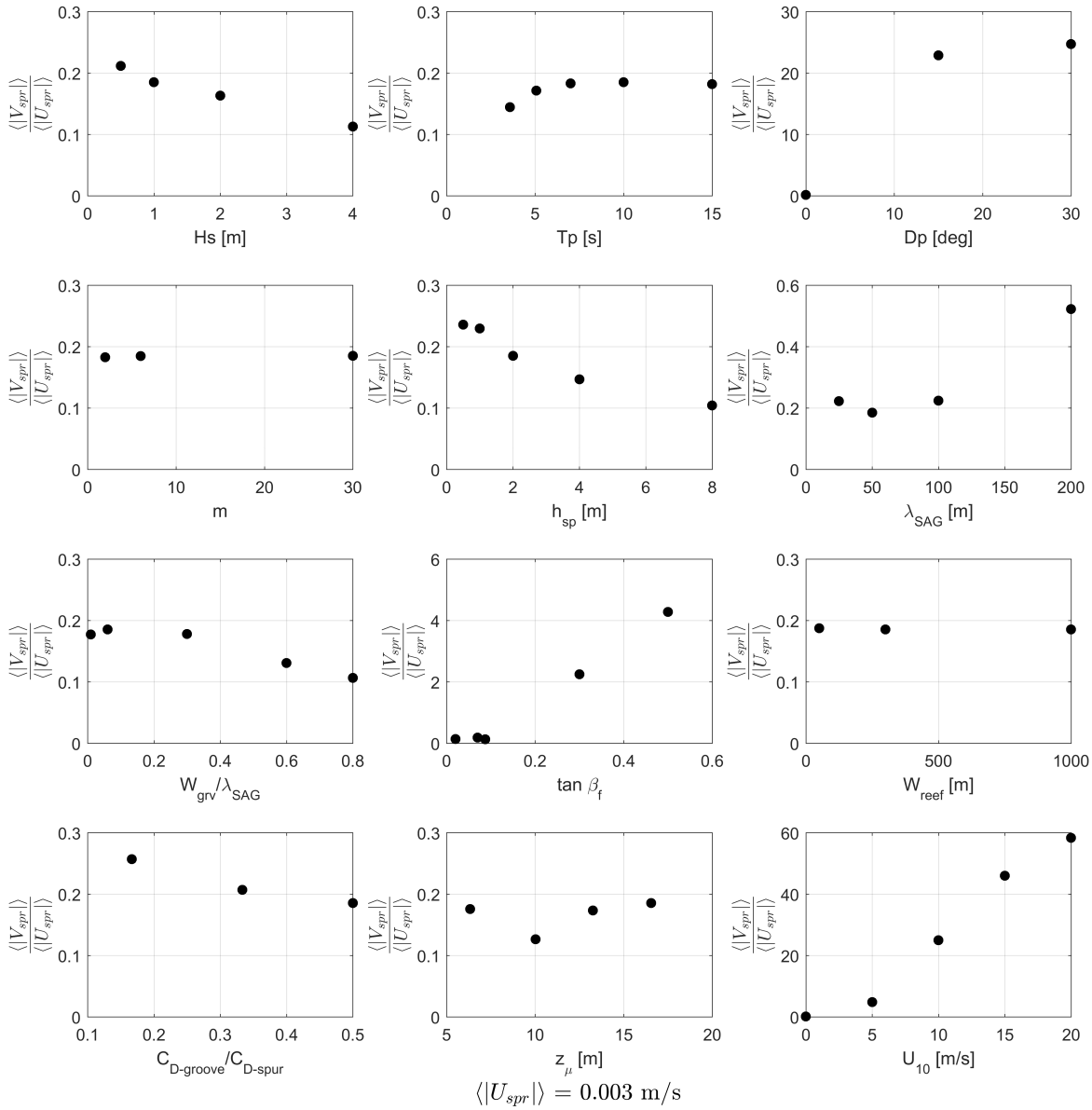

Figure F.8: Results of $\frac{V_{sp}}{U_{sp}}$ for the sensitivity simulations with varying wave angle and directional spreading.

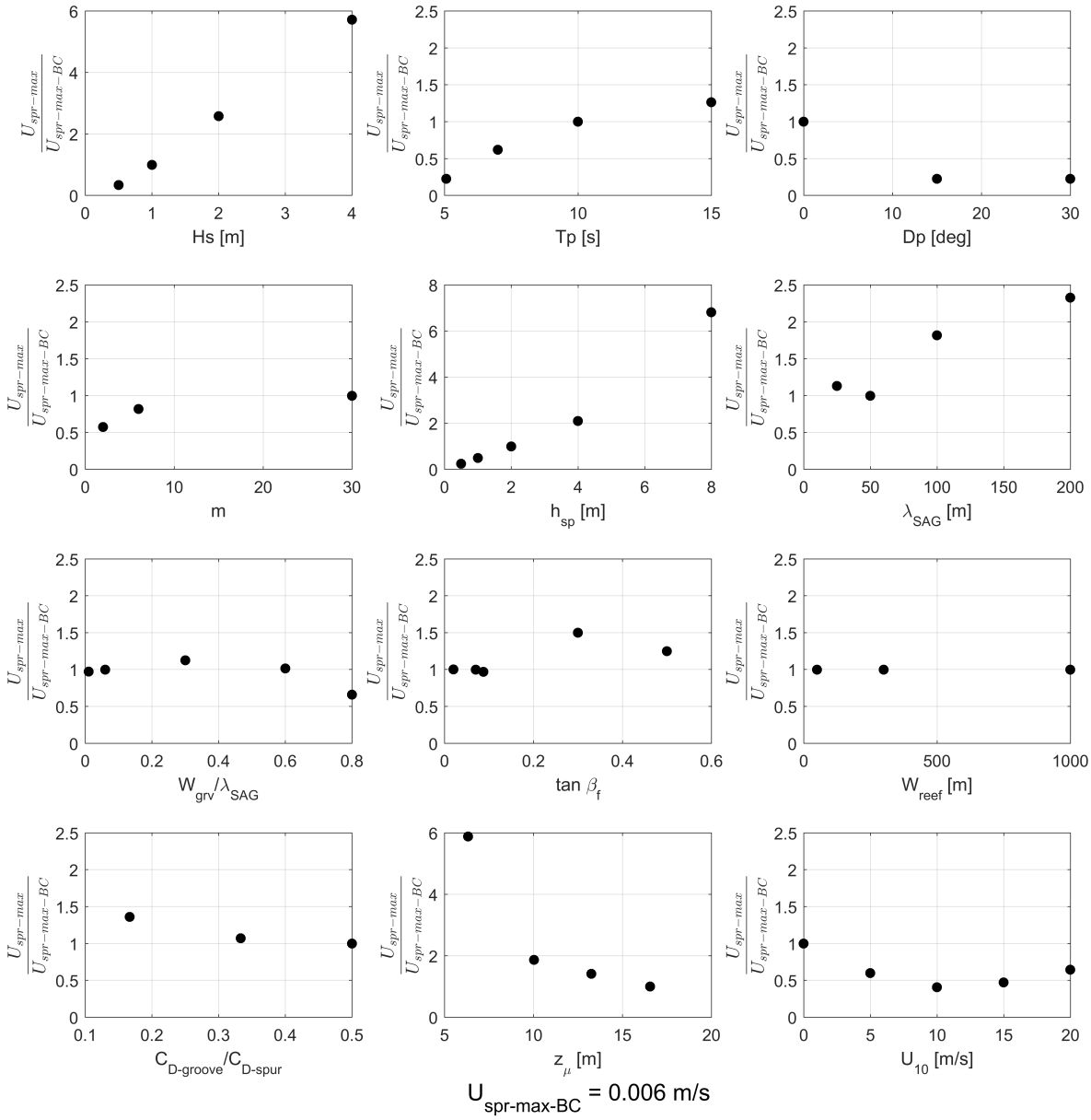

Figure F.9: Results of $\frac{U_{max}}{U_{max\text{-}BC}}$ for the sensitivity simulations with varying wave angle and directional spreading.

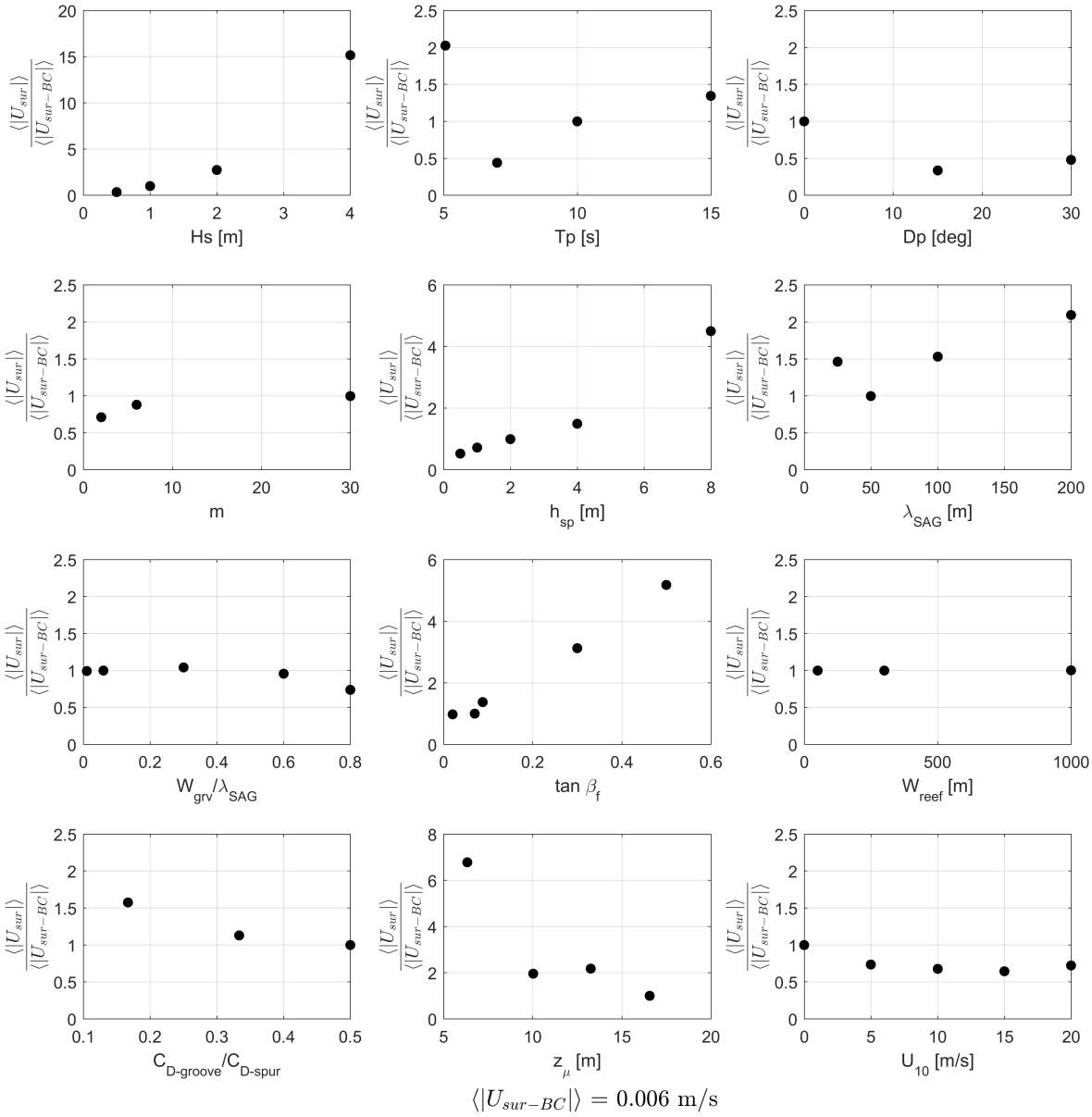

Figure F.10: Results of $\frac{U_{sur}}{U_{sur\text{-}BC}}$ for the sensitivity simulations with varying wave angle and directional spreading.

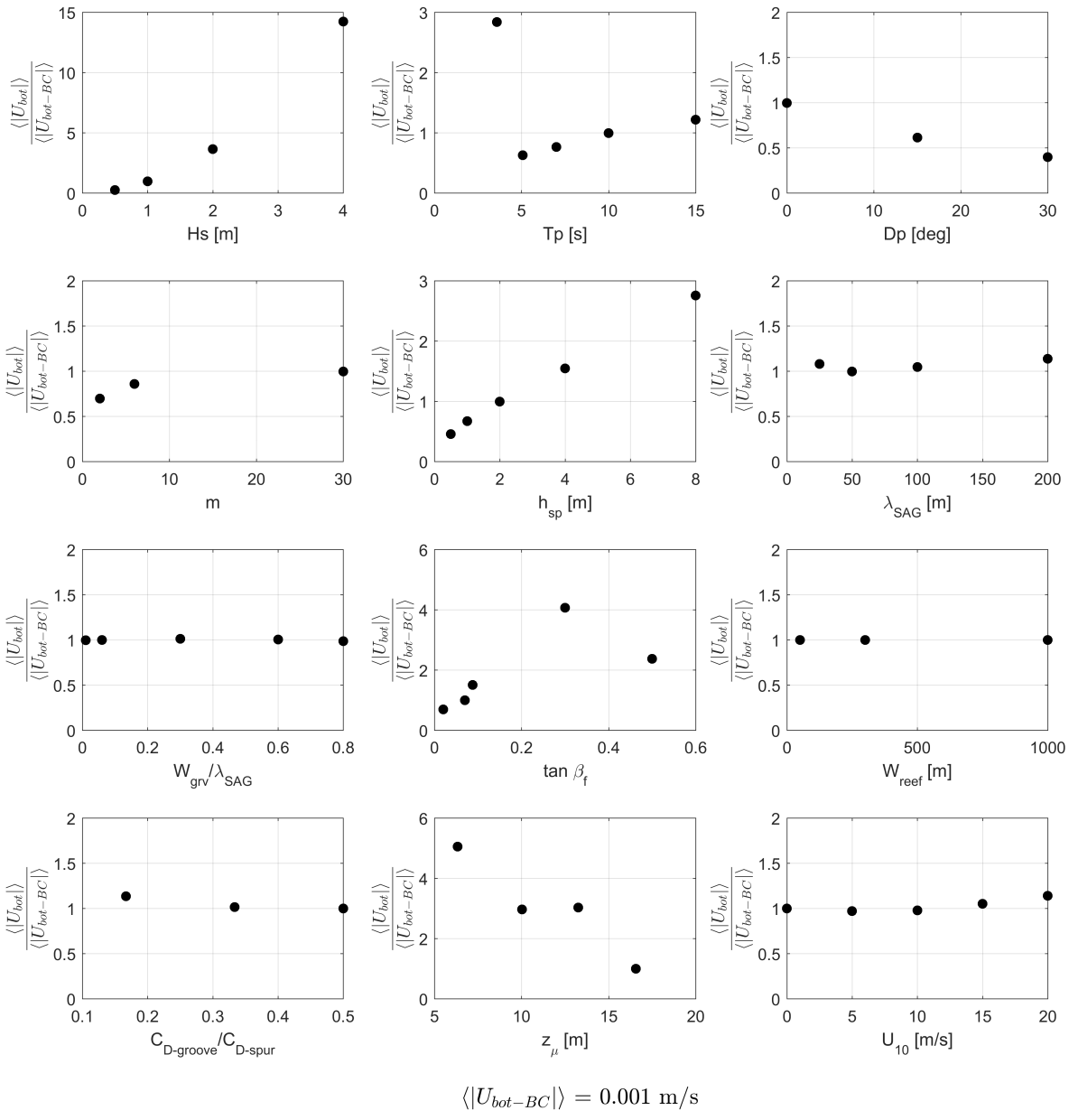

Figure F.11: Results of $\frac{U_{bot}}{U_{bot\text{-}BC}}$ for the sensitivity simulations with varying wave angle and directional spreading.

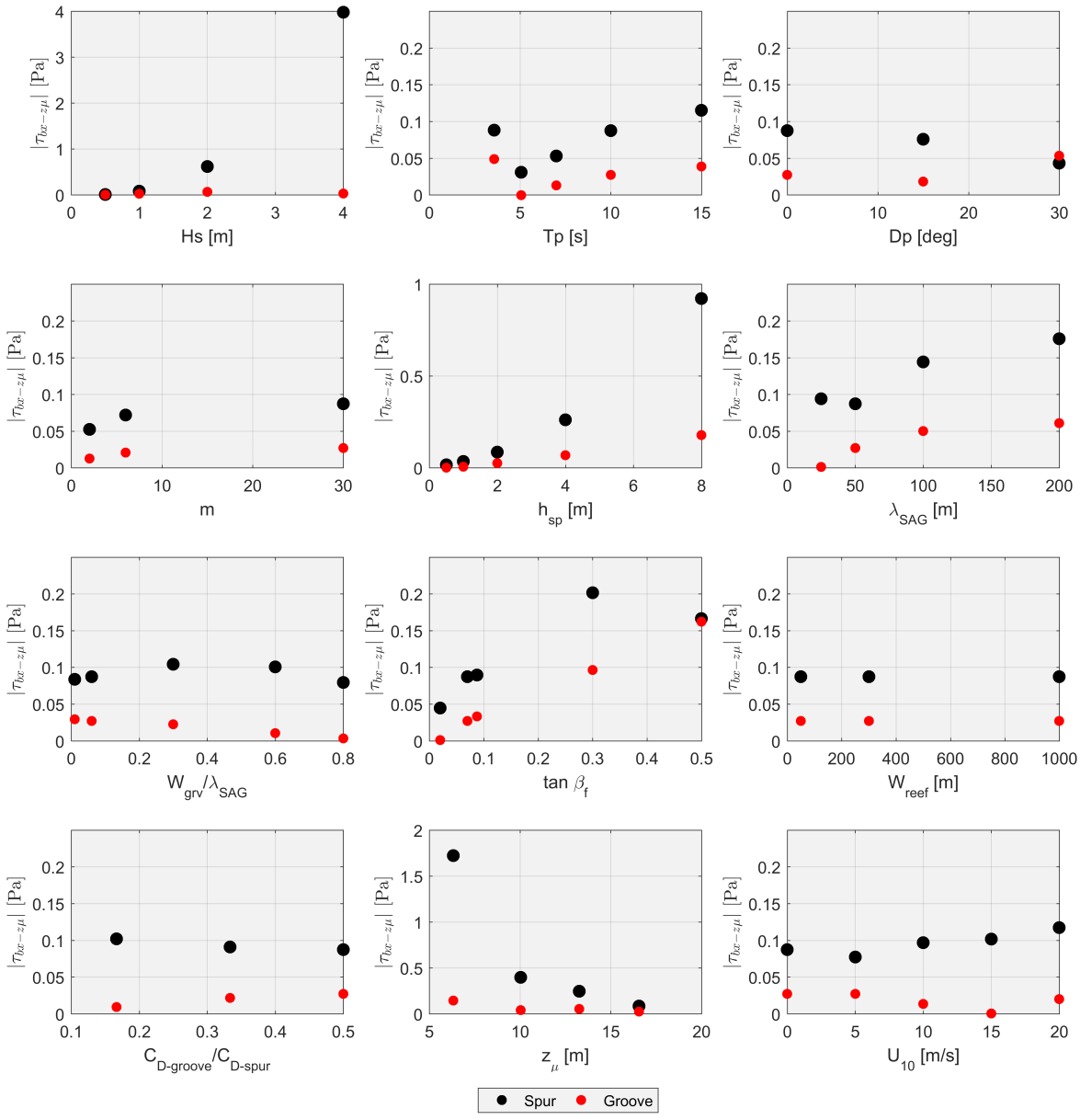

Figure F.12: Results of $\tau_{\text{bx-}z\mu}$ for the sensitivity simulations with varying wave angle and directional spreading.

G

SENSITIVITY FOR HORIZONTAL AND VERTICAL VISCOSITIES

This MSc thesis assumed fixed values of horizontal and vertical viscosities - $\nu_H = 0.1$ m^2/s and $\nu_V = 1 \times 10^{-6}$ m^2/s - for all simulations. This appendix presents the results for sensitivity runs with varying horizontal and vertical viscosities.

The sensitivity simulations assumed spatially constant values, with viscosity ranges of $\nu_H = 0.01 - 1$ m^2/s and $\nu_V = 1 - 100 \times 10^{-6}$ m^2/s.

G.1. INFLUENCE IN THE VELOCITY PROFILE

The influence of the varying viscosities was firstly studied through plots of the velocity profile, both in the cross-shore and in the alongshore direction.

The cross-shore profiles of cross-shore and alongshore Lagrangian velocities u_L on top of spur and grooves for varying horizontal viscosity are shown in Figures G.1 and G.2, respectively. Higher values of ν_H result in moderately stronger SAG circulation, especially in the offshore zone. On the other hand, the lowering of the horizontal viscosities lead to the undermining of the offshore circulation, i.e., groove currents become offshore.

The cross-shore profiles of cross-shore and alongshore Lagrangian velocities $\hat{u_L}$ on top of spur and grooves for varying vertical viscosity are shown in Figures G.3 and G.4, respectively. No significant changes were observed, thus the vertical viscosity is inferred to be a minor parameter in the SAG flow for the tested range of parameters.

G.2. MECHANISMS AND EFFECTS

In order to understand the mechanisms for the changes in the velocity profile, the analysis of the momentum terms for each of the sensitivity runswith varying viscosities were carried out.

In the current analysis, the spatial mean along the cross-shore SAG zone of the depth-averaged momentum terms over the spur was considered for the cross-shore direction. As for the alongshore direction, a mid point between spur and groove was taken for the momentum terms, due to the relatively higher currents found there. Only cross-shore zone region where the spur height is greater than 0.4 m was assumed, so as to capture the circulation mechanisms occurring in the core of the SAG zone. The depth-averaged momentum terms were preferred for that analysis, instead of the RMS values, after sensitivity analysis showed that the overall representation is more consistent for the former ones. Besides all the momentum terms, the spatial mean of the depth-averaged imbalance between wave forces and pressure gradient was also calculated, given that it is insightful in the understanding of how momentum is balanced, as discussed in Chapter 5.1.5.

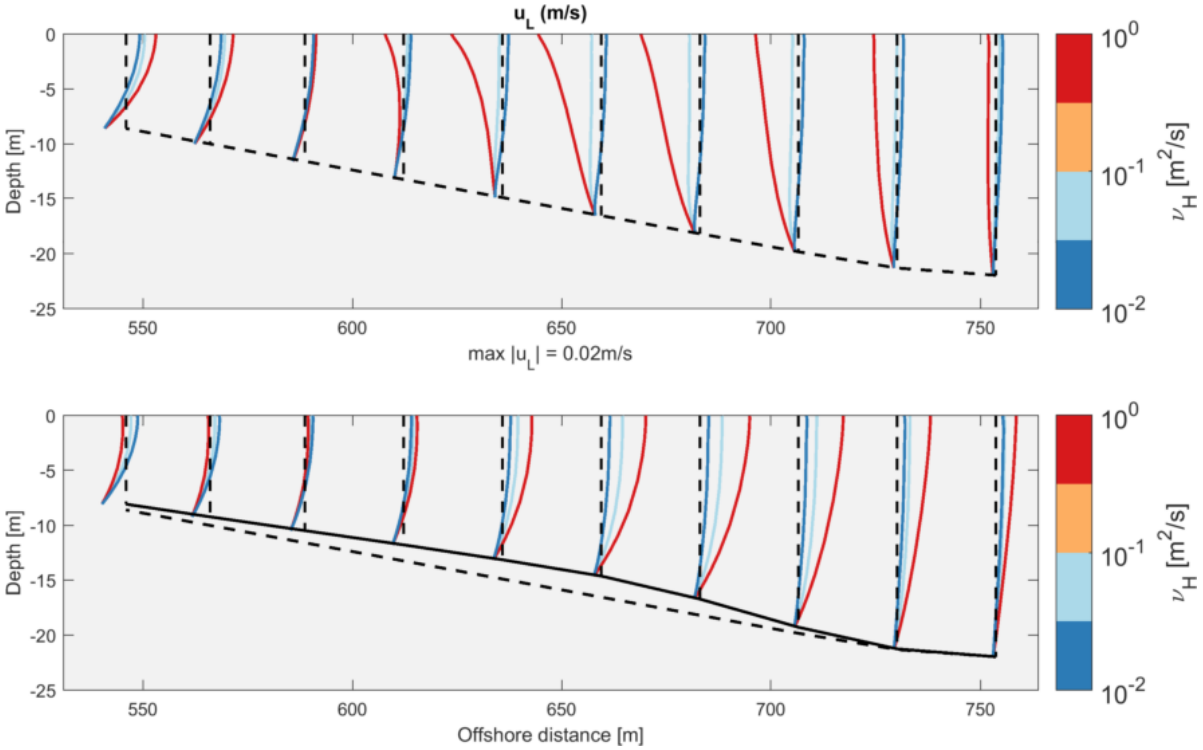

Figure G.1: Cross-shore views of results for alongshore Lagrangian velocity u_L on top of spur and groove for varying horizontal viscosity ν_H.

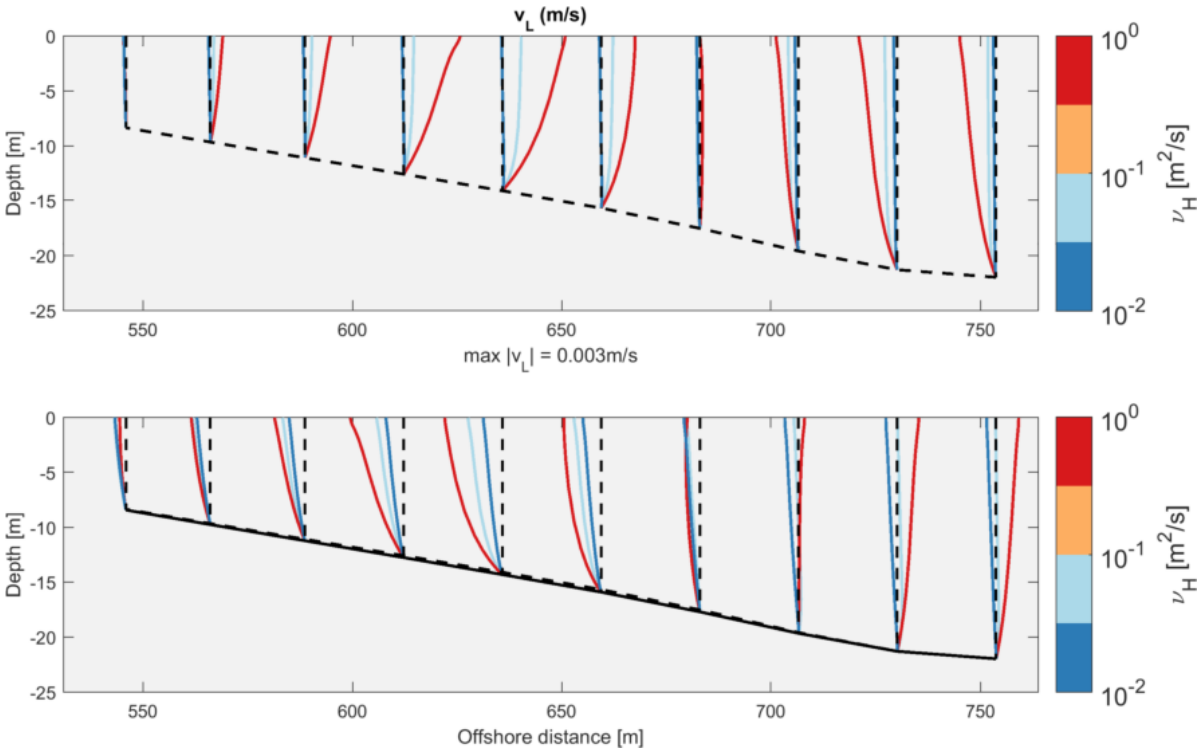

Figure G.2: Cross-shore views of results for alongshore Lagrangian velocity u_L on top of mid points between spurs and grooves for varying horizontal viscosity ν_H.

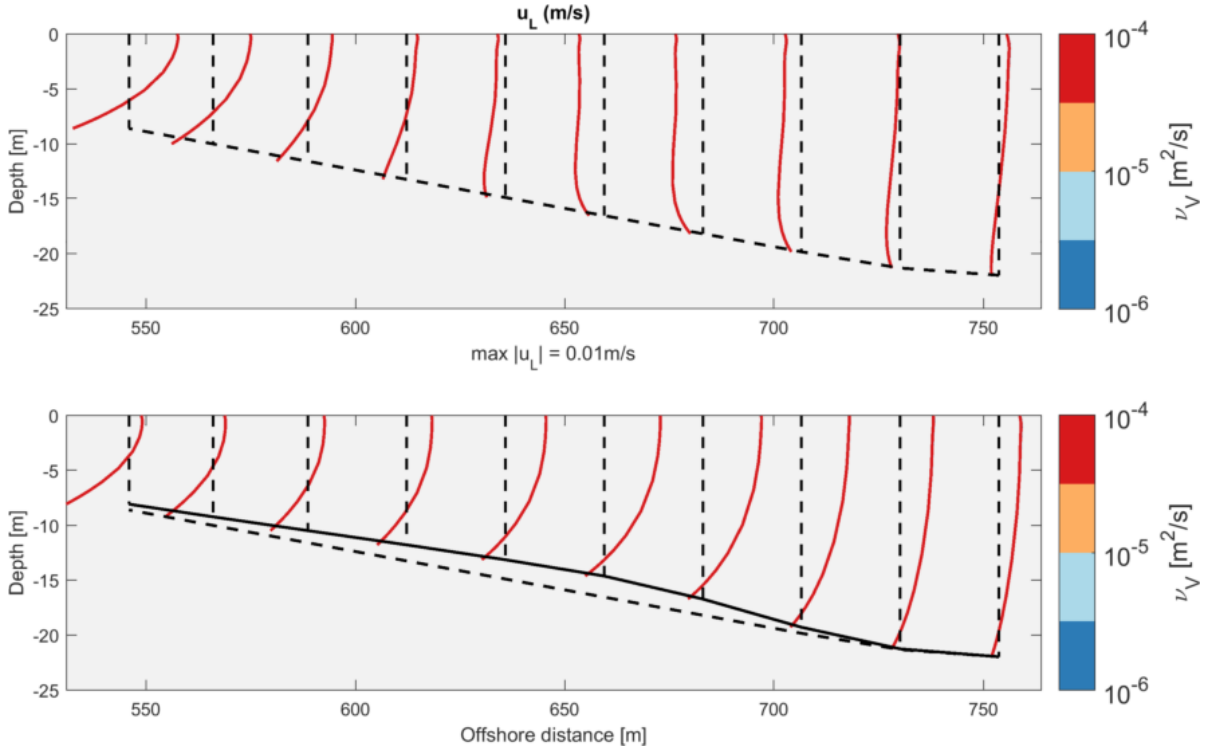

Figure G.3: Cross-shore views of results for alongshore Lagrangian velocity u_L on top of spur and groove for varying vertical viscosity ν_V.

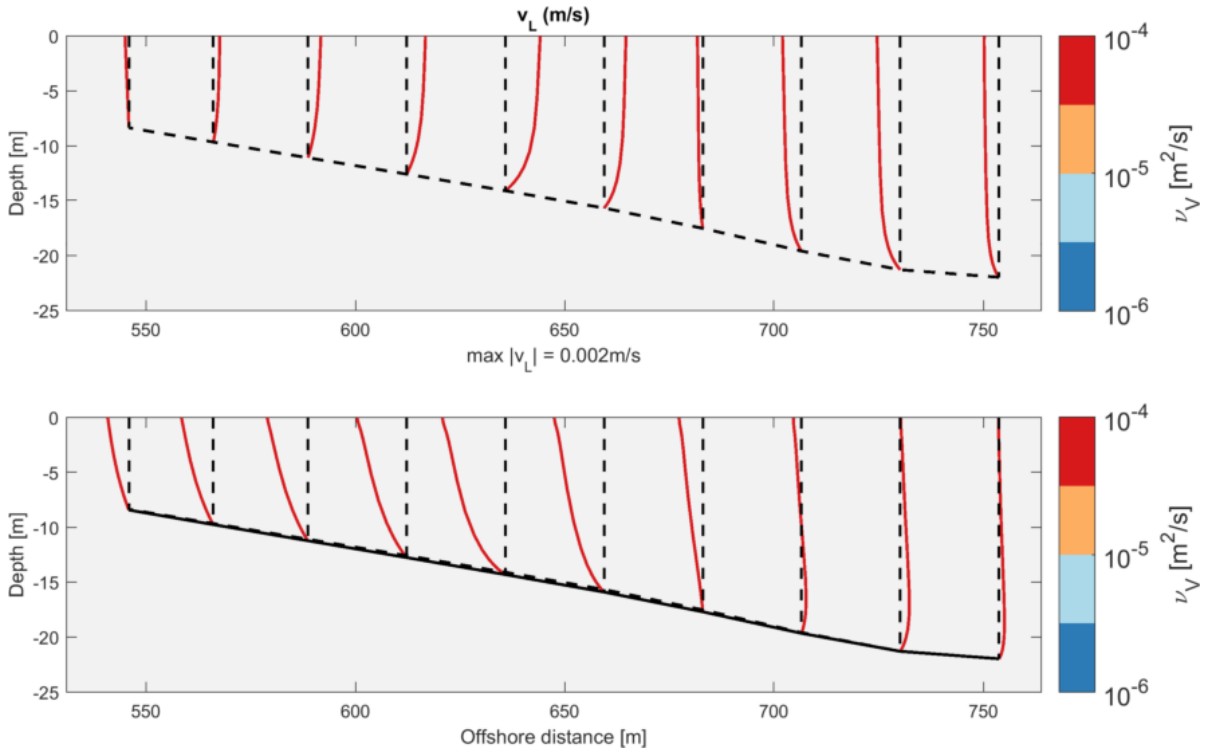

Figure G.4: Cross-shore views of results for alongshore Lagrangian velocity u_L on top of mid points between spurs and grooves for varying vertical viscosity ν_V.

The results of the spatial mean along the SAG zone of the depth-averaged cross-shore momentum terms for varying viscosities are shown in Figure G.5, while for the alongshore momentum terms they are provided in Figure G.6.

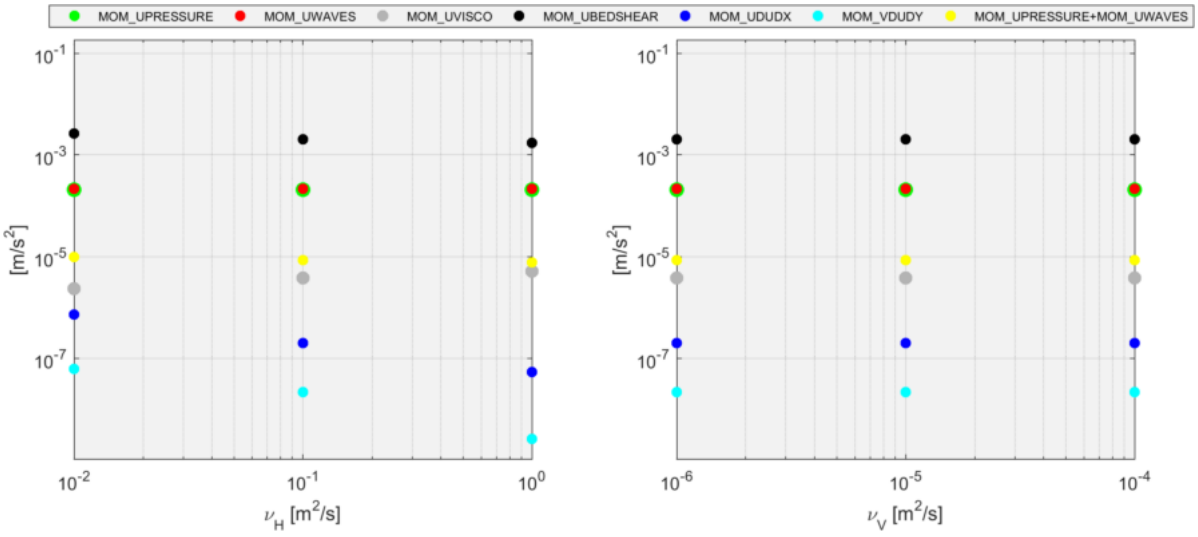

Figure G.5: Results of the spatial mean along the SAG cross-shore section of the cross-shore momentum terms on top of the spur for varying viscosities. MOM_UWAVES, MOM_UPRESSURE, MOM_UBEDSHEAR, MOM_UVISCO, MOM_UDUDX and MOM_VDUDY represent the wave forces, pressure gradient, bottom shear stress, horizontal viscous forces, streamwise and lateral advective accelerations, respectively.

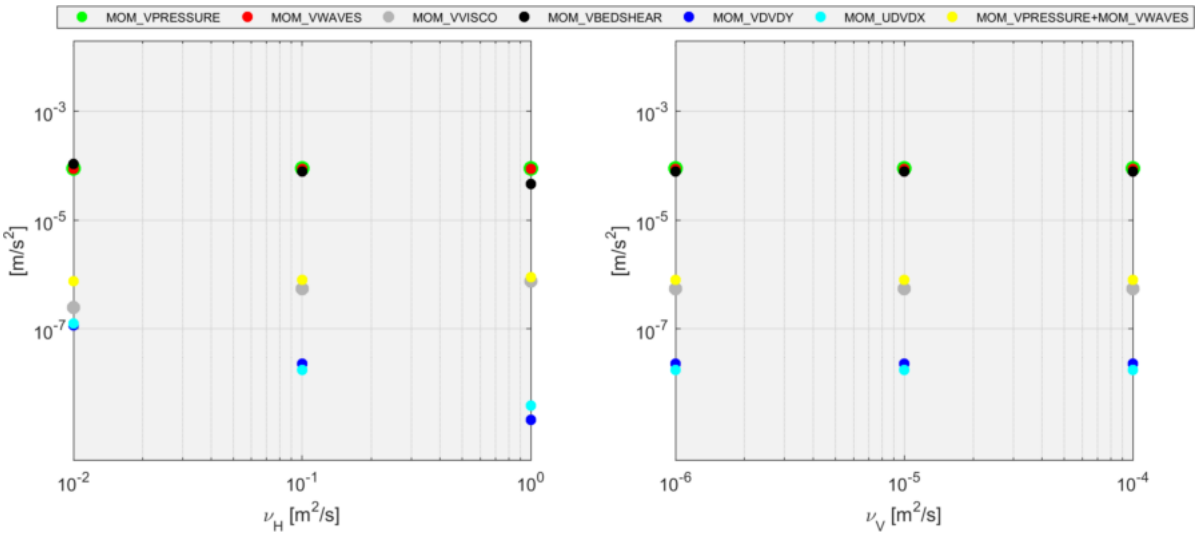

Figure G.6: Results of the spatial mean along the SAG cross-shore section of the alongshore momentum terms on mid point between spur and groove for varying viscosities. MOM_VWAVES, MOM_VPRESSURE, MOM_VBEDSHEAR, MOM_VVISCO, MOM_VDVDY, MOM_UDVDX, and MOM_VWINDFORCE represent the wave forces, pressure gradient, bottom shear stress, horizontal viscous forces, streamwise and lateral advective accelerations, and wind forces, respectively.

Increasing horizontal viscosities lead to increasing horizontal turbulent stresses, and decreasing advective terms. The results suggest that a minimum value of horizontal viscosity is needed to drive the offshore circulation cell. The vertical viscosity was shown not to be associated with changes neither in the flow nor in the momentum terms.

G.3. OVERALL EVALUATION

Overall, results indicate that flow is sensitive to the horizontal viscosity value, and not to the vertical one. Changes in flow pattern are observed in case of low values ($\nu_H = 0.01$ m^2/s), and the strength of the flow is not significantly affected. Accordingly, the horizontal and vertical viscosities used in the research ($\nu_H = 0.1$ m^2/s and $\nu_V = 1 \times 10^{-6}$ m^2/s) were considered to be reasonable.

H

SENSITIVITY FOR WAVE FORCES

The formulation for the wave forces considered throughout this research assumed them as the added effects of radiation stress gradients, dissipation and Stokes Drift divergence, as explained in Chapter 3.1.4. As SAG formations are mainly located in the shoaling zone, where no wave breaking takes place, the vertical imbalance of the wave force previously reported (Chapter 5.1.5) is thought to be due to the Stokes Drift divergence.

The objective of this appendix is to better understand which effects its inclusion causes in the momentum balance. This evaluation was conducted with a research version of D3D-FLOW that does not include the Stokes Drift divergence as part of the wave force output. Namely, the Stokes Drift divergence is still included in the momentum conservation equation - and as such yielding similar final velocity profile -, but not as part of the wave force output.

Firstly, the analysis of the momentum balance terms including and excluding Stokes Drift divergence is shown in Chapter H.1. An overall evaluation of its influence is provided in Chapter H.2.

H.1. MOMENTUM BALANCE

The cross-shore view of the cross-shore momentum terms over spur and groove is shown in Figure H.1. The comparison between the imbalance between pressure gradient and wave forces (red) including (full) and excluding (dashed) Stokes Drift divergence shows significant differences in the vertical profile. When Stokes Drift divergence is neglected, the wave forces become vertically homogeneous along the whole water column, except at the surface, where a small fraction of whitecapping occurs, confirmed with sensitivity runs removing the term for dissipation due to whitecapping.

H.2. OVERALL EVALUATION

The sensitivity runs showed that the distribution of wave force changed significantly in the vertical. The role of Stokes Drift divergence in the SAG flow is recommended to be studied as a further step. Simulations neglecting its inclusion in the momentum conservation equation could be used for that evaluation.

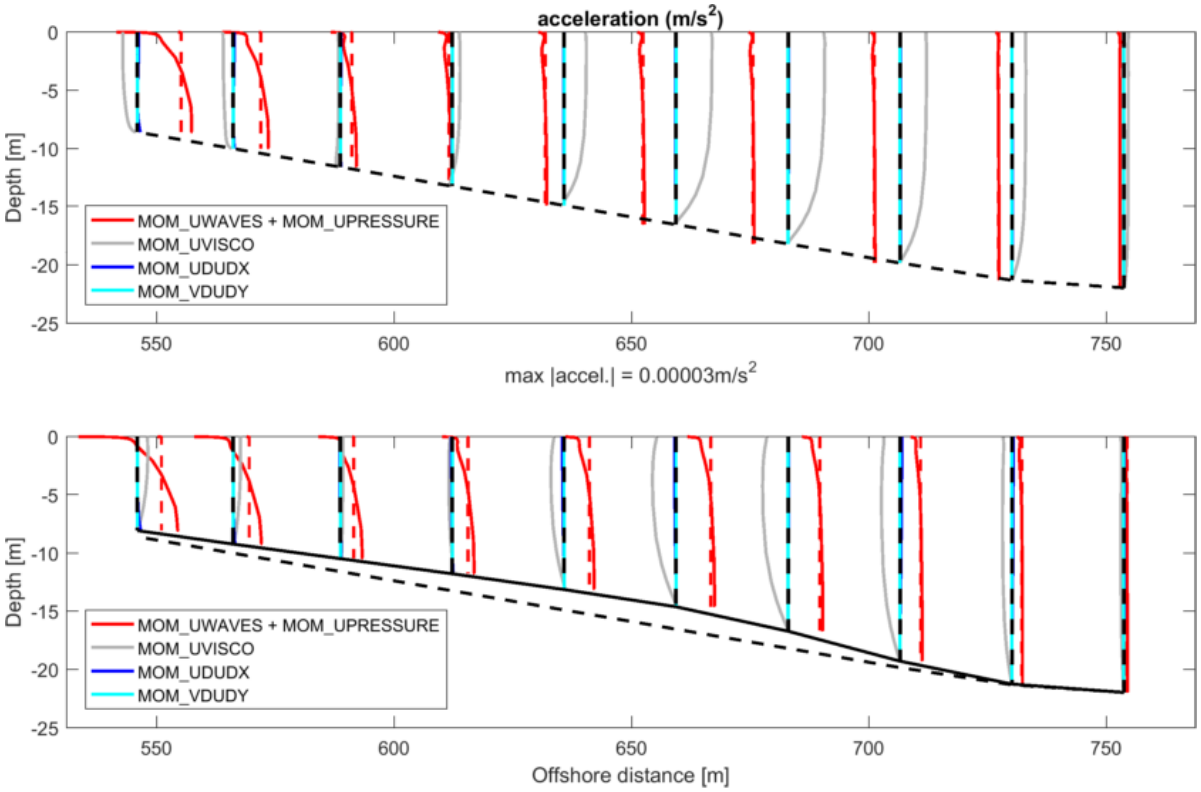

Figure H.1: Cross-shore views of Base Case results for cross-shore momentum terms on top of groove and spur - imbalance between pressure gradient and wave forces. MOM_UWAVES, MOM_UPRESSURE, MOM_UVISCO, MOM_UDUDX and MOM_VDUDY represent the wave forces, pressure gradient, horizontal viscous forces, streamwise and lateral advective accelerations, respectively. Full and dashed lines represent the result of simulation with and without the Stokes Drift divergence as part for the wave force output, respectively.